UNIVERSITEIT VAN PRETORIA
UNIVERSITY OF PRETORIA
YUNIBESITHI YA PRETORIA
Faculty of Engineering, Built Environment and Information Technology

Heat transfer of nanostructure coating on commercially micro-enhanced refrigerant tubes under pool boiling and falling film boiling conditions

Dian Dickson

Master's Degree, Mechanical Engineering

Department of Mechanical and Aeronautical Engineering
University of Pretoria
South Africa

Supervisor: Dr. Bradley D. Bock
Co-supervisor: Prof. John R. Thome

July 2023

Executive Summary

Refrigeration tube manufacturers commercially produce micro-enhanced tubes for the refrigeration industry with the aim to enhance outside heat transfer coefficients. A new engagement on commercially micro-enhanced tubes is to nanocoat these tubes in an inexpensive attempt to further enhance the heat transfer coefficients. Decreased nucleation site dryout because of increased wettability imposed by a hydrophilic copper oxide nanocoating is hypothesised to enhance heat transfer. In this study, commercially micro-enhanced tubes were nanocoated with copper oxide and tested in R134a refrigerant in pool boiling, and falling film boiling conditions; and additionally in condensation and dryout performance tests.

Relevant literature indicated high surface wettability from hydrophilic nanocoatings increasing heat transfer coefficients under pool boiling conditions. This was said to be due to less surface dryout because of the surface's liquid affinity, however, numerous studies resulted in heat transfer coefficient degradation because of nucleation site flooding and high surface energy requirement.

This study proved through scanning electron microscopy that copper oxide nanocoatings successfully coated all microstructured tubes evenly by using a coating procedure and a dedicated tube coating machine without impeding the surface features.

For the uncoated tubes in pool boiling at 5°C, the EHPII and GEWA-B5 tubes were the most independent from heat flux with flat heat transfer coefficient curves. They performed the best with heat transfer coefficients of 299% and 318% higher than a plain roughened tube, whereas the low-finned GEWA-KS performed moderately well with heat transfer coefficients 57% higher than the heat transfer coefficients of the plain roughened tube. An increase in saturation temperature to 25°C decreased the EHPII's heat transfer coefficients by 10%, whereas the GEWA-KS's heat transfer coefficients increased by 25%.

The copper oxide nanocoated tubes in pool boiling at 5°C performed similar to the uncoated tubes in pool boiling. However, the copper oxide nanocoating generally decreased the heat transfer coefficients from the uncoated case, where the EHPII, GEWA-KS and plain roughened tube had heat transfer coefficients approximately 89%, 91% and 85% of the uncoated heat transfer coefficients respectively. The GEWA-B5 was affected the most with heat transfer coefficients approximately 60% of the uncoated heat transfer coefficients.

For the uncoated tubes in falling film boiling at 5°C, the EHPII and GEWA-B5 tubes were the most independent from heat flux with flat heat transfer coefficient curves. They had a similar high heat transfer performance, whereas the GEWA-KS performed moderately well. The plain roughened tube's heat transfer coefficients had an average heat transfer coefficient of 8.6 $kW/m^2 \cdot K$. The increase in saturation temperature to 25°C decreased the EHPII's heat transfer coefficients with 7%, whereas the GEWA-KS's heat transfer coefficients increased with 7% on average.

The copper oxide nanocoated tubes in falling film boiling at 5°C performed with marginal im-

provement compared to the uncoated tubes in falling film boiling. The copper oxide nanocoating generally had a degrading effect on the GEWA-B5 and plain roughened tube achieving about 66% of the uncoated heat transfer coefficients. Moderate enhancement for the EHPII tube with a peak enhancement of 110% at 100 $kW/m^2$was seen, however remained steady at achieving 99% of the uncoated heat transfer coefficients on average. The greatest enhancement was achieved by the GEWA-KS with an average of 119% of the uncoated heat transfer coefficients, and a peak enhancement of about 160% at 20 kW/m^2, similarly seen at 25°C saturation temperature. The dryout performance tests showed no improvement for all tubes through the addition of the nanocoating and further experimental research is required to deduce an optimal multiscale enhancement to increase dryout performance.

The addition of the copper oxide nanocoating is therefore not a reliable option to enhance heat transfer coefficients except for the GEWA-KS tube under falling film conditions. Degradation of the heat transfer coefficients are thought to be due to the flooding of the nucleation sites and the degradation in the hydraulic bubble pumping action of the microstructure capillary channels facilitating the sensible and latent heat transfer.

The condensation tests showed a consistent degradation in heat transfer coefficients and is likely due to the inefficient dry surface exposure because of inadequate liquid expulsion from microstructure cavities and general surface liquid retention by the hydrophilic copper oxide nanocoating.

Publications

This thesis on heat transfer of nanostructure coating on commercially micro-enhanced refrigerant tubes under pool boiling and falling film boiling conditions was used to construct the following articles:

Conference Papers

B. D. Bock, D. Dickson, J. R. Thome, "Proposed Heat Transfer Degradation Mechanisms in Refrigerant Pool Boiling and Condensation on Nanocoated Commercially Enhanced Tubes", presented at the 11th International Conference On Boiling and Condensation Heat Transfer, Edinburgh, Scotland, 15 - 17 May 2023.

B. D. Bock, D. Dickson, J. R. Thome, "The reduction of refrigerant boiling dryout on falling film evaporator tubes through nanostructures, commercial microstructures and multiscale enhancements" to be presented at the 17th International Heat Transfer Conference, Cape Town, South Africa, 14 - 18 August 2023.

Journal Articles

The journal articles are under review at the time of writing:

B. D. Bock, D. Dickson, J. R. Thome, "Multiscale enhancement of refrigerant falling film boiling by combining commercially enhanced tubes with nanostructures", Applied Thermal Engineering, vol. 223, 2023.

D. Dickson, B. D. Bock, J. R. Thome, "Heat transfer of uncoated and nanostructure coated commercially micro-enhanced refrigeration tubes under pool boiling conditions", Applied Thermal Engineering, vol. 223, 2023.

Acknowledgements

This study could not have been performed without the input of the following persons.

Prof. John Thome: For his insight and guidance towards the testing directions in this study.

Prof Nico Theron: For his technical assistance in the management of the required software and concepts about liquid level control.

Dr Bradley Bock: For his constant guidance throughout this study, ideas and insight toward the development of the investigations.

Pr. Eng. Darian Dickson: For his professional advice toward the manufacturing of components, materials and ideas regarding the best approach.

Dr Elsie-Ida Grobbelaar: For her guidance toward ensuring safety, structure and help regarding review.

Dr Nicolaas Johannes Grobbelaar: For his overview of the conducting of experiments and for ensuring a safe environment for partial tests.

Ms Cornelia Weber: For her support and her validation of the chemistry used in the study.

Mr Koos Mthombeni: For his general assistance around the laboratory regarding tools and handwork.

Mr Sudhir Debising: For assistance in laboratory management and providing what was required to perform the study.

Mr Yathil Mathabadal: For his guidance and insight in material sciences for the successful scoping of materials capable of withstanding the chemical treatment procedures used to nanocoat the copper tubes with CuO.

Table of Contents

List of Figures

List of Tables

Nomenclature

Symbol	Description	Unit
A	area	$[m^2]$
C	arbitrary constant	
C_x	thermal heat capacity of	$[J/kg \cdot K]$
D	diameter	$[m]$
Δ	difference	
δ	deviation	
E	error	
$f(x)$	function of	
f	friction factor	
g	gravitational acceleration	$[m/s^2]$
Γ	film flow rate	$[kg/m/s]$
H	height	$[m]$
h_{fg}	latent heat of vaporisation	$[J/kg]$
h	heat transfer coefficient	$[W/m^2 \cdot K]$
k	thermal conductivity	$[W/m \cdot K]$
K	ratio	
m	mass	$[kg]$
μ	dynamic viscosity	$[Pa \cdot s]$
N	count	
Nu	Nusselt number	
P	pressure	$[Pa]$
Pr	Prandtl number	
q	heat flux	$[W/m^2]$
r	radius	$[r]$
R	thermal resistance	$[K/W]$
Re	Reynolds number	
ρ	density	$[kg/m^3]$
T	temperature	$[K]$
U	overall heat transfer coefficient	$[W/m^2 \cdot K]$
x	arbitrary independent variable	
y	arbitrary dependent variable	

Subscript	Description
ave	average
b	bubble
boi	boiling
c	cavity
CuO	copper oxide nanocoated
fc	forced convection
ff	falling film case
fg	latent
fs	falling film sweep
g	gas
Gnie	attributed to Gnielinski's correlation
h	hydraulic (effective Reynolds diameter)
i	with respect to tube inside
mid	midpoint of tube
o	with respect to tube outside
pb	pool boiling case
probe	pertaining to the thermocouple rod
r	refrigerant
sat	saturated state
sh	superheat
t	with respect to the tube wall
tot	total
v	vapour
w	water
wetted	wetted perimeter

Superscript	Description
’	derived
*	modified

Acronyms

CO_2	Carbon dioxide. 23
CuO	copper oxide. iv, v, vii, x–xii, 1–7, 9, 11–17, 20, 32, 35, 37, 53–61, 64–66, 69–86, 89–94, 96–103, 105, 106
R_a	Roughness Average. 32
ALD	Atomic Layer Deposition. 16
CA	Contact Angle. 9
CCV	Computer Controlled Valve. 27–29
CERG	Clean Energy Research Group. 2, 21
CHF	Critical Heat Flux. 14, 16, 17, 70, 76, 79, 86, 92, 105, 106
DAQ	Data Acquisition System. 30, 31
EPFL	École Polytechnique Fédérale de Lausanne. 21
FF rig	Falling Film Boiling Rig. x, 2, 5, 8, 21–23, 27, 29, 30, 32, 42, 47, 48, 50, 51, 104
fpi	fins per inch. 56, 77
fps	frames per second. 30
HTC	Heat Transfer Coefficient. v, xii, 3–5, 7–20, 36, 40–43, 45, 48–51, 53, 54, 56, 57, 59–62, 64, 65, 67–72, 75, 77, 79–98, 101–106
ID	Internal Diameter. 24
LED	Light Emitting Diode. 30
LTCM	Laboratoire de Transfert de Chaleur et de Masse. 21
NI	National Instruments. 30
OD	Outer Diameter. 25
PC	Personal Computer. 30, 31

PCI	Peripheral Component Interconnect. 31
pH	Power of Hydrogen. 33
PID	Proportional Integral and Derivative. 23
PPI	Pores per Inch. 24
PTFE	Polytetrafluoroethylene. 14
Re	Reynolds number. 41
RO water	Reverse Osmosis Water. 32
SEM	Scanning Electron Microscope. 9, 11, 13, 34, 36, 72, 101
UP	University of Pretoria. 2, 21
VI	Virtual Instrument File. 104

1 Introduction

1.1 Background

The field of heat transfer in mechanical engineering provides immeasurable opportunity for study. The Clean Energy Research Group with the Department of Mechanical and Aeronautical Engineering at the University of Pretoria takes great interest in the exploration of this field and is eager to expand on the knowledge of heat transfer.

A particular area of focus in the refrigeration industry is engaged where aspects of tubes used in the condenser and evaporator tube networks are altered and experimentally modified in an effort to see what influence these modifications have on their heat transfer performance. Other than the tube material itself being chosen for the maximum thermal conductivity, these aspects commonly include the profile of the tube inside, the profile of the tube outside, tube thickness and the roughness of the tube surfaces.

Some specialised refrigeration tube manufacturers commercially produce impressive and intricate micro-enhanced tubes for the refrigeration industry which are capable of enhancing the tube outside heat transfer coefficients (HTCs) [1, 2]. A new opportunity on commercially micro-enhanced refrigeration tubes is the nanocoating of these tubes with nanostructures in a quick, easy and inexpensive attempt to enhance the heat transfer coefficients even further.

This study focuses on the investigation of nanocoating Wieland's commercially microstructured refrigeration tubes, namely the EHPII, GEWA-B5 and the GEWA-KS; with a copper oxide (CuO) nanostructure coating. This CuO nanocoating comprises a surface coating of flat and elongated triangular shards on nanoscale, protruding randomly from the surface in mostly an upward direction. The CuO nanostructures which makes up the CuO nanocoating is described by Figure 1.1:

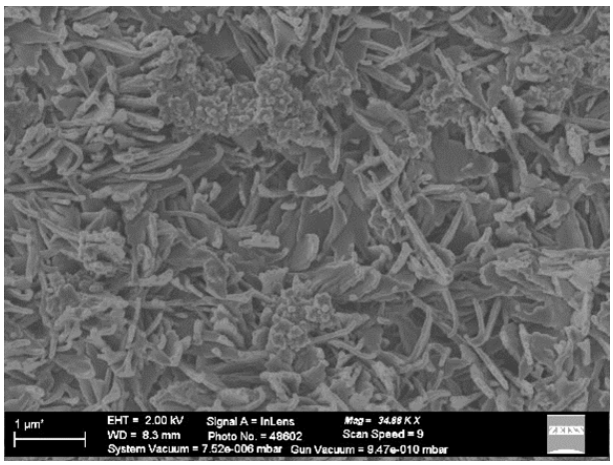

Figure 1.1: Micrograph depicting a typical CuO nanostructure construction in a CuO nanocoating

The schematics in Figure 1.2 depict the nanocoating on Wieland's specialized microstructured tubes where the basic microstructure profile is negligibly altered by the nanocoating:

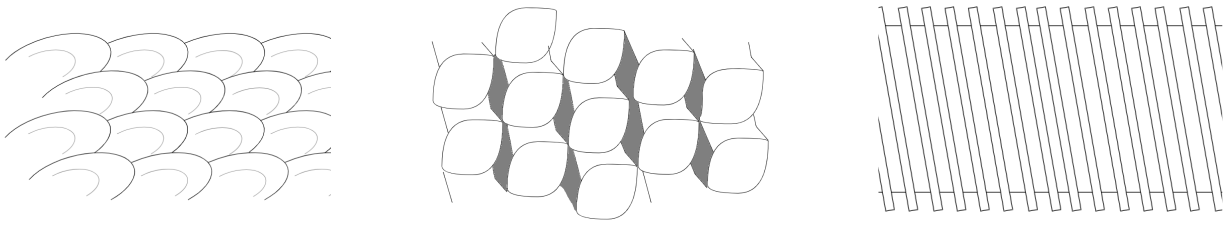

(i) EHPII (ii) GEWA-B5 (iii) GEWA-KS

(a) Uncoated

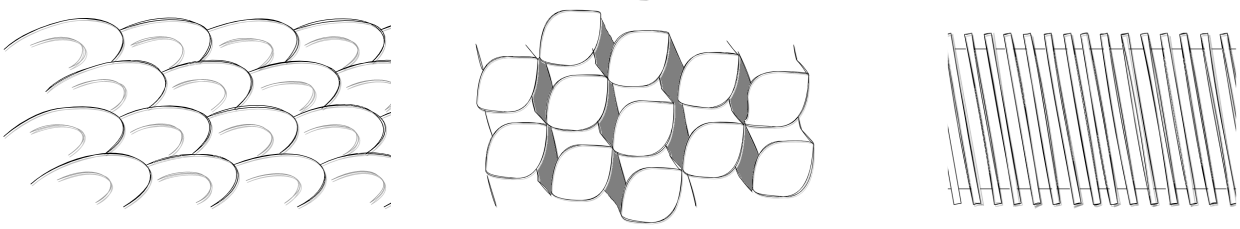

(i) EHPII (ii) GEWA-B5 (iii) GEWA-KS

(b) Nanocoated

Figure 1.2: Uncoated and nanocoated Wieland microstructured tube schematics

The nanocoating on the micro-enhanced tube may introduce additional heat transfer mechanisms on the tube surface depending on its structure. A copper oxide (CuO) coating, used previously at the Clean Energy Research Group (CERG) laboratories, has shown to introduce a wicking action and is hydrophilic.

The speculations surrounding the mechanism by which the nanostructure nanocoatings aid the microstructure layer underneath need to be clarified. The greatest estimate is the advanced capillary action with a subsequent reduced dryout underneath the bubbles at nucleation sites. This wicking action would be expected to abundantly feed the nucleation sites and ensure a prominent superheated refrigerant liquid micro-layer to sustain bubble growth with minimal solid-vapour contact between the tube and the bubbles. However, the experimental rig used in this study cannot directly measure the exact mechanism the combination of the CuO nanocoating with microstructures has on heat transfer, but merely measures the heat transfer change through the addition of the nanocoating.

The tests will be performed using the Falling Film Boiling Rig (FF rig) at the University of Pretoria (UP) Thermoflow Laboratory. The tubes are tested under pool boiling and falling film boiling conditions, along with sufficient past research, guidance, proper equipment and readily available chemicals. The study will develop to see if nanocoating tubes, especially on micro-enhanced tubes, promotes or obstructs heat transfer through falling film and pool boiling heat transfer experiments. The coatings in this study will only consist of CuO nanocoatings on the outer surface of the micro-enhanced tubes (with the inside tube surface left unaltered), where the CuO nanostructure's effects on heat transfer coefficients are observed. There are numerous theories towards why this may or may not be beneficial and must be elucidated.

The falling film boiling configuration also has potential advantages over pool boiling in that it requires much less fluid in the system to function [3].

This study will hereby produce heat transfer results over a testing heat flux range through tube outside Heat Transfer Coefficient (HTC) points, as well as dryout and condensation HTCs to evaluate and compare the influence the addition of a CuO nanocoating on microstructures has on heat transfer performance.

1.2 Problem Statement

The influence on heat transfer coefficients by a nanostructure layer coated onto to a series of different commercial micro-enhanced surfaces is unknown. These studies on nanocoatings on microstructured surfaces have been confined to very specific and small-scale experiments with non-commercial enhancements, or where the heat transfer investigations have been done predominantly with water [1, 4–6].

Furthermore, there is a general lack of understanding regarding the CuO nanocoatings in pool boiling and falling film boiling activity.

The influence on dryout performance by the CuO nanocoating on microstructured tubes under falling film boiling is mostly unexplored.

The research surrounding condensation heat transfer of CuO nanocoated microstructured tubes is also insubstantial.

1.3 Aim

This study aimed to experimentally investigate the influence on heat transfer coefficients through the addition of a CuO nanocoating applied to 3 commercially micro-enhanced (microstructured) refrigeration tubes and a roughened tube internally heated by water in the pool boiling, falling film boiling and condensation heat transfer configurations in R134a refrigerant. Comparisons were made to the respective uncoated microstructured tubes.

The boiling mechanics as a result of the CuO nanocoating were inferred, which particularly included the hydraulic effects surrounding the boiling phenomena. The influence on dryout under falling film boiling by the CuO nanocoating on the tubes were additionally investigated to contribute to the understanding of the mechanics imposed by the CuO nanocoating.

Condensation heat transfer was experimentally investigated to compliment the boiling heat transfer findings for a comprehensive study.

1.4 Objectives

The goals of this study are to elucidate the following using experimental investigation:

- Pool boiling and falling film boiling experimental tests are to be conducted on uncoated and coated sets of the roughened tube, GEWA-B5, GEWA-KS and the EHPII tubes

at 5°C saturation temperature. The uncoated smooth tube is also to be tested under pool boiling and falling film boiling for validation tests. Additionally, the uncoated and coated sets of the GEWA-KS and EHPII tubes must be experimentally investigated under pool boiling and falling film boiling conditions at 25°C saturation temperature. All pool boiling and falling film boiling tests will be conducted with the HTCs recorded at heat flux points ranging from 20 $kW/m^2$to 100 kW/m^2. All falling film boiling tests will be done at a film flow rate of 0.13 $kg/m/s$.

- Condensation heat transfer tests will be performed on uncoated smooth, roughened, GEWA-KS and EHPII tubes. CuO coated GEWA-KS and EHPII tubes will be included in condensation tests. These tests will be performed at a 30°C saturation temperature.
- Dryout performance tests are to be experimentally conducted at a saturation temperature of 5°C where uncoated and coated sets of the GEWA-B5, GEWA-KS and EHPII tubes will be subjected to falling film boiling and the HTCs recorded from a film flow rate of 0.13 $kg/m/s$ up to where boiling becomes unsustainable. The dryout performance tests will be conducted at constant heat fluxes of 20 kW/m^2, 50 kW/m^2 and 80 kW/m^2.
- The visual observation of the CuO nanostructures under SEM analysis must be clarified since there is a large inconsistency in experimental research studies showing of CuO nanostructure formations.
- A standardised method to preparing tubes must be pursued for the consistency in tube conditions amidst heat transfer studies, especially for the nanocoated tubes. The CuO nanocoating's synthesis is therefore to be explored and the reviewed coating procedure to be implemented through a dedicated coating machine.
- Data analysis procedures are required for the analysis of the nanocoating influence on the heat transfer relative to the uncoated tube and must be defined.
- The Wilson Plot internal heat transfer Gnielinski modification factor C_i, must be reliably obtained through the Wilson Plot experimental procedure for all tubes in the study, especially the EHPII tube and the GEWA-KS tube.
- Apart from the plain tube and the GEWA-B5 tube, some pool boiling and falling film heat transfer experimental research to obtain heat transfer performance data (HTC-q) still need to be conducted on the EHPII tube and the GEWA-KS tube. However, all tubes still need to be observed under these conditions being uncoated as well as coated with the same CuO nanocoating.
- It is unclear what effect the saturation temperature has on the heat transfer performance of uncoated GEWA-KS low fin tubes and EHPII tubes, as well as the CuO coated versions of these tubes and must therefore be experimentally investigated.
- All heat transfer experimental tests are to be conducted in R134a refrigerant as the working medium. The tubes will be heated or cooled from the inside using water.

- The motion of the liquid during pool boiling, falling film boiling and condensation is unclear amongst previous research where high speed footage showing the behaviour of boiling is deficient and must therefore be captured during boiling and condensation experiments in order to make viable conclusions.
- Deduce if there are any preferred combinations of microstructure type with the nanocoatings from the heat transfer performance outcome behaviours of the uncoated and coated tubes.
- Identify possible patterns or specific surface features of these microstructured surfaces for respectable heat transfer coefficients observed.

1.5 Overview of Thesis

A brief description of the development of the experimental study is provided as follows:

Chapter **2**: The Literature Review explores the applicable literature and previous research surrounding the characteristic aspects of nanocoatings and CuO nanocoatings. The pool boiling and falling film boiling heat transfer expectations from CuO nanocoatings on microstructured surfaces are also explored, which are complimented by existing heat transfer research on commercially microstructured refrigeration tubes.

Chapter **3**: The Experimental Setup describes the FF rig experimental facility which makes experimental heat transfer investigations possible through pool boiling, falling film boiling and condensation tests, including dryout tests and Wilson Plot tests.

Chapter **4**: The Data Reduction describes the classical heat transfer calculations used in the study as well as standardised mathematical procedures for comparison during analysis.

Chapter **5**: The Validation included pool boiling, falling film boiling, condensation and Wilson Plot tests to compare results to previous research and thereby endorse the integrity of the results to be produced in the current study.

Chapter **6**: The Wilson Plot Analyses experimentally investigate the Wilson Plot coefficients to modify the Gnielinski correlation for each tube type. The internal heat transfer is therefore accounted for to solely compare tube outside HTCs.

Chapter **7**: The Pool Boiling Results and Discussion encapsulate the uncoated and coated tube sets' pool boiling results, as well as the comparisons and analyses thereof.

Chapter **8**: The Falling Film Boiling Results and Discussion encapsulate the uncoated and coated tube sets' falling film boiling results, as well as the comparisons and analyses thereof. The enhancement of the falling film boiling configuration over the pool boiling configuration are studied. The dryout performances of

the uncoated and coated tube sets are also examined.

Chapter **9**: The Condensation Results and Discussion are given as a brief exploration into the influence of the CuO nanocoating on commercially microstructured tubes.

Chapter **11**: A Conclusion to the study is provided which outlines the fundamental discoveries of the investigation. A final decree of the CuO nanocoating on microstructures is outlined.

Chapter **10**: A summarizing compilation of all the significant data evaluations from the study are tabulated.

Chapter **12**: Recommendations towards the possible improvement upon the study are suggested. Other directions of study are proposed towards further development.

2 Literature Review

2.1 Introduction

This chapter provides an overview of the important concepts and previous research with respect to pool boiling, falling film boiling and condensation.

It covers the boiling media, the relevant heat transfer regimes seen in the study, the refrigerant used, saturation temperatures and their effects on HTCs, surface microstructure effects, coating nanostructure effects, surface wettability characteristics, the mechanisms of heat transfer on microstructured surfaces, a comprehensive survey on previous studies and their basic findings on generic boiling on nanostructured surfaces, falling film heat transfer enhancement, falling film dryout and lastly the workings behind condensation heat transfer.

The literature survey facilitates the development of the current study on the heat transfer on CuO nanocoated microstructured tubes.

2.2 Heat Transfer Regimes

Depending on the testing heat flux ranges, the boiling phenomena would have assumed different behaviours that were described by Nukiyama's Boiling Curve as shown in Figure 2.1:

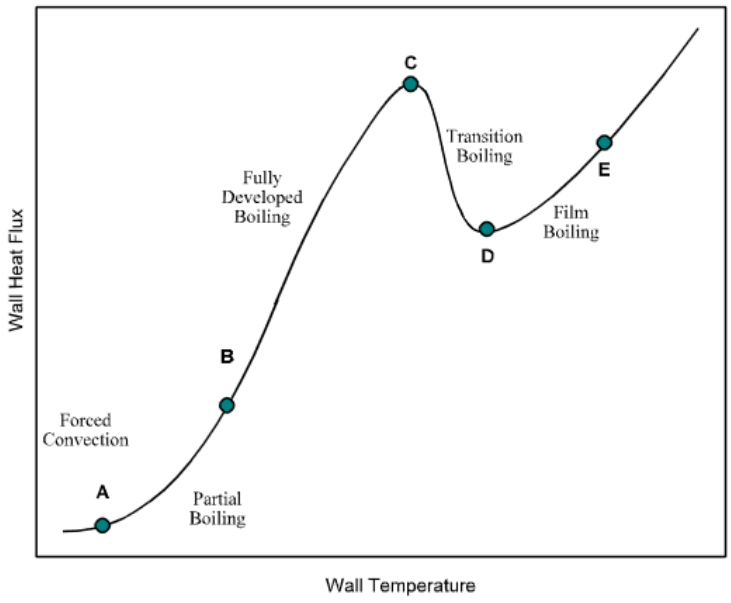

Figure 2.1: Nukiyama's boiling curve showing boiling regimes (adapted from Theron et al. [7])

There were many correlations that described Nukiyama's boiling curve for a particular circumstance with the boiling medium used [7]; however, this boiling curve was shown to be an inherent characteristic of boiling behaviour with increasing heat flux. This was necessary to realize the limitations of this study as well as to understand the possible impediments to heat transfer mechanisms.

According to Figure 2.1, the boiling regimes were classified according to natural convection (A-B), nucleate boiling (B-C), transition boiling (C-D) and film boiling (D-E). It was generally

impractical and inefficient for boiling to operate in the transition boiling and film boiling regimes due to the burnout effect at high heat fluxes as equipment usually suffered damage from this occurrence [8]. The focus of this study was therefore preferably to investigate the natural convection and nucleate boiling regimes (A-C).

Furthermore, the 'falling film' mentioned in the Falling Film Boiling Rig (FF rig) referred to the setup of a thin film layer of liquid flowing over a horizontal tube in a uniform layer under the action of gravity. This must not have been confused with the 'Film Boiling' phenomena which occurred under the Leidenfrost Effect when the temperature difference between the surface and the fluid was great enough to have a vapour layer largely separating the surface and the fluid [8]. The FF rig would have been used to conduct heat transfer experiments on the tubes to determine the heat transfer coefficients both in a pool boiling and falling film boiling configurations. Pool boiling was a configuration setting in the FF rig. The entire surface of the tube was submerged in the cold medium and was stationary, except for the movement induced by the boiling itself [9].

An important repeating event in the boiling phenomena was the emergence of the ebullition cycle during nucleate boiling. The ebullition cycle was a repetitive cycle which pertained to the fluid motion created by the formation, development and release of bubbles from the heating surface. The ebullition cycle was important for the design of the hydraulic action surrounding the refrigerant on microstructured tube and for the optimisation of their heat transfer.

Furthermore, some observations were made regarding the bubble departure diameter which may have indicated surface temperature and temperature superheat qualities corresponding to the boiling regime. It was described in Moita et al. [10] that a bubble's departure behaviour was dependent on buoyancy and surface tension at low superheats. With increasing superheat, the inertial forces in bubble dynamics govern the development thereof and would have resulted in an increase in bubble diameter.

2.3 Saturation Temperature

The common pool boiling theory stated that the HTCs of tubes should generally increase with an increase in saturation temperature mainly due to the latent heat of vaporization being less for easier activation of nucleation sites [11]. However, some discrepancy arose under the testing of microstructured surfaces where there was a decrease in HTCs as saturation temperature increases. This phenomena was explained by Ribatski and Jacobi [3] and noted by Acu [12] where it was thought that the increase in bulk temperature would have created higher thermal gradients which could possibly have inhibited bubble growth dependent on the specific geometry of the microstructure in which nucleation took place. The change in thermal gradients over the profile of the microstructures altered the position along which nucleation originated and could thus have influenced the heat transfer performance to be either improved or be degraded.

2.4 Wettability

The wettability of a surface was its ability to interact with the working fluid so as to cover the liquid over its surface. Wettability was often measured and quantified through water droplet contact angle Contact Angle (CA) measurements, where CAs from 0° to 90° corresponded to high wettability surfaces and CAs between 90° and 180° corresponded to low wettability hydrophobic surfaces [13]. A hydrophilic surface favoured the liquid interaction and had CAs close to 0° where the liquid-surface adhesive forces dominate the liquid cohesive forces. A hydrophobic surface resulted in the liquid being pushed together (forming a distinct droplet with CA close to 180°) as the liquid cohesive forces dominated the surface-liquid adhesive forces.

A study by Köroğlu et al. [14] investigated the surface chemistry, surface interface behaviour and wettability of a CuO coating through a Scanning Electron Microscope (SEM) and contact angle tests on copper tubes. It was found that the wettability could be modified through the molarity of the $NaOH$ in the alkali coating solution used, where the lesser concentration led to the surface being hydrophilic and the greater concentration to a hydrophobic surface [14]. The hydrophobicity of the tube surfaces could hereby be controlled which would be beneficial for future investigations on wettability and its influence on heat transfer.

It was also noted by Moita et al. [10] that boiling media with low surface tension delayed the onset of nucleation as it fully wetted the surface. To proceed to the incipient boiling regime, these high wettability circumstances would have required a larger temperature superheat for a subsequent increase in latent heat of evaporation. Furthermore, the higher surface tension in the boiling media would have facilitated vapour entrapment to form a vapour film over the surface. This would have resulted in a decrease in HTCs [10].

In a study by Sujith et al. [15], very specific surface geometries (cross-sectional profile patterns which were also microstructures) were manufactured, which generated a hydrophobic behaviour on their own and were combined with super-hydrophilic coatings. They have shown to deliver some heat transfer enhancement. It was found that the plain surface coated with a SiO_2 hydrophilic coating performed approximately 21% worse than the plain copper copper surface. However, when combined with a hydrophobic geometry profile, the heat transfer performance was enhanced by approximately 14%. A wide range of heat transfer enhancement was seen by combining the coatings with different geometry patterns, suggesting that there were favourable combinations of geometry profiles and the coating. This will have been observed in the current study where the CuO coating will have been combined with commercially microstructured surfaces, however, the microstructured surfaces in the current study could not be modified or built specifically for the fine tuning with regards to the CuO coating. Furthermore, it was found by Sujith et al. [15] that the bare copper surface (which was moderately hydrophobic in nature as seen by its CA) combined with a geometry pattern which generated a hydrophobic behaviour, outperformed the other surface geometry-coating combinations where a heat transfer enhancement of approximately 35.7% was found. This may suggest that a total hydrophobic surface configuration could have been favourable.

2.5 Microstructures

Microstructures were the extrusions made on top of the surface and were measured comfortably in the units of micrometres (10^{-6} m) in an attempt to have improved heat transfer coefficients. These structures were usually manufactured through machining and came in various repetitive shapes, sizes and complexities. A typical method to produce such structures was to use the technique of knurling executed through a lathe (or similar turning machine) and a die. Examples of the WIELAND GEWA-B5 [16] and the GEWA-KS [17] microstructured tubes with their surface enhancements are shown in Figure 2.2:

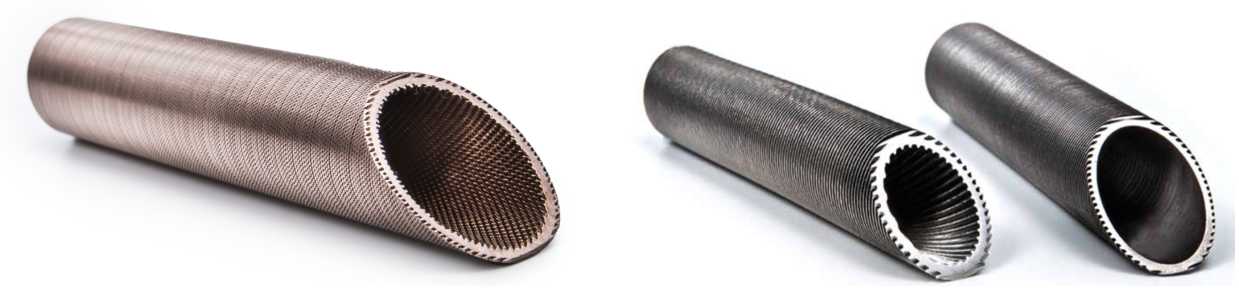

(a) GEWA-B5 (b) GEWA-KS

Figure 2.2: WIELAND microstructured refrigeration tubes

The simplest microstructures were surface roughness cavities. Increasing the surface roughness by roughening tubes with sandpaper increased the number of cavities to promote increased nucleation site density and heat transfer area for enhanced heat transfer [18].

Low fin tubes, such as the GEWA-KS tube, were a simple class of microstructured refrigeration tubes (although they could arguably be classified as macrostructures) whose surfaces have been extruded with fins that spiral along the tubes. They predominantly increased the HTCs through increased surface area created by the fins. A larger surface area allowed greater opportunity for heat transfer [19, 20].

A more sophisticated class of microstructured tubes were tubes with 3D surface enhancements. They had re-entrant cavities which significantly enhanced heat transfer compared to plain and low finned tubes and produced characteristic HTC behaviour. Re-entrant cavities contributed to heat transfer through additional hydraulic action where fluid flowing through the cavities was driven by a bubble pumping action. This bubble pumping action may have greatly assisted sensible heat transfer. The re-entrant cavities also increased nucleation sites and therefore nucleate heat transfer [21].

2.6 Heat Transfer on Microstructured Surfaces

The micro-enhancements on plain tube surfaces were expected to enhance existing heat transfer mechanisms as well as introduce new mechanisms for heat transfer to occur.

Models to describe HTC enhancement by microstructures were provided, however, it was made clear that the parameters were quite heuristic. Hereby, it was noted that a substantial amount

of heat transfer studies could still be performed regarding microstructured surfaces [22].

Two main mechanisms of enhanced boiling heat transfer through microstructures had been identified through experimental investigation by Cooke and Kandlikar [23]:

- **Surface Area:** The microstructures greatly increased surface area in comparison to the plain surfaces where a larger interface between the boiling media and the surface was established for improved heat transfer. This was the primary mechanism of heat transfer enhancement of fins. Kruse et al. [24] indicated that boiling heat transfer enhancement was dominated by the simple increase in surface area. The HTCs in the study by Cooke and Kandlikar [23] were normalised to the tube surface area and produced the same curve behaviour.
- **Bubble Dynamics:** Manipulating the dynamics of the bubble through its specific interaction with the microstructures where this motion could have been dependent on the profile of these microstructures was thought to enhance heat transfer. Some simple bubble and hydraulic behaviours were identified that are thought to influence the effectiveness of boiling heat transfer through the insight of Jung et al. [20]:
  - The nucleation of a bubble was initiated by the microstructures (channels or pores) from where the bubbles grew. A bubble sliding on a superheated base layer or being in close proximity to microstructure channels could be beneficial to heat transfer.
  - Microstructures aided in hydraulic movement where the surface remained flooded for rapid recurring nucleation.
  - The microstructures increased nucleation site density.

The following heat transfer mechanisms for enhanced surfaces identified by Thome [25] further refined and appended to the findings by Cooke and Kandlikar [23]:

- Microstructures, especially those of re-entrant cavity designs, permitted nucleation at lower temperature superheats.
- Stagnant superheated thin film evaporation in nucleation cavities greatly enhanced HTCs.
- Fluid capillary action to sustain a nucleation cavity with liquid feed as well as the evaporation within these cavities could enhance HTCs.

2.7 CuO Nanostructures

Protrusions on a surface which were measured comfortably in the unit of nanometres (10^{-9} m) were termed nanostructures in this study. These nanoscale structures were small enough not to be observable by the naked eye, but discoloured the surface of the tube. These nanostructures could only be perceived completely through a Scanning Electron Microscope (SEM). These nanostructures did not necessarily consist of the same chemical composition as the base layer (copper, as observed in this study). Nanostructures were not usually manufactured through machinery nor through a mechanical process, but rather a chemical process. For example,

nanostructures could be induced through the surface being exposed to a solution and reacting to create the desired nanostructure layer, hereby 'coating' the surface. Importantly, the nanostructure may have been applied either on a plain smooth copper tube, or on a copper tube which had its surface modified with post-process micro-enhancements [26].

The synthesis of CuO nanostructures had many approaches. However, the process of coating through an alkali solution was most common. The concentrations of the reagents in which the copper was oxidized greatly impacted the morphology of the nanostructures as could be seen in the study by Köroğlu et al. [14]. It was observed that lower concentrated $NaOH$ solutions produced sharp shard-like nanostructures on the copper surface which enhanced wettability, as seen in this study, whereas round particulate nanostructures formed at higher concentrations of $NaOH$ which led to a hydrophobic surface.

2.8 Boiling on Nanostructured Surfaces

It would seem that the exact outcome of applying coatings to surfaces with microstructures was vague. For example, in the study by Rau and Garimella [27] jet impingement experiments were performed on uncoated and coated flat and microstructured surfaces. The coating had a negligible to extreme positive and negative effect on the boiling heat transfer performance between testing circumstances. Because of this, some investigations on the preliminary enhancement and degradation of HTCs through nanocoatings applied to various types of surfaces were explored.

2.8.1 HTC Enhancement

Many types of nanostructures could be synthesised of varying sizes, shapes, porosities, interconnectivities and chemical properties. Some nanostructured surfaces could promote heat transfer while others depreciate heat transfer [28].

A comprehensive study was performed by Sujith et al. [29] where the hydraulic mechanisms were explored around heat transfer on nanostructure coatings. A focus on the reaction of carbon nanotubes and the flow velocity of the boiling medium were accentuated where a high flow rate, a low flow rate and the vapour film thickness on the nanocoating was explored as well as the effect of the coating with these flow rates on the boundary layer thicknesses. It was stated that the porosity of the coatings had to be favourable where the modulation height of the nanostructures must be close to the 'pitch value' of the nanostructures for great heat transfer enhancement. It was also stated that heat transfer enhancement at higher heat fluxes was attributed to the effective hydraulic mechanisms of the sufficient capillary wicking action, vapour-liquid counter flow, capillary evaporation and the favourable higher interaction between bubbles [29].

Porous surfaces were accredited for the local pumping action from the pores on their surface where nucleation sites' bubbles had a greater departure frequency and in turn greater heat transfer performance. Furthermore, it was found that the hydrophobic surfaces induced the

Cassie-Baxter state, whereas the hydrophilic surfaces were prone to induce Wenzel states (these findings were observed on micro-pillar and micro-hole nanocoatings). An important hydraulic disparity between the hydrophilic and the hydrophobic surfaces from nanocoatings, and the surfaces they were coated on, were with respect to the ebullition cycle: During bubble departure, the entire bubble tended to depart from the hydrophilic surface, whereas small residual bubbles tended to stay behind on hydrophobic surfaces. Sujith et al. [29] explained that this caused a 'waiting period' for the next bubble to form along with the ebullition cycle whereas there was no waiting period on the hydrophobic surface and the heat transfer performance was thus greater on the hydrophobic surface than the hydrophilic surface at the same heat flux testing point. It was deduced that the hydrophobic surface thus seeded the next bubbles for easier bubble development.

A study by Hee et al. [30] investigated pool boiling on a bare and vertically aligned multiwalled carbon nanotube coated silicon wafers. Nucleate boiling heat transfer was enhanced by approximately 23%. It was believed that the enhancement was mainly due to increased nucleation site density, increased surface area and a high quality bubble departure frequency as well as a discontinuous thermal micro-layer which was disrupted by the protruding carbon nanotubes [30]. It must be noted that the nanostructures were seen from the SEM to be well organised. Furthermore, the wettability of the nanostructures were not alluded to in the study by Hee et al. [30].

A brief falling film boiling investigation on CuO nanocoated plain tubes which focused on falling film dryout tests was performed by Köroğlu et al. [14]. The falling film dryout tests (film Reynolds sweeps) were experimental tests where the tube outside HTCs were measured as the falling film flow rate was decreased. It was consistently found that heat transfer was enhanced by the nanocoating and it was speculated that this was due to the increased wettability ensuring less dryout and dryspots on the tubes [14]. These were similar to the findings by Bock [1] where HTCs were enhanced by a maximum factor of 1.2 by a CuO nanocoating on a plain tube at 5°C in R134a and 1.5 at 25°C in pool boiling, and where HTCs were enhanced by maximum factor of 1.2 at 5°C and 1.8 at 25°C in falling film boiling [1].

A study by Kunugi et al. [31] found great HTC enhancement through a CuO nanocoating performing 180% better than the standard case by analysing a co-current heat exchanger. A finite molecular model simulation was also constructed to pursue the explanation of heat transfer. It was found that the exact mechanism for this heat transfer remained vague and required further investigation [31]. A significant observation was that the cases in which HTC enhancement took place, mostly included a porous nanocoating. Other researchers, however, such as Lee et al. [32], attempted to have created porous layers by coating plain tubes with copper powders to enhance wettability and improve wicking. It was found that the heat transfer was doubled through the aid of the coating, facilitating capillary wicking for complete wetting.

An experimental investigation by Patel et al. [33] testing boiling of water on CuO nanocoated copper plates, showed that the hydrophilic surface increased HTCs between 40% and 80%. The

CuO coating synthesis was, however, executed through a spinning technique which increased the wettability and nucleation site density [33]. The roughness was also significantly increased by this particular CuO coating type and this could be attributed to the significant increase in nucleation site density.

The CuO nanocoating applied to a stainless steel surface using a sol-gel dipping technique by Joseph et al. [21] was explored under pool boiling circumstances and compared to the plain surface. It was found that the CuO surface which was generated from a 1 M (molarity or concentration typically measured in mol/L) concentrated solution enhanced the HTC by a maximum of 30%. The study indicated that the CuO surface was more comparable to a hydrophobic surface. It was found that increasing the molarity of the coating solution from 0.5 M to 1 M increased the porosity, roughness, hydrophobicity and, as a result, the increase in active nucleation sites and heat transfer performance; whereas the further increase in molarity from 1 M to 1.5 M of the coating solution decreased the active nucleation site density and the heat transfer performance [21]. It would hereby have been viable to investigate the different concentrations of CuO coating molarities (concentration) applied to the microstructured surfaces, since both a hydrophobic and hydrophilic nature could be induced on the surface for boiling heat transfer research.

Regarding engineered surfaces, as a highly controlled construction of a surface with desired properties through nanostructure coatings (a coating which introduces microscopic structures on a substrate surface), it was documented by Attinger et al. [34] that surfaces engineered to be hydrophobic promoted boiling. This was determined through the analysis of Gibbs free energy equations where it was determined that the ϕ grouping term tend to zero with superhydrophobic surfaces to result in nucleation at low superheats. This conformed to the findings by Rahman and McCarthy [35] where the Polytetrafluoroethylene (PTFE) coatings were shown to lower the superheat required for nucleation and consequently enhanced HTCs.

2.8.2 HTC Degradation

A comprehensive study on the enhancing mechanisms was performed by Rahman and McCarthy [35] to analyse the mechanisms of HTC enhancement by CuO nanocoated plain surfaces. It was clearly found that CuO nanostructure coatings degraded HTCs significantly by approximately 35% through restricting nucleation sites. It was, however, indicated that Critical Heat Flux (CHF) was increased through the increased wettability. Nucleation activation was indicated to rather be improved by a hydrophobic surface. The design of an intricate surface of superior heat transfer performance was undertaken through the collected results: A heterogeneous surface was intuitively constructed by alternating superhydrophobic Polytetrafluoroethylene (PTFE) and CuO coated strips on the surface to induce mixed wettability and to enhance both HTCs and the CHF. This combination proved to have greatly enhanced the ebullition cycle to specifically have the hydrophilic surface where liquid wickability was desired and the hydrophobic surface where nucleation and heat transfer was desired. These biphilic surfaces outperformed normal nanocoated surface with a 270% increase in HTCs [35].

Additionally, it was documented that hydrophilic coatings were thought to deliver lower HTCs than hydrophobic coatings, but outperformed the hydrophobic coatings with higher CHF points to sustain boiling [36].

2.9 Multiscale Enhancement

There existed a limited amount of literature available for review prior to the current study regarding general heat transfer on microstructures that were augmented with CuO nanostructures. Other nanostructures, however, were tested in multiscale enhancement setups. The heat transfer on microstructures coupled with nanostructures remained a field of opportunity for research, although contemporary studies have emerged for review and set the drive for research in motion.

A case of heat transfer enhancement was observed by Xu and Li [37] where the HTCs were increased through a CuO nanocoated grooved plate by a maximum of 15%. They tested an uncoated and a CuO nanocoated flat grooved plate where the coating specifically featured CuO nanoflowers as would be seen in the current study. However, the experiments conducted by Xu and Li [37] indicated the heat transfer enhancement took place during tests where the flat plate was simultaneously heated and cooled at different regions on the plate and where boiling occurred continuously. It was speculated that the heat transfer enhancement was due to the super-hydrophilic surface created by the CuO nanocoating, where the prevention of dryout was enforced by coolant being wicked to the dryout spots as opposed to the uncoated flat plate.

Additionally, falling film boiling studies have been performed on plain, condensation and boiling (microstructured) tubes by Jin et al. [38] where uncoated tube HTCs were compared to the HTCs of tubes that have been coated with a hydrophobic coating. The hydrophobic coating in the study was generated by coating the tube surfaces with chlorofluoro material [38]. Insignificant changes in heat transfer performance were seen between the uncoated and coated plain and condensation tubes, however, a substantial increase of up to 60% in HTCs was found from the uncoated boiling tube to the hydrophobic boiling tube. It was noteworthy that great enhancement in the higher heat flux ranges was found where the HTC typically did not increase anymore in normal falling film boiling studies [36].

It was also speculated that the hydrophobic coating offered less frictional resistance for two-phase flow through the micro capillary channels to aid in the liquid supply to nucleation sites and to assist in the bubble pumping action [38].

An experimental study by Sen et al. [39] conducted water pool boiling heat transfer on CuO nanocoated copper plate surfaces that have been previously prepared with grade 1000 grit sandpaper to micro-enhance the tube for more nucleation sites. The study included alkali coating solutions with slightly different molarities than in the current study. Both hydrophilic and hydrophobic surfaces were created by changing the reagent proportions in the alkali coating solution. It was found that the enhanced capillary action feeding water to the microstructure nucleation sites prohibited early onset of vapour blanket formation in order to increase the

CHF point. It was found that the CuO nanocoated hydrophobic surface enhanced the heat transfer the most, with HTCs approximately 2 times more than the bare copper surface. The hydrophilic surface also enhanced heat transfer, where the HTCs were approximately 1.3 times more than the bare copper surface HTCs at best. It was stated that the hydrophobic surface required less surface energy for the onset of nucleate boiling, but reached the CHF point very soon as opposed to the hydrophilic surface [39].

It must be noted that the heat flux testing range was from 200 kW/m^2 to 1600 kW/m^2 from where heat transfer enhancement was observed. It may therefore have been a beneficiary venture forward for the current study which only observed heat transfer between 20 kW/m^2 and 100 kW/m^2.

The HTC enhancement by falling film boiling was briefly interpreted as the microstructures promoting convective effects to enhance both sensible and latent heat mechanisms where optimized thin-film microlayer evaporation was accredited for great HTC enhancement [4]. A comprehensive review by Kim et al. [4] was compiled for the exploration of nucleate boiling heat transfer and critical heat flux performance on micro/nanostructured multiscaled surfaces which included a wide array of mechanically machined, coated, chemical processed and Micro/Nano-electro mechanical system (MEMS/NEMS) surfaces (the MEMS surfaces were created through a lithography procedure and iron etching). In a case where microstructures were constructed on a copper tube through a rolling process to create re-entrant cavities as well as similarly having tunnelled surfaces with a porous coating, it was discovered that the hydraulic behaviour of the boiling of R134a and 2-Propanol changed so that the bubbles developed differently. The bubbles also departed and slid differently compared to the various surfaces tested, suggesting that the hydraulics surrounding microstructured and added upon nanostructure coatings had an influence on the boiling phenomena [4].

It was noted that nucleate boiling heat transfer enhancement through multiscale constructed surfaces included bubble ejection frequency being higher, as well as increased the active nucleation site density whilst accommodating the ease of vapour to escape from the microstructured re-entrant cavities. Such enhanced surfaces with hydrophobic natures seemed to have enhanced HTCs. This could be observed in a study by Kim et al. [40] where they compared pool boiling heat transfer performance on a plain surface, to that of multiscale enhanced nanostructures on microstructures on silicon wafers using MEMS techniques. ZnO nanorods were used for nanostructures, which increased the wettability of the wafers. It was found that higher HTCs were found on the multiscale surfaces than on the plain surfaces, where the heat transfer enhancement was attributed to nucleation behaviour and bubble growth. Furthermore, the high wettability caused over a doubling of the CHF point [40].

The CHF enhancement was investigated in a study by Feng et al. [6, 41] where a rough (microstructured) Pt wire was coated with alumina through Atomic Layer Deposition (ALD) to create a coated Pt/Al_2O_3 wire which seemed to have conserved its microstructure base. The coating created a super-hydrophilic surface. An uncoated Pt wire and the coated Pt wire was

tested in pool boiling where it was found that the heat transfer was marginally better on the coated wire, but that the CHF point was significantly enhanced with 102%. This was attributed to the high wicking nature of the surface to swiftly cover it, including hot regions, with water [41].

Hybrid enhancement techniques in multiple studies have been reviewed by Laing and Mudawar [6] where microstructure fins have been coated with an ABM aluminium coating which seemed to have increased the HTCs. It was noted that the increase in heat transfer was due factors such as the ease of the vapour escaping the microstructures and the re-wetting resistance. It was important to note that the multiscale enhancements were not always beneficiary, as some studies yielded lower HTCs from multi-enhanced finned surfaces than the plain finned surface [6]. Furthermore, microstructured copper surfaces with channels have also been explored with sintered copper powder coatings which seemed to have degraded heat transfer at lower heat fluxes. This degradation was alleviated with a careful balance between surface wickability and nucleation site density to enhance heat transfer. Additional to micro-channel multiscale enhancements, copper microchannels have been oxidized to create a CuO nanocoating by Chu et al. [5, 6], where the CHF point was of particular interest and was enhanced twice that of a plain surface. Vertical copper dendrites multiscale enhancements have also been used to create very intricate enhanced surfaces, which resulted in boiling HTCs as much as twice that of the plain copper surface [6, 42], indicating that the field surrounding multiscale enhancements is vast and holds great potential for the enhancement of pool boiling heat transfer.

2.10 Falling Film Boiling Heat Transfer Enhancement

The falling film boiling configuration posed heat transfer enhancement over the common pool boiling configuration [36]. Falling film boiling mechanics comprised the bubbles departing by coalescence where the bubble contact area was also greater in comparison to pool boiling. The bubbles also detached through the falling film action which was comparatively a weak force to expel bubbles. The bubbles detached through buoyancy in pool boiling [43].

A significant contribution by Cerza and Sernas [44] have been made to describe the specific mechanisms of the falling film boiling configuration concerning the HTC enhancement over pool boiling. These included:

- Energetic boiling and releasing of bubbles from the surface to agitate the falling film.
- Transient heat conduction through the thin falling film at the base of the sliding bubble.
- A continuous heat transfer gradient was ensured by the sliding bubble's base since it moved faster than the liquid beneath it.
- Sliding bubbles assisted to seed nucleation sites they encounter for bubbles to develop faster.

The falling film boiling HTCs could be up to 65% greater than those in pool boiling at lower

heat fluxes [43]. It was noted, however, by Ji et al. [43] that the falling film boiling HTCs were not always higher than those in pool boiling, but declined typically by 30% from pool boiling at higher heat fluxes due to dryout. This was a major concern in falling film boiling at low flow rates [9, 43].

2.11 Falling Film Boiling on Microstructures

It was found by Jin et al. [38], through the comparison of boiling exponents, that significant dryout occurred in the channels of microstructured capillary channels during falling film not just in the higher heat flux regimes as pointed out by Rohsenow et al. [9], but also in the lower heat fluxes. It would be a probable cause that some HTC deterioration may have been attributed to any mechanism which promoted dryout within the capillary channels.

Zhao et al. [45] performed falling film boiling tests combined with dryout tests on 4 unnamed microstructured tubes and a plain smooth copper tube. The 1st enhanced tube had L-shaped protrusions on its surface to look much like the GEWA-B5 tube. The 2nd had skew Y-shaped protrusions, the 3rd had skew T-shaped protrusions and the 4th tube had rotated vertical protrusions in a line around the tube surface. These tubes were all compared to the smooth plain copper tube in R134a refrigerant in falling film boiling at 6°C to determine the heat transfer enhancement ratios which ranged from approximately 2 to 2.9 across the range of conditions tested.

The microstructured tubes tended to enhance the HTCs the most at lower heat fluxes, however, the observation point was subjected to greater uncertainty at lower heat fluxes. As described by Jin et al. [46], the film liquid layer was thinner at lower film flow rates (lower film Reynolds numbers) which allowed trapped vapour in the re-entrant microstructure cavities to escape and therefore resulted in higher HTCs compared to the HTCs (generally in a plateau nature) at higher film flow rates.

The results from Zhao et al. [45] also indicated a special phenomenon where the HTCs of the microstructured undergo an HTC 'hump' at approximately 0.02 $kg/m/s$ in the dryout test as the falling film flow rate was decreased. This behaviour was characteristic to microstructured tubes and did not occur on smooth tubes.

It was also seen that microstructured tubes performed marginally better in dryout performance compared to the smooth tube from where they could sustain boiling up to approximately 0.01 $kg/m/s$, whereas the smooth tube managed slightly below 0.02 $kg/m/s$. The great dryout performance of the microstructured tubes were likely due to a greater quality of film distribution along the microstructured surface. The organised re-entrant and micro-cavities caused the microstructured tube to be more independent of the reducing film flow rate than a plain smooth tube [45].

A falling film boiling study was performed by Jin et al. [46] where an unnamed microstructured tube with L-shaped, raised scale, microstructures was tested through a heat flux sweep. The microstructured tube results were compared to those of a plain copper tube. The tested tube

was in a tube stack bundle formation.

The behaviour of the microstructured tube with its flatter HTC curve was more independent from heat flux than the plain tube. The microstructured tube was also seen to significantly enhance HTCs in falling film boiling, where the maximum enhancement factor of approximately 10 times was obtained at lower heat fluxes and a minimum enhancement of approximately 1.3 times was obtained at higher heat fluxes.

Furthermore, an experimental study by Ji et al. [43] determined that an enhanced tube with scale microstructures produced falling film boiling HTCs 2.1 to 4.9 times that of a plain tube under falling film boiling conditions.

It was observed by Ji et al. [43] that the enhancement mainly took place below 30 kW/m^2, from where it decreased. It was declared that, despite the bubbles and the film being propelled downwards by the falling film, the heat transfer was mainly due to phase change heat transfer [43].

A great falling film boiling study had also been conducted by Christians and Thome [2] to observe the nature of the Turbo-B5 and the GEWA-B5 microstructured tubes and also compared their heat transfer performance to the pool boiling case.

In close correlation to the findings from Ji et al. [43], it was found that enhancement was marginal from pool boiling to falling film boiling and that the falling film boiling HTCs tended to become in line with the pool boiling HTCs at higher heat fluxes where nucleate boiling became dominant.

2.12 Falling Film Dryout

The falling film boiling configuration had a high susceptibility to dryout since liquid boiled away from the surface could not readily be replaced by more liquid as with the pool boiling configuration, especially when the superheated microlayer at the base of the sliding bubbles became very thin [1].

The following mechanisms had been identified by researchers such as Rohsenow et al. [9] and Ganic, Getachew and Gross as recognized by Acu [12] to have been the main causes of falling film dryout in falling film evaporators:

- A change in the liquid inertial force when coming to stagnation over obstructing microstructures on the tube may depreciate the rewetting ability. The nanostructure coating may further cause impedance.
- An increase in surface tension causes dry patches to grow where the dynamic force of the falling film is too weak in the force balance to rewet the dry patches.
- The Marangoni effect with fluctuations in surface tension due to the surface thermal gradient having an influence on thermophysical properties may cause liquid to tend to seep away from thin liquid layers.

Furthermore, the following basic factors to this study leading from the above which had an influence on the dryout of microstructured tubes would include:

- The influence of different types of microstructures.
- The addition of the CuO nanocoating on the microstructured tube.

2.13 Condensation Heat Transfer

A study by Belghazi et al. [47] investigating condensation heat transfer on enhanced surface tubes led to the following observations that were key toward defining effective condensation heat transfer:

- A thinner film condensate layer seemed to insinuate better heat transfer performance, where the accumulation of liquid on the tube surface posed a significant thermal resistance and deteriorates condensation heat transfer.
- A thick liquid layer across the microstructures due to the accumulation of liquid deteriorated HTCs. A liquid layer that followed the profile of the microstructures so that the layer remained locally thin showed to be a more effective configuration for condensation heat transfer.

The remarks above for effective condensation heat transfer was supported by the array of low fin tubes condensation study by Kumar et al. [48] where performance was governed by the tube's condensate drainage ability and the condensate thickness over the surface.

2.14 Summary

The key points in consideration for the study to follow from the literature review were summarized and noted to be useful.

The natural convection and nucleate boiling regimes were applicable and deemed relevant, along with the coupled common pool boiling theory that indicated the HTCs of tubes should generally increase with an increase in saturation temperature. However, microstructured tubes may oppose this. The referred microstructures were mechanically developed surface modifications, whereas coatings were usually chemically induced and greatly influenced the surface wettability.

Variable enhancement results indicated a preferable microstructure-coating combination. However, it was given that microstructures enhanced HTCs through increased surface area and nucleation site density, along with hydraulic mechanisms like bubble pumping action.

Regarding nanocoatings and other coatings, HTC enhancement through hydrophilic coatings, which had increased surface wettability, was attributed to the decreased nucleation site dryout due to the wicking action. However, HTC degradation is possible through delayed bubble development. HTC enhancement through hydrophobic surfaces was seen to be possible with higher bubble development rates and lower surface energy for onset of nucleate boiling. It also may offer less frictional resistance for liquid flow during boiling.

3 Experimental Setup

The Falling Film Boiling Rig (FF rig) was a large experimental test facility designed to obtain a wide array of heat transfer data from performing boiling and condensation tests on the outside of horizontal tubes with refrigerant. This experimental rig, as seen below in Figure 3.1, was designed for falling film boiling, pool boiling and condensation. It was originally assembled and used in the laboratory Laboratoire de Transfert de Chaleur et de Masse (LTCM) at École Polytechnique Fédérale de Lausanne (EPFL) in Switzerland under the supervision of Professor John R. Thome. The FF rig was located in the Thermoflow Laboratory at the University of Pretoria (UP) under the management of the Clean Energy Research Group (CERG) in the Department of Mechanical and Aeronautical Engineering.

Many heat transfer studies had been conducted on the FF rig. Researchers who utilized the facility most recently included Bock who investigated the effects of varying surface roughnesses, materials and nanocoatings on heat transfer [1]; Christians who compared tube bundle effects of enhanced tubes in boiling compared to single tube arrays [2]; Habert who studied boiling on plain tubes and enhanced tubes in bundle formation [49]; Roques who studied boiling of enhanced tubes [50]; and Gstöhl who investigated the influence of flow modes on condensation tests with plain and enhanced tubes [51].

(a) Front View (b) Side view

Figure 3.1: The falling film boiling rig

The facility consisted of three water loops, along with a glycol loop that conditioned the refrigerant loop that contained the refrigerant to be boiled. It also contained a sophisticated data acquisition system and also accommodated a high speed camera.

3.1 Refrigerant Loop

The refrigerant was circulated through a closed loop system in the FF rig. R134a was used in the current study and was kept uncontaminated throughout this isolated loop from oils or atmospheric air. The operating pressures ranged from approximately 350 kPa (5°C boiling tests) to 770 kPa (30°C condensation tests). The design pressure limit of this system was 1000 kPa gauge, and was protected through a mechanical pressure relief valve attached to the pressure chamber, as well as electronic pressure sensors linked to the emergency stop functions.

The refrigerant loop is shown in the schematic of Figure 3.2 below:

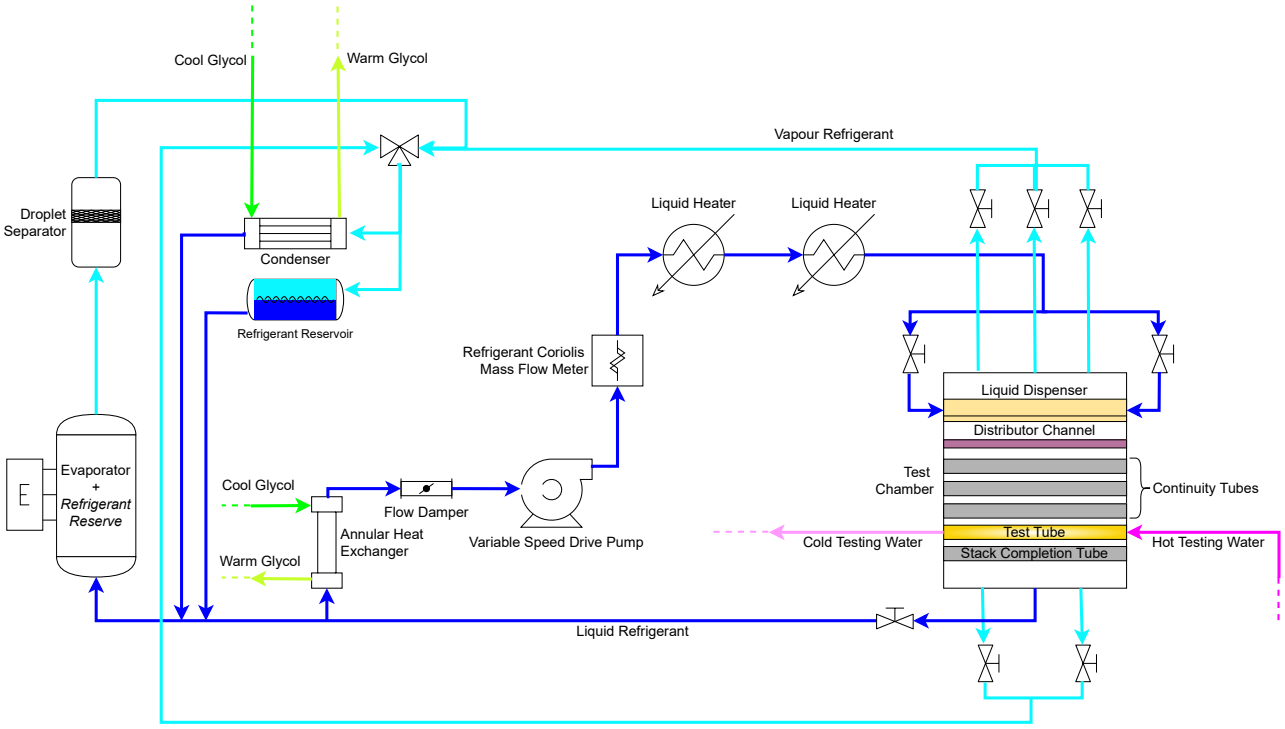

Figure 3.2: Refrigerant loop

In order to ensure only refrigerant was present in the system with minimal non-condensable gases such as air, the FF rig's refrigerant loop was vacuumed before each use with a *Just Better Vacuum Pump* and the system monitored with a *Just Better DV-40 SUPERNOVA* micron gauge until an absolute pressure of less than 100 Pa was reached before being charged with refrigerant. The success of this approach was confirmed by comparing the calculated saturation temperature, based on the pressure measured by the pressure transducers in the test chamber, to the temperature measured by the thermocouples situated in the test chamber. The temperature values and the theoretical saturation temperature calculated from the measured pressure were compared to ensure no non-condensable gases are present and it was observed that the difference between the measured and the calculated temperature readings never exceeded 0.1°C.

According to 3.2, liquid refrigerant from the bottom of the rig is pumped by a *Siemens* variable speed pump through a *KROHNE Corimass MFM4085 10G* Coriolis mass flow meter to the liquid distributor. The refrigerant is ensured to be a liquid so as not to damage the variable

speed drive through cavitation from the presence of refrigerant vapour by passing the refrigerant through a glycol-cooled annular heat exchanger ahead of the pump. The liquid refrigerant at the bottom of the rig is thus slightly sub-cooled and needs to be heated on the way to the liquid distributor by 2 stages of Proportional Integral and Derivative (PID) controlled heaters capable of maintaining the flowing liquid to within 0.5°C of the desired saturation temperature before it may enter the test chamber. The liquid refrigerant enters the test chamber's liquid distributor through a manifold by which the division of liquid fed into the liquid distributor is controlled through manual valves on either side to regulate the liquid distribution in the test chamber. The liquid refrigerant is then boiled in the test chamber on the outside of the horizontal tube by the testing water flowing inside the test tube. All remaining liquid refrigerant exits the bottom of the test chamber to collect at the bottom of the FF rig again.

The desired saturation pressure in the rig was accomplished through a combination of a PID controlled flooded evaporator situated at the bottom of the FF rig and an overhead glycol-cooled condenser. The vapour from the evaporator rose to the overhead manifold through a droplet separator which connected to the test chamber at 2 positions to control the saturation pressure: on either side of the lower end of the test chamber, and the top of the test chamber. The connection at the top of the test chamber also allowed for evaporated refrigerant vapour produced by the boiling process to rise and exit to the overhead manifold. The 3-way valve was set to allow refrigerant vapour to flow up to the condenser.

Refrigerant vapour was cooled and condensed in the overhead glycol-facilitated condenser. The saturation pressure was automatically controlled through the balancing of the heat loads between the evaporator, the overhead condenser and the testing water flowing through the test chamber.

An inherent safety feature was implemented in the evaporator through a liquid level gauge to cause the evaporator to trip to avoid hazardous burning out of the heating element.

To alleviate some vibrations in the system which may affect sensor readings (especially the pressure transducers in the testing chamber), a flow damper existed between the variable speed pump and the annular heat exchanger at the bottom of the rig. This ensured smooth liquid refrigerant flow to the test chamber so that the influence from hydraulic perturbations to the system were kept minimal.

This fluoridated refrigerant was the most commonly used refrigerant in mechanical ventilating and air conditioning systems since 1990. However, while non-toxic and non-flammable, it was harmful to the environment as it had a greenhouse effect of 1430 times more than Carbon dioxide (CO_2). R134a would thereby be prohibited for use in light motor vehicle systems from 2022 in developed nations to alleviate compromise [52].

It was thereby necessary for systems making use of R134a refrigerant to be well-designed and robust to effectively contain the refrigerant. Despite R134a being a greenhouse gas, it was one of the few higher vapour pressure refrigerants that were not ozone depleting [20].

The R134a refrigerant had a very large database of comparative heat transfer studies and still made it a valuable research fluid.

3.2 Test Chamber

The test chamber, as shown in the schematic of Figure 3.3, has dimensions of 554 × 200 × 20 mm, and provides the environment for the falling film boiling, pool boiling and condensation tests.

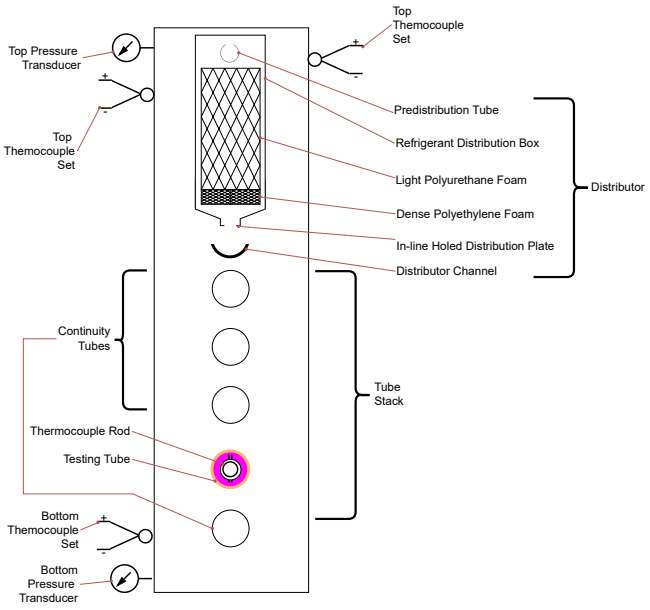

Figure 3.3: Cross-section of test chamber

The liquid refrigerant enters at the top of the chamber into the distribution box through the 13 mm Internal Diameter (ID) predistribution tube with 3 mm holes at the top along its length spaced 5 mm apart. The refrigerant then passes through 2 sections of foam in the distribution box for distribution. The liquid first flows through light 150 mm high polyurethane foam block of 60 Pores per Inch (PPI) and 200 μm pore diameter, where after it flows through a dense 10 mm high polyethylene foam block of 37% porosity and 35 μm pore diameter. A brass plate with 268 center-line holes (1.5 mm diameter and 2 mm apart) was positioned at the bottom of the refrigerant distribution box. To further assist in creating an even distribution of liquid over the tube stack at low flow rates, a 20 mm diameter distributor channel made from a stainless steel pipe cut in half catches the liquid which flows over the edges on either side of the channel. A sharp machined edge at the bottom of the channel causes the liquid film to fall uniformly down the center of the channel onto the first tube beneath it in the tube stack [51]. During operation, it was observed that the distributor was very reliable in ensuring a well-distributed falling film over the tube stack. The distributor channel can be adjusted by looking through the side observation windows on either side of the test chamber and rotating the channel until the falling film was visually confirmed to be landing on the very centre of the uppermost tube. The film flow was sensitive to an event called slinging as described by Gstöhl [51] if the fluid was not at the top centre.

In this study tubes were tested individually in the tube stack. The tube stack comprises a single

column of 10 horizontally stacked tubes at a pitch of 22.3 mm. The 3/4" plain tubes tested had a 19.05 mm Outer Diameter (OD) except for the enhanced tubes, which varied slightly in OD. For a falling film boiling test, at least 4 tubes are placed above and at least 1 tube was placed below the testing tube to further assist in distribution. The untested tubes in the stack are insulated at the ends to reduce external influence on the test chamber.

As the testing water flowed inside the testing tube and boils the liquid refrigerant on the outside of the tube in the test chamber, the refrigerant vapour from this boiling process exited the top of the chamber as indicated in section 3.1. The rising vapour flow was proved to have negligible influence to the uniformity of the falling film and the heat transfer, since the speed of the vapour flow in this study was much less than the vapour speed needed to affect the heat transfer seen in Ribatski and Thome [53].

Heat transfer during boiling and condensation was measured using a thermocouple rod inserted in the testing tube, with the testing water flowing between the thermocouple rod and the tube. The thermocouple rod was further described in section 3.3.

There are 2 pressure transducers attached to the test chamber in 3.3, as well as 8 K-type thermocouple probes in 3 rows spaced around the test chamber. One pressure transducer was is at the top and the other is at the bottom of the chamber. The thermocouple probes measure the refrigerant temperature all around the test chamber to measure homogeneous saturation conditions.

3.3 Thermocouple Rod

The thermocouple rod was a specially constructed measuring device used to measure temperature data along the length of the testing tube. This device is depicted in Figure 3.4 below:

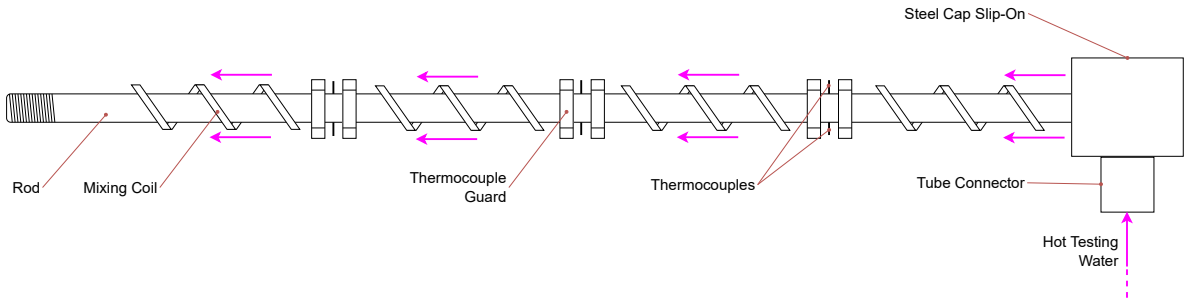

Figure 3.4: Thermocouple rod

The thermocouple rod comprises an 8 mm diameter hollow steel tube through which 6 K-type steel-sheathed thermocouples of 0.5 mm diameter are drawn through. The thermocouples are positioned in opposite extending pairs and equidistant to cover the 554 mm of the span of the rod. Thermocouple guards are placed on either side to protect the exposed thermocouple ends from the testing tube when the rod was inserted or removed.

A copper mixing coil is wound around the rod between the thermocouple pairs to mix the testing water for the best possible uniform cross-sectional temperature as the water flows.

A 2nd degree polynomial fit through all 6 temperature measurements was used to obtain a temperature profile along the length of the tube.

The presence of the thermocouple rod along the length of the tube being tested was assumed not to significantly influence the axial heat conduction of the water in the test tube as all tests were performed in the turbulent flow regime (Re between 5 400 and 7 000) where the temperature read by the thermocouples extending out of the rod measured an assumed constant radial test water temperature. The ends of the steel thermocouple rod was also bound by water past the entry and exit of the test chamber to limit premature thermal heat conduction out of the testing water in the test chamber. The steel thermocouple rod having a much higher thermal heat conductivity than the water supports the assumption of the rod being the same temperature as the testing water. Any axial effects would also be compensated for through the Wilson plot analysis with its resultant modification factor.

3.4 Test Chamber Configurations

In the current study, both falling film and pool boiling configurations are used as shown in Figure 3.5:

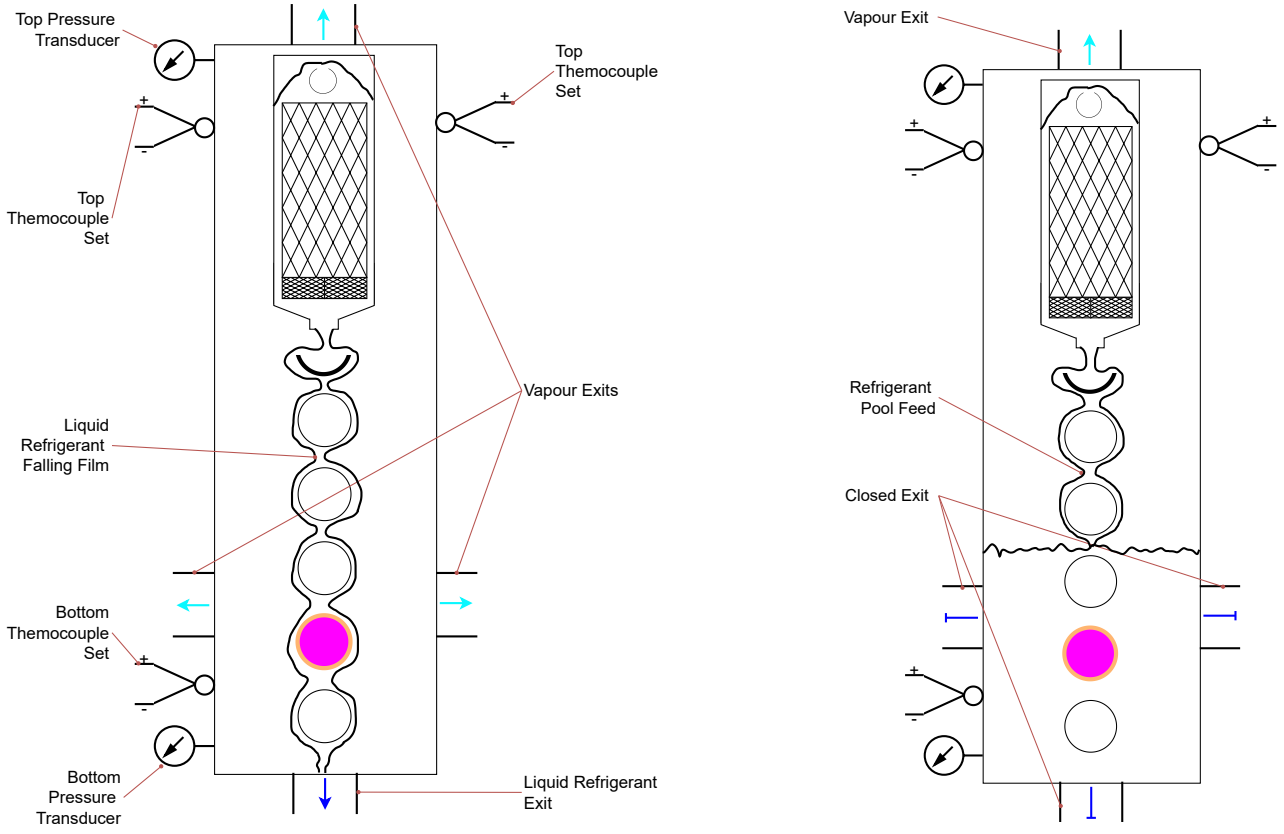

(a) Falling film setup (b) Pool boiling setup

Figure 3.5: Test chamber configurations

In the falling film configuration as seen in Figure 3.5a, all valves around the test chamber are in the open position so that refrigerant vapour from boiling can rise up out of the chamber to the overhead manifold to be condensed (or through the sides of the test chamber, depending on the 3-way valve setting). The remaining liquid refrigerant drains out of the test chamber

through the exit at the base of the test chamber to go to the bottom of the FF rig.

In the pool boiling configuration as seen in Figure 3.5b, all the vapour valves are closed except for the top exit valve where refrigerant vapour can rise and exit to the overhead manifold.The bottom liquid drain valve was closed so that a pool of liquid refrigerant covers the testing tube for pool boiling to take place.

The liquid level height of the pool was maintained by the normal feed of the falling film to the desired liquid level (above the testing tube) as set by the user in LabVIEW. The FF rig automatically regulates the liquid level height using the difference in pressure between the top pressure transducer (which was exposed to vapour) and the bottom pressure transducer (which was underneath the liquid level). The working of this controller was described in Appendix A.

3.5 Testing Water Loop

The testing water flowed inside the testing tube and provided the heating for boiling tests and cooling for condensation tests. The testing water loop is schematically depicted in Figure 3.6:

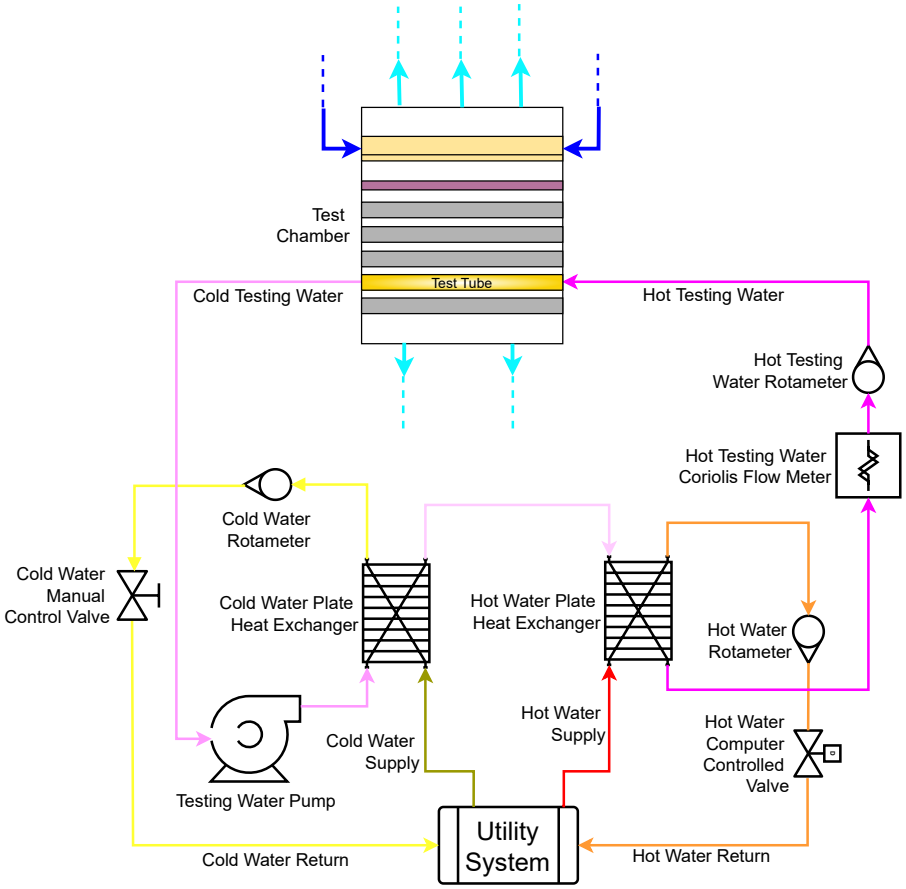

Figure 3.6: Testing water loop

The testing water is pumped with a variable speed centrifugal pump through a plate heat exchanger where the testing water can be cooled by the utility cold water supply from at -5°C and is controlled by a manual cold water control valve [49]. The water then proceeds to another plate heat exchanger where it is heated by the hot water utility supply, which is automatically controlled by the hot water Computer Controlled Valve (CCV). The hot water

utility supply temperature is changed as needed for the tube tested. The testing water flow rate is then measured with the testing water *KROHNE Corimass MFM4085 100G* Coriolis mass flow meter.

The rotameters are used to visually confirm that flow was taking place in the respective lines and are used for bundle tests to ensure an even split of liquid between the bundle tubes.

The hot water and the cold water from the utility supply is measured directly with a thermocouple where it enters from the utility feeds, however, this measurement is only necessary for monitoring and resultant control purposes. The important water measurements are sampled at the *Test Tube* point in Figure 3.6 with a thermocouple rod inserted in this tube (see section 3.3).

3.6 Glycol Loop

The glycol loop's function was to remove energy from the refrigerant loop. This aids control over the saturation temperature and to condense the refrigerant to a liquid. The glycol loop schematic is depicted in Figure 3.7:

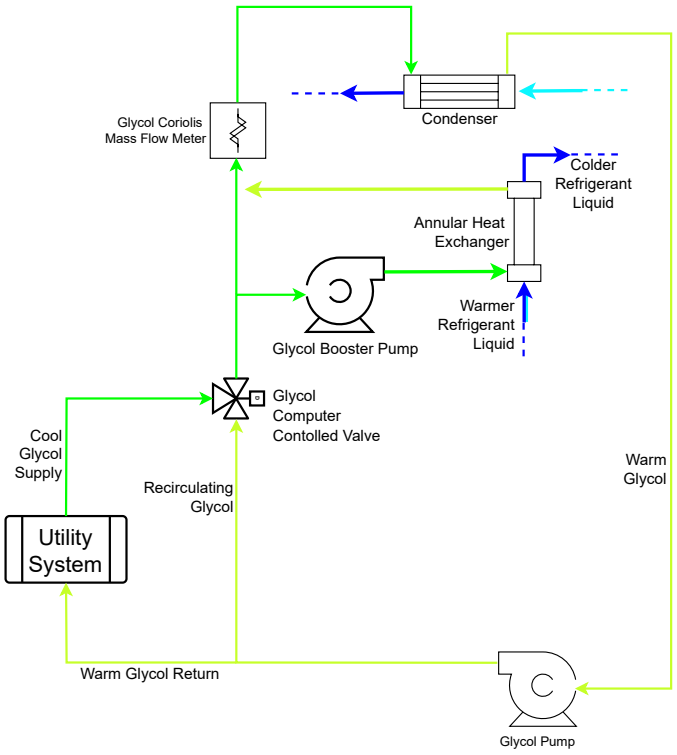

Figure 3.7: Glycol loop

The medium in the glycol circuit is a mixture of 50% water and 50% propylene glycol [1].

The glycol is propelled through the loop by the glycol pump. This glycol enters the glycol CCV, which connects the glycol coming from the pump and the -20°C cold glycol supply from the utility system to the rest of the glycol loop. The setting of the CCV is used to control the rate of heat removal from the refrigerant loop through the amount of fresh cold glycol being allowed into the glycol loop. The glycol line then follows to a *KROHNE Corimass MFM4085*

100G Coriolis flow meter, which is used to calculate the heat removal rate of the condenser. The glycol then enters the condenser where heat was removed from the refrigerant to the glycol. The warm glycol then travels back to the pump to be served to the CCV again as recirculating glycol.

A booster pump is added between the CCV and the Coriolis flow meter to regulate flow to the annular heat exchanger where refrigerant was sub-cooled to ensure it to be a liquid before entering the variable speed drive as seen in section 3.1.

The temperature of the glycol was measured directly in the glycol line from the utility system's feed with a thermocouple as it entered the FF rig. However, this reading was only for monitoring and consequent control purposes.

3.7 External Utility Supply System

The Thermoflow Laboratory had a utility supply system on the roof, which maintains supply lines at set temperatures. A hot water supply, a chilled water supply and a cold glycol supply were used by the FF rig. The set-points of each of these lines were adjusted as required in order to reach the heat fluxes for the experiments performed, based on the type of tube tested but typical set-points are 60°C, 5°C and -20°C respectively.

Hot water was prepared by an *ACQUACIAT 2* heat pump, followed by a boiler and a pump for its circuit. The chilled water was maintained by a *ACQUACIAT 2* chiller unit followed by its pump to supply the lab. The glycol temperature was maintained by an *CLIMAVENETA* chiller unit, followed by the glycol circuit pump.

3.8 High Speed Camera

Visual analysis was also performed during testing by recording high speed video of the boiling events through the observation windows of the test chamber. There were 3 windows on either side of the test chamber, each 250 mm high and 120 mm wide. The observation windows are visible in Figure 3.8:

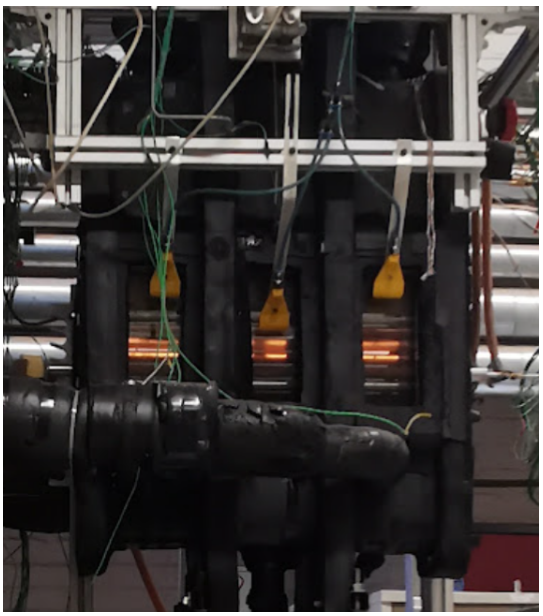

Figure 3.8: Observation windows of the FF rig

The camera used was a *Photron FASTCAM Mini UX100* [1], set to record at 2 000 frames per second (fps) for this study with a *Tokina 100 mm f/2.8 AT-X PRO 1:1 Macro* lens. The raw recorded footage was rendered using the *Photron FASTCAM PFV4* software package and condensed with *HandBrake v1.2.2* software.

Sufficient lighting was provided by *GS Vitec PT* Light Emitting Diode (LED) lights, mounted on either side of the test chamber for front and back lighting [1].

3.9 Data Acquisition, Software and Control

The controlling and measuring aspects of the FF rig were performed with two Personal Computer (PC)s, namely: the Control PC and the Measure PC. The Control PC employs LabVIEW 32-bit 2010 SP1 and the Measure PC LabVIEW 32-bit 2009 SP1. The software integrated with a comprehensive National Instruments (NI) system implemented throughout the FF rig used for control and for measurement.

The control of the FF rig was performed by measuring sensor voltages through a NI SCXI-1303 isothermal terminal block and by measuring sensor currents through a NI SCXI-1308 isothermal terminal block. Both were connected to the control NI SCXI-1000 Data Acquisition System (DAQ) chassis with NI SCXI-1102 input modules. Commands were sent to equipment and sensors through a NI SCXI-1000 DAQ using an NI SCXI-1124 output module and an NI SCXI-1325 isothermal terminal block [1].

All thermocouples were sampled through the use of an NI TC-2095 standard rack mount adapter, which inherently incorporated reference junction compensation by having all the cold junctions on the same metallic plate with a thermal resistor to determine the reference temperature [1]. This adapter then proceeded directly into the NI SCXI-1102 input module which connected to the NI SCXI-1000 measure DAQ chassis.

Pressure transducers produced current signals which were converted into DC voltage signals and amplified by a SIRAX TV 808 plug-in module mounted on a BP 902 interface backplane. The output from the amplifier was served into an NI TC-2095 standard rack mount adapter which incorporated a preliminary analog 2 Hz low-pass filter to reduce signal noise [1]. Both control and measure DAQ chassis were connected to the control PC and the measure PC through PCI-MIO-16XE-50 cards that interfaced with the computers through Peripheral Component Interconnect (PCI) slots on the motherboards.

Each data-point at a setpoint was an average of 30 recordings, where each recording was an average of 800 samples. The sampling rate was set at 100 Hz, resulting in a sampling period of 4 min at steady state.

3.10 Calibration

The calibration of all the sensors and were performed according to the detailed descriptions provided in Appendix B. The sensors' readings were compared to accurate and externally calibrated reference sensors through a polynomial fit equation. The reference sensors were locally available in the Thermoflow laboratory.

A *LAUDA Digical DCS2* digital thermometer was used as the reference sensor for the calibration of all thermocouples and a *WIKA CPT 6400* pressure transducer was used for the calibration of all pressure transducers.

The *KROHNE CORIMASS MFM4085* 100G and 10G model coriolis mass flow meters were of a non-modular design and it was determined that their measuring accuracy satisfied the KROHNE factory standard through diagnostic tests performed at a KROHNE facility. The output signals of the coriolis mass flow meters were only calibrated for the LabVIEW software to match the readings on the coriolis mass flow meters' displays (through the method in Appendix C).

A post-calibration check was always performed after each calibration to ensure the sensor readings fell within the acceptable deviation ranges from the reference sensors as explored by previous researchers.

3.11 Tube Preparation

3.11.1 Uncoated Tubes

All the uncoated tubes were prepared with the same procedure. The tubes collected for the study were of different ages and to had been exposed to different environmental conditions. Thus, the following steps were used to clean all tube surfaces: The tubes were fully submerged in a weak 5% acidity acetic acid solution (white spirit vinegar) for 1 hour to clean the surface of any debris, to bind with the sediments and to remove the uneven copper carbonate layer that naturally forms over time when copper is exposed to the open atmosphere. This cleaning process ensures that a fresh and volatile copper surface exists that can then bind again with

the atmosphere in a controlled environment.

After cleaning, the tubes were left exposed to still atmosphere to age for 12 hours after which they were rinsed with Reverse Osmosis Water (RO water) and acetone before being placed in the FF rig's test chamber for the vacuuming process to begin.

The smooth tubes were prepared using G1200 sandpaper and the roughened tube with G40 sandpaper by longitudinally sanding the tubes without using water. The sanding of the tubes mechanically removes the surface sediments and copper carbonate layers and thus they were also aged in air and rinsed afterwards with RO water and acetone before insertion.

Surface roughness was measured on a flat copper plate that was sanded with the same relative intensity as the tube with a Mitutoyo SJ 210 Surftest Profilometer using the ISO 1997 standard and a cutoff length of 0.8 mm were used (the direct surface roughness cannot be measured on the tube). The tube and the flat plate were sanded by the same person and with the same intensity with the utmost care. It was hereby assumed that both flat plate and tube surface to deliver the same roughness measurement. The results of the measured roughnesses were recorded in Table D.3 in Appendix D. The smooth tube was found to have a Roughness Average (R_a) of 0.042 with a standard deviation of 0.012, whereas the roughened tube's R_a was 0.749 with a standard deviation of 0.066.

It should be noted that the surface roughnesses measured in this study did not match those of Bock [1], despite the same grit sandpapers being used.

3.11.2 Coated Tubes

A set of sanded tubes and micro-enhanced tubes were surface coated with a copper oxide (CuO) nanocoating. The tubes to be coated were prepared according to a specific set of steps, as there are numerous types of CuO coatings which may display different chemical behaviours and different heat transfer performances. The CuO Type I coating of Nam and Ju [26] and Enright et al. [54] was used in this study.

The chemicals used for the coating process are summarised in Table 3.1 below, indicating the constituent proportions in weight percentage:

Table 3.1: Chemicals for CuO coating constituent weight percentages in solution

Chemical	**wt %**
$NaClO_2$	3.75
$NaOH$	5
$Na_3PO_4 \cdot 12H_2O$	10
H_2O	100

The chemical coating event was a 2-step process where Copper (I) oxide is first produced as described in equation (3.1) which then binds with the free suspended hydroxide ions to produce

Copper (II) oxide, as described in equation (3.2) [26, 54]:

$$2 \cdot Cu^{+} + 2OH^{-} \rightarrow Cu_2O + H_2O \tag{3.1}$$

$$Cu_2O + 2OH^{-} \rightarrow 2 \cdot CuO + H_2O \tag{3.2}$$

The complete description of a *Tube Coating Machine* as well as the detailed CuO coating procedure could be found in Appendix E.

The resultant CuO nanostructures on the surface have previously been described as having sharp-like point structures with prominent blade protrusions throughout the coating with an approximate height of 1 μm, blade width of 300 nm and a blade thickness of 100 nm [54, 55]. At certain Power of Hydrogen (pH) values there should be different visible elements that constitute the nanostructures which consist of CuO nanorods at $pH = 8$, CuO nanosheets at $pH = 10$ and CuO nanoflowers at $pH = 11$ [56]. The pH of the coating solution was calculated in Appendix F to be 12.56. At this pH, all the nanostructure elements should be present in the resultant coating. This is verified with their identification in Figure 3.9:

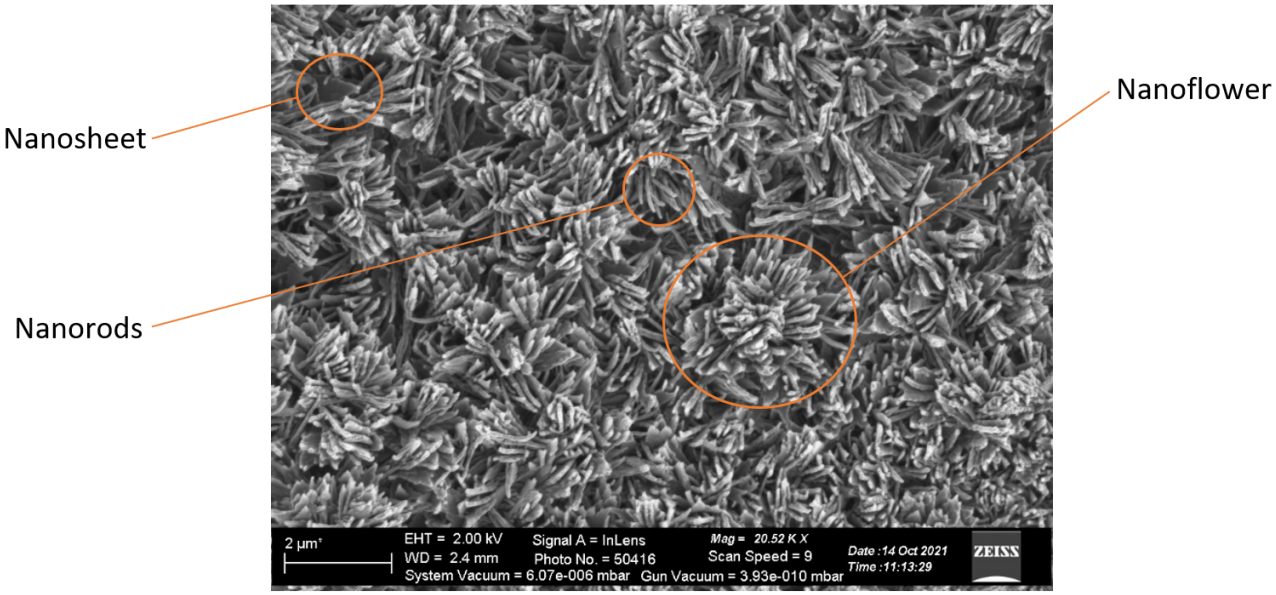

Figure 3.9: Nanostructure identification on SEM photograph of CuO coated copper sample coated in $pH = 12.56$ solution

The thermal properties of CuO are unattractive if it were primarily considered as a thermal conductor. The thermal conductivity of CuO was estimated to be as low as 33 W/mK [57]. Hereby, the thermal insulation effect that the coating presents upon the system must be deduced. By comparing the thermal resistance of the CuO coating to that of the thermal resistance of a plain copper tube wall, it could be shown that the CuO coating only increases the wall thermal resistance by 1.2% and was thus not a significant factor to consider regarding its influence on heat transfer. The calculation of the thermal resistance of the CuO nanocoating is found in Appendix G.

3.12 Scanning Electron Microscopy

The coatings on all the commercially micro-enhanced tubes used in this study were investigated under a high power Scanning Electron Microscope (SEM) to view the coating structure. It was important to determine whether the coating is successful, where a uniform coating along the profile of the micro-enhanced tube surface was preferred, and whether any clogging or obstruction of the microstructures occurred imputed to the nanostructure coating.

The CuO material was extremely non-conductive. This caused the surface to charge up with electrons when subjected to the electron beam in the SEM so that the electrons were not reflected off the surface to successfully render an image. This charging event caused objects and protrusions on the surface to appear flat or portray a zero-thickness structure. To alleviate this problem, the samples were first carbon coated with a thin layer of carbon using a *Quorum Q150T ES Carbon Coater* and vaporizing pure carbon sticks in a sealed vacuum chamber. The deposited conductive layer did not affect the nanostructures beneath, but merely made them possible for viewing. Additional SEM micrographs could be found in Appendix H.

3.12.1 Roughened Tube

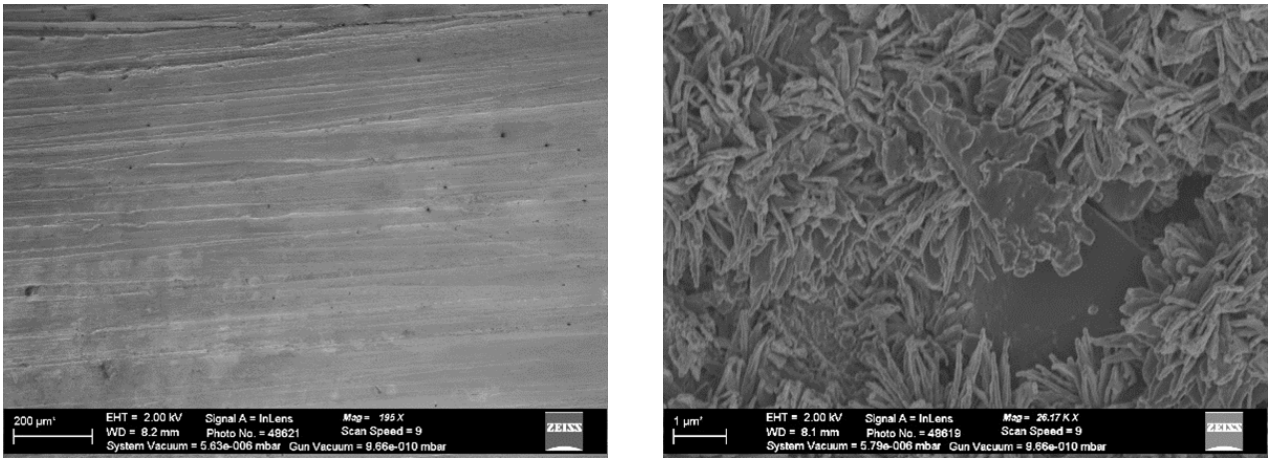

(a) Uncoated (b) Coated

Figure 3.10: Uncoated and coated roughened tube SEM observation

The roughened tube was coated with a CuO nanocoating. The difference between an uncoated and coated roughened surface is shown in 3.10 above. The coating successfully managed to also coat the grooves on the surface. The rough profile of the tube surface is moderately flattened out by the coating, but a rougher surface profile is still evident.

3.12.2 GEWA-KS

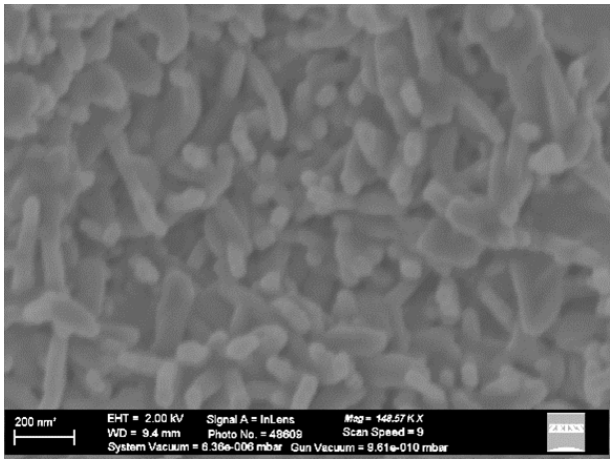

Figure 3.11: Close-up SEM of coated GEWA-KS low finned tube

The GEWA-KS low-fin micro-enhanced tube is shown to be successfully coated with CuO nanostructures in Figure 3.11. The profile of the tube is undisturbed and the CuO nanocoating managed to completely coat the surface with ease since the fin spacing is large in comparison to the other micro-enhanced tube microstructures.

3.12.3 GEWA-B5

The GEWA-B5 micro-enhanced tube was seen to be coated with a CuO nanocoating. It was confirmed by the uncoated and coated comparison through SEM inspection that the coating on such an intricate profile was uniform and that the coating clearly did not block or clog the micro-enhancement pores of the GEWA-B5 tube.

The inside of the pores must also be CuO coated for a uniform coating. A close investigation of the CuO coated pores in Figure 3.12 shows that the inside of the pores are indeed fully coated with CuO nanostructures. There is no evidence of micro-structure pore impediment from the coating inside the pores.

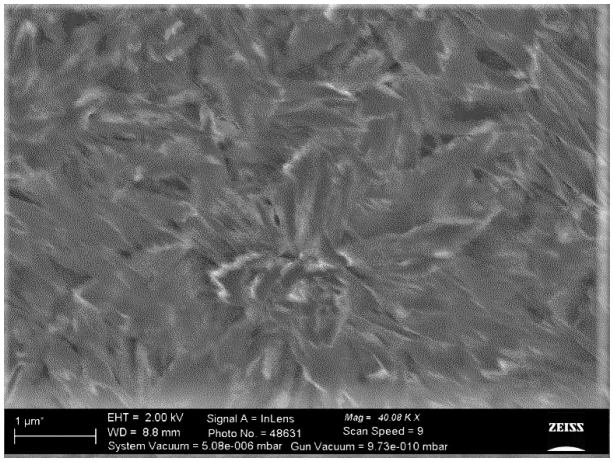

Figure 3.12: Pore inside

3.12.4 EHPII

The EHPII micro-enhanced tube was seen through SEM inspection to be successfully coated. It was clearly seen from the uncoated and coated comparison that the main intricate profile of the surface was preserved.

The extent of the possible obstruction of the CuO nanocoating was investigated. The close observation of the scales on the surface is shown in Figure 3.13:

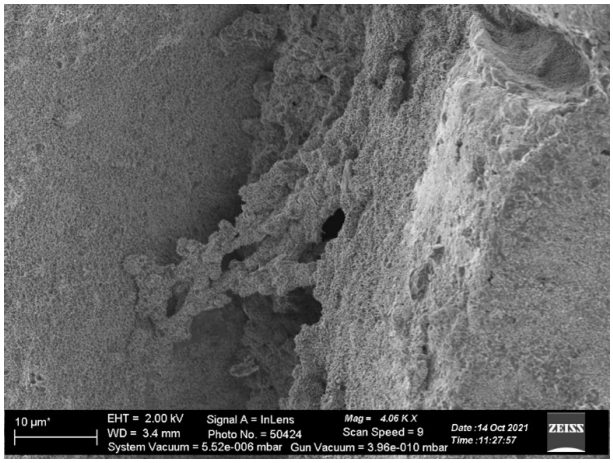

Figure 3.13: Pore inside

It can be seen that it is possible for the CuO nanocoating to obstruct the microstructure scales by partially filling the crevices between the scales. It must be noted that the coating does not fully coat the crevices and in such instances the obstruction is in the form of a porous webbing.

It is also observed that the blockages are not at every crevice, where an estimated 12.5% of all scales have these blockages. A possible depreciation in HTCs could be attributed to this considerable portion of blocked microstructures where they could impose an impedance to convective heat transfer and a decrease in surface area for heat transfer to take place.

3.12.5 Coating Resilience

From the above SEM micrograph inspections it was concluded that the coating of commercially micro-enhanced copper refrigeration tubules are possible, and that the coating could uniformly covered the entirety of the intricate surfaces, especially with the GEWA-B5 and EHPII tubes. This characteristic of the CuO nanocoating was attributed to the self-limiting nature by which the coating solution binds with the copper surface. This nature also probably ensured an evenly thick coating around and along the tube. Due to the different profiles of microstructured tubes being coated, it was indefinite that all tubes would have the same coating thickness, however, the effective thickness would be assumed to be close to 1.5 μm due to the self-limiting coating process consistently performed [54].

It was observed that obstructions are possible among the microstructures, however, the microstructures were not completely clogged in these instances.

The wettability of the surfaces were altered as intended, where only the wettability was greatly

enhanced. This was explored by water droplet contact angle tests on all the tubes. The hydrophobic uncoated tubes produced water droplet contact angles between 60° to 80°, where the super hydrophilic CuO coated tubes produced water droplet contact angles of 0° (immeasurable).

Furthermore, the CuO coating SEM images coincided with the CuO nanostructure SEM images captured by Sen et al. [39], who investigated hydrophilic and hydrophobic CuO nanostructure coated copper surfaces.

3.13 Experimental Test Matrices

This study's scope included the observation and comparison of uncoated and coated micro-enhanced tubes in the cases of pool boiling, falling film boiling, falling film dryout tests and condensation tests. The tests were performed using water as the heating medium and R134a refrigerant as the boiling medium. Wilson Plot analysis tests formed part of the characterization of each tube type, which also required their own tests.

3.13.1 Wilson Plot Analysis Matrix

Each of the Wilson Plot analyses tests were were a modified pool boiling test where the heat flux was maintained constant and the inside testing water mass flow rate varied from the fastest pump setting to the slowest. The main objective of the Wilson Plot tests were to obtain the inside characterization coefficient, $C_{i,x}$, for each tube type. The layout of these tests are shown in Table 3.2, more than one test was performed for each tube type as per constant heat flux entry:

Table 3.2: Wilson plot analysis test matrix

						Testing Water Reynolds Number Range		
Saturation Temperature [°C]	**Surface Condition**	**Tube Name**	**Constant Heat Flux**			**Minimum**	**Maximum**	**Wilson Plot Internal Coefficient**
5	Uncoated	Smooth	20			8 000	15 000	$C_{i,US}$
		Roughened	50			8 000	15 000	$C_{i,UR}$
		GEWA-B5	100			6 000	14 000	$C_{i,UB}$
		GEWA-KS	100	100	100	7 000	15 000	$C_{i,UK}$
		EHPII	100	100	100	7 000	15 000	$C_{i,UE}$
	Coated	GEWA-KS	100	100		7 000	15 000	$C_{i,CK}$
		EHPII	100	100		7 000	15 000	$C_{i,CE}$

3.13.2 Condensation Matrix

The condensation tests were only performed on the GEWA-KS and the EHPII micro-enhanced tubes. This can be seen in Table 3.3:

Table 3.3: Condensation test matrix

Saturation Temperature [°C]	**Surface Condition**	**Tube Name**	ΔT_{sh} **[°C]**
30	Uncoated	Smooth	±20
		Roughened	±20
		GEWA-KS	±22
		EHPII	±22
	Coated	GEWA-KS	±22
		EHPII	±22

3.13.3 Pool Boiling and Falling Film Boiling Matrix

The test matrix used for pool boiling and repeated for falling film boiling is shown in Table 3.4. The effect of 25°C was observed for the GEWA-KS and EHPII tubes:

Table 3.4: Pool boiling experimental test matrix

Saturation Temperature [°C]	**Surface Condition**	**Tube Name**	**Heat Flux [kW/m]**								
5	Uncoated	Smooth	20	30	40	50	60	70	80	90	100
		Roughened	20	30	40	50	60	70	80	90	100
		GEWA-B5	20	30	40	50	60	70	80	90	100
		GEWA-KS	20	30	40	50	60	70	80	90	100
		EHPII	20	30	40	50	60	70	80	90	100
	Coated	Roughened	20	30	40	50	60	70	80	90	100
		GEWA-B5	20	30	40	50	60	70	80	90	100
		GEWA-KS	20	30	40	50	60	70	80	90	100
		EHPII	20	30	40	50	60	70	80	90	100
25	Uncoated	GEWA-KS	20	30	40	50	60	70	80	90	100
		EHPII	20	30	40	50	60	70	80	90	100
	Coated	GEWA-KS	20	30	40	50	60	70	80	90	100
		EHPII	20	30	40	50	60	70	80	90	100
			Camera				**Camera**				**Camera**

3.13.4 Falling Film Dryout Test Matrix

The falling film boiling case was observed similar to the above, where the testing heat flux was maintained at 20 kW/m^2, 50 kW/m^2 and 80 kW/m^2. This is shown in Table 3.5:

Table 3.5: Falling film dryout test matrix

Saturation Temperature [°C]	**Surface Condition**	**Tube Name**	**Constant Heat Flux**		
5	Uncoated	GEWA-B5	20	50	80
		GEWA-KS	20	50	80
		EHPII	20	50	80
	Coated	GEWA-B5	20	50	80
		GEWA-KS	20	50	80
		EHPII	20	50	80
			Camera	Camera	Camera

The falling film was decreased from 0.13 $kg/m/s$ until dry-out was achieved where heat flux became unsustainable.

4 Data Reduction and Uncertainty

The computations of all results have been implemented in a Python data processing script accommodating all quantities defined below. The thermophysical properties were obtained through the CoolProp v.6.4.1 open-source module. A sample of the basic Python code which was used as a basis to process the data is found in Appendix I.

All the properties of the R134a refrigerant including the heating water were obtained from the open-source CoolProp v.6.4.1 library.

The module has been compared to the NIST REFPROP library [58] by Bell et al. [59] and Nicola et al. [60] and found to be suitable for open source replacement.

The Wilson Plot analyses were preformed using a MATLAB script making use of the REFPROP v.8 library for thermophysical properties.

The outline of the procedures were based upon previous researchers' methods such as Bock [1], Roques [61] and Habert [49] for consistency and comparability of data.

4.1 Local Heat Flux

The local heat flux calculated at the centre of the tube length was used to determine the local HTCs at that point. The following equation (4.1) is used to calculate heat flux:

$$\dot{q} = \frac{\dot{m}_w C_{w,p}}{\pi D_o} \cdot \frac{dT_w}{dx} \tag{4.1}$$

A 2nd degree polynomial fit was applied to the temperatures measured along the length of the tube to obtain the temperature profile. Additional heat flux observations were made in Appendix J.

4.2 Overall Heat Transfer Coefficient Relative to Outside Tube Surface

The local overall HTC at the tube midpoint was simply calculated using the heat flux calculated using the outside tube surface. This parameter is calculated, starting from defining the tube midpoint testing water temperature provided in equation (4.2):

$$T_{w,mid} = f(x_{mid}) \tag{4.2}$$

The quantity $T_{w,mid}$ again refers to the local evaluation performed at the middle point of the tube. The local midpoint overall HTC is then calculated from equation (4.3), using the theoretical refrigerant saturation temperature, $T_{r,sat}$, obtained from the saturation pressure served to CoolProp:

$$U_{o,mid} = \frac{\dot{q}_{o,mid}}{T_{r,sat} - T_{w,mid}} \tag{4.3}$$

4.3 Tube Wall Thermal Resistance

The thermal wall resistance is defined by equation (4.4):

$$R_t = \frac{D_o \ln(\frac{D_{or}}{D_i})}{2k_t} \tag{4.4}$$

Where the thermal conductivity used is $k_t = 340\ W/m \cdot K$ [62].

4.4 Internal Heat Transfer Coefficient

The internal heat transfer coefficient was calculated using a modified Gnielinski correlation by altering the leading coefficient C_i through a Wilson Plot analysis to account for the inner tube enhancements and the presence of the tube mixer. The Wilson Plot is described in section 6.

The internal HTC is calculated in equation (4.5) using the Nusselt number from Gnielinski's correlation:

$$h_i = Nu^*_{Gnie} \cdot \frac{k_w}{D_h} \tag{4.5}$$

The modified Gnielisnki correlation [8] is used with the characterized C_i, which is determined through the Wilson Plot analysis, to determine the Nusselt number above in equation (4.6):

$$Nu^*_{Gnie} = C_i((f/8)(Re_w - 1000)Pr_w)/(1 + 12.7(f/8)^{0.5}(Pr_w^{2/3} - 1)) \tag{4.6}$$

The Reynolds number (Re) number is calculated in equation (4.7), followed by the Prandtl number (Pr) in equation (4.8):

$$Re_w = \frac{4 \cdot m_w}{\pi \cdot D_{wetted} \cdot \mu_w} \tag{4.7}$$

$$Pr_w = \frac{\mu_w \cdot C_{w,p}}{k_w} \tag{4.8}$$

Where the properties of water μ_w (dynamic viscosity) and k_w (thermal conductivity) were obtained from *CoolProp* at the midpoint water temperature.

The friction factor is calculated with the Petukhov's formulation in equation (4.9) [63]:

$$f = (0.79 \ln(Re_w) - 1.64)^{-2} \tag{4.9}$$

The hydraulic diameter, D_h, and the wetted perimeter, D_w, are calculated in equation (4.10) and equation (4.11) below:

$$D_h = D_i - D_{probe} \tag{4.10}$$

$$D_{wetted} = D_i + D_{probe} \tag{4.11}$$

4.5 Outside Tube Surface Heat Transfer Coefficient

Considering the thermal network, the overall heat transfer is given by equation (4.12):

$$\frac{1}{U_o A_o} = \frac{1}{h_o A_o} + R_{wall} + \frac{1}{h_i A_i} \tag{4.12}$$

Therefore, the outside HTC is given, when normalized to outside tube surface area, by equation (4.13):

$$h_o = \left(\frac{1}{U_o} - R_t - \frac{1}{h_i} \cdot \frac{D_o}{D_i} \right)^{-1} \tag{4.13}$$

The outside tube surface thermal resistance and the inside tube surface thermal resistance is typically the most dominant terms in equation (4.13). This can be seen by Figure L.15b in Appendix L where the outside and inside tube thermal resistances are relatively the same magnitude (typically averaging around 0.5 K/W over Reynolds number when normalised), where the wall thermal resistance is negligible due to high thermal conductivity.

4.6 Condensation

As part of the validation study of the FF rig, condensation tests were performed and then compared to the theoretical condensation solutions.

The tube outside surface temperature, T_o, is:

$$T_o = T_{sat} - \frac{\dot{q}_o}{h_o} \tag{4.14}$$

The temperature difference between the refrigerant saturation temperature and the tube outside surface temperature as the superheat, ΔT_{sh}, is defined as in equation (4.15):

$$\Delta T_{sh} = |T_{sat} - T_o| \tag{4.15}$$

The theoretical Nusselt solution (without inundation) [64] is calculated for the testing conditions (4.16). This Nusselt correlation is used to produce the Nusselt solution data:

$$h_{o,Nusselt} = 0.728 \left(\frac{\rho_{r,l}(\rho_{r,l} - \rho_{r,v}) g h_{fg} k_{r,l}^3}{\mu_{r,l} \Delta T_{sh} D_o} \right)^{0.25} \tag{4.16}$$

Where the refrigerant properties, h_{fg} (latent heat of vaporization), $\rho_{r,l}$ (liquid density), $\rho_{r,v}$ (vapour density), $k_{r,l}$ (liquid thermal conductivity) and $\mu_{r,l}$ (liquid dynamic viscosity) are all obtained from CoolProp v.6.4.1 at the saturation pressure.

4.7 Normalized External Heat Transfer Coefficient

In order to compare external HTC data-sets, h_o, for studies where the refrigerant flow rate was varied at a constant testing heat flux, the complete HTC data-set was divided by the HTC at a film flow rate of $\Gamma_r = 0.13\ kg/m/s$, $h_{o,ff}$, for normalization since the this film flow rate is the base flow rate of all falling film boiling tests. This is implied by equation (4.17) and defined as parameter $h_{o,fs,norm}$:

$$h_{o,fs,norm} = \frac{h_{o,fs}}{h_{o,ff}} \tag{4.17}$$

4.8 Falling Film Heat Transfer Enhancement Ratio

The HTC obtained during the falling film configuration was compared to the HTCs obtained during the pool boiling configuration as a ratio in equation (4.19):

$$K_{ff} = \frac{h_{o,ff}}{h_{o,pb}} \tag{4.18}$$

4.9 Coating Heat Transfer Influence Ratio

The heat transfer influence the CuO coating imposes on HTCs from boiling tests are measured by the ratio of the heat transfer performance of the CuO coated tube, $h_{o,CuO}$, to the heat transfer performance of the same uncoated tube, h_o. This calculation was performed by fitting a polynomial equation to the h_o and $h_{o,CuO}$ data to have the curves go through most of the points without over-fitting. This ratio is defined as K_{CuO} and is given by:

$$K_{CuO} = \frac{h_{o,CuO}}{h_o} \tag{4.19}$$

4.10 Film Flow Rate

The film flow rate, Γ_r is the total refrigerant mass flow into the testing chamber $\dot{m}_r$, per one side of the tube, per length of the tube L and is given by [1]:

$$\Gamma_r = \frac{\dot{m}_r}{2L} \tag{4.20}$$

The falling film Reynolds number is given by:

$$Re_r = \frac{4\Gamma_r}{\mu_{r,l}} \tag{4.21}$$

4.11 Nucleation Site and Bubble Density

The number of bubble nucleation sites were investigated through visual analysis of high-speed video footage taken of boiling experiments. The nucleation site densities were determined by identifying where each bubble originated on the surfaces of the tubes in the space captured by the high-speed video camera. The camera was positioned to focus on the same axial position.

Difficulty in identifying nucleation sites became apparent with micro-enhanced tubes and high heat fluxes. Therefore, nucleation site density assessments through visual bubble density were made only at low heat flux cases where possible. The nucleation site density was therefore estimated by counting the number of visible bubbles in still frames throughout the videos and then averaged to be indicative of the nucleation site density.

Theoretical nucleation site densities could be calculated using the Hsu (1962) model of minimum and maximum active cavity radii determined by parametric equations as explored by Xiao et al. [65]. This could be applied to micro-enhanced surfaces, but would not be deemed a visual investigation.

The nucleation site densities were often impossible to determine due to the nucleation sites becoming obscured by the great amount of bubbles. The bubble densities on-screen were used instead to visually inspect the physics during boiling.

The nucleation site density could not be determined on the falling film cases, as it was prominently unclear where the bubbles originated from on top of the tube and coalesce further downwards with the falling film to obscure the view.

4.12 Average Deviation

The average deviation compared measured data against theoretical predictions or correlations. This approach is given by equation (4.22) [1]:

$$\delta_{ave} = \frac{1}{N} \cdot \sum_{i=1}^{N} \left| \frac{x_{t,i} - x_i}{x_i} \right| \times 100 \tag{4.22}$$

Where δ_{ave} is the average deviation, N the total number of data-points, x_i the measured point and $x_{t,i}$ the theoretical solution for that testing point.

4.13 Uncertainty Study

An uncertainty analysis of commercially micro-enhanced tubes was performed. The GEWA-B5 tube was subject to this study where its uncertainties were quantified and compared to micro-enhanced tube studies by Christians [2]. The outcome of this investigation was to condition the interpretation of the micro-enhanced tube's heat transfer data and further ascertain the comparability of data-sets. The uncertainty percentages for heat flux and heat transfer coefficients are depicted below in Figure 4.1:

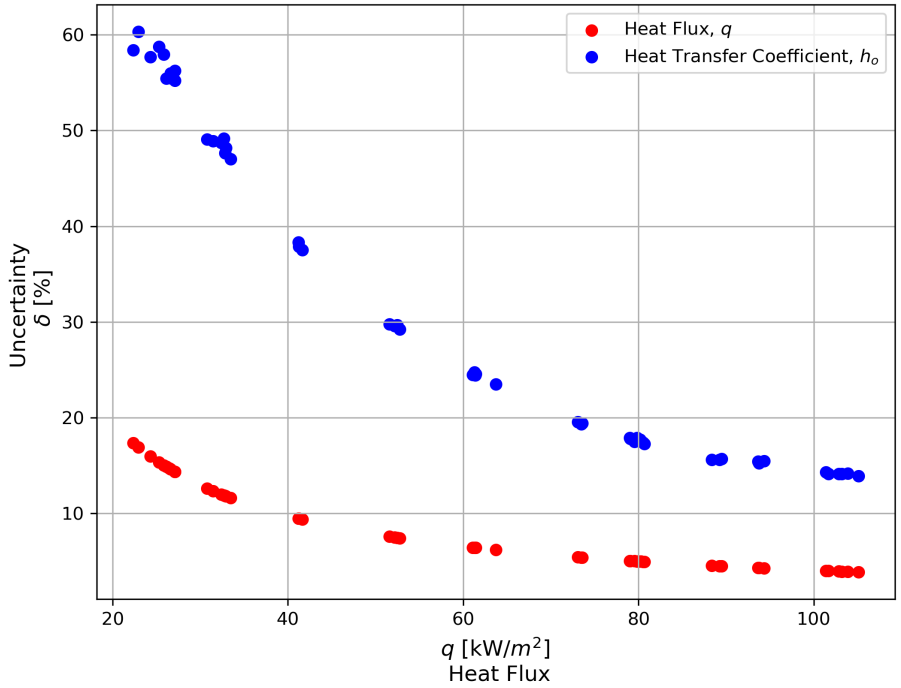

Figure 4.1: GEWA-B5 uncertainties during pool boiling at 5°C

Figure 4.2 below contains the heat transfer coefficients along with the HTC uncertainty in the vertical direction and heat flux uncertainties in the horizontal direction:

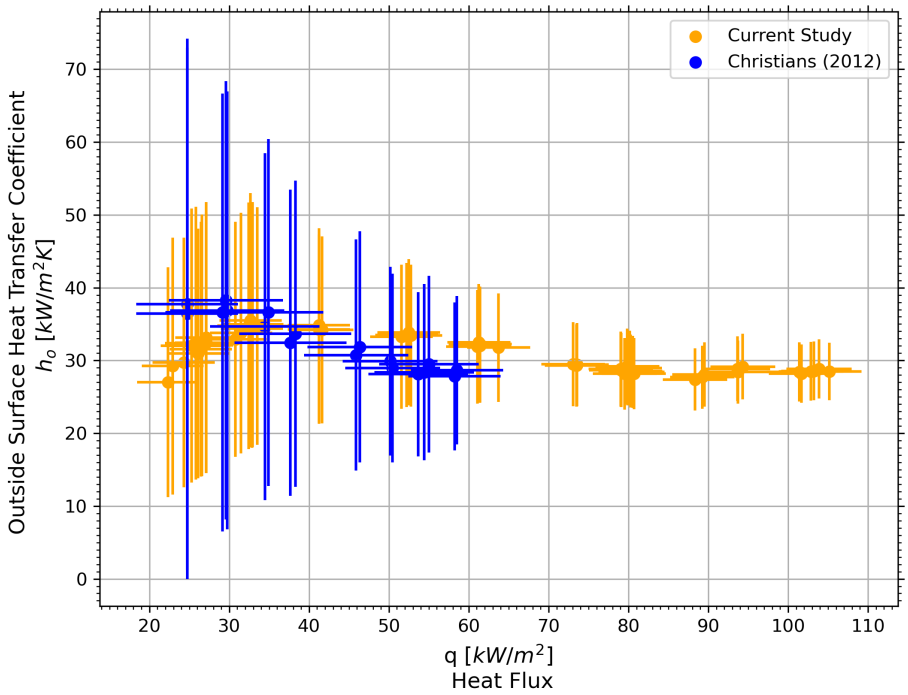

Figure 4.2: Uncoated GEWA-B uncertainty analysis for pool boiling in R-134a at 5°C saturation temperature

The current study's uncertainties are compared to GEWA-B5 pool boiling studies by Christians [2] where the they display satisfactory performance as they fall in the ranges of both HTCs and heat fluxes compared to Christians' findings in Figure 4.2. Further exploration into the uncertainties can be found in Appendix C.

The behaviour of the uncertainties of the significant quantities in this study are illustrated in Figure 4.3 for both pool boiling and pool boiling cases:

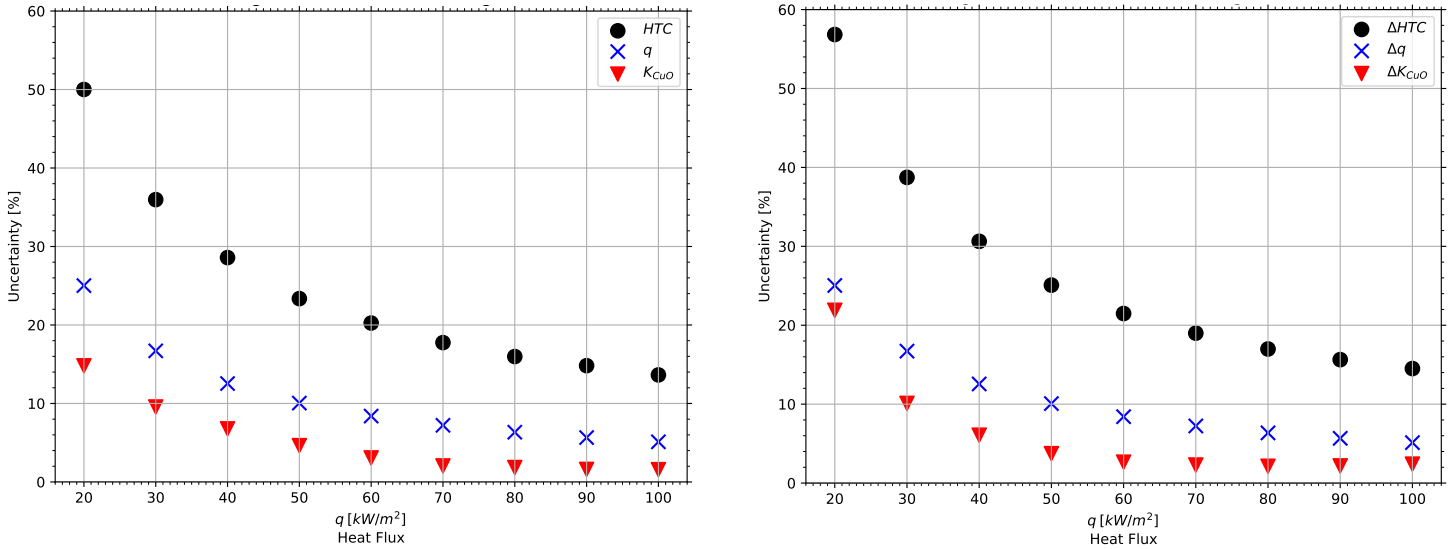

(a) Pool Boiling

(b) Falling Film Boiling

Figure 4.3: Uncertainty percentages of significant quantities over heat flux in the current study

The complete summary of the uncertainties of the significant quantities in the current study from Figure is contained in Table 4.1:

Table 4.1: Summary of uncertainties of significant quantities

Quantity	**Overall average uncertainty** [%]	**Average uncertainty at 20 kW/m2** [%]	**Average uncertainty at 100 kW/m2** [%]
q	10.8	25.0	5.1
h	25.5	53.4	14.1
K_{CuO}	5.5	18.3	2.0

5 Validation

The reliability of the experimental data produced from tests performed on the FF rig was validated by successful comparison between the FF rig and other data sources using the smooth copper tube. Internal validation was performed through comparison to previous results on the same FF rig by previous researchers. External validation was performed through comparison to condensation, pool boiling, falling film boiling and Wilson Plot analyses test data of other researchers. Comparison to relevant boiling correlations were also observed. The Nusselt solution in condensation was more significant since this comparison was generally concentrated upon for validation amongst experimental researchers.

Based on the findings from all validation tests, the FF rig's reliability was then deduced to ascertain the validity of all experimental data produced on the rig.

5.1 Condensation

Condensation tests were performed on the FF rig at a refrigerant saturation temperature of 30°C; and a heat flux range of 5 kW/m^2 to 25 kW/m^2. The resultant condensation heat transfer coefficient was then compared to the Nusselt correlation [66]. The Nusselt solution for tubes in the absence of flooding as previous work was shown that data falls approximately 5% within this solution [1] [51].

Previous research on boiling phenomena display a significant distribution between respective investigations [1]. It is hereby difficult to validate the FF rig's output by only considering boiling data and this is the motive for the use of condensation tests for validation.

The data is compared to the theoretical Nusselt solution, which was produced by equation (4.16), and internally validated against Bock [1] and Gstöhl [51] condensation data, as well as other external research data in Figure 5.1:

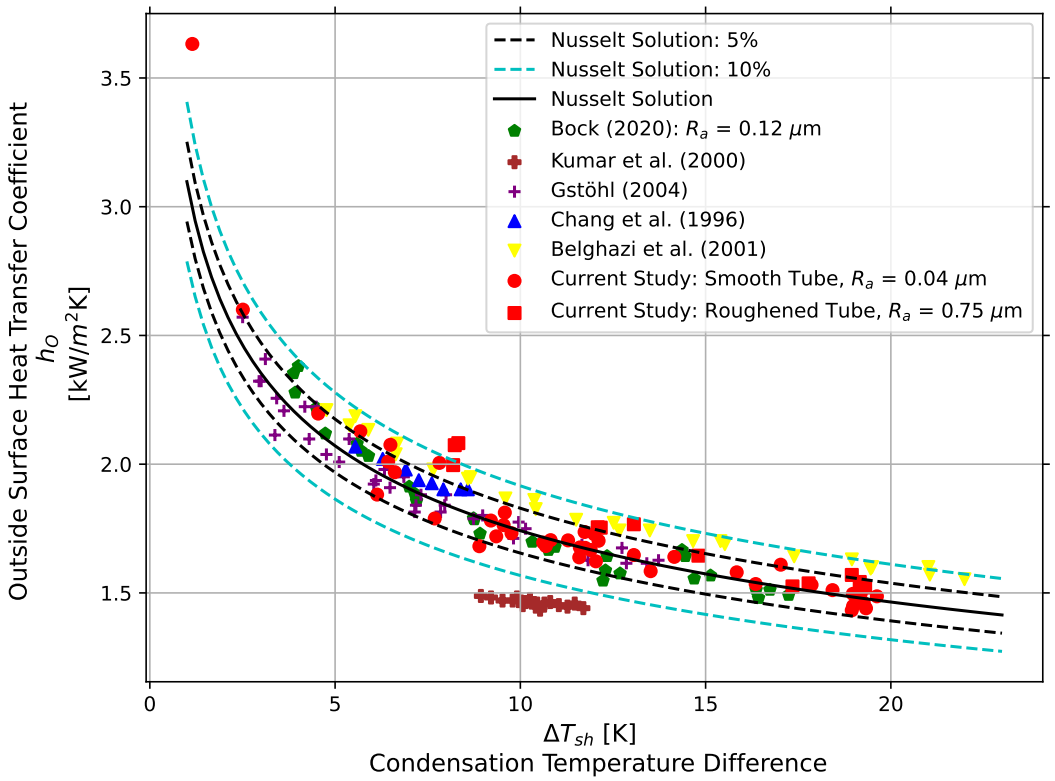

Figure 5.1: Condensation test data at 30°C saturation temperature

Analyzing Figure 5.1, it is found that the condensation data of the current study to generally be in reasonable alignment to to other research data. It is also found that the condensation data to compare very well with the Nusselt solution, where the smooth tube performed the best and the roughened tube deviated at lower temperature superheats. A good 91% of the smooth tube HTCs fell in the 5% deviation band from the Nusselt solution. The average deviation of the complete smooth tube data-set is 2.77% from the theoretical Nusselt solution.

Additional condensation results and comparisons can be found in Appendix K.

5.2 Pool Boiling

Boiling tests were performed on the FF rig in the pool boiling configuration, using a tube that was prepared to relate to previous researchers' tested samples. The Cooper correlation [67] and the Gorenflo and Kenning Model [68] were compared to the pool boiling results. The accuracy of the Cooper correlation [67] was investigated by Ji et al. [69] to deduce its credibility to measure against.

Figure 5.2 illustrates pool boiling results conducted on a smooth tube ($R_a = 0.04\ \mu m$) with its Cooper correlation [67] and Gorenflo and Kenning Model [68]; Bock [1] with a smooth tube ($R_a = 0.12\ \mu m$) with its Cooper correlation [67] for determination of its validity; and Ji et al. [69] with a tube of a an assumed roughness of $R_a = 0.3\ \mu m$.

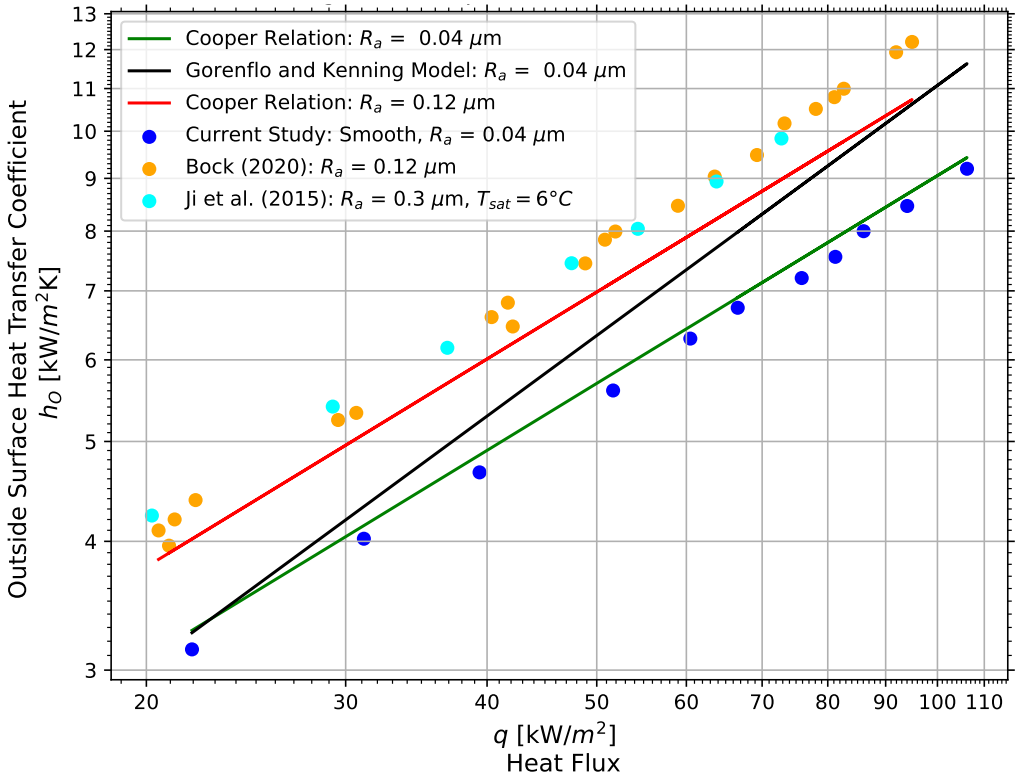

Figure 5.2: Smooth tube pool boiling validation test

With this, it is established in Figure 5.2 that there are many influences on pool boiling HTCs yet to be properly researched and documented, leading to a general lack in consistency in pool boiling results among studies. This is especially observed in Figure 5.2 where Ji et al. [69] and Bock [1] produced approximately the same results where the surface tube roughness of Bock [1] is about half of Ji et al. [69].

It is seen that the data from the current study matches the Cooper correlation [67] well with an average deviation of 3.3%, where no divergence takes place across the heat flux range. The Gorenflo and Kenning Model [68] related very well in the beginning but diverged significantly (up to 17%) with increased heat flux. These results support the findings the by by Li and Hrnjak [70] and discovered by Gorenflo et al. [71], that the Gorenflo and Kenning Model [68] is more accurate at lower heat fluxes, and that a greater investigation into the thermophysical properties, especially surface tension, of the working fluid need to be incorporated into the models for industrial pool boiling applications. The same trends surrounding the Cooper [67] and Gorenflo and Kenning Model [68] in Figure 5.2 is seen regarding the initial high accuracy and divergence in a comparative study performed by Sajjad et al. [72].

The lower HTCs from the current study compared to Bock were most likely due to the lower surface roughness, with the Cooper correlation [67] using an input of 0.04 μm and 0.12 μm which illustrated this.

5.3 Falling Film Boiling

A similar approach to the validation of the FF rigs performance with regards to falling film boiling was conducted as was done with pool boiling. Internal validation was done using previous data from Bock with a surface roughness average $R_a = 0.12\,\mu m$. External validation was done against a smooth tube by Zhao with a claimed roughness of $R_a = 0.3\,\mu m$. The results are captured and compared in Figure 5.3:

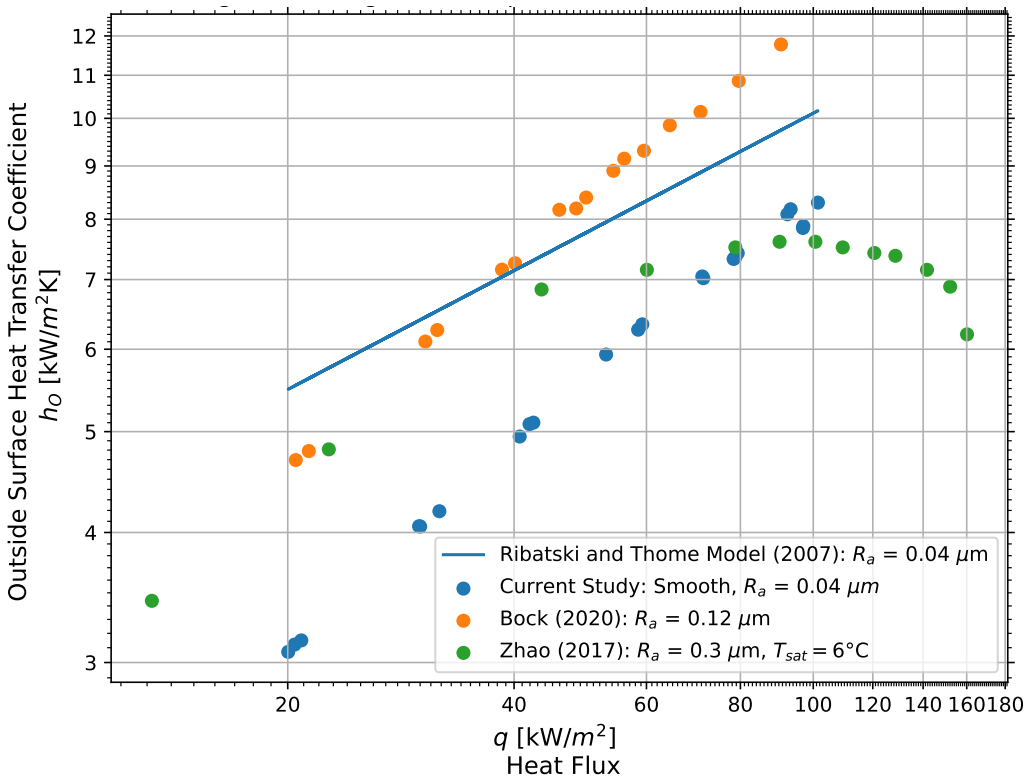

Figure 5.3: Smooth tube falling film boiling validation test

Similar to the deductions from the pool boiling test, it can be inferred to the lower surface roughness of the tube in the current study largely causes the lower HTCs seen compared to tube of Bock and Zhao. It is again observed that the heat transfer coefficients of Zhao show discrepancy when compared to Bock with a tube where the claimed roughnesses do not correspond yet have similar heat transfer performance (the dimensions and materials of the tubes are the same). Furthermore, the gradient of the heat transfer coefficient curve of this study compares well to that of Bock. Zhao shows a declining gradient in the higher heat flux range (from 60 kW/m^2 to 100 kW/m^2), but this may be a result of dryout. The current study deviates significantly from the Ribatski and Thome [50] correlation. The deviation from the model at 100 kW/m^2 is 28% and a large deviation of 80% at a low heat flux of 20 kW/m^2. A similar finding was documented in Bock where the larger deviation from the Ribatski and Thome model was found at higher heat fluxes. This was accredited to major uncertainties that exist in the lower heat fluxes which influenced the development of the Ribatski and Thome model [1].

5.4 Wilson Plot

A Wilson plot analysis was performed on a smooth tube of roughness $R_a = 0.04\,\mu m$ to calculate the internal heat transfer modifying coefficient C_i which is used to fit the Gnielinski correlation to reliably predict the internal heat transfer effects based on water flow through the tube as described in section 3. The test was conducted at a constant heat flux of 20 kW/m^2 and changing the internal flow rate where a modifying coefficient of $C_i = 1.26$ was calculated, compared to common modifying coefficients found by Bock as $C_i = 1.25$ [1] and $C_i = 1.27$ by Roques [61]. The test is hereby satisfactory and the Wilson plot analysis may be reliably performed on future tubes.

5.5 Validity

A successful validation investigation was performed through 4 relevant case comparisons.

The condensation results from the current study compared well to previous researchers in both internal and external respects. With the smooth tube having an average deviation of 2.77% from the Nusselt solution and falling well within the prescribed 5% band, the condensation test asserts the FF rigs validity.

The pool boiling test was performed and its results compared against internal and external research data.The results compared well, where the pool boiling curve trends are equivalent and the lower HTCs are attributed to much lower surface roughness. The comparison to the Cooper correlation [67] was satisfactory with an average deviation of 3.3%, which closely matches the average deviation of previous research studies.

The same findings for the falling film boiling case are observed as for pool boiling, where the lower surface roughness most likely results in lower HTCs compared to previous research studies.

Lastly, a Wilson Plot analysis was performed on the smooth copper tube where the inside Wilson Plot Coefficient, C_i, of 1.26 was obtained. This coefficient closely agreed with previous researcher's findings and proves a successful conduction of this test with accurate measurements.

As all 4 case studies in this validation suffices the theoretical models and previous research with logical explanations for deviations, the FF rig is expected to produce reliable results in the progression of this study.

6 Wilson Plot Analyses

The inside Wilson Plot characterisation coefficients for the tubes tested had been determined through a Wilson Plot analysis. The experimental execution of this special test was as outlined in section 3.13.1.

The Wilson Plot calculations were executed, as described in detail by Bock [1], which involved a 2-step regression iterative procedure to obtain the inside Wilson Plot coefficient, C_i, the boiling exponent, m, and the outside Wilson Plot coefficient C_o. For all practical applications, only the inside Wilson Plot coefficient was relevant for data processing.

The inside Wilson Plot coefficient is principally obtained from extracting the leading coefficient from a linear regression fit line on the Wilson Plot. This coefficient, C_i, is seen in equation (6.1):

$$\left(\frac{1}{U_o} - R_t \cdot A_o\right) \cdot q_o^m = \frac{1}{C_i} \cdot \frac{A_o \cdot q_o^m}{A_i \cdot h_{Gnie}} + \frac{1}{C_o} \tag{6.1}$$

Per the requirements of Christians, Van Rooyen and Thome [73] for micro-enhanced tubes, the Wilson Plot test configuration should be so that the thermal resistance being investigated (characterised) is aimed to be the largest in comparison to the other thermal resistances so as to dominate. A change in the parameter of focus ought to have the greatest effect on the Wilson Plot analysis result. Hereby, the inside thermal resistance was sought to be the dominant resistance [73].

Some exploration into a non-iterative and simplified procedure (CERG) for the Wilson Plot analysis was also undertaken and can be found in Appendix L.

The overall Wilson Plot coefficients for the enhanced tubes were summarised in Table 6.1 below, where the values in blue cells would be used as a resultant from the standard and accepted Wilson Plot methodology (LTCM). The LTCM methodology utilized linear line regression where the goodness of fit line was based on the uncertainties at each point. It was ensured that the goodness of fit achieved was a coefficient of determination of 0.9 or more with each test:

Table 6.1: Overall Wilson Plot coefficients of enhanced tubes tested

Tube Name	1st	2nd	3rd	4th	5th	Average	Standard Deviation	Uncertainty	Analysis Method
Smooth	1.26							0.10	LTCM
Roughened	1.22							0.10	
GEWA-B5	4.08							0.15	
GEWA-KS	3.74	3.65	3.68	3.60	3.70	3.67	0.05	0.09	
EHPII	4.17	4.15	4.17	3.92	3.96	4.07	0.11	0.22	
Smooth	1.28								CERG
Roughened	1.20								
GEWA-B5	4.20								
GEWA-KS	3.91	3.86	3.83	3.83	3.85	3.86	0.03	0.06	
EHPII	4.48	4.50	4.52	4.24	4.29	4.41	0.12	0.23	

7 Pool Boiling Results and Discussion

The 4 tubes in this study were investigated under pool boiling conditions in R134 refrigerant. Heat transfer was observed at a saturation temperature of 5°C. The effect of increasing the saturation temperature to 25°C was also observed for the GEWA-KS and EHPII tubes. Tests were conducted where HTCs were recorded across a range of heat fluxes (heat flux sweeps) to produce boiling curves.

Each tube type is discussed individually and the CuO nanocoating's influence is observed through the calculated coating heat transfer influence ratio. A brief overview of the pool boiling performances of all the tubes is given afterwards in a collective summary. The average deviation of the micro-enhanced tubes with respect to the reference roughened plain tube is also used to perceive the difference in HTC magnitudes.

7.1 Roughened Tube

The uncoated and coated roughened tube HTC results are displayed in Figure 7.1. Pool boiling data from Bock [1] of similar surface roughness average is included as additional reference:

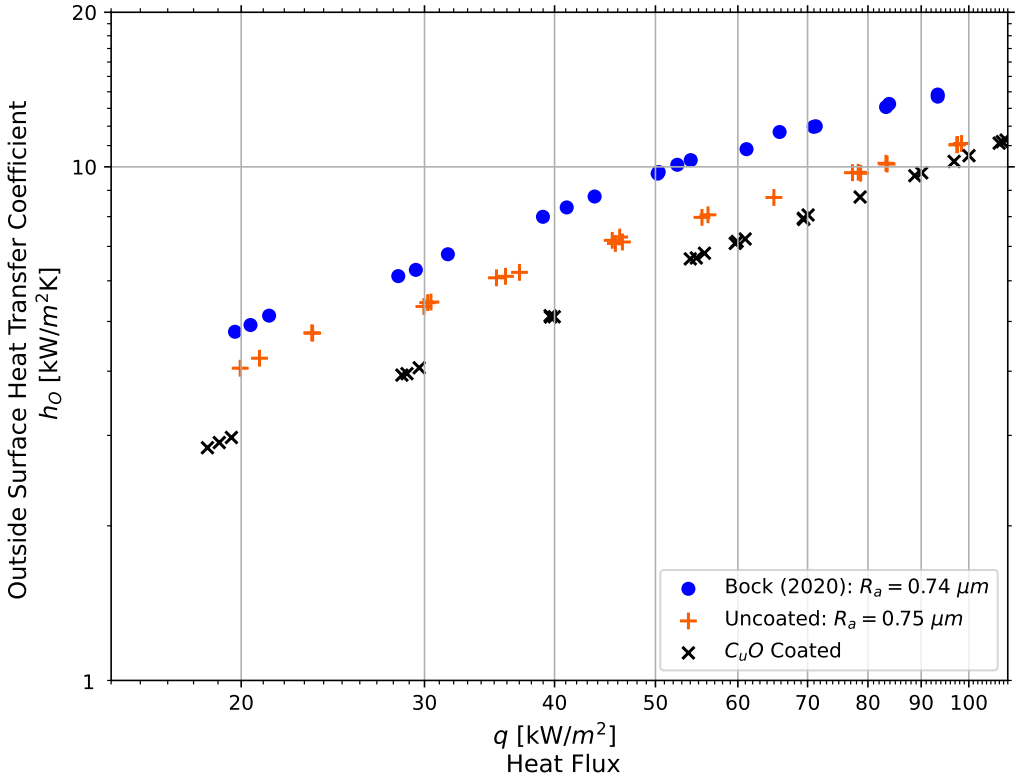

Figure 7.1: Uncoated and coated pool boiling of roughened tube at a saturation temperature of 5°C in R134a

It is seen in Figure 7.1 that the uncoated roughened tube compares relatively well to the data from Bock [1] considering the established surface roughness variations of hand-sanded tubes. Both the uncoated and coated roughened tube increased linearly on the log-log plot as the nucleation site density increased through the activation of nucleation sites at higher heat fluxes.

It is observed that the CuO coated roughened tube under-performs consistently compared to the uncoated roughened tube up to approximately 100 kW/m^2. The uncoated and coated roughened tube were fairly dependent on the testing heat flux range. The HTCs increased by 8.8% across the testing heat flux range whereas the HTCs increased by a greater 9.5%. The coated tube's HTCs were on average -15.9% lower than the uncoated tube and indicated a considerable decline in heat transfer performance.

With the coated tube's higher gradient in Figure 7.1, it is suggested that the HTCs tend to be enhanced at higher heat fluxes relative to the uncoated tube and that the HTCs should be investigated at heat fluxes higher than 100 kW/m^2 for possible HTC enhancement.

A likely cause of the deterioration specifically to the coated roughened tube is the slight smoothing of the grooves on the roughened tube surface by the CuO coating as is seen in Figure 3.10 and the resultant decrease in nucleation site density. The extreme wettability of the CuO coated surface may cause nucleation flooding as described by Li et al. [28] to deteriorate the HTCs and is also pointed out by Attinger et al. [34] for plain hydrophilic surfaces. Despite this, it was documented by Attinger et al. [34] through experimental investigation that extreme wettable surfaces may perform just as well or better than the uncoated base surfaces at very high heat fluxes, which was contrary to their suggested model. It may be that the liquid in the flooded nucleation sites on a CuO coated surface would tend to form a fast-evaporating microlayer at higher heat fluxes when liquid evaporates more readily for greater heat transfer performance where the uncoated nucleation sites would suffer from dryout. This development may also describe the coated tube's marginally higher increase in HTCs over the heat flux range compared to the uncoated tube.

The coating heat transfer influence ratio is calculated to quantify the deterioration of the HTCs at specific points by the CuO coating on the roughened tube and is collected in Figure 8.17.

In order to investigate the mechanism of HTC deterioration of the roughened tube, high speed footage of the 20 kW/m^2 and 100 kW/m^2 cases are compared below:

(i) Uncoated (ii) CuO coated

(a) 20 kW/m^2

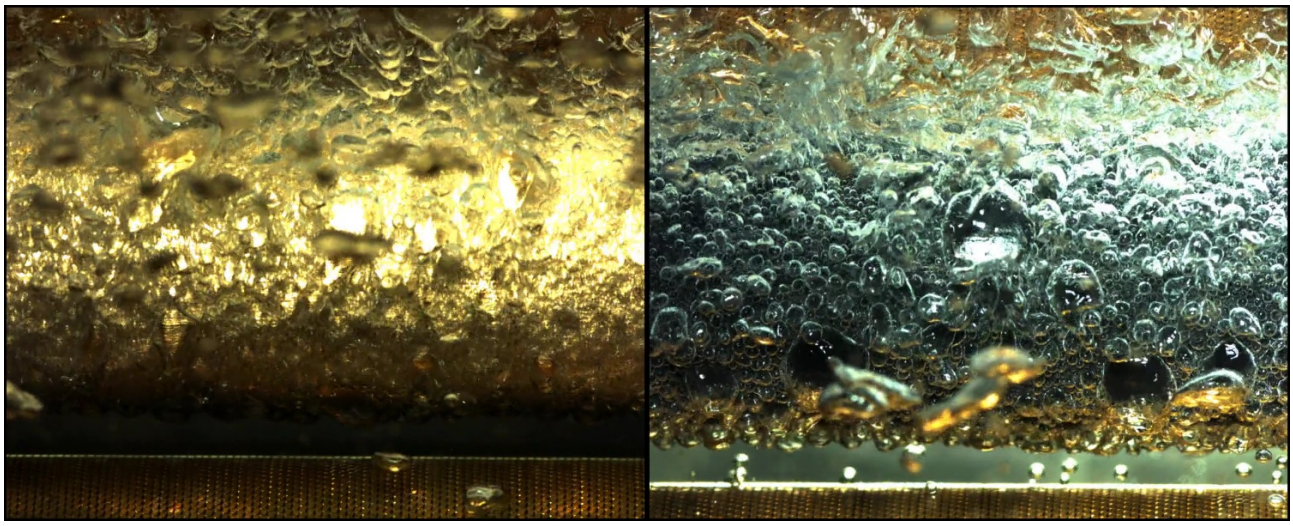

(i) Uncoated (ii) CuO coated

(b) 100 kW/m^2

Figure 7.2: Pool boiling comparison of roughened tube at 5°C saturation temperature

It is seen from Figure 7.2 that with an increase in heat flux, there is an increase in bubble density in both uncoated and coated cases as is to be expected. Upon close inspection of the high speed video, the bubble densities are visually observed to be slightly less for the CuO coated tube in the 20 kW/m^2 case in Figure 7.2a, whereas it is found that the bubble density for the coated and uncoated tube in the 100 kW/m^2 case is similar.

It is also noted where bubbles' behaviour became more apparent in the higher 100 kW/m^2 case from Figure 7.2b, that the bubbles appeared to be larger in size for the coated tube than for the uncoated tube.

7.2 GEWA-KS

Uncoated and coated GEWA-KS low finned, 19 fins per inch (fpi), tubes were tested in pool boiling in R134a at saturation temperatures 5°C and 25°C. No previous research data could be found for the GEWA-KS tube in pool boiling under these conditions, however, the linear HTCbehaviour of integral-fin tubes could be gained from studies by Webb and Pais [74]. The HTC results are indicated in Figure 7.3:

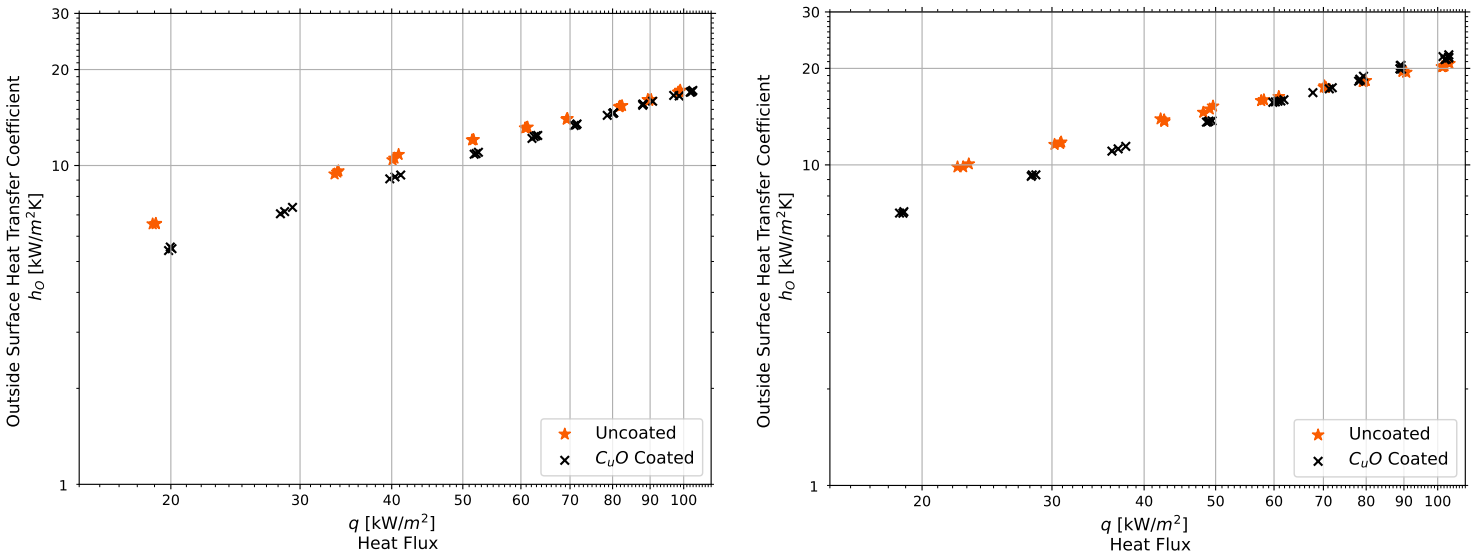

(a) 5°C (b) 25°C

Figure 7.3: Uncoated and coated pool boiling of GEWA-KS at saturation temperatures of 5°C and 25°C in R134a

Inspecting Figure 7.3, similar deductions as for the roughened tube are made, where the HTCs increased linearly on the log-log plot for both uncoated and coated tubes at both saturation temperatures. The nature of the GEWA-KS tube HTC curves being similar to that of a plain tube seen in Figure 7.1 may be granted due to the low fin tube's surface being analogous to a plain tube surface with no micro-enhanced channels. The great increase in HTCs from the plain roughened tube to the GEWA-KS are a resultant of the significant increase in surface area from the comparatively large fins on the low fin tube surface.

The increase in HTC of the GEWA-KS HTCs over the testing heat flux range were determined to be 13.1% for the uncoated tube and 14.1% for the coated tube in 5°C to indicate a slightly greater dependence on heat flux than the roughened tube. A similar outcome was observed in the 25°C case where the uncoated tube's HTCs increased with 13.7% and those of the coated tube with 17.6% to show a stronger dependence on heat flux.

An overall decrease in HTCs from the uncoated tube to the coated tube is seen in the 5°C case of Figure 7.3a, where the heat transfer performance declines by 9% through the CuO coating. A similar outcome is seen for the influence of the HTC coating in the 25°C case where the heat transfer declines by 5.5%.

The HTCs increased for both the uncoated and coated tube with an increase in saturation

temperature from 5°C to 25°C in correspondence to boiling theory [11]. An HTC increase of 25.5% for the uncoated tube and a slightly greater increase of 29.9% was observed for the coated GEWA-KS tube when increasing the saturation temperature from 5°C to 25°C.

In both saturation temperatures it is seen that the uncoated GEWA-KS tube performed marginally better than the coated tube over the tested heat flux range. There is a slight difference in gradients where the coated tube's boiling curve is steeper than the uncoated tube, thus causing a possibility that the coated GEWA-KS tube's HTC curve could cross the uncoated tube's HTCs around 100 kW/m^2 at 5°C saturation temperature in Figure 7.3a; and a crossing is observed at 80 kW/m^2 for the 25°C saturation temperature case in Figure 7.3b. It may be of investigative interest to explore HTC behaviour at higher heat fluxes for the uncoated and coated GEWA-KS tube at both saturation temperatures.

To further inspect the effect the CuO coating has on the GEWA-KS tube, the coating heat transfer influence ratio is calculated for both saturation temperatures and is collected in Figure 8.17.

To view boiling behaviour of the uncoated and coated GEWA-KS tube, high speed footage is compared for the 20 kW/m^2 and 100 kW/m^2 cases at both 5°C and 25°C saturation temperatures in Figures 7.4, 7.5, 7.6 and 7.7:

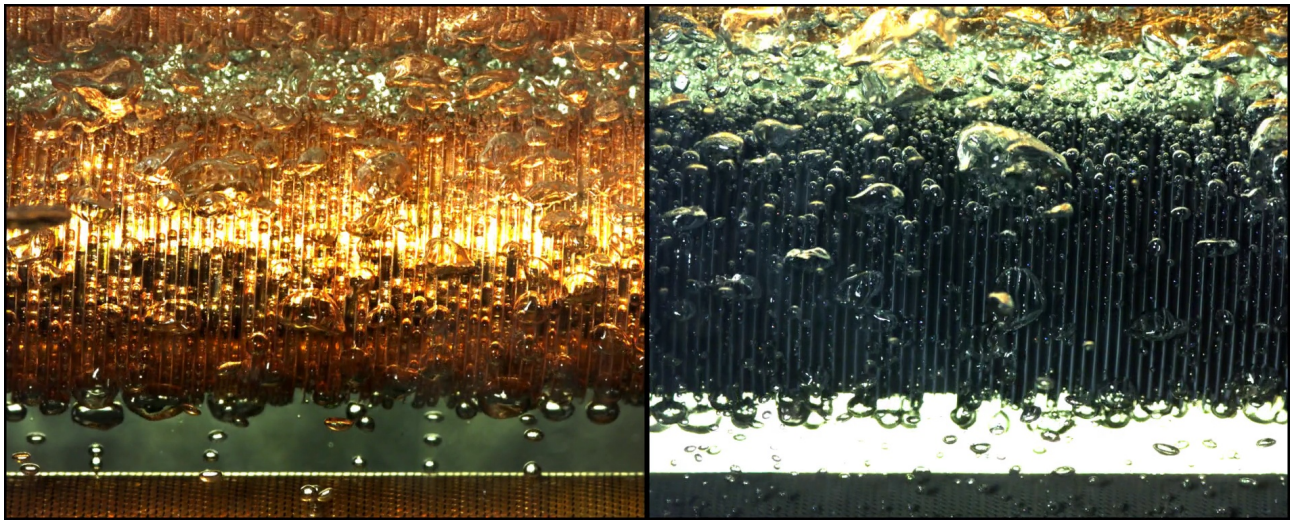

(a) Uncoated (b) CuO coated

Figure 7.4: Pool boiling comparison at 5°C saturation temperate of GEWA-KS at 20 kW/m^2

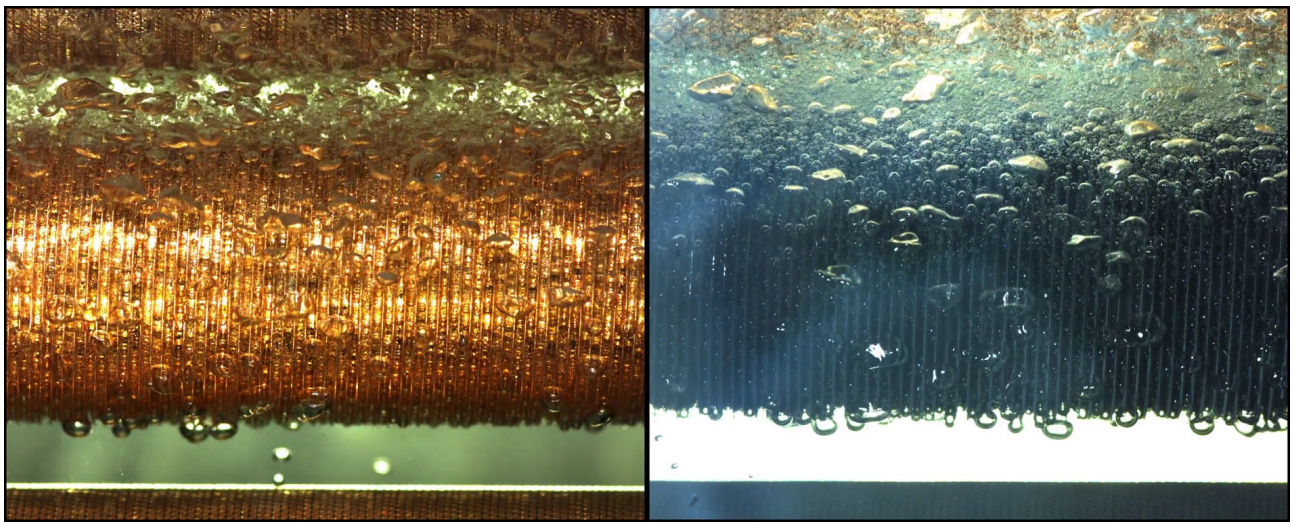

(a) Uncoated (b) CuO coated

Figure 7.5: Pool boiling comparison at 25°C saturation temperate of GEWA-KS at 20 kW/m^2

Upon close examination of the high speed footage in Figures 7.4 and 7.5, a consistent observation is that the bubbles for the coated tube at both saturation temperatures seemed to be slightly larger than those of the uncoated GEWA-KS tube. The largest bubbles were found at 5°C saturation temperature in Figure 7.4.

As expected, the bubble sizes for both uncoated and coated GEWA-KS tubes were larger at 5°C than at 25°C because of the greater saturation pressure exerted on the bubbles at 25°C at the same heat flux.

Another important observation for both saturation temperatures is that the bubble density for the uncoated GEWA-KS tube to be greater than that of the coated GEWA-KS tube and is clearly visible in Figure 7.5. It is also observed that the bubbles are smaller.

Some high speed footage is also inspected at both saturation temperatures at 100 kW/m^2. The comparison is displayed in Figure 7.6 and 7.7 below:

(a) Uncoated (b) CuO coated

Figure 7.6: Pool boiling comparison at 5°C saturation temperate of GEWA-KS at 100 kW/m^2

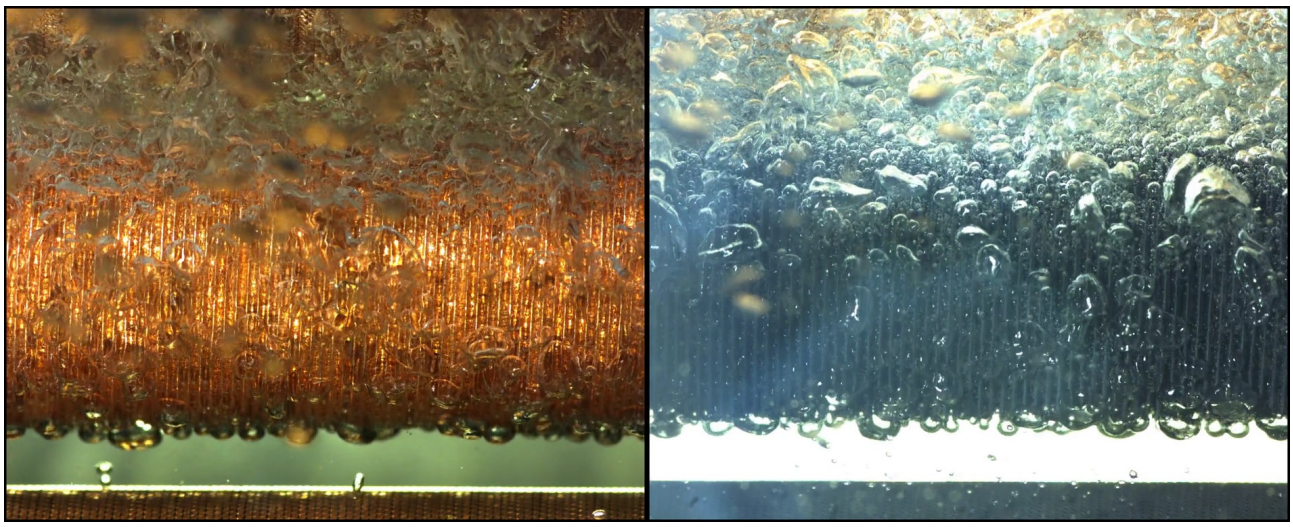

(a) Uncoated (b) CuO coated

Figure 7.7: Pool boiling comparison at 25°C saturation temperate of GEWA-KS at 100 kW/m^2

Investigating the 100 kW/m^2 case above in 7.6, it seems that the bubble density and size to be more equivalent between the uncoated and the coated GEWA-KS tube at 5°C and 25°C saturation temperature, which coincide with their similar performances as is observed by the uncoated and coated HTC pool boiling curves in Figure 7.3b.

As is with the roughened tube, the frequency of nucleation and bubble densities for all uncoated and coated tubes are generally much more intense at the higher heat fluxes than at the lower heat fluxes.

7.3 GEWA-B5

The HTC results for the uncoated and coated GEWA-B5 tubes are displayed in Figure 7.8 below, where pool boiling data of an uncoated GEWA-B5 tube from Christians [2] is included as additional reference. As an additional objective, the importance of cleaning the tubes according to section 3.11.1 is demonstrated where the HTC results of an aged uncoated GEWA-B5 tube is also included:

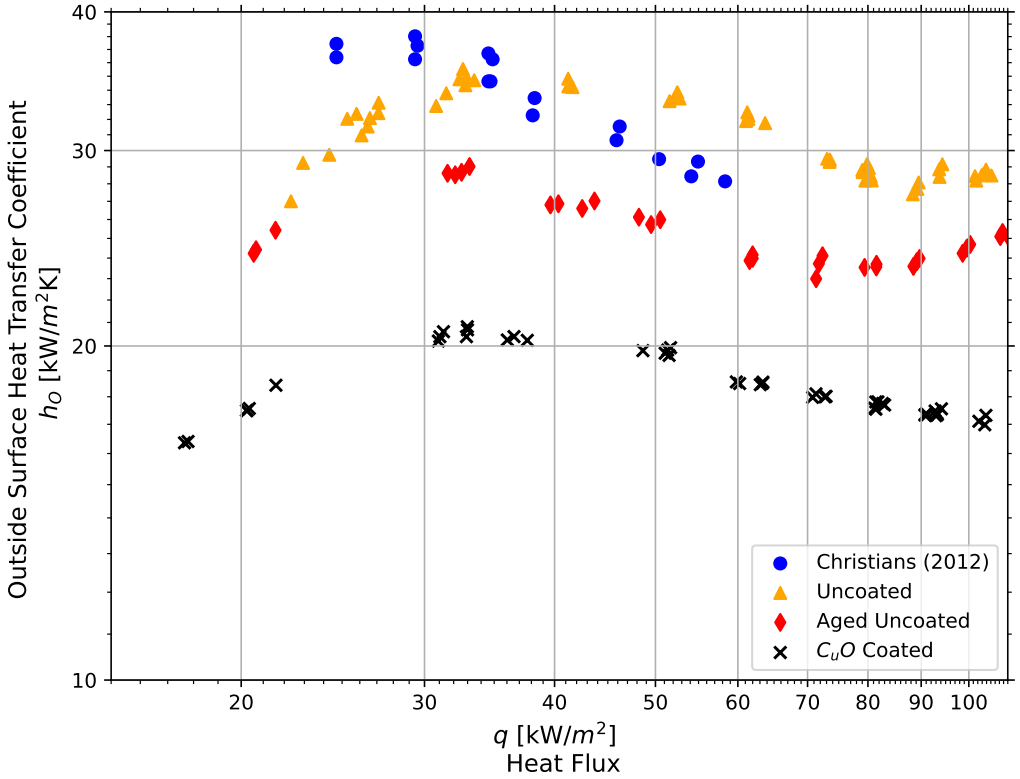

Figure 7.8: Uncoated and coated pool boiling of GEWA-B5 at 5°C saturation temperature

It is seen in Figure 7.8 that the HTCs of all tubes did not increase uniformly with heat flux. The HTCs of the uncoated, aged and coated tubes were the highest around 35 kW/m^2. This is distinctive behaviour of micro-enhanced tubes seen in previous studies such as in Christians [2]. The HTCs of the uncoated and coated GEWA-B5 tubes are are steady across the testing heat flux range with an of 3.1% for the uncoated tube and -0.4% for the coated tube. Both tubes' heat transfer performance thus display strong independence from heat flux. The CuO coating heavily decreased the HTCs with an average deviation of -39.2% for the coated tube with respect to the uncoated tube. The coated tube also consistently under performs against the uncoated tube with no likelihood of enhancing the HTCs at higher heat fluxes. The CuO coating is not suitable for enhancing HTCs on the GEWA-B5 micro-enhanced tube.

The aged uncoated GEWA-B5 tube's HTCs are seen in Figure 7.8 to be a proportional shift downwards from the refurbished uncoated GEWA-B5 tube. It is thus evident that the copper carbonate and sediment mixture surface layer on the tube surface as a result of exposure to the atmosphere caused the heat transfer performance of the aged tube to decrease. After the tube was cleaned, the uncoated GEWA-B5 performance was again up to standard by comparing its

HTCs to Christians [2]. This finding suggests that heat transfer performance of tubes may be improved simply through a refurbishment process.

Considering the intricate geometry of the GEWA-B5, the substantial decrease in HTCs suggest that a core heat transfer mechanism the micro-enhanced surface layer has been obstructed by the CuO nanocoating. In order to identify the impeding effect the coating induces on the heat transfer mechanism, high speed footage is examined at 20 kW/m^2, 60 kW/m^2 and 100 kW/m^2:

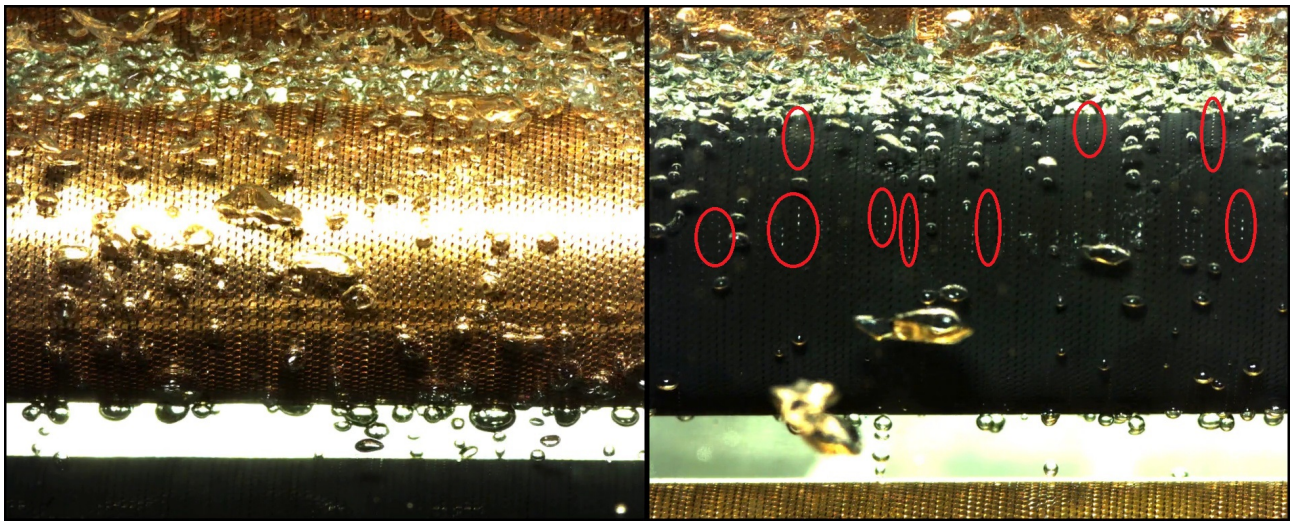

(i) Uncoated (ii) CuO coated

(a) 20 kW/m^2

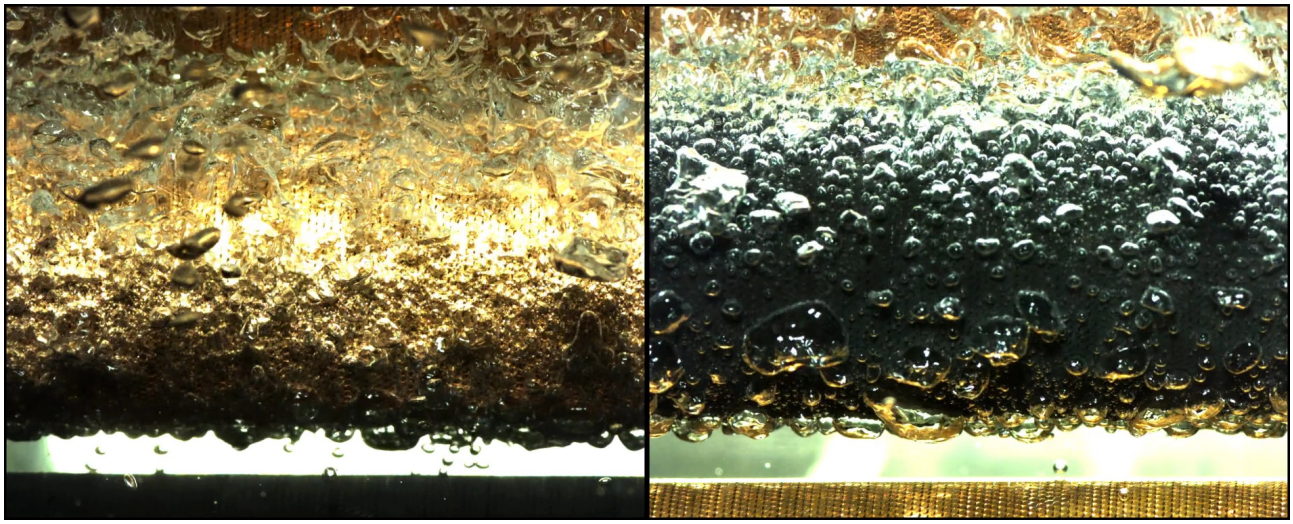

(i) Uncoated (ii) CuO coated

(b) 100 kW/m^2

Figure 7.9: Pool boiling of GEWA-B5 comparison at 5°C in R134a

Inspecting Figure 7.9, it is seen again that the nucleation site density to increase with heat flux in both uncoated and coated tube cases, despite all having similar HTC performance. This may be an onset of dryout with the microchannels at higher heat fluxes, or the deterioration of the complex hydraulic mechanism by inundation of bubbles and vapour. It is suspected that the short capillaries connecting the re-entrant cavities of the GEWA-B5 microstructure steadily supply the nucleation sites with liquid in order to sustain the superheating micro-layer for rapid evaporation. It may be at high heat fluxes that vapour fills these capillary channels and dries out so not to be as effective in feeding the micro-layers in the re-entrant cavities.

A pattern is recognised in the visual inspection of the tubes, where it is noted that the nucleation site density of the uncoated tube to be more than the coated tube in all cases. This is especially seen in the 20 kW/m^2 case of Figure 7.9a through the nucleation site density and the bubble density. The nucleation site density was determined by manually counting the nucleation sites on both the uncoated and coated tube on a still frame and the bubble density was determined by counting the individual appearances of bubbles on 3 different still frames throughout the high speed video. The nucleation site density of the coated tube was approximately 71% of that of the uncoated tube and the bubble density was approximately 68% of that of the uncoated tube. The nucleation site and bubble counting for this case where it was possible can be seen in Appendix M.

It is again noted that the bubble sizes are much larger for the coated tube than for the uncoated tube and this is clearly visible in the 100 kW/m^2 case in Figure 7.9b.

The GEWA-B5 tube has intricate internal micro-channels as part of its surface micro-enhancements which consist of re-entrant cavities that are interconnected with micro-capillary channels running through the circumference of the tube. It is suggested that this creates an additional hydraulic heat transfer component by which the ejection of the bubbles at the re-entrant cavity draws liquid through the capillary channels for excellent sensible heat transfer. A focus of design in advanced microstructure geometries are to supply the re-entrant cavities with liquid [28] through capillary action and thereby prevent the onset of dryout in the cavities. It is suspected that this pumping mechanism is either obstructed by the coating, or the nucleation process itself is diminished.

A peculiar phenomena is detected in the boiling of the coated GEWA-B5 at 20 kW/m^2, shown in Figure 7.9a. The uncoated GEWA-B5 tube boiled as expected, where the active nucleation sites produced bubbles that are ejected from micro-channel crevices followed by a new bubble in periodic fashion. The coated GEWA-B5 seems to have non-periodic bubble generation and slow nucleation at the micro-channel crevices, where substantial vapour entrapment occurs within these crevices. Instances of this entrapment are indicated with red circles in Figure 7.9a. An enlarged visual of the vapour entrapment is displayed in Figure 7.10 below:

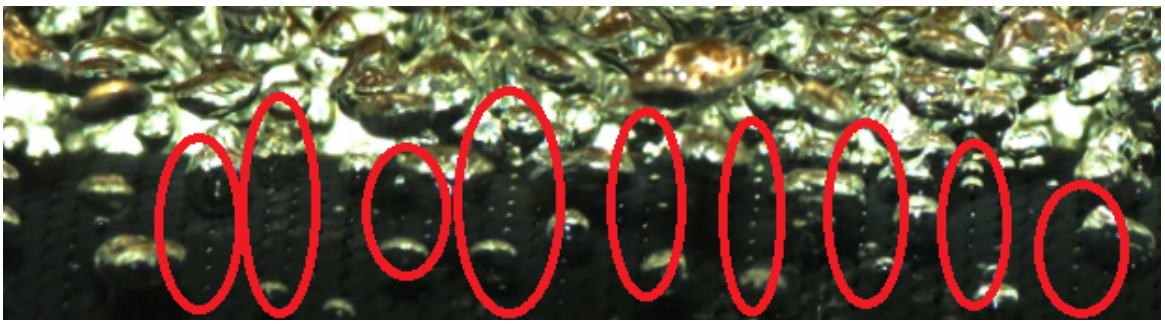

Figure 7.10: Vapour entrapment in the GEWA-B5 re-entrant cavities in pool boiling at $20kW/m^2$ and 5°C in R134a

This entrapped vapour in the crevices, as indicated by the red ovals in Figure 7.10, is prominent and pulsates with an occasional release of a bubble drawing the vapour downwards. This behaviour of the coated surface was present at higher heat fluxes too.

It is likely that part of the heat transfer performance loss can be attributed to this behaviour of the coated surface, where bubble release is hindered and a significant portion of the surface could be covered by a vapour lining in a film boiling fashion. This is especially so if this lining is in the micro-channels which were initially intended to enhance nucleation heat transfer, but would not be visible from the video as it is hidden within the micro-enhancements.

7.4 EHPII

A set of uncoated and coated EHPII tubes was tested under pool boiling conditions. No previous research data was available for comparison. The uncoated and coated EHPII tube set was investigated at both 5°C and 25°C saturation temperatures to observe the effect of increasing the saturation temperature in R134a refrigerant. The HTC results are displayed in 7.11 below:

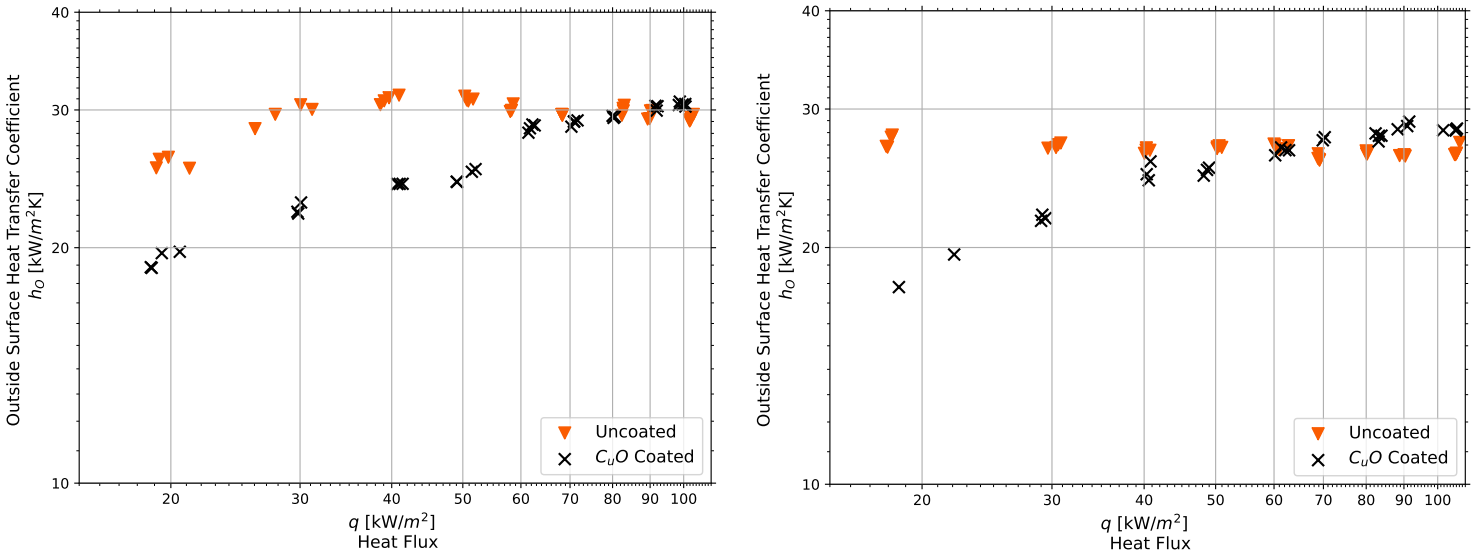

(a) 5°C (b) 25°C

Figure 7.11: Uncoated and coated pool boiling of EHPII at saturation temperatures of 5°C and 25°C in R134a

From Figure 7.11, the typical behaviour of a micro-enhanced tube is again observed where the HTCs were more constant as heat fluxes were increased for the uncoated EHPII tube. The uncoated tube increase over the heat flux range was found to be 4.2% at 5°C and -1.1% at 25°C to indicate a large degree of independence from heat flux as the HTCs are very stable across the testing heat flux range. The CuO coated tube, however, had an increase in HTCs of 13.8% at 5°C and 12.5% at 25°C to indicate a much greater dependence on the testing heat flux and that the HTCs tend to increase with increasing heat flux.

It is seen that the CuO coating lowered the HTCs from the uncoated EHPII tube for both 5°C and 25°C saturation temperature cases at heat fluxes below 60 kW/m^2, while similar HTCs were seen above 60 kW/m^2. It was found that the CuO coating generally decreased the HTCs from the uncoated tube with an average of -11% at 5°C and with -4.3% at 25°C.

It is noted that a minor decrease in HTCs from the 5°C to the 25°C saturation temperature case occurred which opposes boiling theory as there was not the expected increase in HTCs with an increase in saturation temperature, as the latent heat of vaporization is less and less wall superheat is required for the activation of more nucleation sites [11]. This leads to the deduction that with the increase in saturation temperature, the thermal gradient from the surface is altered to lead to an unfavourable nucleation position on the EHPII microstructure scales to result in less effective boiling [53]. With an increase in saturation temperature from

5°C to 25°C, the uncoated tube decreased with an average deviation of -10% where the coated tube decreased with a smaller change of -3.2%. This heat transfer reduction is further inspected through high speed video analysis in Figures 7.12 to 7.13 and is discussed below.

To quantify the degree of the deterioration of HTCs from the uncoated to the coated EHPII tubes at 5°C and 25°C saturation temperatures, the coating heat transfer influence ratios are calculated and collected in Figure 8.17.

High speed footage for both saturation temperatures are analysed in Figures 7.12 and 7.13 at 20 kW/m^2, 60 kW/m^2 and 100 kW/m^2 since the HTCs display non-uniform behaviour over the tested heat flux range:

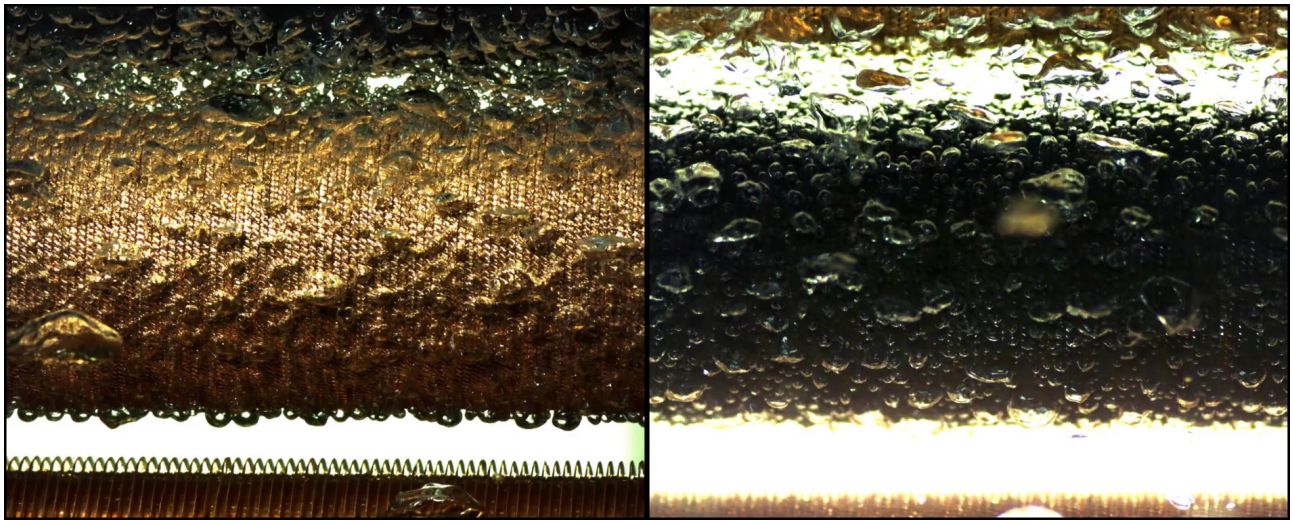

(i) Uncoated (ii) CuO coated

(a) 5°C

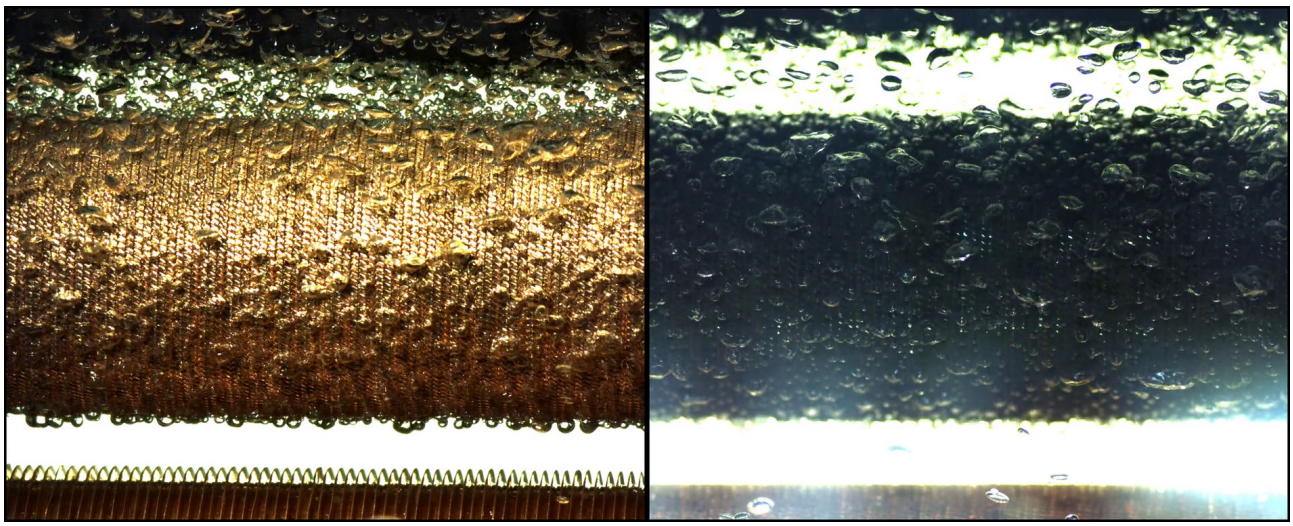

(i) Uncoated (ii) CuO coated

(b) 25°C

Figure 7.12: Pool boiling comparison of EHPII at 20 kW/m^2 at saturation temperatures of 5°C and 25°C in R134a

For the lowest testing heat flux seen in Figure 7.12 where the uncoated tube outperforms the

coated tube in both saturation temperature cases, it is again seen that the bubble site density of the uncoated tube to be significantly greater than for the coated tube. The bubble sizes are also seen to be much larger for the coated tube than for the uncoated tube.

For this heat flux case where the EHPII tube in the 25°C saturation temperature generally performed better than in the 5°C saturation temperature, it can be seen across from the 5°C to the 25°C cases that the bubbles will decrease in size as expected, however the bubble densities remain indistinguishable. The observation for the 60 kW/m^2 case, which portrays similar information as given by the 20 kW/m^2 case is found in Appendix K.

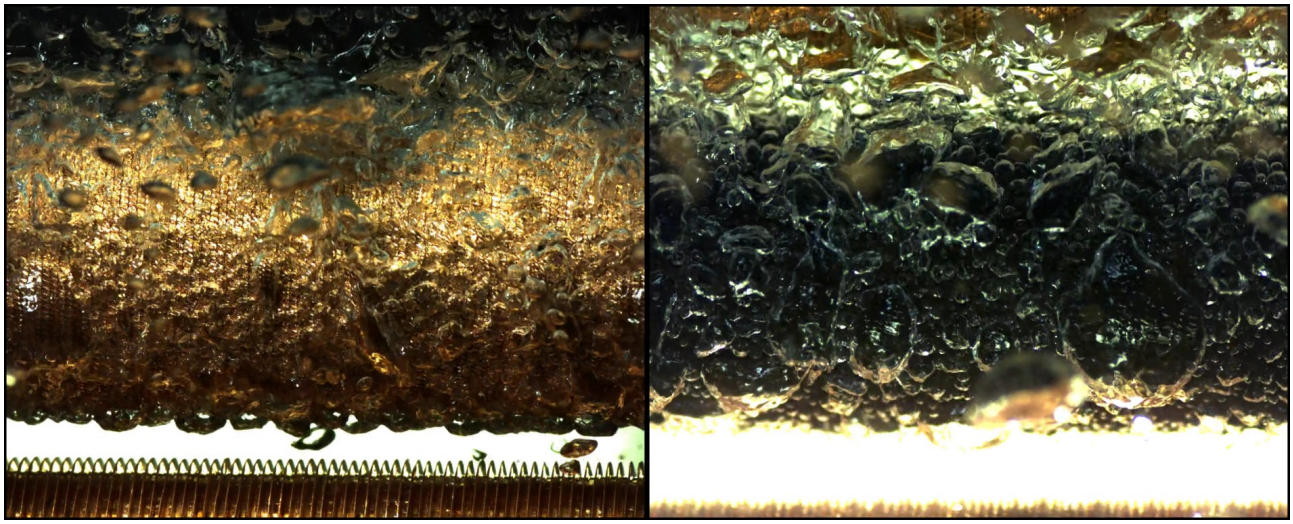

(i) Uncoated (ii) CuO coated

(a) 5°C

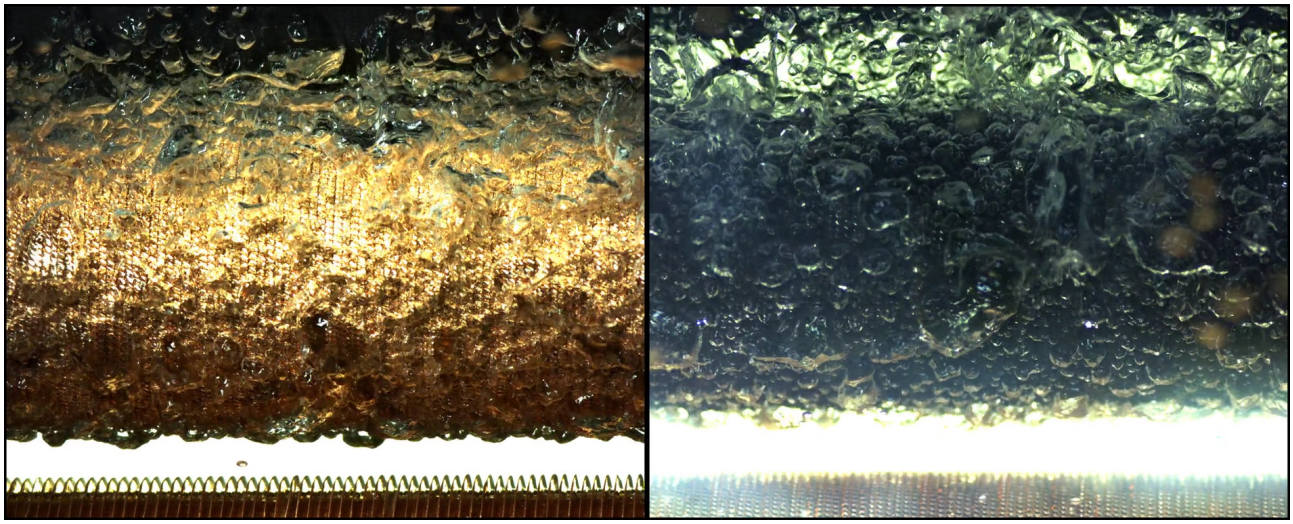

(i) Uncoated (ii) CuO coated

(b) 25°C

Figure 7.13: Pool boiling comparison of EHPII at 100 kW/m^2 at saturation temperatures of 5°C and 25°C in R134a

There appears to be little difference in bubble density between the uncoated EHPII tube and the coated EHPII tube in both saturation temperature cases at the heat flux of 100 kW/m^2.

The only difference is the larger bubble sizes on the coated EHPII tube compared to those on the uncoated EHPII tube.

The general decrease of HTCs from the 5°C saturation temperature to the 25°C saturation temperature for the uncoated EHPII tube can be due to a number of reasons. It is seen from Figure 7.13 that all of the nucleation sites are already activated at 5°C for there to be no further increase in active nucleation sites at higher heat flux. Hereby, other reasons for heat transfer impedance must be considered. Regarding the simple nucleation equation, it may also be due to the decrease in the liquid-vapour-metal interface surface tension forces [25] from the increase in saturation temperature to lower the activation superheat. With the high density of scale-like microstructures instigating nucleation, this may have caused a vapour layer phenomena within the microstructures as a result of bubble coalescence. This decrease in heat transfer performance at 25°C is further explored in section 7.6 and fully explained.

7.5 Pool Boiling Overview

The overview of pool boiling HTCs of the uncoated and coated micro-enhanced tubes at 5°C and 25°C saturation temperature are shown in Figure 7.14 and 7.15 below:

7.5.1 Uncoated

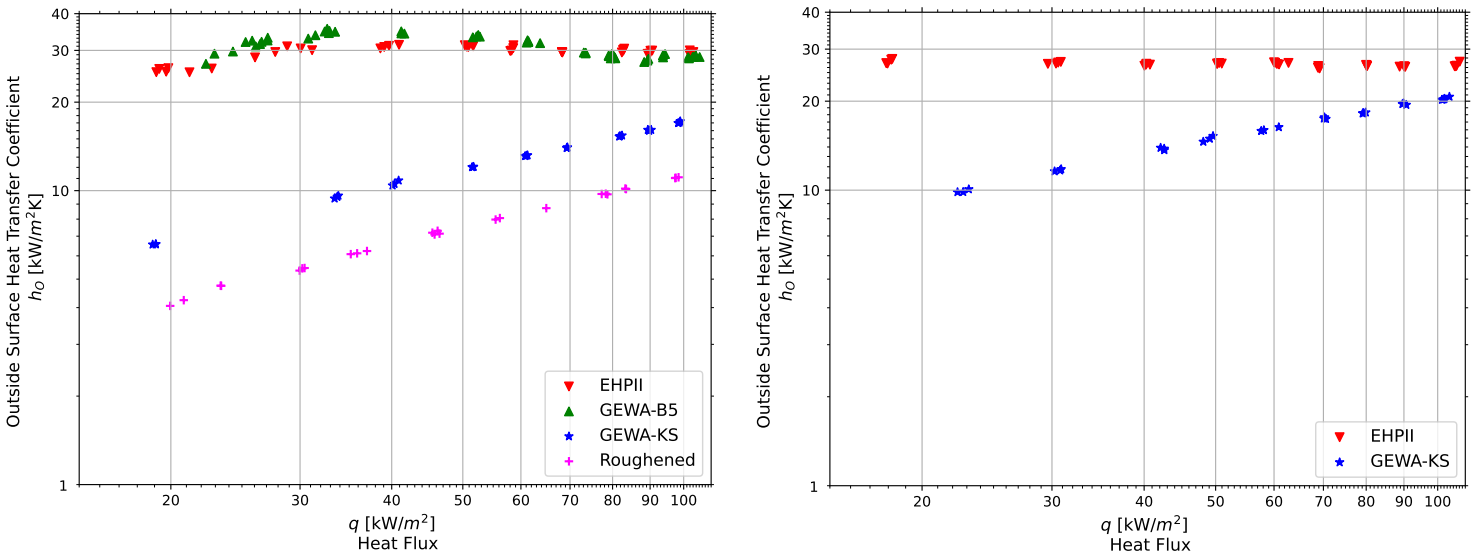

(a) 5°C (b) 25°C

Figure 7.14: Pool boiling overview of uncoated micro-enhanced tubes in R134a at saturation temperatures of 5°C and 25°C

It is observed in Figure 7.14a for 5°C that the EHPII tube and the GEWA-B5 tube together performs the best with very little dependency on heat flux, whereas the GEWA-KS tube followed with lower HTCs and an increase in HTC of 13% across the heat flux range. The roughened tube performed with the lowest HTCs and with an increase in HTC of 8.8% across the heat flux range.

The order of best performance correlates with the complexity of microstructure types, where the GEWA-B5 capillary pore and EHPII scaled micro-enhanced surfaces outperformed the low-finned GEWA-KS and plain roughened tubes. The EHPII tube and GEWA-B5 had HTCs 298.3% and 318% respectively greater than the roughened tube, whereas the GEWA-KS also performed better than the roughened tube with an average improvement of 57%.

Observing Figure 7.14b, the EHPII and GEWA-KS tube in 25°C saturation temperature are found to be in the same position relative to each other as in the 5°C saturation temperature case, but where the performance of the GEWA-KS improves and that of the EHPII slightly declines. The EHPII tube persists with little dependency on heat flux with a decrease in HTC of -1.18% over the testing heat flux range, whereas the GEWA-KS tube with a 13.8% in HTCs displays the same degree of heat flux dependency as in the 5°C saturation temperature.

The EHPII tube's HTCs average deviation of -10% compared to the 5°C saturation temperature case indicates a minor decline in heat transfer performance, whereas the GEWA-KS with an average improvement of 25.5% compared to the 5°C saturation temperature shows great

improvement with an increase in saturation temperature.

7.5.2 Coated

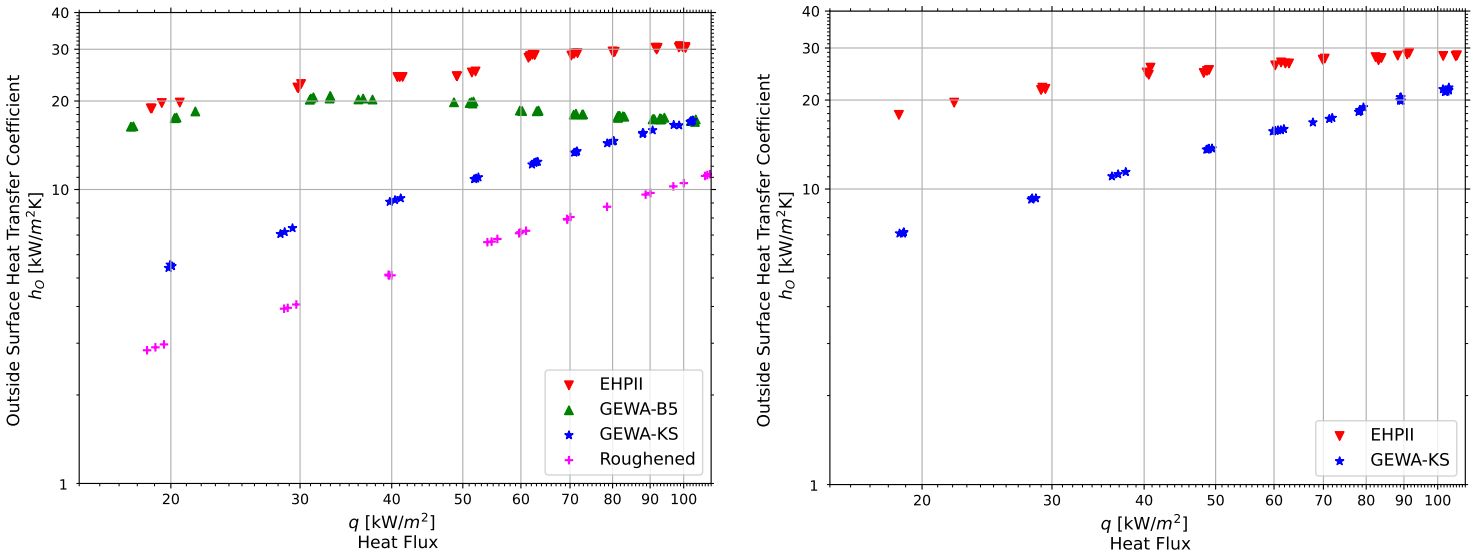

(a) 5°C (b) 25°C

Figure 7.15: Pool boiling overview of CuO coated plain and micro-enhanced tubes in R134a at saturation temperatures of 5°C and 25°C

As seen in Figure 7.15a for 5°C saturation temperature, the HTCs of the coated EHPII tube and the GEWA-B5 tube significantly perform better than the GEWA-KS tube followed by the roughened tube. As with the uncoated case, the HTCs of the GEWA-KS and roughened tube increase linearly on the log-log plot.

The HTCs in 5°C saturation temperature was again individually compared to the HTCs of the coated roughened plain tube. The coated EHPII tube performed the best with HTCs increasing by 13.5% over the heat flux range and were generally 315% greater than those of the coated roughened tube. The GEWA-B5 tube followed with HTCs decreasing slightly with -0.3% over the heat flux range, but were generally 214% greater than those by the coated roughened tube. The GEWA-KS had HTCs increasing with 14.2% over the heat flux range and were generally 70% greater than the coated roughened tube's HTCs. The coated roughened tube had HTCs which increased linearly with 9.4% across the heat flux range on the log-log plot.

With an increase in saturation temperature, it is seen in Figure 7.15b for 25°C that the coated EHPII tube has an increase in HTCs of 13% and the GEWA-KS tube has an overall increase of 18% across the heat flux range.

Furthermore, increasing the saturation temperature from 5°C to 25°C, the same behaviour was seen where the coated EHPII tube's HTCs decreased by an average of -3.4%. The coated GEWA-KS tube's HTCs increased with an average deviation of 30%.

7.6 Pool Boiling Analysis

7.6.1 Influence of the CuO Coating

The coating heat transfer influence ratios of all the pool boiling cases above are calculated and are collectively presented in Figure 8.17 below. The HTC enhancement or deterioration are hereby described through a K_{CuO} respectively greater or smaller than 1:

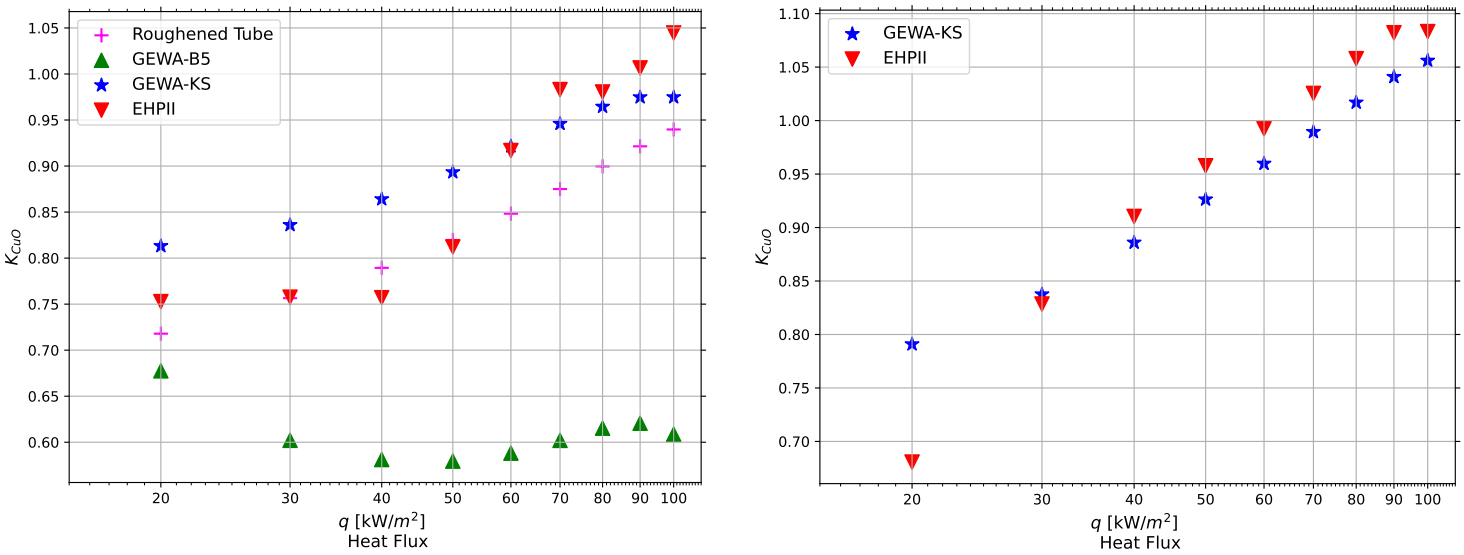

(a) 5°C (b) 25°C

Figure 7.16: Coating heat transfer influence ratios of the plain and micro-enhanced tubes in R134a at saturation temperatures of 5°C and 25°C

The CuO coating did not improve HTCs on the roughened tube with an average K_{CuO} of 0.85 across the range of heat fluxes tested. From the noted potential to enhance HTCs at higher heat fluxes with the upwards trend of the K_{CuO} values in Figure 8.17a, further investigative interest will lie in the observation of HTCs much higher than the heat fluxes tested in this study to observe heat transfer behaviour and CHF points of the uncoated and coated roughened plain tubes.

The CuO nanocoating on the GEWA-KS low fin tube is observed in Figure 8.17 to have minimal influence on heat transfer where the average K_{CuO} value was 0.91 for a 5°C saturation temperature and 0.95 for a 25°C saturation temperature. With the average K_{CuO} values being slightly lower than 1, heat transfer is only slightly diminished. However, the general upward trends of the coating heat transfer ratios in both saturation temperatures may indicate that the coating could be beneficial at higher heat fluxes than tested in the current study.

It is further seen in Figure 8.17a that the CuO nanocoating on the GEWA-B5 tube significantly degrades heat transfer performance with the CuO coated tube HTCs being between 0.7 to 0.58 of those of the uncoated GEWA-B5 tube and an average K_{CuO} of 0.6. It is seen that the GEWA-B5 was influenced the most by the coating relative to the roughened tube in Figure 7.15a, where it previously performed with HTCs 318% greater than those of the roughened plain tube in the uncoated case. The overall downward trend of the K_{CuO} in Figure 8.17a

implies that investigation into higher heat fluxes would be unproductive and the nanocoating unsuitable for complex re-entrant cavity micro-structures.

The CuO nanocoating on the EHPII tube is seen not to have a great impact on the heat transfer since the average K_{CuO} in Figure 8.17 is 0.89 for the 5°C saturation temperature case and a slightly higher 0.97 for the 25°C case. At high heat fluxes, the HTCs seen are unchanged at 5°C but are slightly enhanced at 25°C. However, at low heat fluxes, the coating lowered heat transfer performance with the K_{CuO} value being as low as 0.7 for both saturation temperatures. The general upward trends of the K_{CuO} values for both saturation temperatures in Figure 8.17 suggest further investigation of possible even greater heat transfer enhancement at very high heat fluxes outside of those tested.

Hereby, it is found that the application of the CuO coating has the best influence on the EHPII tube, but not to a viable degree where the HTCs are insignificantly improved in the higher heat flux region. The worst result from the coating is found in the case of the GEWA-B5 tube, where the HTCs are almost halved. This would suggest that the CuO coating to be unfavourable by very complex surface geometries which constitute prominent microchannels and re-entrant cavities.

7.6.2 Heat Transfer Analysis

From the above results, the following remarks are essential to comprehend the difference in pool boiling phenomena between the uncoated and CuO coated enhanced tube sets:

- The HTCs of the CuO nanocoated tubes are generally less or not much higher than the HTCs of the uncoated tubes.
- The bubble density (indicative of nucleation activity) of the CuO nanocoated tubes in pool boiling are generally much less dense or equivalent to that of the uncoated tubes.
- The bubble diameters upon departure of the CuO nanocoated tubes in pool boiling are much larger than those of the uncoated tubes.
- The HTC gradients of the CuO nanocoated tubes are generally slightly greater than those of the uncoated tubes.

Regarding the plain addition of the CuO coating: The points above align with the visual findings of a research study conducted by Li et al. [28] who conducted an investigation of the effects of different types of nanostructure coatings on wire-surfaces on heat transfer in pool boiling. It is found from the study that the nanocoatings that decreased HTCs boiled with a nucleation site density much less than the uncoated control surfaces. It is also noted that the nanocoated surfaces boiled with much larger bubble diameters than those of the uncoated surfaces.

The nature of the nanocoating used by Li et al. [28] that lowered HTCs were high surface wettability coatings of oxide compositions with compact nanostructures, low porosities and separated nanopores which were not well interconnected. The CuO nanocoating used in the

current study may be of the same nature as seen by the SEM analysis in section 3.12 where the behaviour of the nanostructures are random and irregular (not specifically constructed to be optimised for inter-connectivity).

It is initially expected that some of these rough CuO nanostructure protrusions may have posed opportunity to undergo nucleation themselves and is a matter to be addressed. It is proposed that it cannot be assured that the overall nucleation site density is increased by the nanostructures themselves, since the irregular nanostructure cavities and possible poor inter-connectivity throughout the coated surface cannot guarantee successful nucleation [28].

A modelling approach is taken similar to that conveyed by Rohsenow et al. [9] and briefly by Li et al. [28] for heterogeneous nucleation to interpret the further degradation of the HTCs due to the simple addition of the CuO nanocoating to a surface. This can be found in Appendix N, which concludes that some of the CuO nanostructure cavities are too small to be activated, especially at such lower testing saturation pressures where only larger cavities tend to be activated. The outcome of this modelling is in accordance to the visual analysis above where no cases are observed with the coated surface having a greater bubble density than the uncoated surface.

Regarding the combination of micro-enhanced surfaces and the CuO coating: The HTCs are enhanced by the bigger microstructures on the uncoated micro-enhanced surfaces for nucleation to take place at lower superheats as well as single phase heat transfer due to the bubble pumping action. It is expected that the micro-enhanced surfaces are designed to incur an even spread of nucleation sites. It is possible that this part of the heat transfer degradation is due to the great increase in wettability to cause flooding of micro-cavities to potentially render most of them inactive, leading to a subsequent decrease in nucleation site density and a decrease in HTCs [34] [28].

Furthermore, with the bubble growth rate impeded by the flooding, this overall hydraulic mechanism the microstructures and microchannels originally posed by commercially micro-enhanced tubes is broken down where liquid in the cavities seem to become stagnant due to an overabundance of liquid with no rapid bubble ejection. Observations of the individual components of the possible heat flux distribution influencing the bubble growth rate are included in Appendix N.

It is seen that this sluggish bubble development as a cause of the flooding led to a vapour entrapment scenario and can be seen on the coated GEWA-B5 surface of Figure 7.10. It seems that the bubbles are kept in place by the overhangs of the re-entrant cavities without the aid of a superheating microlayer for the bubble to rapidly grow and overcome the liquid surface tension.

A further reason for the heat transfer degradation may be an alteration in the hydraulics surrounding the micro-enhanced surface. It is posed that the hydraulic movement of the refrigerant liquid is weakened by the addition of the CuO coating and consequently depreciates the heat transfer performance. Since the rate of bubble growth and vapour generation is decelerated,

the ejection of bubbles from the re-entrant cavities are much slower and the ebullition cycle (the overall churning motion of a fluid induced by the boiling or bubbling the fluid) is worsened, leading to a weaker bubble pumping action at the cavity openings causes for an overall slower fluid movement through the micro-channel network, causing a weaker thermal gradient and a subsequent lower sensible heat transfer. Therefore, the micro-layer evaporative heat transfer as well as the sensible heat transfer mechanisms are diminished.

Additionally, the CuO coating's SEM inspection showed that the coating constituted many thin shard-like protrusions to create an irregular surface. This surface construction may pose great resistance to general liquid flow within the micro-channels. This may depreciate the boiling heat transfer performance with slower liquid flow within the micro-channels, where fresh liquid is introduced to the surfaces less often. Complementary findings were obtained from the deductions of Jin et al. [38] where a hydrophobic coating on commercially micro-enhanced boiling tubes with re-entrant cavities similar to what is used in the current study were found to have a great enhancement in falling film heat transfer performance, especially at higher heat fluxes. It was stated that the nature of the hydrophobic coating posed much less surface energy and would therefore offer less friction to two-phase fluid flow in the micro-channels. This will allow for easy and fast elimination of vapour from the channels and the re-entrant cavities to re-introduce the surfaces of the re-entrant cavities and micro-channels with liquid and enhance superheated micro-layer evaporation and ultimately boiling heat transfer.

8 Falling Film Boiling Results and Discussion

The tubes in the study were investigated under falling film boiling conditions where two types of testing occurred. Heat flux sweeps used a constant falling film flow rate of 0.13 $kg/m/s$ and varied the test heat flux, while film flow rate sweeps used constant heat flux conditions and their refrigerant film flow rates were reduced until dryout.

Each of the tube types were individually investigated. The coating heat transfer influence ratio was calculated to inspect the effect the CuO nanocoating has on heat transfer performance. The falling film heat transfer enhancement ratios were also calculated to observe the effect the possible advantage the falling film configuration posed compared the pool boiling configuration. In order to effectively compare the large group of curves, best-fit curves via polynomial regression were used on display, where the individual data sets could be found in Appendix O. Lastly, a brief overview of the collective performances of the tubes was presented, whereafter falling film boiling tests were further analysed.

8.1 Roughened Tube

An uncoated and coated roughened tube were observed under falling film boiling conditions at 5°C saturation temperature to produce boiling curves from where their heat transfer performances are inspected and compared. Falling film boiling data for the roughened tube from Bock [1], with a roughness average value of $R_a = 0.74\ \mu m$, is included for comparison:

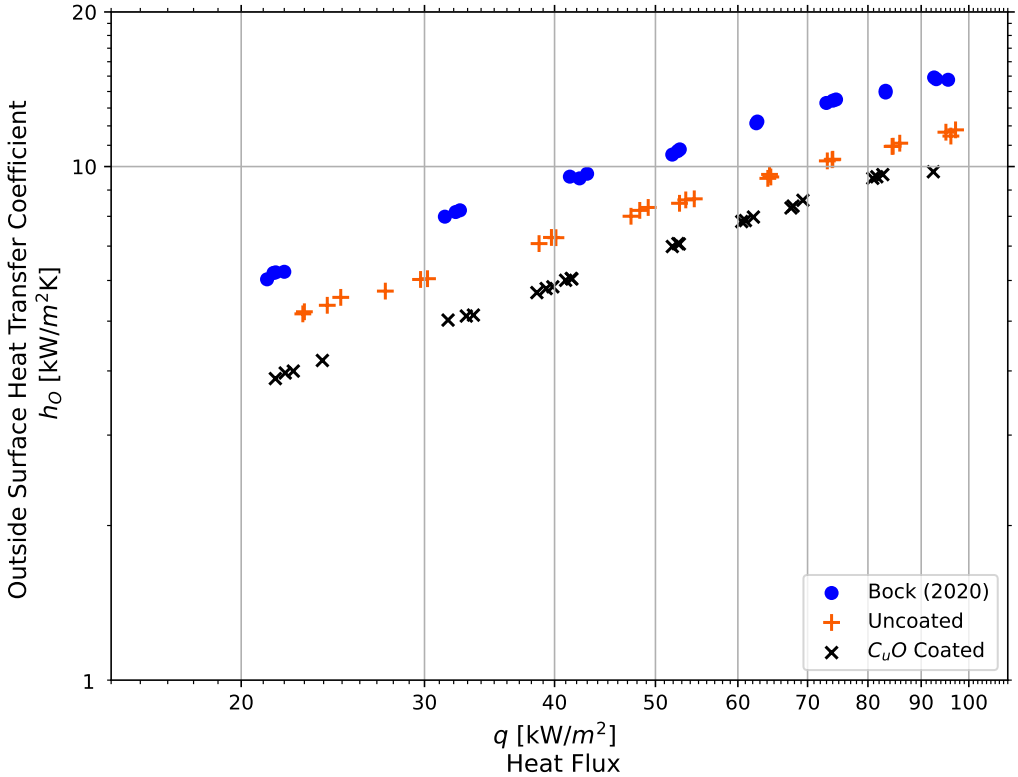

Figure 8.1: Falling film boiling of uncoated and coated roughened tube at 5°C saturation temperature in R134a at 0.13 $kg/m/s$

From Figure 8.1 it is seen that the uncoated roughened tube heat transfer performance com-

pared relatively well to Bock [1].

It is found in Figure 8.1 that the uncoated tube performs better than the CuO nanocoated tube. The overall performance of the roughened tube was reduced through the coating by an average of -17%.

Both uncoated and coated roughened tube HTCs increased linearly on the log-log plot with similar gradients. The uncoated tube's HTCs increased with 8.8% over the testing heat flux range whereas the nanocoated tube's increased with 7.3%.

The CuO nanocoating induced early onset of the departure from nucleate boiling of the coated roughened tube at 91 kW/m^2. Bock [1] similarly saw an early onset of departure from nucleate boiling at higher testing heat fluxes during falling film boiling. The behaviour of the coated tube's HTCs with the departure from nucleate boiling could be further perceived in the falling film dryout test performed at 100 kW/m^2.

Some high speed footage at 20 kW/m^2 and 100 kW/m^2 is inspected to observe the boiling phenomena of the uncoated and coated roughened tube:

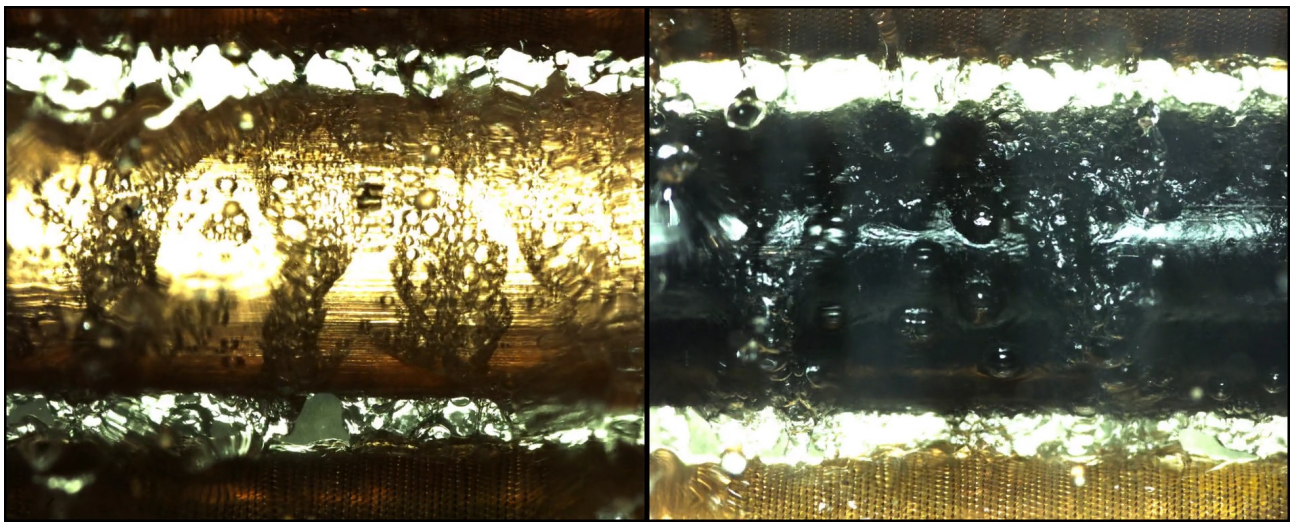

(a) Uncoated (b) CuO coated

Figure 8.2: Falling film boiling comparison of roughened tube at 20 kW/m^2 in R134a at 5°C saturation temperature

From Figure 8.2, it is hypothesised that the uncoated tube has a thinner layer of liquid on its surface compared to the coated tube which is to be flooded with a thicker layer of liquid refrigerant. It is upon scrupulous examination of the high speed footage that this suspicion could be confirmed. Furthermore, it is observed that after nucleation, the bubbles are carried away downwards by the falling film where after they continue to grow and burst later on the uncoated surface. The liquid seemed stagnant on the coated surface because of the liquid retention caused by the super-hydrophilic CuO nanocoating so as to imitate a pool boiling case. The flooding of nucleation sites can be a major contribution to the depreciation in HTCs. It is clear that after nucleation, the bubbles grew and burst prominently in a stationary position. The super-hydrophilic surface seems to work against the effect of the falling film under the

force of gravity.

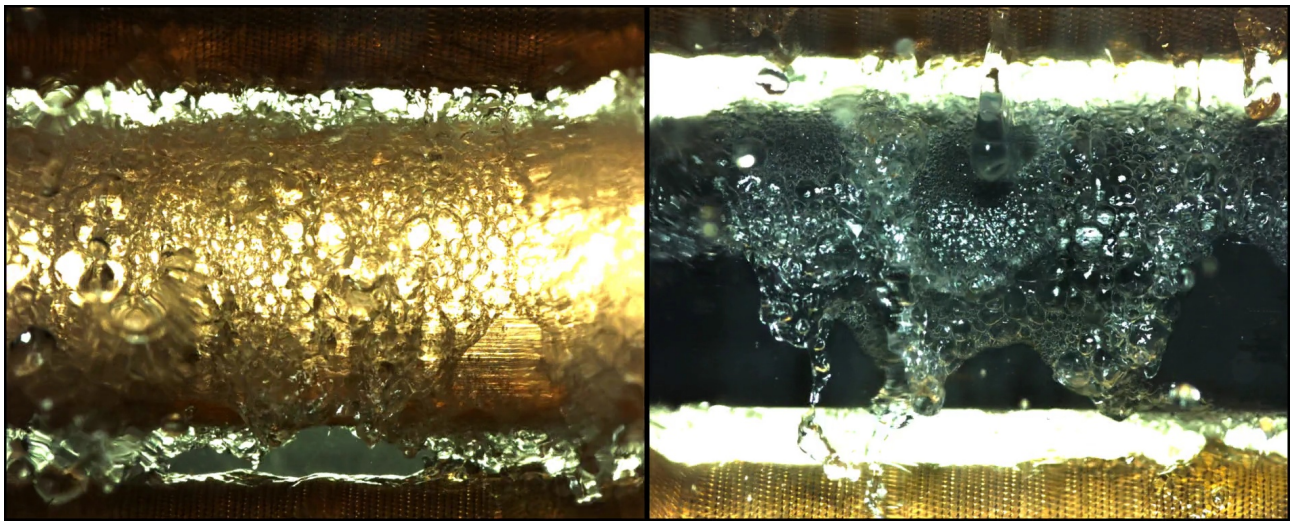

(a) Uncoated (b) CuO coated

Figure 8.3: Falling film boiling comparison of roughened tube at ± 100 kW/m^2 in R134a at 5°C saturation temperature

Figure 8.3 shows greater regions of dry spots on the coated tube at the higher heat flux that are seldom rewetted. It is distinct that as soon as the droplets hit the surface they will instantly splatter out into bubbles and burst at stagnant spots on the nanocoated surface without being swept downwards, whereas a constant film feed is observed on the uncoated surface with stable nucleation and growth of bubbles with the falling film. The dryout visually observed on the nanocoated surface may be the beginning stages of CHF seen in Figure 8.1.

8.2 GEWA-KS

Uncoated and CuO coated GEWA-KS low-fin tubes were tested under falling film boiling conditions at 5°C and 25°C saturation temperatures and are illustrated in Figure 8.4. There was no heat transfer data available for a 19 fpi low-fin micro-enhanced tube in the open literature at the time of the current study for comparison.

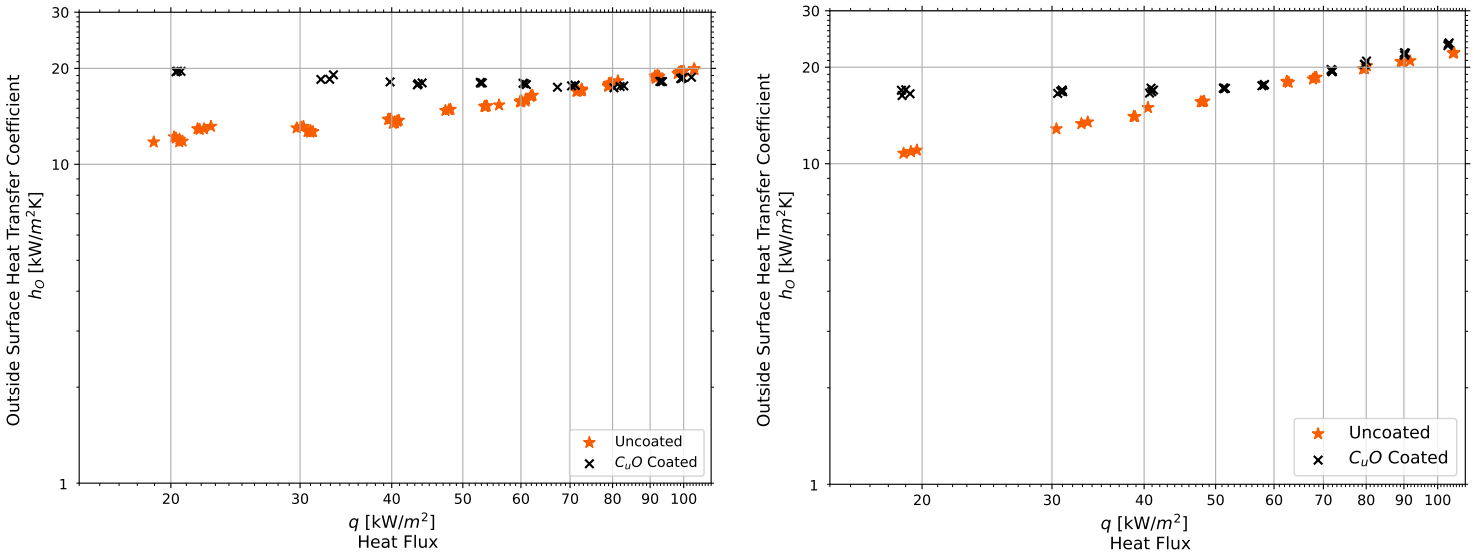

(a) 5°C (b) 25°C

Figure 8.4: Falling film boiling of GEWA-KS at 0.13 $kg/m/s$

It is seen in both saturation temperature cases in Figure 8.4 that the HTCs of the uncoated GEWA-KS tube increase linearly on the log-log plot with increasing heat flux whereas the CuO nanocoated GEWA-KS tube's HTCs remained relatively constant.

The CuO nanocoated tube performed better than the uncoated tube where its HTCs were 18.6% for 5°C and 13.8% for 25°Chigher on average. There is no heat transfer enhancement in the higher heat fluxes where the HTCs of the CuO nanocoated tube met up with those of the uncoated tube between 60 kW/m^2 to 70 kW/m^2 and stayed consistent with the uncoated tube in both saturation temperature cases. This may suggest that the enhancement is rather as a result of the falling film configuration and once boiling becomes dominant at higher heat fluxes, the HTCs are the same. This is explained in greater detail in section 8.6. The combination of the finned microstructures and the CuO coating work favourably in the falling film boiling case with the GEWA-KS tube.

For both uncoated and coated GEWA-KS tubes, there was a slight increase in HTCs from 5°C to 25°C saturation temperature. The HTCs of the uncoated tube were raised by an average of 6.7% where the HTCs of the coated tube increased with an average of 3.9%.

The falling film boiling phenomena of the uncoated and coated GEWA-KS tubes are visually inspected through high speed footage at 20 kW/m^2 and 100 kW/m^2 for the 5°C saturation temperature in Figure 8.5:

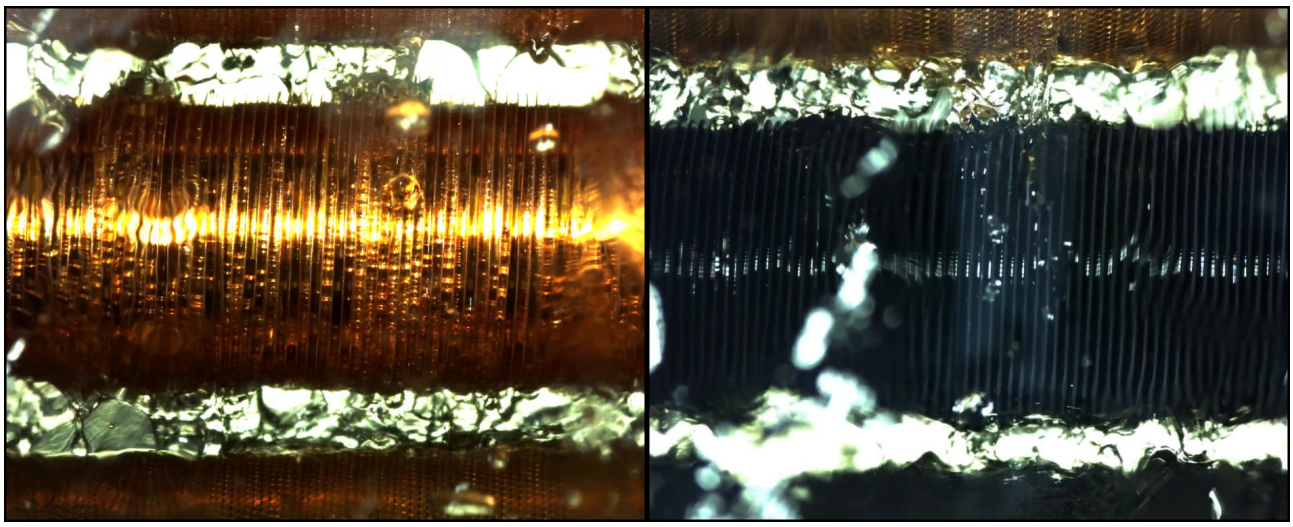

(i) Uncoated (ii) Coated

(a) 20 kW/m^2

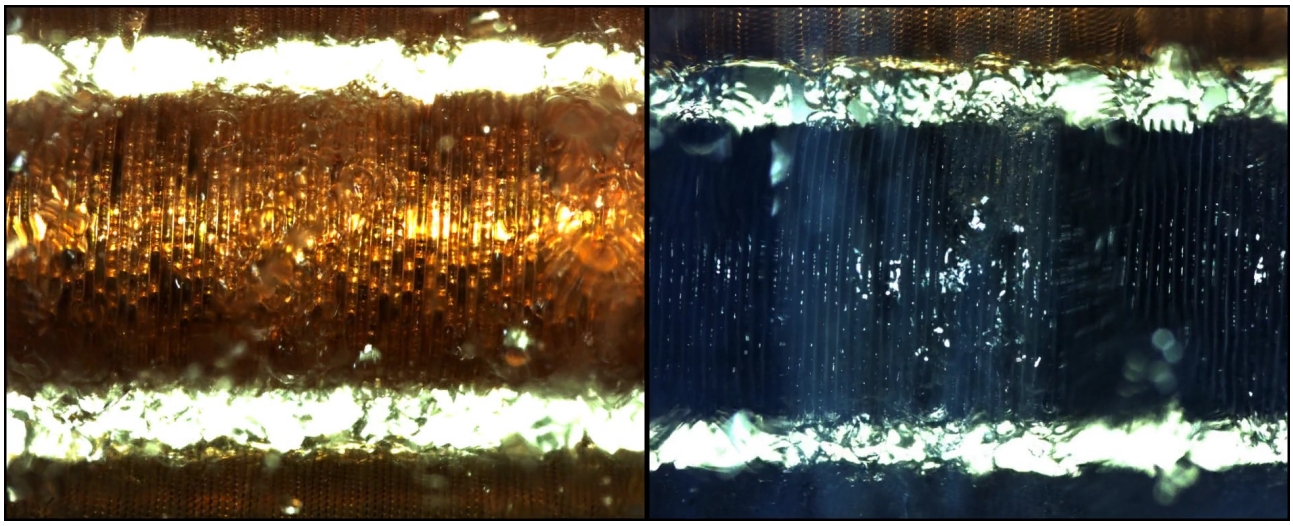

(i) Uncoated (ii) Coated

(b) 100 kW/m^2

Figure 8.5: Falling film boiling comparison of GEWA-KS in R134a at 5°C saturation temperature

In the visual comparison above, it is found in all cases that there were no dry spots on either of the uncoated or coated GEWA-KS tubes. Nucleation is more prominent on the uncoated GEWA-KS tube compared to the CuO coated GEWA-KS tube at all heat fluxes, however this could be a result of the lighting on the dark CuO surface. It appeared that sensible heat transfer on the CuO coated GEWA-KS tube is better than the uncoated GEWA-KS tube's heat transfer performance where nucleation did occur as seen in the low heat flux case of Figure 8.5a because of a more steady, uniform falling film flow over the coated tube. Heat transfer may therefore be better with greater contact to fresh liquid refrigerant over the surface and uphold a steady thermal gradient. Upon examination of the high speed footage, it would appear that the liquid film fell slower over the coated GEWA-KS tube than over the uncoated GEWA-KS tube.

Some falling film boiling dryout tests were performed to investigate the ability for the uncoated and coated GEWA-KS tube to maintain boiling heat transfer where the film flow rate was varied and the testing heat flux kept constant. They are illustrated in Figure 8.6:

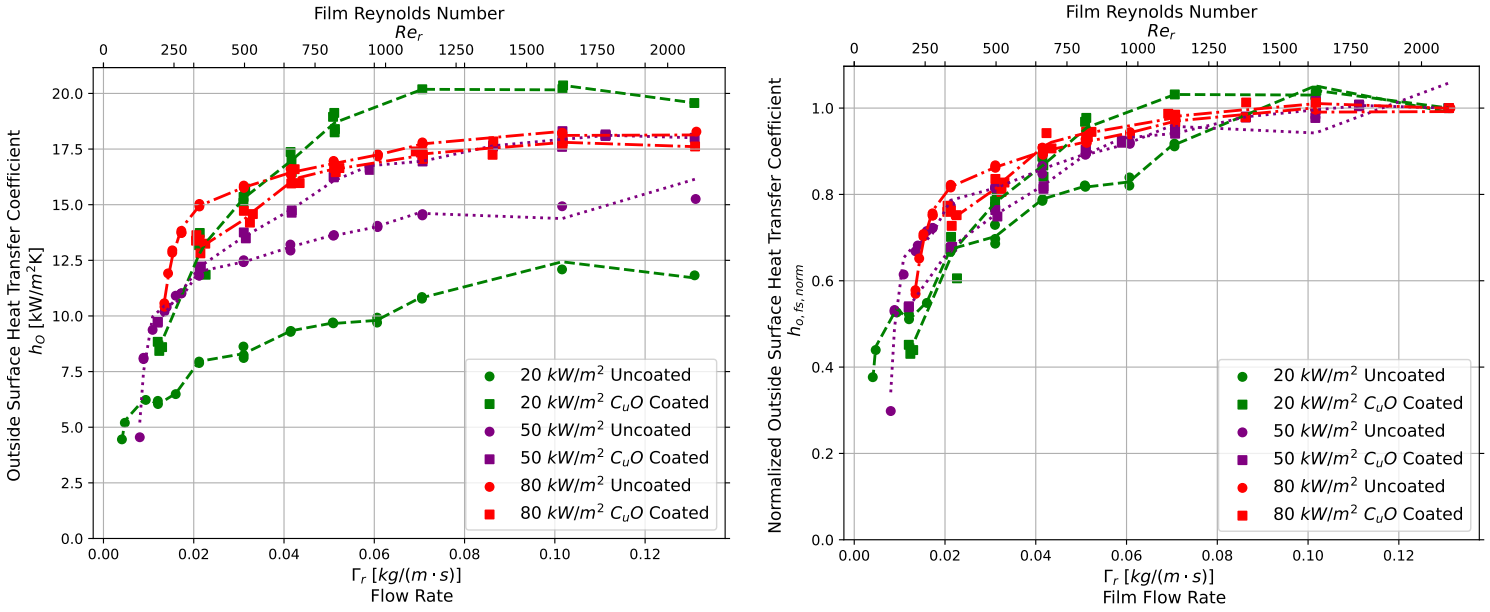

(a) HTCs

(b) Normalized HTCs

Figure 8.6: Uncoated and coated GEWA-KS falling film dryout test at 5°C saturation temperature in R134a

Figure 8.6 shows a typical dryout curve where the HTCs form a plateau at higher film flow rates which is followed by dryout where the HTCs drop at the lower film flow rates. Microstructured tubes have a characteristic HTC hump before total dryout, however there is no clear HTC hump in the film dryout test of the uncoated and coated GEWA-KS tubes.

It is seen in Figure 8.6 that there is no significant difference in wettability between the uncoated and coated GEWA-KS tubes. All tubes' dryout points were between 0.01 $kg/m/s$ and 0.02 $kg/m/s$, where the uncoated GEWA-KS tube is able to sustain heat transfer slightly longer at lesser film flow rates than the coated GEWA-KS tube, but to no significant degree.

It is found that with the decrease in film flow rates, the heat transfer becomes relatively unpredictable with the coated GEWA-KS tube and was noted during testing at the higher heat flux case of 80 kW/m^2. The volatility may be due to the combination of the increased temperature superheat posed by the CuO nanocoating at higher heat fluxes and the instability of the falling film due to enhanced surface tension.

Nanocoating the GEWA-KS tube with CuO is not seen to be a viable option to significantly enhance the HTCs in falling film boiling at high or low film flow rates. Only if the operating point is in the lower heat flux range is there some benefit to the coating. It will be of interest to investigate the dryout capabilities of uncoated and coated GEWA-KS tubes at very high heat fluxes as it may be so that the coated tube could sustain a higher CHF than the uncoated GEWA-KS tube.

8.3 GEWA-B5

The CuO nanocoated and an uncoated GEWA-B5 commercially micro-enhanced tubes were observed under falling film boiling conditions at a constant film flow rate of 0.13 $kg/m/s$ and are illustrated in Figure 8.8. The heat transfer performance of an unclean, aged tube and GEWA-B5 falling film boiling data from Roques [50] is included for reference:

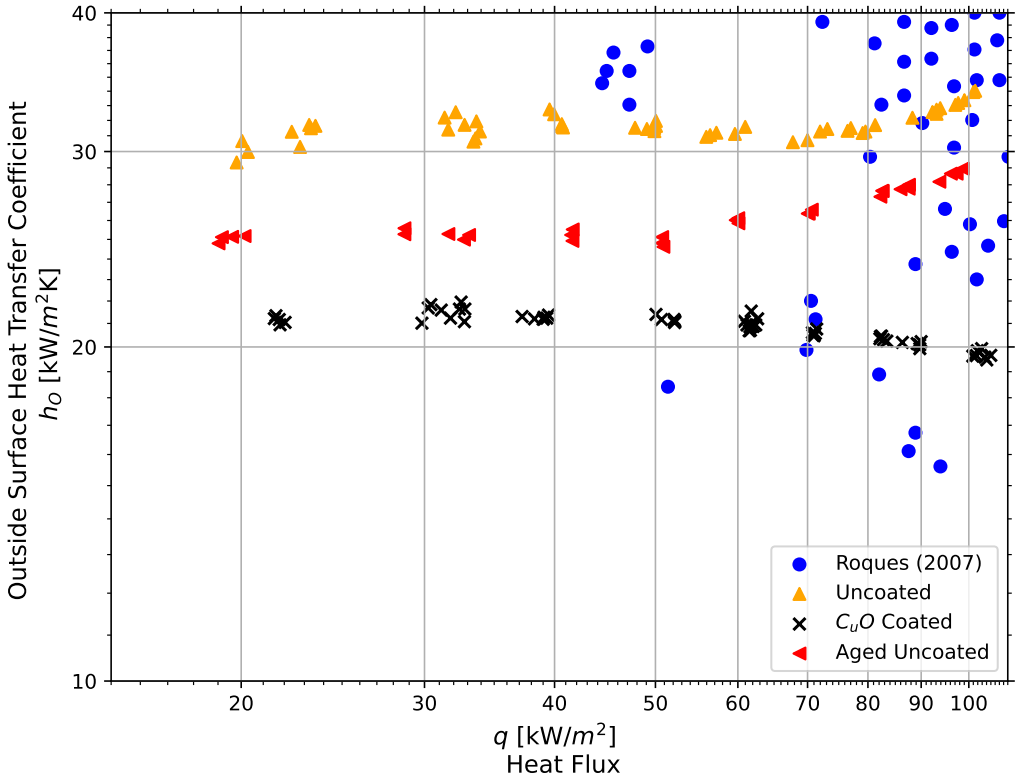

Figure 8.7: Uncoated and coated falling film boiling of GEWA-B5 at 5°C saturation temperature in R134a at 0.13 $kg/m/s$

From Figure 8.8 it can be seen that the aged surface significantly under-preforms compared to the uncoated reconditioned surface by 16.4%. The reconditioned tube's HTCs in the falling film boiling case seem to be very stable across the testing heat flux range and is in order with the HTC magnitudes of Roques [50]. The uncoated, aged tube had HTCs which follows the same profile as the uncoated, reconditioned tube, but under-performs consistently where the HTCs are stable across the testing heat flux range up to approximately 50 kW/m^2 from where the HTCs started to increase similar to the uncoated, reconditioned tube. The uncoated, aged tube did, however, performs better than the CuO nanocoated tube where the uncoated, aged tube has HTCs approximately 39.2% greater than the CuO nanocoated tube. Hereby, significant heat transfer enhancement is possible simply through ensuring the original surface condition is maintained.

It is seen that the CuO nanocoated GEWA-B5 tube under-performs compared to the uncoated, reconditioned GEWA-B5 tube.

The CuO coated tube's HTCs had and average of -34.3% of the uncoated tube's HTCs. The uncoated tube's HTCs increased with 4.3% and the coated tube's HTCs increased with -1.4%

over the heat flux range, meaning they were largely invariable across the testing heat flux.

These results are comparable to the findings in the pool boiling case where there seems to be no possibility of heat transfer enhancement by the CuO nanocoating, even at higher testing heat fluxes. It is possible that the CuO nanocoating to causes an obstruction to the hydraulics inside the intricate capillary network of the GEWA-B5 micro-enhancements and to cause an worsened distribution of nucleation sites to depreciate the HTCs.

High speed footage of the uncoated and coated GEWA-KS tubes can be compared for two heat flux cases below:

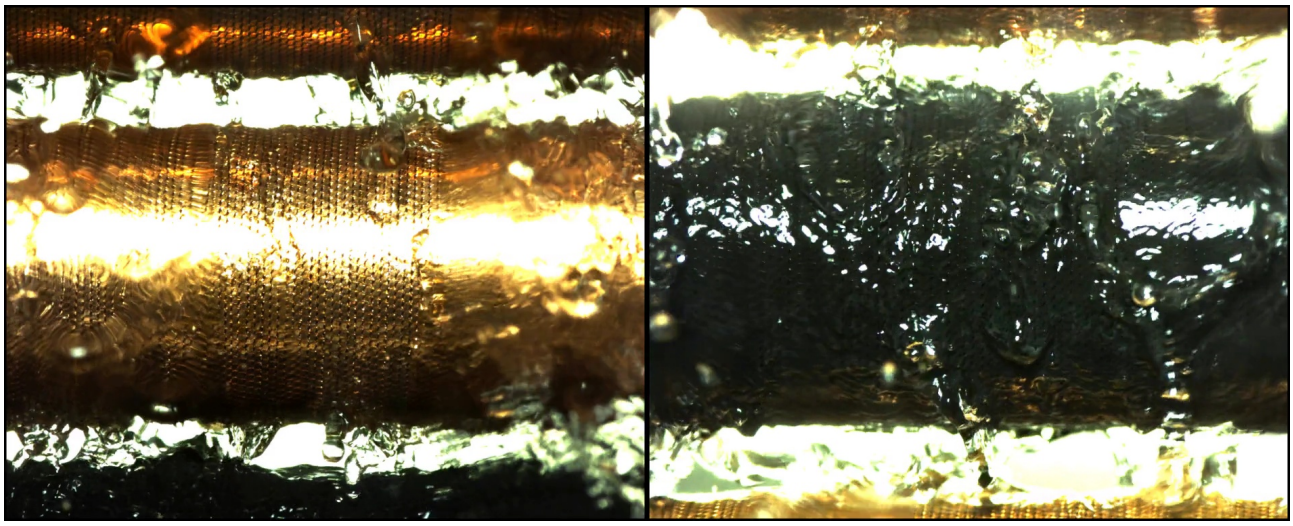

(i) Uncoated (ii) Coated

(a) 20 kW/m^2

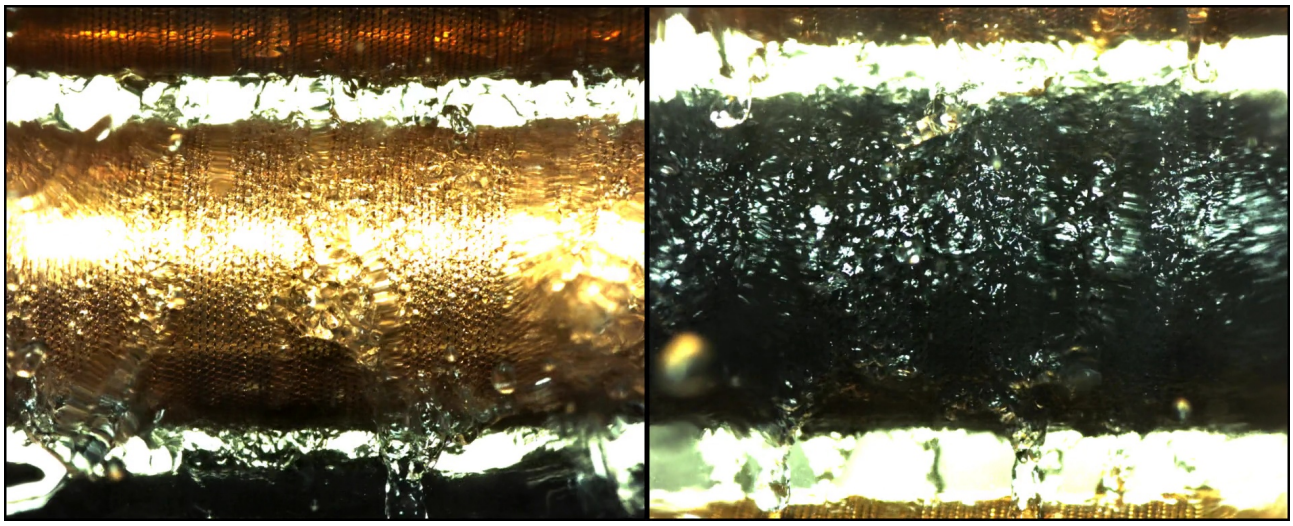

(i) Uncoated (ii) Coated

(b) 100 kW/m^2

Figure 8.8: Falling film boiling comparison of GEWA-B5 at 5°C saturation temperature in R134a at 0.13 $kg/m/s$

Through the comparison in Figure 8.8 above, it is seen for both heat flux cases that there are no dry spots on either the uncoated or coated surfaces. Upon careful inspection of the high

speed footage, the liquid refrigerant layer on the coated GEWA-B5 is discernibly thicker than on the uncoated tube. This observation may be difficult to recognise on still images such as in Figure 8.8. It is also distinct that the coated GEWA-B5 tube retaining the liquid refrigerant displays significant resistance in the liquid moving downwards through the falling film under the action of gravity.

The uncoated tube has a thinner liquid layer on its surface where bubbles clearly develop as they are swept downwards by the film after nucleation. The uncoated case seems to be in a much more steady state than the CuO coated tube.

The dryout performance of the uncoated and coated GEWA-B5 tubes were inspected by decreasing falling film flow rates at constant heat fluxes as illustrated in Figure 8.9. The normalized HTCs were also calculated in order to compare the uncoated and coated GEWA-B5 tubes.

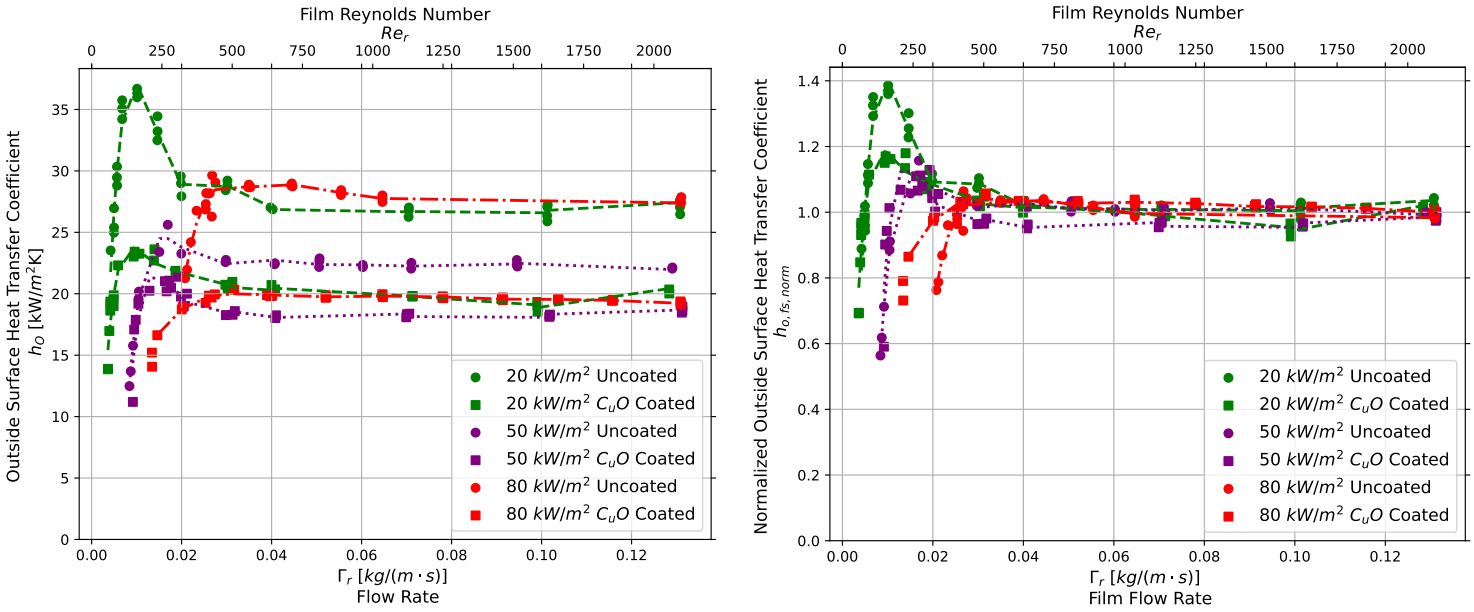

(a) HTCs

(b) Normalized HTCs

Figure 8.9: Uncoated and coated GEWA-B5 falling film dryout test at 5°C saturation temperature in R134a at 0.13 $kg/m/s$

Figures 8.9 show that there are no enhancements, nor deterioration of the tubes' wettability between the uncoated and coated GEWA-B5 tubes. At the lower 20 kW/m^2 and 50 kW/m^2 testing heat fluxes the dryout occurr at the same falling film rates around 0.01 $kg/m/s$.

A distinct and short-lived rise in HTCs for both uncoated and coated GEWA-B5 tubes occurs with a reduced falling film flow rate between 0.01 $kg/m/s$ and 0.04 $kg/m/s$ just before dryout occurred. This is also observed by Bock [1] and Chyu et al. [75, 76] where a stable thinned super-evaporating microlayer on the surface of the tube is thought to cause a brief increase in HTCs and were attributed to improved wettability of micro-enhanced tubes and nanocoated tubes.

It is seen in Figure 8.9b that there is some improvement in the dryout performance of the CuO nanocoated GEWA-B5 tube compared to the uncoated tube at 80 kW/m^2, but it is not

perceived to be significant.

From the above heat transfer experimental investigation, it is determined that nanocoating the GEWA-B5 with CuO is not a feasible option to enhance heat transfer performance in falling film boiling. The HTCs are decreased significantly by the nanocoating and remain consistently lower than the uncoated HTCs over the entire testing heat flux range. There is no operation point where heat transfer could possibly be favourable, even at higher heat fluxes where other tubes showed potential increase from a positive trajectory.

8.4 EHPII

An uncoated and a coated EHPII commercially micro-enhanced tube were tested under falling film conditions in both 5°C and 25°C saturation temperatures. The HTCs were recorded throughout the testing heat flux range at a constant film flow rate of 0.13 $kg/m/s$ and are shown in Figure 8.10. Existing falling film boiling data for the uncoated EHPII tube was not available for comparison.

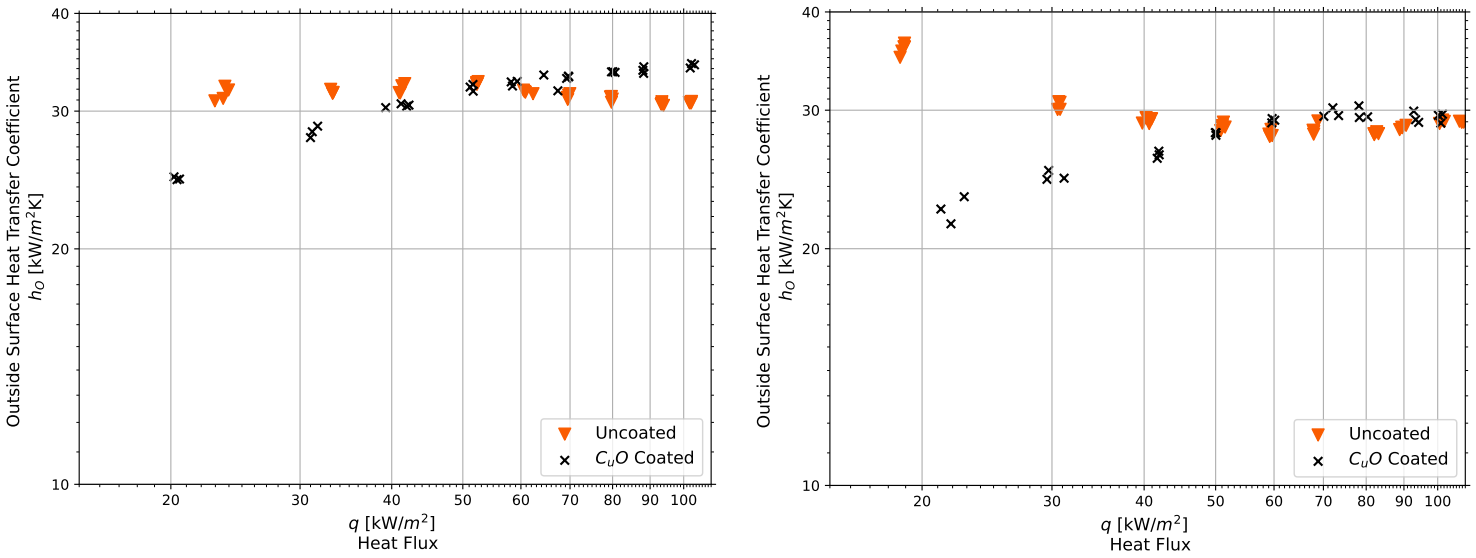

(a) 5°C (b) 25°C

Figure 8.10: Uncoated and coated falling film boiling of EHPII at 5°C saturation temperature in R134a at 0.13 $kg/m/s$

It is seen from Figure 8.10 that the CuO coated EHPII tube under-performs at lower heat fluxes compared to the uncoated EHPII tube at both 5°C and 25°C saturation temperatures. However, the coated tube's HTCs cross over the uncoated EHPII HTCs in both saturation temperatures between 50 kW/m^2 and 60 kW/m^2 so as to enhance heat transfer at 5°C.

Overall, the CuO nanocoated EHPII tube generally incurred very little difference at a saturation temperature of 5°C as given by its average deviation of -0.6% relative to the uncoated tube. There was a slight decline in HTCs imposed by the CuO nanocoating at a saturation temperature of 25°C where the coated tube's HTCs had an average deviation of -5.7% relative to the uncoated tube.

For a saturation temperature of 5°C the CuO nanocoated EHPII tube's HTCs increased with 12.2% over the testing heat flux range, whereas the uncoated EHPII tube's decreased with -1.9%. Similar behaviour was seen in the 25°C saturation temperature where the nanocoated tube increased with 9.9% and the uncoated tube decreased by -7.6%.

It was observed that there was an overall decrease in HTCs from 5°C to 25°C saturation temperature, similar to the pool boiling results, where the HTCs decreased by an average of 6.6% for the uncoated tube and -12.2% for the coated tube. It is hypothesised that the increase in saturation temperature adversely altered the local thermal gradients between the refrigerant

and the microstructure surface cavities to result in an 'offset' nucleation position on the EHPII microstructure scales for ineffective boiling [53].

A visual analysis is performed by inspecting high speed footage at 20 kW/m^2 and 100 kW/m^2 for falling film boiling in the 5°C saturation temperature case where an enhancement of HTCs were seen to be possible. This is illustrated in Figure 8.11:

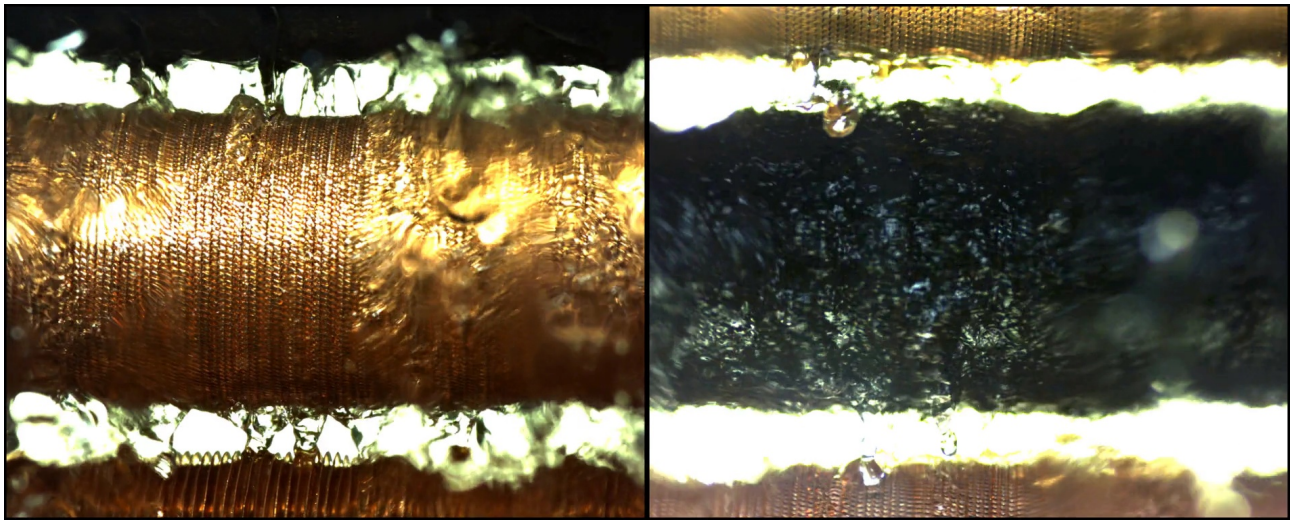

(i) Uncoated (ii) Coated

(a) 20 kW/m^2

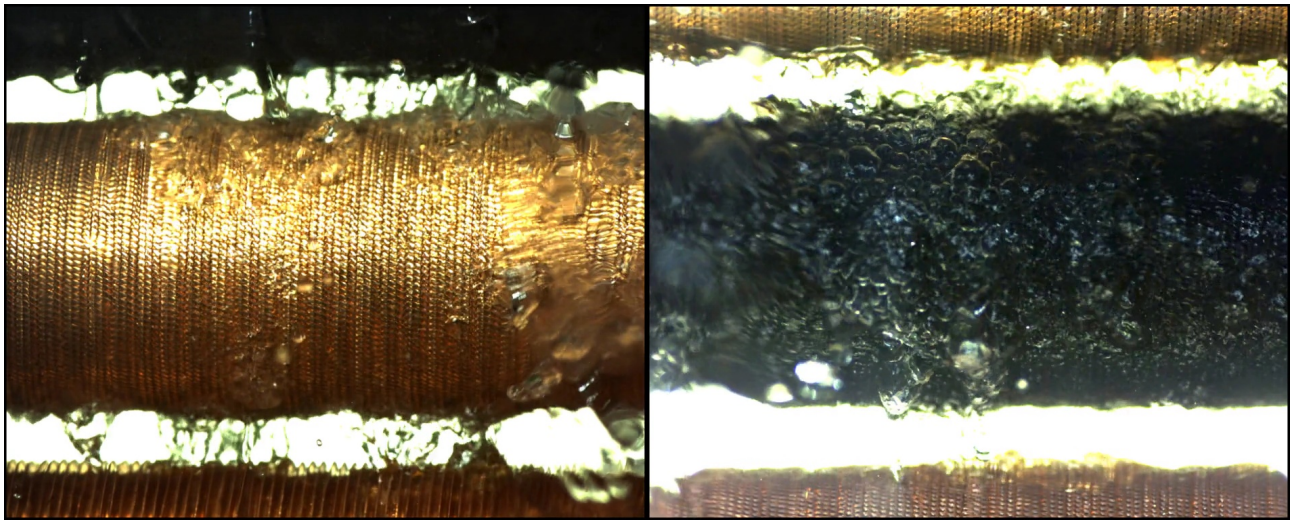

(i) Uncoated (ii) Coated

(b) 100 kW/m^2

Figure 8.11: Falling film boiling comparison of EHPII at 5°C saturation temperature in R134a

It is evident from inspecting the high speed footage that the refrigerant liquid layer is much thicker on the coated EHPII tube than on the uncoated EHPII tube at 20 kW/m^2 in Figure 8.11a. At this point there is a decrease in HTCs due to by the nanocoating. Similar to the GEWA-B5, liquid retention is again hypothesised to be present on the surface of the CuO nanocoated EHPII tube. This may cause lower HTCs, however other factors are also likely in effect to cause the decrease in HTCs.

The difference between the uncoated and coated EHPII tube footage at 100 kW/m^2 include more nucleation activity and a slightly thicker liquid layer on the surface of the coated tube.

Some falling film dryout tests were performed to inspect the wettability of the uncoated and coated EHPII tubes and are illustrated in Figure 8.12:

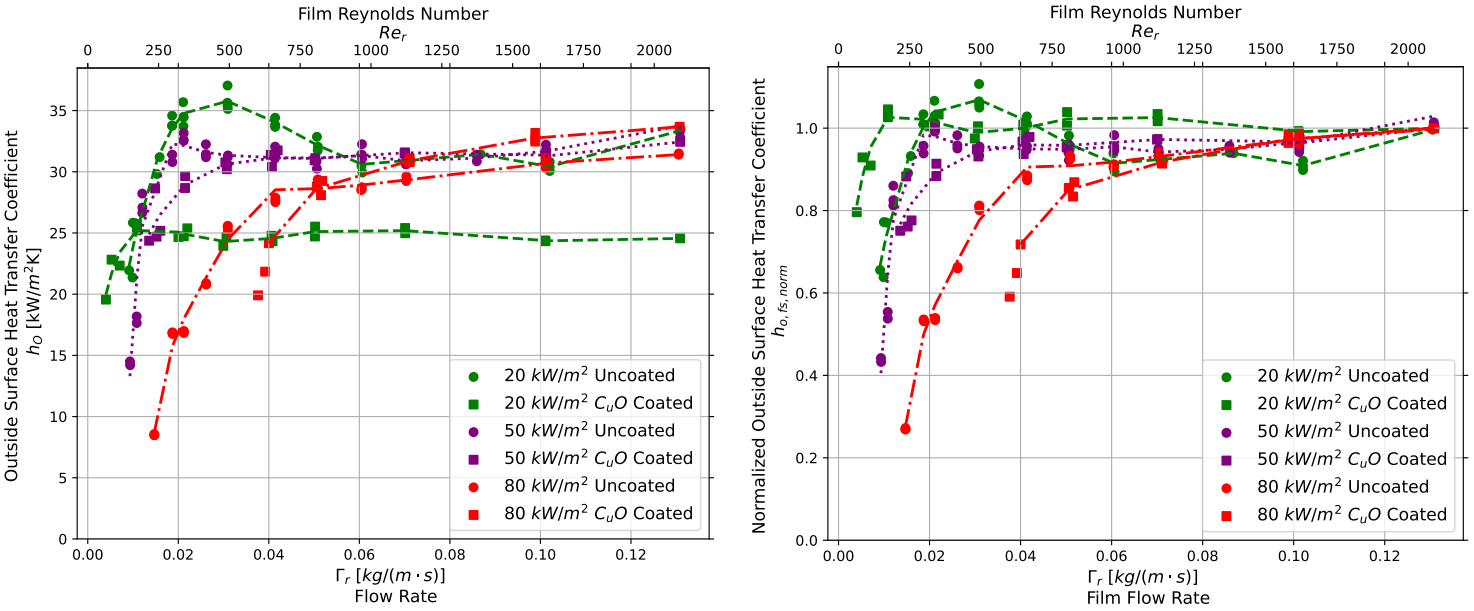

(a) HTCs

(b) Normalized HTCs

Figure 8.12: Uncoated and coated EHPII falling film dryout tests at 5°C saturation temperature in R134a

It is seen in Figure 8.12 that at 20 kW/m^2 and 50 kW/m^2 the wettability of the uncoated and coated EHPII tubes are very similar. All tubes seem to have undergone total dryout at approximately 0.01 $kg/m/s$, except the 80 kW/m^2 coated tube with a dryout point closer to 0.04 $kg/m/s$ to indicate poorer dryout performance.

Further investigative interest will be to inspect the CHF points of the uncoated and coated tubes, as well as to investigate the possible HTC enhancement at very high heat fluxes, especially in the 5°C saturation temperature case as alluded by Figure 8.11a.

Figure 8.12 shows the uncoated and coated EHPII tubes' HTCs to endure a flat plateau region as the flow rate is decreased from 0.13 $kg/m/s$ to approximately 0.06 $kg/m/s$ in general, from where there is a steep drop-off in heat transfer performance. Similar to the other micro-enhanced tubes, there is a heat transfer 'hump' before the steep decline and is more prominent at lower heat fluxes. The hump, however, is much smaller than other observed micro-enhanced tubes. The very flat HTCs in the film dryout tests indicate that the surface liquid retention hypothesis is scrutinised, since the HTCs do not increase with a decreasing film flow rate and the HTC hump follows appropriately at lower film flow rates.

It is deduced from the experimental investigation that nanocoating the EHPII tube with CuO is not a reliable method of enhancing the HTCs. The coating may only be considered if the operation point is higher than 70 kW/m^2 at a 5°C saturation temperature, whereas there is no

benefit at a higher saturation temperature of 25°C.

8.5 Falling Film Boiling Overview

8.5.1 Uncoated

A summarising overview of the uncoated heat transfer performances of the micro-enhanced tubes are provided in Figure 8.13 for 5°C and 25°C for falling film boiling:

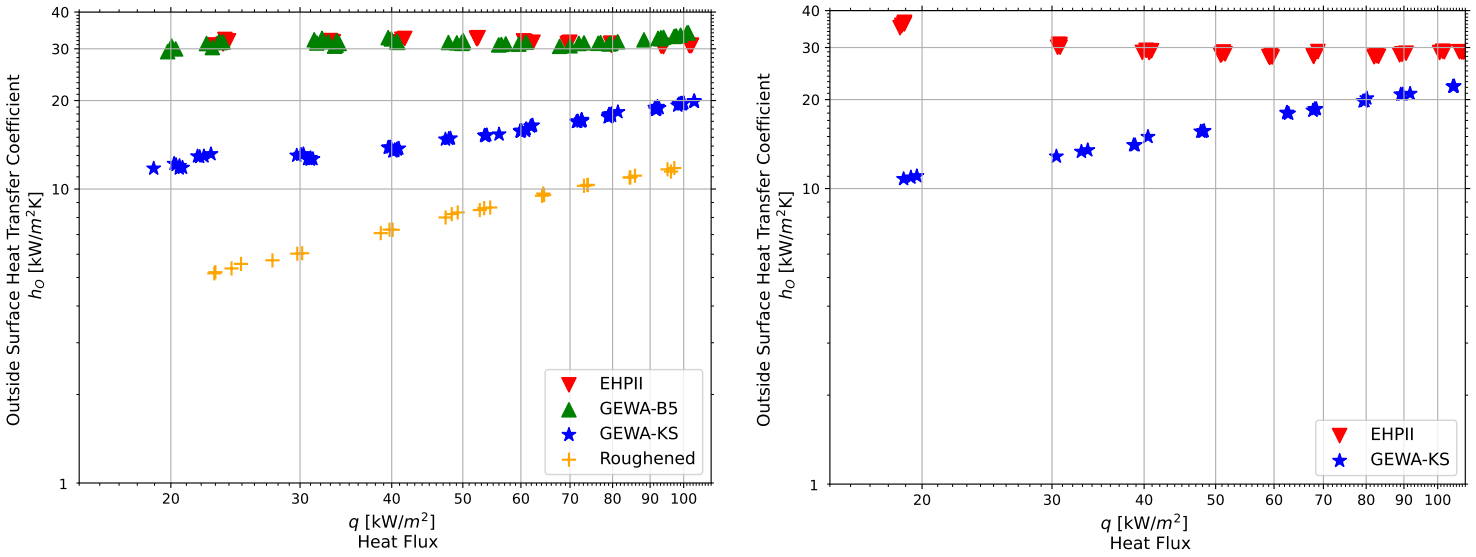

(a) 5°C (b) 25°C

Figure 8.13: Falling film boiling overview of uncoated micro-enhanced tubes at saturation temperatures of 5°C and 25°C in R134a at a film flow rate of 0.13 $kg/m/s$

The EHPII tube and the GEWA-B5 performed similar and have higher HTCs than the GEWA-KS and roughened tubes. Comparing all the micro-enhanced tube performances to that of the roughened tube in Figure 8.13, it is seen that the positions of the tubes correlate with the intricacies of their microstructures. The uncoated EHPII, GEWA-B5 and GEWA-KS tubes outperform the roughened tube. The EHPII tube perform the best with its HTCs being 287% higher than the roughened tube on average, along with the GEWA-B5 with 284% higher than those of the roughened tube. They are followed by the GEWA-KS which had HTCs being 85% higher than the roughened tube's HTCs on average. The roughened tube have the lowest heat transfer performance. The EHPII and GEWA-B5 tubes display very insensitive HTCs behaviours, whereas the GEWA-KS and roughened tubes have linearly increasing HTCs with increasing heat flux on the log-log plot. The GEWA-KS outperforms the roughened tube likely as a result of its larger surface area.

For the HTCs in the 5°C saturation temperature case in Figure 8.13a, the EHPII tube's HTCs increased by -1.9% and the GEWA-B5 by 4.3% across the heat flux range, illustrating that their HTCs were more independent from heat flux than the GEWA-KS tube which increased by 9.3% and the roughened tube by 8.8%.

Regarding the HTCs in the 25°C saturation temperature case in Figure 8.13b, the EHPII

tube's HTCs degraded by -7.6% over the testing heat flux range, showing that at the increased saturation temperature, the HTCs had a slight decline with increasing heat flux. Conversely, the GEWA-KS tube's HTCs increased by 13.4% over the testing heat flux range, showing that its HTC gradient tended to be steeper with an increase in saturation temperature.

Furthermore, similar to the pool boiling findings, it is again seen that there is an overall decline with -6.6% in HTCs on average for the EHPII tube when increasing the saturation temperature from 5°C to 25°C, while the HTCs of the GEWA-KS tube increased with an overall 6.7% with an increase in saturation temperature which are both well within experimental error.

8.5.2 Coated

An overview of the coated heat transfer performances of the micro-enhanced tubes are provided in Figure 8.14 at 5°C and 25°Cat a film flow rate of 0.13 $kg/m/s$.

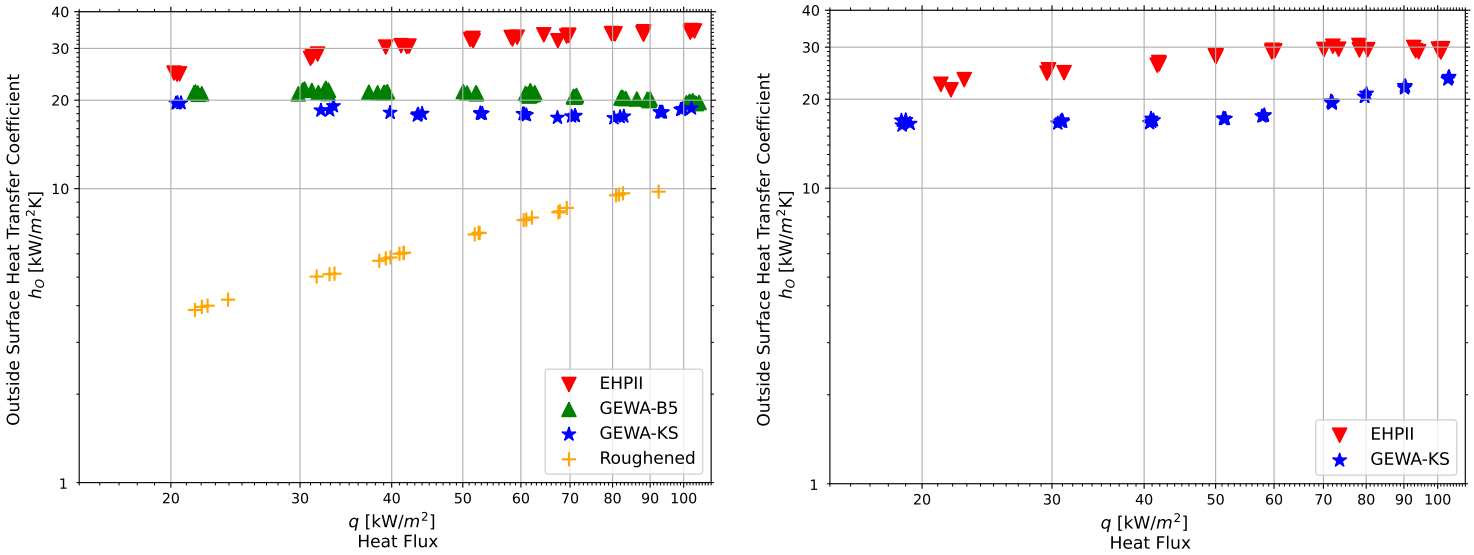

(a) 5°C (b) 25°C

Figure 8.14: Falling film boiling overview of coated micro-enhanced tubes at saturation temperatures of 5°C and 25°C in R134a at a film flow rate of 0.13 $kg/m/s$

Comparing the heat transfer performances of the coated micro-enhanced tube to that of the coated roughened plain tube in 5°C saturation temperature, it is seen that the EHPII tube performed the best with an average deviation of 355%, followed by the GEWA-B5 with 214% and the GEWA-KS with 177% compared to the roughened tube. The heat transfer performances relative to the roughened tube are slightly greater than what was seen for the uncoated tube comparison above.

Observing the coated micro-enhanced and plain tubes collectively for the 5°C saturation temperature case in Figure 8.14a, the HTCs for the EHPII tube increased the most with heat flux with 12.2% followed by the roughened tube with 7.3%. The GEWA-B5's HTCs increased with -1.4%, and the GEWA-KS with -1.1% and thus showed great independence from heat flux where their heat transfer performance were quite constant across the testing heat flux range.

Increasing the saturation temperature to 25°C as seen in Figure 8.14b, it was found that the

coated EHPII tube gained some independence from heat flux with a lower increase of 9.9%, whereas the GEWA-KS became more dependent with a general increase in HTCs of 8%.

The average deviation of the coated EHPII tube's HTCs with respect to those of the 5°C saturation temperature case again showed a decline in heat transfer performance with an overall change of -12%. The coated GEWA-KS HTCs stayed roughly the same, with a 4% change to its HTCs recorded in 5°C saturation temperature.

8.6 Falling Film Boiling Enhancement

The HTC enhancement posed by the falling film boiling configuration compared to pool boiling is illustrated through the falling film heat transfer enhancement ratios which were calculated for both uncoated and coated tubes in Figures 8.15 and 8.16 below at 5°C and 25°C respectively:

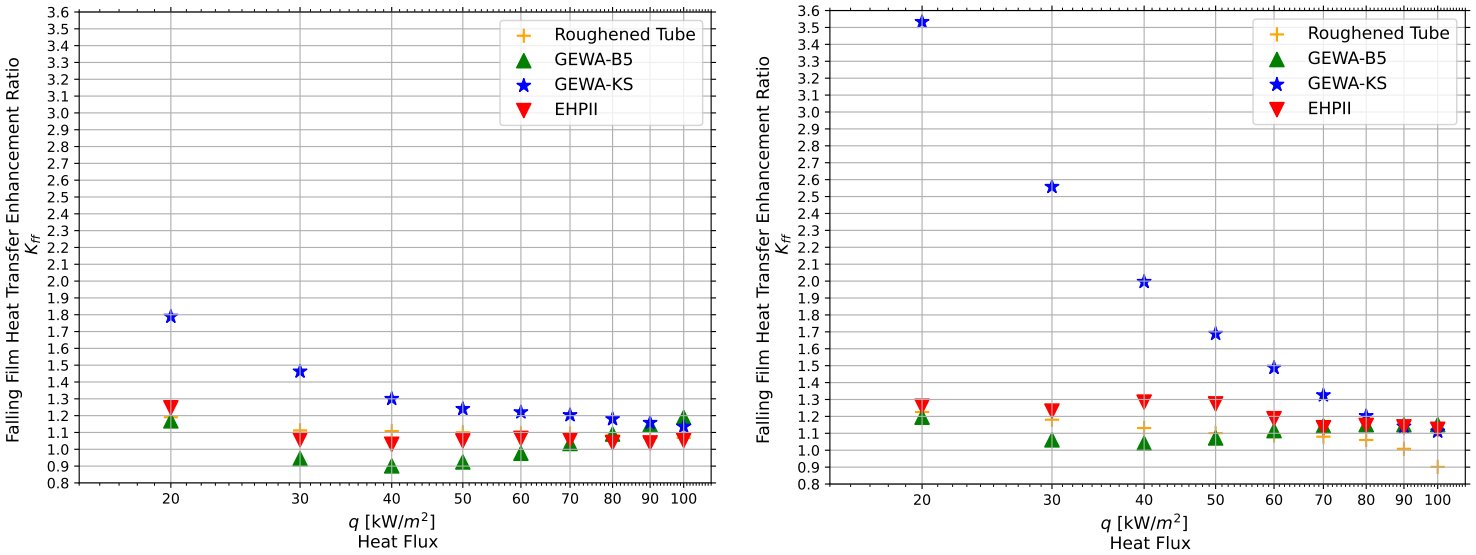

(a) Uncoated

(b) *CuO* coated

Figure 8.15: Falling film heat transfer enhancement ratio for 5°C saturation temperature in R134a

It is seen from the above Figure 8.15 that the falling film configuration has a positive influence on the heat transfer compared to pool boiling where HTCs are generally enhanced over the testing heat flux range. The enhancement typically tend to be greater at lower HTCs for both the uncoated and *CuO* coated tubes.

An average K_{ff} enhancement ratio of 1.1 for the uncoated roughened tube and 1.09 for the coated roughened tube was obtained. The similar enhancement indicates negligible influence of falling film conditions on the coating on the roughened tube.

A significant difference is found between the average K_{ff} of 1.3 for the uncoated GEWA-KS and 1.8 for the *CuO* coated GEWA-KS tubes where the coated tube performed much better. The K_{ff} ratio ranged from a great 3.6 to 1.1 and it is suspected that the coating aided the tube's vertical microstructure fins in maintaining the falling film integrity for great heat transfer with a uniform film stream. This finding is very interesting, since the uncoated and coated roughened tube influence on falling film enhancement is very similar, indicating that the microstructure

fins must benefit from the coating. It may be that the coating wicks the liquid up to the tips to make use of the area on the tips where the uncoated tube's fin tips could have been dried out. The wetted fin tips could also have ensured that a high falling film quality was maintained so that an efficient supply of refrigerant could be given to a more available heat transfer area.

Not much enhancement was posed on the GEWA-B5 uncoated and coated tubes where the K_{ff} ratios were relatively constant. The coated tube with an average K_{ff} of 1.1 benefitted slightly more from the falling film configuration than the uncoated tube which had an average K_{ff} of 1. Marginal improvement was observed for the EHPII tube with the coated tube having an average K_{ff} of 1.2 over the uncoated EHPII tube with an average of 1.1.

The falling film heat transfer enhancement ratios are also calculated at 25°C for the uncoated and coated GEWA-KS and EHPII tube sets and are illustrated in Figure 8.16:

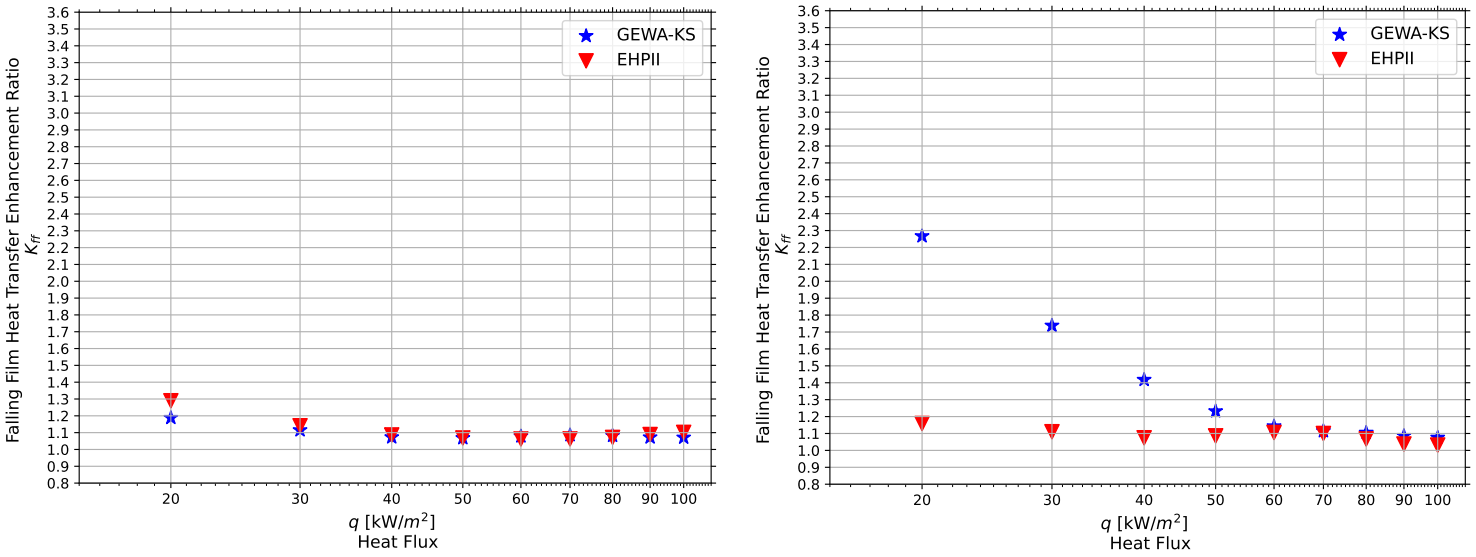

(a) Uncoated

(b) CuO coated

Figure 8.16: Falling film heat transfer enhancement ratio for 25°C saturation temperature in R134a

As seen by Figure 8.16 above, the falling film configuration tend to favour the coated GEWA-KS tube the most as seen with higher K_{ff} values while the uncoated GEWA-KS and the EHPII tubes were enhanced up to 30% and 20% respectively at low heat fluxes. The mechanisms of heat transfer unique to the falling film boiling are used to a greater extent by the coated GEWA-KS tube and it is suspected that it is because of the integrity of the film being upheld by the vertical fins by the CuO coating. The downward trend observed in Figure 8.16b indicates that the advantage of using the coated surface for falling film boiling instead of pool boiling would only be useful at lower heat fluxes for the CuO coated GEWA-KS tube as seen in other studies [36], as the boiling process is dominated by nucleate boiling at higher heat fluxes. This theory is explored in section N.26 in Appendix N.

The K_{ff} ratios ranging from 2.3 to 1.1 with an average of 1.4 for the CuO coated GEWA-KS tube shows more enhancement than the uncoated GEWA-KS with an average K_{ff} of 1.1. The uncoated HTC enhancement was relatively stable across the heat flux range for the uncoated

GEWA-KS tube where the K_{ff} ratios only declined from 1.2 to 1.1.

Not much difference was seen between the uncoated and coated EHPII tubes where the CuO coated tube's K_{ff} values ranged from 1.3 to 1.1 with an average of 1.1; and similarly for the uncoated EHPII tube ranging between 1.2 and 1 with an average of 1.1 too.

8.7 CuO Enhancement

To evaluate the influence of the CuO nanocoating on the plain and commercially micro-enhanced tubes, the coating heat transfer influence ratio are calculated for both 5°C and 25°C saturation temperatures in Figure 8.17:

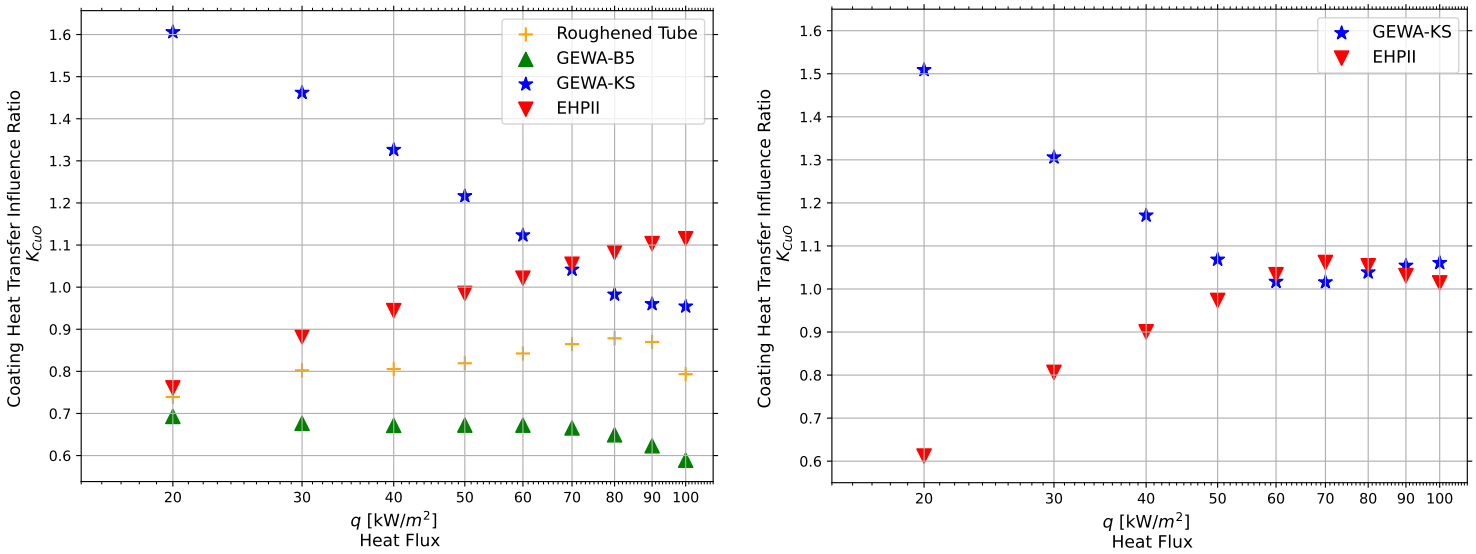

(a) 5°C (a) 25°C

Figure 8.17: Coating heat transfer influence ratio for CuO nanocoated tubes at saturation temperatures of 5°C and 25°C in R134a

It is easily seen from Figure 8.17 that the potential for HTC enhancement by the CuO coating is only applicable for the GEWA-KS tube, mostly at lower heat fluxes, and possibly the EHPII tube at higher heat fluxes beyond $100kW/m^2$ where the K_{CuO} factor is above 1 for both saturation temperature cases.

With an average coating heat transfer influence ratio of 0.82 for the roughened tube in Figure 8.17a, the coating is seen to degrade the heat transfer performance. The general increasing trend of the heat transfer influence ratio may suggest that there could have been a tendency to enhance HTCs if dryout did not occur with the coated roughened tube. The dryout on the roughened tube may be because of the strong inherent tendency of the uncomplicated surface to reach very high surface temperatures to dominate the wettability the CuO nanocoating poses.

An overall HTC enhancement on the GEWA-KS tube is seen for both saturation temperature cases. The degree of the enhancement is relatively equal with an average K_{CuO} of 1.2 for the 5°C saturation temperature and 1.1 for the 25°C saturation temperature case. It is seen that the coating generally did not significantly enhance the HTCs over the entire range of the testing heat flux, but did greatly enhance the HTCs at lower heat fluxes. The enhancement factor

ranged broadly from 1.6 to 0.95 indicating great influence by the coating for both saturation temperatures. At low heat fluxes where the convective effects of the falling film boiling arrangement are dominant, the coating may contribute by wetting a larger area of the tube such as the fin tips and therefore poses a greater heat transfer performance, the higher heat fluxes will be dominated by the nucleate boiling. The tendency of heat transfer in falling film boiling is that the HTCs approached the same magnitudes as those of pool boiling at higher heat fluxes as the nucleate boiling dominated over the falling film forced convective effect present at lower heat fluxes [36].

With an average coating heat transfer influence ratio of 0.66 for the GEWA-B5 at 5°C saturation temperature in Figure 8.17a, it is clear that the nanocoating effectively reduced the HTCs of the GEWA-B5. It is hereby deduced that the combination of a CuO nanocoating and the complex GEWA-B5 micro-enhanced surface is not a viable option to enhance heat transfer where the K_{CuO} value consistently remained below 1.

It is found for the EHPII tube that an average coating heat transfer influence ratio of 1.0 for 5°C saturation temperature and 0.9 for 25°C saturation temperature, it is not viable to enhance HTCs through the CuO nanocoating. In fact, at low heat fluxes, the HTCs were decreased by as much as 20% by the CuO nanocoating.

With the general upwards trend of the K_{CuO} at 5°C saturation temperatures in Figure 8.17a it would have been of interest to investigate CHF points and possible HTC enhancement at very high heat fluxes.

It is known for falling film boiling to have a few advantages over the pool boiling configuration. This is seen as there was an increase in HTCs for the falling film boiling results in section 8 compared to the pool boiling results in section 7. The HTC enhancements were identified by Cerza [36] to be the evaporation of thin liquid zones on the surface of the tubes from the turbulent falling film as well as embedded bubbles in the film enhancing heat transfer by microlayer evaporation through the bubbles' bases. It is further theorized that nucleation sites were initiated from the entrapped bubbles in the film bursting [77]. The mentioned heat transfer features of falling film boiling could be used to understand the influence the CuO nanocoating has on the tubes.

From the above falling film boiling investigation on uncoated and CuO coated commercially micro-enhanced tubes at 5°C and occasionally 25°C saturation temperatures in R134a refrigerant, the following 5 remarks has been identified to be possible explanations of the degradation of HTCs due to the CuO nanocoating:

- The uncoated micro-enhanced surfaces are prominently covered with a thin refrigerant liquid layer, whereas the coated micro-enhanced surfaces are extensively flooded with a thick layer of refrigerant liquid at lower heat fluxes as observed in the comparative high speed video footage.
- The coated surfaces are much more sensitive to dry spots at higher heat fluxes, whereas

this is not seen with the uncoated surfaces.

- The uncoated surfaces display a much more stable fashion of falling film boiling with distinct waiting, unbinding and freestream stages; where the integrity of the film on the coated surfaces seem unstable with volatile nucleation activity. After nucleation on the coated surfaces, the bubbles were much more stationary and burst prominently without being swept away to grow downstream such as observed with the uncoated surfaces.
- At stable nucleation cases on the coated surfaces, it is apparent that the bubble diameters were larger than on the uncoated surfaces, but not to the same degree as observed in pool boiling.
- High tendencies of dry spots on the coated surfaces are not rewetted, whereas the uncoated surfaces were. This is especially seen from the falling film dryout tests.

The most significant observation from all the remarks above are the distinct stagnant, thick liquid layers covering the CuO coated surfaces despite the falling film acting out a dynamic force over the tubes. The uncoated surfaces did not suffer from this, where a much thinner liquid layer falling down the tube and carrying growing bubbles to burst much later.

In the cases where HTC enhancement is seen through the addition of the CuO nanocoating in the EHPII tube and the lower heat fluxes of the GEWA-KS tube, it is visually noted they have a good quality falling film integrity.

9 Condensation

Condensation tests were performed on the uncoated and coated GEWA-KS and EHPII micro-enhanced tubes at 30°C saturation temperature and were done to investigate the heat transfer abilities of the coated tubes compared to the uncoated tubes. The coating heat transfer influence ratios were calculated to quantify the effects of the CuO coating on the heat transfer performance.

9.1 Uncoated Micro-Enhanced Tubes Overview

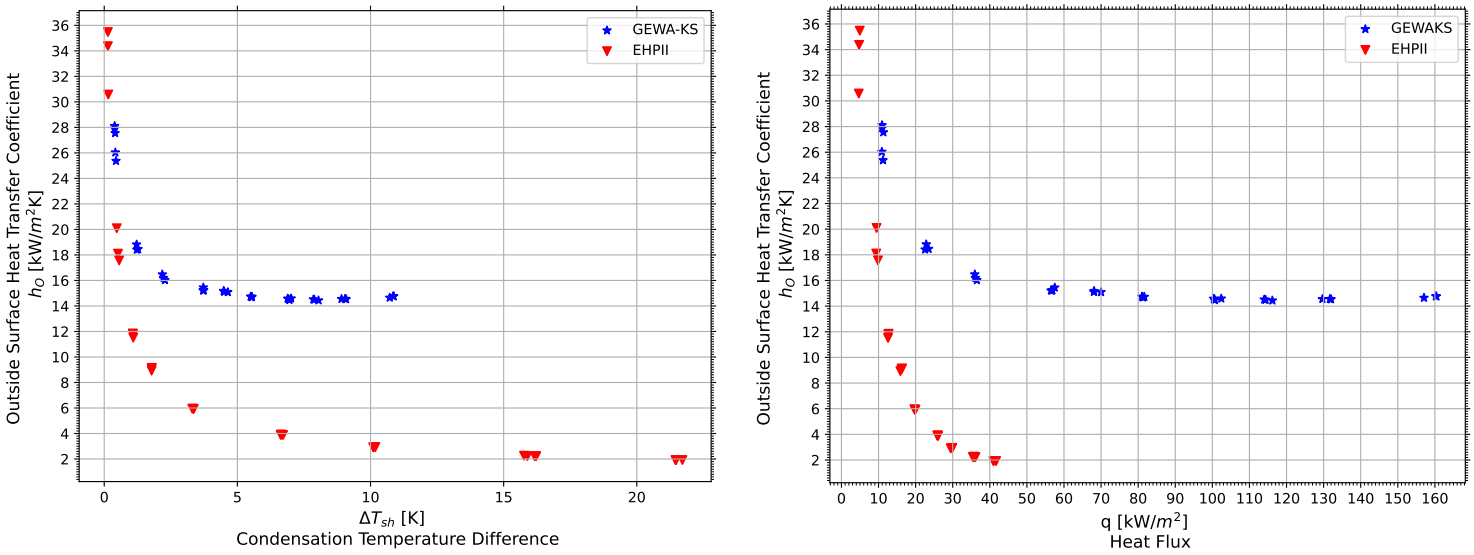

(a) Temperature domain

(b) Heat flux domain

Figure 9.1: Condensation tests overview of uncoated micro-enhanced tubes at a saturation temperature of 30°C in R134a

It was seen in Figure 9.1 that the uncoated GEWA-KS tube performed significantly better than the uncoated EHPII tube in during condensation. Using the same maximum operational limit of the testing facility for both tubes, it was found that the GEWA-KS could reach around 160 kW/m^2 whereas the EHPII could only attain 42 kW/m^2. The GEWA-KS was also had much greater HTCs than the EHPII tube at the same condensation temperature differences which made it more effective in condensing the R134a.

It was suspected that the better heat transfer performance by the GEWA-KS to be attributed to a much larger area posed by the micro-structure fins. The EHPII tube had finer microstructure scales on its surface to suggest a smaller surface area.

9.2 Coated Micro-Enhanced Tubes Overview

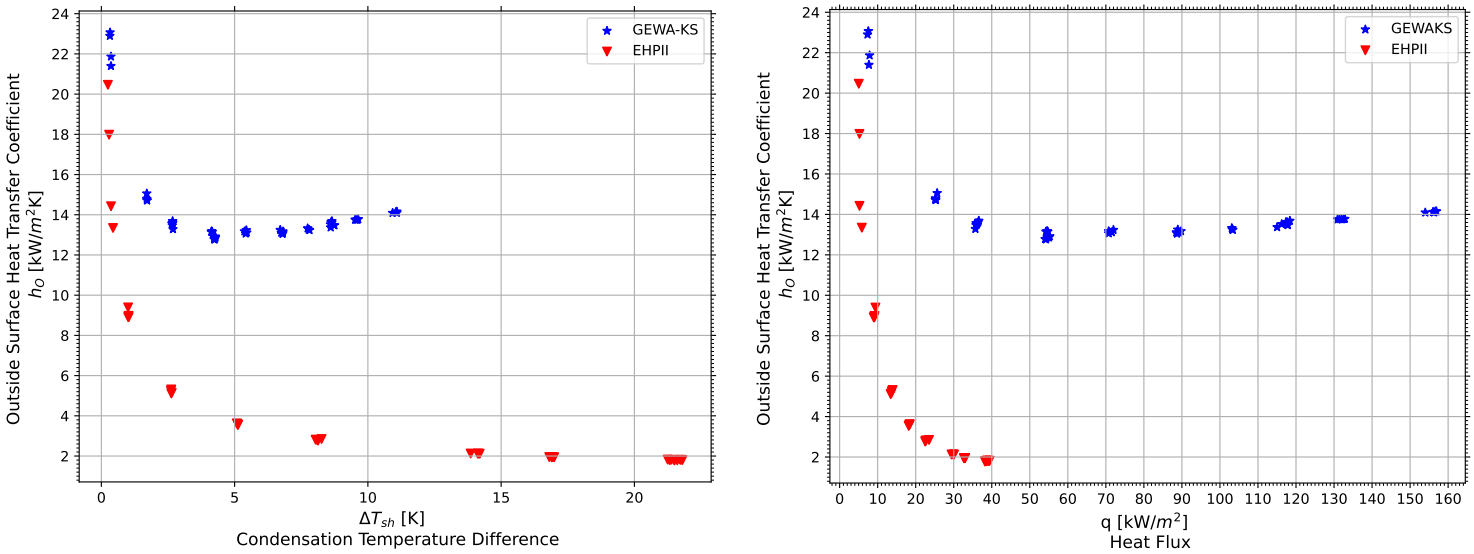

(a) Temperature domain

(b) Heat flux domain

Figure 9.2: Condensation tests overview of coated micro-enhanced tubes at a saturation temperature of 30°C in R134a

Figure 9.2 delivered the same outcome as with Figure 9.1 that the coated GEWA-KS tube performed better than the coated EHPII tube in condensation. The GEWA-KS could reach around 157 kW/m^2 whereas the EHPII could manage 40 kW/m^2. The coated GEWA-KS was also had much greater HTCs than the coated EHPII tube, where the coated GEWA-KS high heat flux HTCs were approximately 7 times greater than the coated EHPII tube.

It was again suspected that the better heat transfer performance by the GEWA-KS to be attributed to a much larger area posed by the micro-structure fins.

9.3 GEWA-KS

An uncoated and a coated GEWA-KS micro-enhanced tubes were subjected to condensation tests at 30°C saturation temperature. The condensation results were as follows in Figures 9.3 and 9.4:

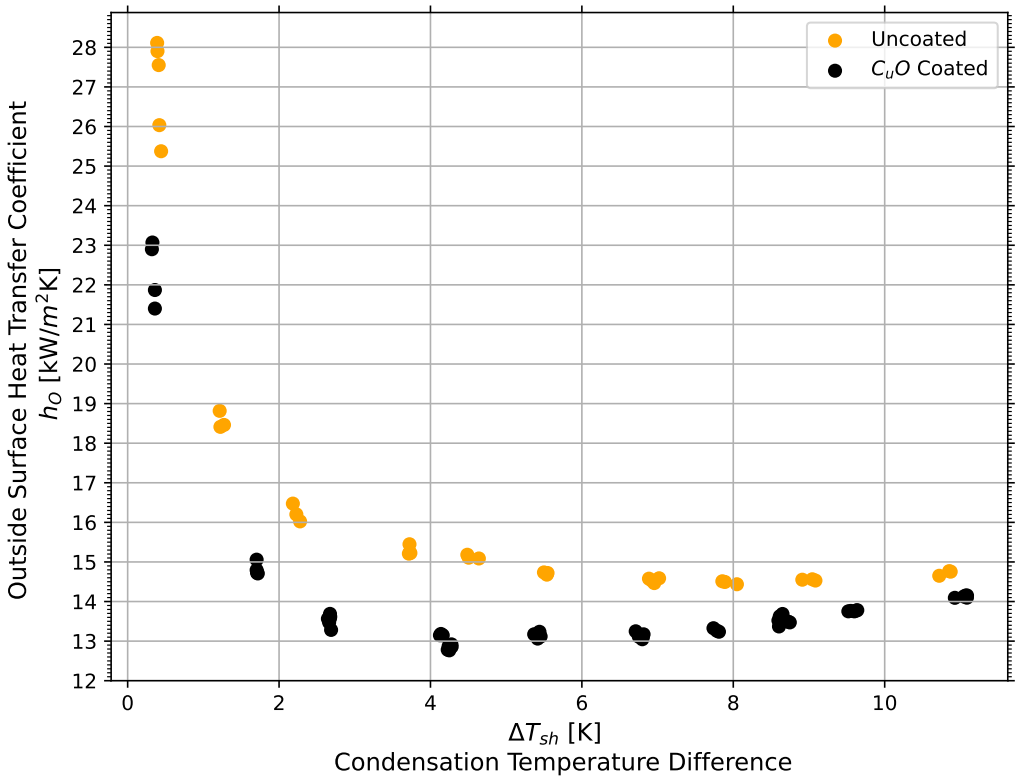

Figure 9.3: Condensation test of GEWA-KS per condensation temperature difference at a saturation temperature of 30°C in R134a

From the above condensation results, it was seen that the coated GEWA-KS tube performed worse in condensation than the uncoated GEWA-KS with lower HTCs, especially at lower temperature differences.

To inspect the total effect of the CuO nanocoating on the GEWA-KS during condensation, the coating heat transfer influence ratio was calculated below:

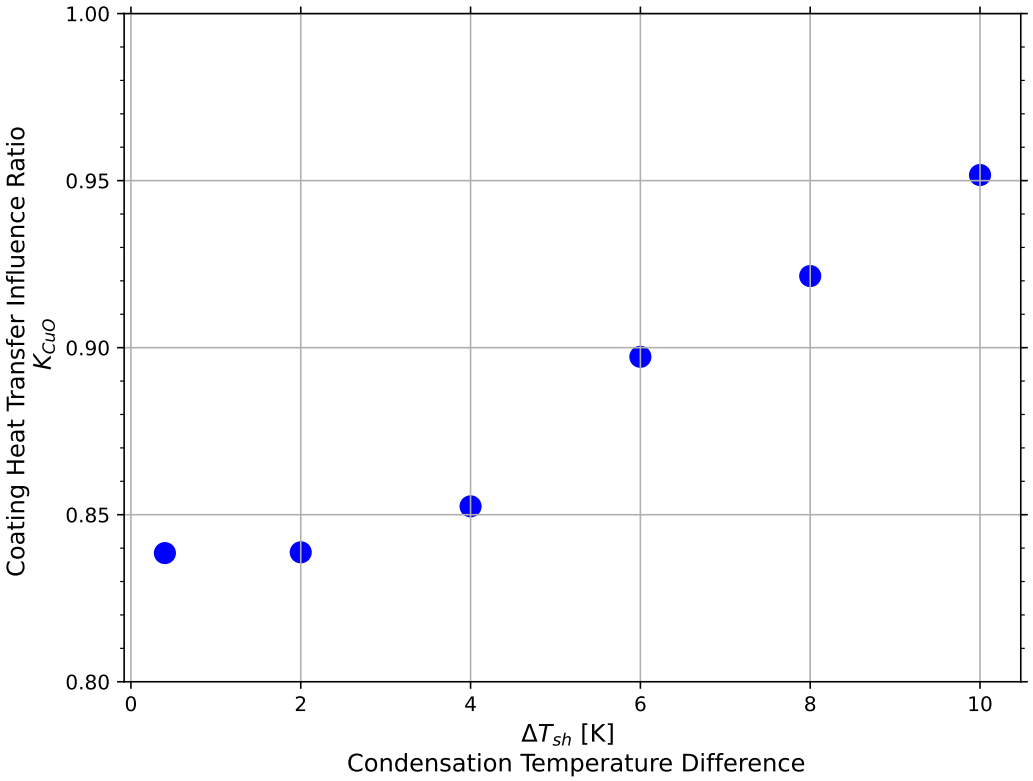

Figure 9.4: GEWA-KS condensation heat transfer influence ratio

It was seen with an average coating heat transfer influence ratio of 0.89 that there was no significant overall effect of the CuO coating on the GEWA-KS condensation performance. The deterioration imposed by the coating was present, however not extreme.

The condensation heat transfer deterioration may be because of the extreme liquid retention on the surface by the wettable CuO nanocoating, covering the surface with liquid. The thick covering layer could then serve to insulate the surface from further condensing the refrigerant vapour. It was also seen from the high speed footage that the liquid retention is very strong where liquid removal from the condensing surface by the action of gravity was very slow, causing the overall rate of condensation to be slow.

With the general upwards trend of the coating heat transfer influence ratio in Figure 9.4, it may be profitable to have investigated possible HTC enhancement at higher heat fluxes than tested on this stand.

9.4 EHPII

An uncoated and a coated EHPII micro-enhanced tubes were subjected to condensation tests at 30°C saturation temperature. The condensation results were as follows in Figures 9.3 and 9.6:

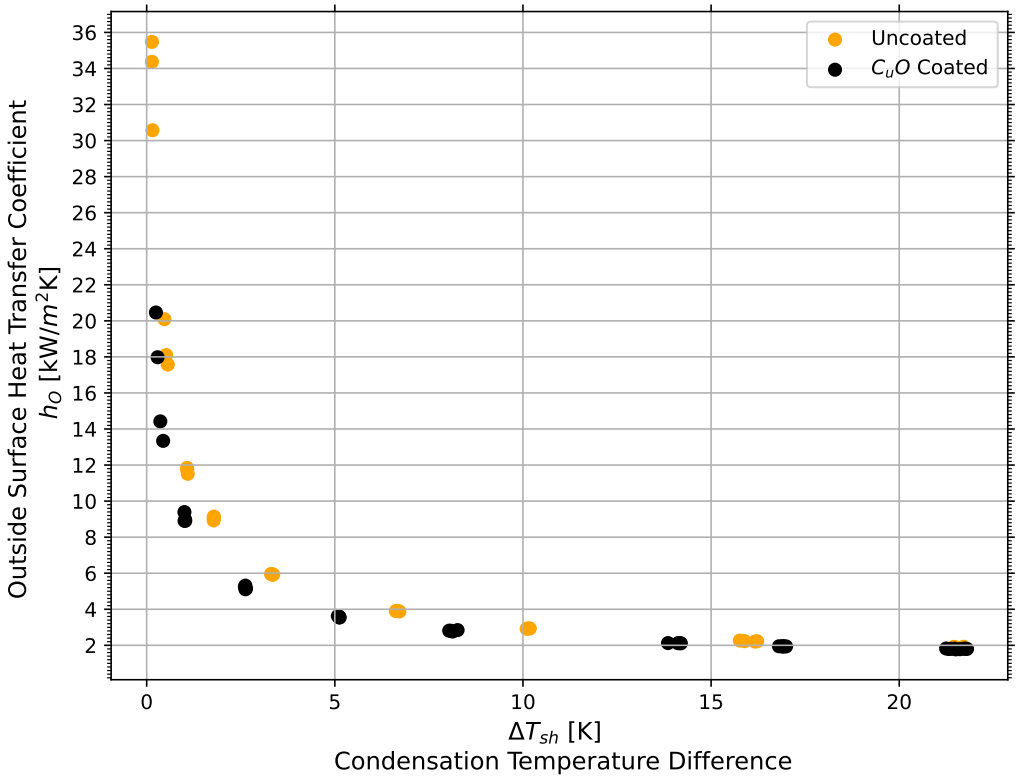

Figure 9.5: Condensation test of EHPII per condensation temperature difference at a saturation temperature of 30°C in R134a

It was seen from the condensation tests above that the uncoated EHPII tube performed better than the CuO coated EHPII tube to transfer heat. The deterioration of the HTCs are more distinct on the coating heat transfer influence plot of Figure 9.6.

To investigate the effective influence the CuO coating had on heat transfer performance of the EHPII tube, the coating influence heat transfer ratio was calculated below:

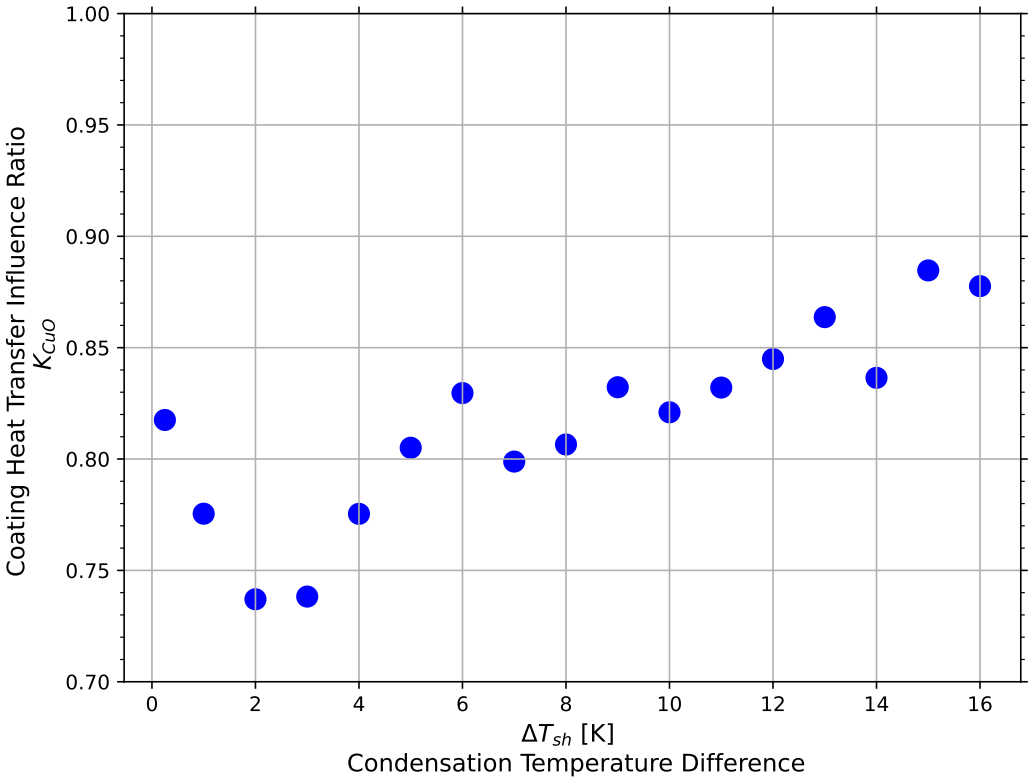

Figure 9.6: EHPII condensation heat transfer influence ratio

With an average coating influence heat transfer ratio of 0.81, the overall effect of the CuO coating on the condensation heat transfer of the EHPII tube was slightly diminishing.

Apart from the inherent effect of the CuO coating to retain retain liquid to the condensing surface as was observed in the case of the GEWA-KS tube, the additional effect of the thick liquid layer around the tube in this case would also comprise the flooding of the microstructure scale pores to make them ineffective for condensation. This is if the pores were not preliminary flooded on the uncoated tube, since it is not clear from the high speed footage whether these pores may have been flooded on the uncoated tube.

The CuO coating was not a reliable addition to the EHPII tube to enhance heat transfer during condensation. With no apparent trend in the coating heat transfer influence ratio of Figure 9.6, the CuO coating should not be considered for any condensation heat transfer improvement.

10 Summary

A concise summary of all the resultant deviations from the uncoated and CuO nanocoated roughened tube at all cases were populated in Table 10.1 to 10.4:

Table 10.1: Summary of pool boiling results at 5°C saturation temperature in R134a

Tube Name	Relative to Roughened Tube				K_{CuO}
	Uncoated		Coated		
	Average [%]	Maximum [%]	Average [%]	Maximum [%]	
EHPII	298	519	315	552	0.89
GEWA-KS	57	64	70	83	0.91
GEWA-B5	318	539	214	483	0.60
Roughened					0.85

Table 10.2: Summary of pool boiling results at 25°C saturation temperature in R134a

Tube Name	Relative to 5°C Tube				K_{CuO}
	Uncoated		Coated		
	Average [%]	Maximum [%]	Average [%]	Maximum [%]	
EHPII	-10	6	-3	2	0.97
GEWA-KS	25	35	30	34	0.95

Table 10.3: Summary of falling film boiling results at 5°C saturation temperature in R134a

Tube Name	Relative to Roughened Tube				K_{ff}		
	Uncoated		Coated				
	Average [%]	Maximum [%]	Average [%]	Maximum [%]	Uncoated	Coated	K_{CuO}
EHPII	287	549	355	568	1.1	1.2	0.99
GEWA-KS	85	145	177	433	1.3	1.8	1.19
GEWA-B5	284	509	214	471	1.0	1.1	0.66
Roughened					1.1	1.1	0.82

Table 10.4: Summary of falling film boiling results at 25°C saturation temperature in R134a

Tube Name	Relative to 5°C Tube				K_{ff}		
	Uncoated		Coated				
	Average [%]	Maximum [%]	Average [%]	Maximum [%]	Uncoated	Coated	K_{CuO}
EHPII	-7	9	-12	-10	1.1	1.1	0.94
GEWA-KS	7	12	4	23	1.1	1.4	1.14

11 Conclusion

This study aspired towards mainly understanding the influence of the addition of a CuO nanocoating to different types of commercially microstructured tube surfaces. This was achieved through experimental heat transfer investigations in conjunction to high speed footage of the boiling phenomena. Uncoated and coated sets of roughened, GEWA-KS, GEWA-B5 and EHPII tubes were observed under pool boiling, falling film boiling and condensation in R134a by recording the HTCs at a range of heat fluxes. This study was successful to expand upon the knowledge of multiscale enhancement.

The CuO nanocoatings on the microstructured tubes were synthesised by bathing the tubes, in a hot alkali solution to oxidise the clean copper surface to form the CuO nanostructures. It was found through SEM analysis that the nanocoating to have not impeded the microstructures significantly and that the underlying microstructures to have been well-preserved.

Furthermore, the study accomplished obtaining HTCs over a specified testing heat flux range for uncoated and coated tubes, where the EHPII and GEWA-KS data are more valuable regarding the scarcity of data on these tubes at the time of the current study.

In the pool boiling case, the uncoated GEWA-B5 tube performed the best with HTCs being 318% greater than those of the roughened tube on average, followed by the EHPII tube with 298% and the GEWA-KS tube with 57%. The performance was similar in the falling film case, where the uncoated EHPII tube performed the best with HTCs 287% higher than those of the roughened tube, followed closely behind by the GEWA-B5 with 284% and finally the GEWA-KS with 85%. A notable finding from the heat transfer experimental investigation on the uncoated tube set in both pool boiling and falling film boiling conditions was that the microstructured EHPII and GEWA-B5 to have significantly enhanced heat transfer in comparison to the plain roughened tube.

From all the experimental heat transfer tests performed, it was deduced that the addition of a CuO nanocoating generally not to be a viable option towards significantly enhancing the HTCs compared to the uncoated tube cases.

The CuO nanocoating usually degraded the HTCs, or did not have any significant influence in the pool boiling case. The only heat transfer enhancement recorded through the addition of the CuO nanocoating in pool boiling was seen by the nanocoated EHPII tube in the higher heat flux range at 5°C saturation temperature with a minor HTC increase of approximately 5%; and the nanocoated GEWA-KS and EHPII tubes in the higher heat flux range at 25°C saturation temperature with a minor increase of approximately 5% and 10% respectively.

The addition of the CuO nanocoating in the falling film boiling case led to similar findings as with the pool boiling case. The significant heat transfer enhancement recorded in falling film boiling included the nanocoated GEWA-KS tube in a lower heat flux range and the nanocoated EHPII tube in a higher heat flux range in the 5°C saturation temperature case, with a maximum HTC increase of approximately 60% and 10% respectively. The 25°C saturation temperature

case in falling film boiling exhibited great HTC enhancement with the nanocoated GEWA-KS in a lower heat flux range, increasing the HTCs with approximately 50% compared to the uncoated case. The great enhancements were mainly attributed to a possible better uniform spread of the falling film as imposed by the highly wettable surfaces. Marginal HTC enhancement was seen with the nanocoated EHPII at a saturation temperature of 25°C in the mid-range heat fluxes with an approximate HTC enhancement of 10%.

The falling film boiling configuration's heat transfer enhancement compared to the pool boiling configuration was explored in this study. Some falling film enhancement was seen in all the tubes, where there were no cases where the heat transfer was degraded from those obtained in the pool boiling configuration. All tubes at both saturation temperatures displayed an average enhancement ratio,K_{ff}, between 1.0 and 1.2 with 1.1 as the most frequent, apart from the GEWA-KS tube which had a significant K_{ff} of 1.3 in the uncoated case and a K_{ff} of 1.8 in the coated case at 5°C saturation temperature. The coated GEWA-KS also showed significant falling film enhancement at 25°C with a K_{ff} ratio of 1.4. The coated GEWA-KS was hereby found to perform very well in falling film conditions in comparison to the pool boiling case. The falling film boiling configuration did not have such an extensive effect on the uncoated GEWA-KS such as on the coated tube, but both showed similar or greater enhancement than the coated and uncoated EHPII tube.

This study also managed to document the dryout performance of the uncoated and coated tube sets, of which were also of limited availability in past research. It was discovered that no significant increase in dryout performance was achieved through the addition of the CuO nanocoating in all cases.

The effect of the saturation temperature was also explored on the GEWA-KS and EPHII tubes, where the HTCs on the GEWA-KS tended to marginally increase, whereas the HTCs in the EHPII tube tended to decrease. This decrease in heat transfer performance was possibly due to adverse hot spots and heating profiles on the scale microstructures for inefficient nucleation.

The liquid motion and hydraulics in pool boiling and falling film boiling as a result of the CuO nanocoating have also been addressed. A reason for the degraded heat transfer may be that the hydrophilic surface prematurely and readily flooded the nucleation sites, destroying the superheated refrigerant microlayer lining in the nucleation sites to degrade the evaporative heat transfer. This flooding may also have led to the hindrance of the bubble pumping action and the sensible heat transfer in the micro-capillaries. However, this reasoning is speculation, for where the exact causes of the degradation should be investigated in greater detail in a study capable of providing concrete proof. However, a confirmed heat transfer degradation mechanism was the trapped bubbles in the nanocoated re-entrant microstructures as seen in pool boiling with the nanocoated GEWA-B5 tube.

The CuO nanocoating applied to microstructured surfaces seemed not to be a reliable method of enhancing HTCs, where a particular combination of the CuO nanocoating and a specific microstructure profile could not be easily identified. The best possible combination could be

the CuO nanocoating on the GEWA-KS tube, where an enhancement of approximately 60% could be obtained in the range of 20 kW/m^2. The GEWA-KS may also promise some coating enhancement at very high testing heat fluxes in pool boiling in this study, but of which were not explored in this study.

Furthermore, the condensation heat transfer on uncoated EHPII and GEWA-KS tubes similarly showed a moderate decrease in HTCs, of which the degradation was attributed to the liquid retention on the hydrophilic surface. The microstructure cavities could not be evacuated of liquid easily for the saturated vapour to reach the cooling surface to condense efficiently.

12 Recommendations

Throughout the study, some recommendations had been collected concerning the improvement of the testing facility, the current study as well as suggestions on the developments upon the current study:

12.1 Testing Facility

During the course of research and the utilisation of the FF rig facility, the following recommendations were made for better control, stability and calibrations:

- For improved pressure calibration and to make the process easier and faster, it should be considered to purchase a *WIKA* 5-pin bayonet USB data interface cable in order to link the *WIKA CPH 6400* display to the LabVIEW calibration Virtual Instrument File (VI). This would enable automatic reading of volatile reference pressure values directly into the program to instantaneously capture both reference and sensor values at the same point in time for a more reliable calibration point – and without having the reference value change too much such as seen at high pressures.
- It was seen that the chilled water and hot water utility supply temperatures to fluctuate extensively (especially with the roof system boiler in action), leading to poor reliability of overall stability during testing. Better control over testing water temperatures could be obtained through using a high capacity thermal bath and thereby removing the dependency on the roof utility system, or using a temperature regulator valve connected to the testing water line to operate in conjunction to the roof utility system to finely control the testing water temperature.
- The propagation of error became very high at lower heat fluxes. It should thereby be profitable to investigate alternative means of upgrading instrumentation or the calibration procedures thereof to decrease the uncertainties in HTC so that lower HTCs could be observed and compared with reasonable confidence.
- The FF rig facility is in danger of becoming obsolete from outdated components. It should be considered to replace and upgrade components throughout the FF rig, and preferably with open-source alternatives, to avoid high cost of replacement with scarce compatible components.
- Modify the FF rig in order to test longer tubes in in the testing chamber. The testing conditions with longer tubes would resemble industrial scale heat exchangers even more and would also enable testing to be easier with a greater temperature difference between the inlet and outlet of longer testing tubes.
- Modify the FF rig to cater for wider condensation end points by accommodating stronger heating and cooling media. This would be especially relevant for tubes that do not perform well under condensation, from where these tubes could be then thoroughly compared to tubes that do perform well under condensation.

12.2 Development Upon the Nanocoated Micro-Enhanced Tubes and Further Study

The following are suggested for the development upon the current study and the findings from the current study. A wide array of options regarding the testing of the commercially micro-enhanced surfaces are available as well as simply altering the chemical formulae in the coating bath for additional heat transfer studies:

- Employ a standardized method of sanding tubes with sandpaper so that the entire tube is of uniform roughness. A specialized jig to hold the sandpaper at a consistent pressure against a tube in a lathe is suggested, where the tube is sanded so that uniform grooves are circumferential on the tube. Hereby, the tube's roughness can directly be measured on the tube with roughness testing machines, which can accommodate measurement of surface roughness (against the grain) on concave surfaces.
- It may be beneficial to include the Jakob number, Ja, in analysis. This alludes to the fraction of the sensible heat and the latent heat during boiling as well as the Marangoni number, Ma, as a fraction of the surface tension and the viscous force if they are attainable during experiments [78]. These relevant dimensionless numbers may increase the quality of deduction for future studies.
- Develop a setup whereby the dynamic force (gravity) can be increases in falling film boiling cases, from where the wettability and the ability for dry patches to be mitigated can be investigated.
- Investigate higher heat fluxes where HTCs may be enhanced with the CuO nanocoating and their complete behaviour observed until full dry-out.
- Investigate the high potential of CHF enhancement in the pool boiling case, since the CuO coating in the current study may prolong dryout compared to the uncoated surfaces.
- Quantify the surface tension forces with in the interaction between the CuO surface and the R134a refrigerant at the testing saturation temperatures.
- Quantify the exact contact angles of the liquid refrigerant and the CuO surface in the applicable configurations in order to effectively use the models developed to better understand departing bubble sizes and wicking characteristics.
- Newer models and correlations could be used for validation such as those developed by Shah [79, 80] as well as some prediction models constructed by van Rooyen and Thome [81, 82] for the affirmation of micro-enhanced tubes.
- Consider the correlations developed by Zhao et al. [83] for falling film boiling heat transfer in the partial dryout and fully wetted regimes during validation studies to further ascertain the integrity of the experimental facility.
- Investigate and incorporate advanced bubble growth prediction methods such as those developed by Raj et al. [84] into pool boiling on nanostructure analyses. Using these

methods require more parameters to be recorded such as the α and β angles of a bubble as well as the surface inclination angle. Using predictive methods could provide insight into the enhancement or degradation factors of boiling on nanostructured surfaces in comparison to conventional findings. It may also direct to a specific quantity in the model that is being influenced to deduce a cause.

- Further development upon the construction of the micro-enhanced surfaces could be pursued through controlled nano-particle deposition as described in a study by Kim et al. [4] in order to create a geometry through micro-pillar, micro-pin and micro-fin construction to specify the micro-channels and cavities for the enhancement of CHF and HTCs. The constructed geometries are finely created to induce specific and favourable hydraulics. The complex profiles could then be combined with a CuO coating as described in the current study to pursue HTC and CHFenhancement.
- Further heat transfer investigations can be performed on commercially micro-enhanced refrigeration tubes by combining the surfaces in a hybrid surface configuration using the fabrication techniques developed by Khan et al. [85]. The researched nanocoating techniques were specially developed for the enhancement of heat transfer and it would be of interest to explore the heat transfer enhancement when coating through sintering, hot powder sintering, hot powder sintering and reduction, hot powder compaction and the matured states of these surfaces [85].
- For the future of utilising CuO nanocoatings on microstructured surfaces to enhance heat transfer, it may be most plausible by applying a more precise engineered coating procedure for an organised nanostructure morphology. As was suggested by Xiangdong et al. [28], that the fabrication of nanocoatings with high surface wettability characteristics should be finely controlled to produce a high interconnected, porous morphology where liquid could be supplied through the base and vapour removed through the nucleation site openings by independent paths. Designing a microstructure to make use of underlying micro-channel heating to facilitate phase change before reaching the nucleation sites would also have been beneficial to enhancing HTCs if a capillary wicking action is to be used productively to supply the evaporating menisci at a steady rate to enhance both HTCs and CHFs.

  Hydrophobic surfaces may be a better option over the hydrophilic surfaces as explored in the current study. As explained by Attinger [34] where the surface energy of hydrophobic surfaces required for nucleation and bubble development may be less than hydrophilic surfaces leading to higher HTCs. The hydrophobic surfaces may also impose less resistance to the boiling phenomena as described by Jin et al. [38], in particular the ease of ejection of bubbles from re-entrant cavities and the easier movement of liquid through capillary channels which is facilitated by an enhanced bubble pumping action. A CuO coating which is of a hydrophobic nature may be possible through by altering the reagents or their concentrations during coating [14].

References

[1] Bradley D Bock. "Surface influences on falling film boiling and pool boiling of saturated refrigerants". In: (2020), p. 191.

[2] Marcel Christians and John Richard Thome. "Falling film evaporation on enhanced tubes, part 1: Experimental results for pool boiling, onset-of-dryout and falling film evaporation". In: *International Journal of Refrigeration* 35.2 (Mar. 2012), pp. 300–312. ISSN: 01407007. DOI: 10.1016/j.ijrefrig.2011.10.020. URL: https://linkinghub.elsevier.com/retrieve/pii/S0140700711002684 (visited on 07/06/2022).

[3] Gherhardt Ribatski and Anthony M. Jacobi. "Falling-film evaporation on horizontal tubes—a critical review". In: *International Journal of Refrigeration* 28.5 (Aug. 2005), pp. 635–653. ISSN: 01407007. DOI: 10.1016/j.ijrefrig.2004.12.002. URL: https://linkinghub.elsevier.com/retrieve/pii/S0140700704002622 (visited on 12/01/2022).

[4] Dong Eok Kim et al. "Review of boiling heat transfer enhancement on micro/nanostructured surfaces". In: *Experimental Thermal and Fluid Science* 66 (Sept. 2015), pp. 173–196. ISSN: 08941777. DOI: 10.1016/j.expthermflusci.2015.03.023. URL: https://linkinghub.elsevier.com/retrieve/pii/S0894177715000928 (visited on 01/27/2023).

[5] Kuang-Han Chu et al. "Hierarchically structured surfaces for boiling critical heat flux enhancement". In: *Applied Physics Letters* 102.15 (Apr. 15, 2013), p. 151602. ISSN: 0003-6951, 1077-3118. DOI: 10.1063/1.4801811. URL: http://aip.scitation.org/doi/10.1063/1.4801811 (visited on 03/20/2023).

[6] Gangtao Liang and Issam Mudawar. "Review of pool boiling enhancement by surface modification". In: *International Journal of Heat and Mass Transfer* 128 (Jan. 2019), pp. 892–933. ISSN: 00179310. DOI: 10.1016/j.ijheatmasstransfer.2018.09.026. URL: https://linkinghub.elsevier.com/retrieve/pii/S0017931018330321 (visited on 03/17/2023).

[7] Theron D. Marshall, Dennis L. Youchison, and Lee C. Cadwallader. "Modeling the Nukiyama Curve for Water-Cooled Fusion Divertor Channels". In: *Fusion Technology* 39.2 (Mar. 2001), pp. 849–855. ISSN: 0748-1896. DOI: 10.13182/FST01-A11963345. URL: https://www.tandfonline.com/doi/full/10.13182/FST01-A11963345 (visited on 08/12/2022).

[8] Yunus A. Çengel and Afshin J. Ghajar. *Heat and mass transfer: fundamentals and applications*. Fifth edition. OCLC: ocn870517093. New York, NY: McGraw Hill Education, 2015. 968 pp. ISBN: 978-0-07-339818-1 978-1-259-17330-1 978-981-4595-27-8.

[9] Warren M. Rohsenow, J. P. Hartnett, and Young I. Cho, eds. *Handbook of heat transfer*. 3rd ed. McGraw-Hill handbooks. New York: McGraw-Hill, 1998. 1 p. ISBN: 978-0-07-053555-8.

[10] A S Moita, E Teodori, and A L N Moreira. "Influence of surface topography and wettability in the boiling mechanisms". In: (2011), p. 15.

[11] Ashok K. Dewangan et al. "Pool boiling heat transfer on a plain tube in saturated R-134a and R-410A". In: *Heat and Mass Transfer* 56.4 (Apr. 2020), pp. 1179–1188. ISSN: 0947-7411, 1432-1181. DOI: 10.1007/s00231-019-02779-8. URL: http://link.springer.com/10.1007/s00231-019-02779-8 (visited on 10/19/2022).

[12] Andreu Alonso Acu. "Saturation temperature effects on heat transfer performance of a falling film evaporator using enhanced tubes". In: (2011), p. 100.

[13] Jinping Liu et al. "Hierarchical nanostructures of cupric oxide on a copper substrate: controllable morphology and wettability". In: *Journal of Materials Chemistry* 16.45 (2006), p. 4427. ISSN: 0959-9428, 1364-5501. DOI: 10.1039/b611691d. URL: http://xlink.rsc.org/?DOI=b611691d (visited on 07/24/2022).

[14] Batikan Köroğlu, Kee Sung Lee, and Chanwoo Park. "Nano/micro-scale surface modifications using copper oxidation for enhancement of surface wetting and falling-film heat transfer". In: *International Journal of Heat and Mass Transfer* 62 (July 2013), pp. 794–804. ISSN: 00179310. DOI: 10.1016/j.ijheatmasstransfer.2013.03.040. URL: https://linkinghub.elsevier.com/retrieve/pii/S0017931013002470 (visited on 08/14/2022).

[15] C.S. Sujith Kumar, Yao Wen Chang, and Ping-Hei Chen. "Effect of heterogeneous wettable structures on pool boiling performance of cylindrical copper surfaces". In: *Applied Thermal Engineering* 127 (Dec. 2017), pp. 1184–1193. ISSN: 13594311. DOI: 10.1016/j.applthermaleng.2017.08.069. URL: https://linkinghub.elsevier.com/retrieve/pii/S1359431117326893 (visited on 01/27/2023).

[16] Wieland. *GEWA-B*. 2022. URL: https://www.wieland.com/en/Media/Files/brochures/gewa-b.pdf.

[17] Wieland. "LOW FINNED TUBES GEWA-K, GEWA-KS". In: (2022), p. 12.

[18] Anil S. Katarkar et al. "Experimental investigation of pool boiling heat transfer performance of refrigerant R-134a on differently roughened copper surfaces". In: *Materials Today: Proceedings* 47 (2021), pp. 3269–3275. ISSN: 22147853. DOI: 10.1016/j.matpr.2021.06.452. URL: https://linkinghub.elsevier.com/retrieve/pii/S221478532104846X (visited on 07/06/2022).

[19] JE Myers and DL Katz. "Boiling coefficients outside horizontal tubes". In: Chemical Engineering Progress Symposium Ser 49.5 (1953).

[20] Dongsoo Jung, Kwangyong An, and Jinseok Park. "Nucleate boiling heat transfer coefficients of HCFC22, HFC134a, HFC125, and HFC32 on various enhanced tubes". In: *International Journal of Refrigeration* 27.2 (Mar. 2004), pp. 202–206. ISSN: 01407007. DOI: 10.1016/S0140-7007(03)00124-5. URL: https://linkinghub.elsevier.com/retrieve/pii/S0140700703001245 (visited on 07/29/2022).

[21] Albin Joseph et al. "An experimental investigation on pool boiling heat transfer enhancement using sol-gel derived nano-CuO porous coating". In: *Experimental Thermal and Fluid Science* 103 (May 2019), pp. 37–50. ISSN: 08941777. DOI: 10.1016/j.expthermflusci.2018.12.033. URL: https://linkinghub.elsevier.com/retrieve/pii/S0894177718306368 (visited on 01/27/2023).

[22] Mathieu Habert. *Falling film evaporation on a tube bundle with plain and enhanced tubes*. EPFL, 2009.

[23] Dwight Cooke and Satish G. Kandlikar. "Pool Boiling Heat Transfer and Bubble Dynamics Over Plain and Enhanced Microchannels". In: *ASME 2010 8th International Conference on Nanochannels, Microchannels, and Minichannels: Parts A and B*. ASME 2010 8th International Conference on Nanochannels, Microchannels, and Minichannels collocated with 3rd Joint US-European Fluids Engineering Summer Meeting. Montreal, Quebec, Canada: ASMEDC, Jan. 1, 2010, pp. 163–172. ISBN: 978-0-7918-5450-1 978-0-7918-3880-8. DOI: 10.1115/FEDSM-ICNMM2010-31147. URL: https://asmedigitalcollection.asme.org/ICNMM/proceedings/ICNMM2010/54501/163/360586 (visited on 08/12/2022).

[24] Corey M. Kruse et al. "Enhanced pool-boiling heat transfer and critical heat flux on femtosecond laser processed stainless steel surfaces". In: *International Journal of Heat and Mass Transfer* 82 (Mar. 2015), pp. 109–116. ISSN: 00179310. DOI: 10.1016/j.ijheatmasstransfer.2014.11.023. URL: https://linkinghub.elsevier.com/retrieve/pii/S0017931014009958 (visited on 04/01/2023).

[25] J. R. Thome. *Enhanced Boiling Heat Transfer*. Hemisphere Publishing Corporation, 1990. ISBN: 0-89116-745-5. (Visited on 10/21/2022).

[26] Youngsuk Nam and Y. Sungtaek Ju. "A comparative study of the morphology and wetting characteristics of micro/nanostructured Cu surfaces for phase change heat transfer applications". In: *Journal of Adhesion Science and Technology* 27.20 (Oct. 2013), pp. 2163–2176. ISSN: 0169-4243, 1568-5616. DOI: 10.1080/01694243.2012.697783. URL: http://www.tandfonline.com/doi/abs/10.1080/01694243.2012.697783 (visited on 07/22/2022).

[27] Matthew J. Rau and Suresh V. Garimella. "Confined Jet Impingement With Boiling on a Variety of Enhanced Surfaces". In: *Journal of Heat Transfer* 136.10 (Oct. 1, 2014), p. 101503. ISSN: 0022-1481, 1528-8943. DOI: 10.1115/1.4027942. URL: https://asmedigitalcollection.asme.org/heattransfer/article/doi/10.1115/1.4027942/373225/Confined-Jet-Impingement-With-Boiling-on-a-Variety (visited on 08/14/2022).

[28] Xiangdong Li, Ivan Cole, and Jiyuan Tu. "A review of nucleate boiling on nanoengineered surfaces – The nanostructures, phenomena and mechanisms". In: *International Journal of Heat and Mass Transfer* 141 (Oct. 2019), pp. 20–33. ISSN: 00179310. DOI: 10.1016/j.ijheatmasstransfer.2019.06.069. URL: https://linkinghub.elsevier.com/retrieve/pii/S0017931019302601 (visited on 10/24/2022).

[29] C.S. Sujith Kumar et al. "Elucidating the mechanisms behind the boiling heat transfer enhancement using nano-structured surface coatings". In: *Applied Thermal Engineering* 137 (June 2018), pp. 868–891. ISSN: 13594311. DOI: 10.1016/j.applthermaleng.2018.03.092. URL: https://linkinghub.elsevier.com/retrieve/pii/S1359431117381073 (visited on 01/27/2023).

[30] Hee Seok Ahn, V. Sathyamurthi, and D. Banerjee. "Pool Boiling Experiments on a Nano-Structured Surface". In: *IEEE Transactions on Components and Packaging Technologies* 32.1 (Mar. 2009), pp. 156–165. ISSN: 1521-3331, 1557-9972. DOI: 10.1109/TCAPT.2009.2013980. URL: http://ieeexplore.ieee.org/document/4787051/ (visited on 10/24/2022).

[31] Tomoaki Kunugi, Katsumi Muko, and Masahiko Shibahara. "Ultrahigh heat transfer enhancement using nano-porous layer". In: *Superlattices and Microstructures* 35.3 (Mar. 2004), pp. 531–542. ISSN: 07496036. DOI: 10.1016/j.spmi.2004.04.002. URL: https://linkinghub.elsevier.com/retrieve/pii/S0749603604001338 (visited on 08/14/2022).

[32] Sangsoo Lee, Batikan Köroğlu, and Chanwoo Park. "Experimental investigation of capillary-assisted solution wetting and heat transfer using a micro-scale, porous-layer coating on horizontal-tube, falling-film heat exchanger". In: *International Journal of Refrigeration* 35.4 (June 2012), pp. 1176–1187. ISSN: 01407007. DOI: 10.1016/j.ijrefrig.2011.11.015. URL: https://linkinghub.elsevier.com/retrieve/pii/S0140700711002957 (visited on 08/14/2022).

[33] G Patel et al. "Experimental investigation on nucleate pool boiling heat transfer enhancement for nano-structured copper oxide coated heating surface". In: *Journal of Physics: Conference Series* 1240.1 (July 1, 2019), p. 012093. ISSN: 1742-6588, 1742-6596. DOI: 10.1088/1742-6596/1240/1/012093. URL: https://iopscience.iop.org/article/10.1088/1742-6596/1240/1/012093 (visited on 08/14/2022).

[34] Daniel Attinger et al. "Surface engineering for phase change heat transfer: A review". In: *MRS Energy and Sustainability* 1.1 (Jan. 2014), p. 4. ISSN: 2329-2229, 2329-2237. DOI: 10.1557/mre.2014.9. URL: http://link.springer.com/10.1557/mre.2014.9 (visited on 11/06/2022).

[35] Md Mahamudur Rahman and Matthew McCarthy. "Boiling Enhancement on Nanostructured Surfaces with Engineered Variations in Wettability and Thermal Conductivity". In: *Heat Transfer Engineering* 38.14 (Oct. 13, 2017), pp. 1285–1295. ISSN: 0145-7632, 1521-0537. DOI: 10.1080/01457632.2016.1242961. URL: https://www.tandfonline.com/doi/full/10.1080/01457632.2016.1242961 (visited on 08/14/2022).

[36] M. Cerza. "Nucleate boiling in thin falling liquid films". In: *Pool and External Flow Boiling*. ASME (1992).

[37] Pengfei Xu and Qiang Li. "Visualization study on the enhancement of heat transfer for the groove flat-plate heat pipe with nanoflower coated CuO layer". In: *Applied Physics Letters* 111.14 (Oct. 2, 2017), p. 141609. ISSN: 0003-6951, 1077-3118. DOI: 10.1063/1.4986318. URL: http://aip.scitation.org/doi/10.1063/1.4986318 (visited on 08/14/2022).

[38] Pu-Hang Jin et al. "Liquid film boiling on plain and structured tubular surfaces with and without hydrophobic coating". In: *International Communications in Heat and Mass Transfer* 125 (June 2021), p. 105284. ISSN: 07351933. DOI: 10.1016/j.icheatmasstransfer.2021.105284. URL: https://linkinghub.elsevier.com/retrieve/pii/S0735193321001780 (visited on 12/12/2022).

[39] Pulak Sen et al. "Pool Boiling Heat Transfer on a Micro-Structured Copper Oxide Surface with Varying Wettability". In: *Chemical Engineering & Technology* 45.5 (May 2022), pp. 808–816. ISSN: 0930-7516, 1521-4125. DOI: 10.1002/ceat.202100558. URL: https://onlinelibrary.wiley.com/doi/10.1002/ceat.202100558 (visited on 03/12/2023).

[40] Seontae Kim et al. "Effects of nano-fluid and surfaces with nano structure on the increase of CHF". In: *Experimental Thermal and Fluid Science* 34.4 (May 2010), pp. 487–495. ISSN: 08941777. DOI: 10.1016/j.expthermflusci.2009.05.006. URL: https://linkinghub.elsevier.com/retrieve/pii/S0894177709000806 (visited on 03/20/2023).

[41] Bo Feng, Keith Weaver, and G. P. Peterson. "Enhancement of critical heat flux in pool boiling using atomic layer deposition of alumina". In: *Applied Physics Letters* 100.5 (Jan. 30, 2012), p. 053120. ISSN: 0003-6951, 1077-3118. DOI: 10.1063/1.3681943. URL: http://aip.scitation.org/doi/10.1063/1.3681943 (visited on 03/20/2023).

[42] Ya-Qiao Wang et al. "Copper vertical micro dendrite fin arrays and their superior boiling heat transfer capability". In: *Applied Surface Science* 422 (Nov. 2017), pp. 388–393.

ISSN: 01694332. DOI: 10.1016/j.apsusc.2017.05.251. URL: https://linkinghub.elsevier.com/retrieve/pii/S0169433217316306 (visited on 03/20/2023).

[43] Wen-Tao Ji et al. "Falling film evaporation and nucleate pool boiling heat transfer of R134a on the same enhanced tube". In: *Applied Thermal Engineering* 147 (Jan. 2019), pp. 113–121. ISSN: 13594311. DOI: 10.1016/j.applthermaleng.2018.10.062. URL: https://linkinghub.elsevier.com/retrieve/pii/S1359431118336317 (visited on 07/06/2022).

[44] M. Cerza and V. Sernas. *Nucleate boiling in thermally developing and fully developed malinar falling water films*. 1988.

[45] Chuang-Yao Zhao et al. "Experimental investigations of R134a and R123 falling film evaporation on enhanced horizontal tubes". In: *International Journal of Refrigeration* 75 (Mar. 2017), pp. 190–203. ISSN: 01407007. DOI: 10.1016/j.ijrefrig.2016.12.013. URL: https://linkinghub.elsevier.com/retrieve/pii/S0140700716304261 (visited on 03/11/2023).

[46] Pu-Hang Jin et al. "Experimental study of falling film evaporation in tube bundles of doubly-enhanced, horizontal tubes". In: *Applied Thermal Engineering* 170 (Apr. 2020), p. 115006. ISSN: 13594311. DOI: 10.1016/j.applthermaleng.2020.115006. URL: https://linkinghub.elsevier.com/retrieve/pii/S1359431119363513 (visited on 03/11/2023).

[47] M. Belghazi, A. Bontemps, and C. Marvillet. "Filmwise condensation of a pure fluid and a binary mixture in a bundle of enhanced surface tubes". In: *International Journal of Thermal Sciences* 41.7 (June 2002), pp. 631–638. ISSN: 12900729. DOI: 10.1016/S1290-0729(02)01357-1. URL: https://linkinghub.elsevier.com/retrieve/pii/S1290072902013571 (visited on 10/17/2022).

[48] Ravi Kumar, H. K. Varma, and Bikash Moh. "Condensation of R-134a Vapor over Single Horizontal Circular Integral-Fin Tubes with Trapezoidal Fins". In: *Heat Transfer Engineering* 21.2 (Mar. 2000), pp. 29–39. ISSN: 0145-7632, 1521-0537. DOI: 10.1080/014576300271004. URL: https://www.tandfonline.com/doi/full/10.1080/014576300271004 (visited on 10/17/2022).

[49] M. Habert and J. R. Thome. "Falling-film evaporation on tube bundle with plain and enhanced tubes—Part I: Experimental results". In: *Experimental heat transfer* 23.4 (2010). Publisher: Taylor and Francis, pp. 259–280.

[50] J.-F. Roques and J. R. Thome. "Falling Films on Arrays of Horizontal Tubes with R-134a, Part II: Flow Visualization, Onset of Dryout, and Heat Transfer Predictions". In: *Heat Transfer Engineering* 28.5 (May 2007), pp. 415–434. ISSN: 0145-7632, 1521-0537.

DOI: 10.1080/01457630601163736. URL: http://www.tandfonline.com/doi/abs/10.1080/01457630601163736 (visited on 07/06/2022).

[51] Daniel Gstöhl. *Heat transfer and flow visualization of falling film condensation on tube arrays with plain and enhanced surfaces*. EPFL, 2004.

[52] United States Environmental Protection Agency. *Refrigerant Transition and Environmental Impacts /textbar US EPA*. May 12, 2022. URL: https://www.epa.gov/mvac/refrigerant-transition-environmental-impacts (visited on 08/14/2022).

[53] Gherhardt Ribatski and John R Thome. "A Visual Study of R134a Falling Film Evaporation on Enhanced and Plain Tubes". In: (2005), p. 13.

[54] Ryan Enright et al. "Condensation on Superhydrophobic Copper Oxide Nanostructures". In: *Journal of Heat Transfer* 135.9 (Sept. 1, 2013), p. 091304. ISSN: 0022-1481, 1528-8943. DOI: 10.1115/1.4024424. URL: https://asmedigitalcollection.asme.org/heattransfer/article/doi/10.1115/1.4024424/366655/Condensation-on-Superhydrophobic-Copper-Oxide (visited on 07/22/2022).

[55] Youngsuk Nam et al. "Characterization and Modeling of the Heat Transfer Performance of Nanostructured Cu Micropost Wicks". In: *Journal of Heat Transfer* 133.10 (Oct. 1, 2011), p. 101502. ISSN: 0022-1481, 1528-8943. DOI: 10.1115/1.4004168. URL: https://asmedigitalcollection.asme.org/heattransfer/article/doi/10.1115/1.4004168/470318/Characterization-and-Modeling-of-the-Heat-Transfer (visited on 08/14/2022).

[56] Kavita Sahu, Rahul Singhal, and Satyabrata Mohapatra. "Morphology Controlled CuO Nanostructures for Efficient Catalytic Reduction of 4-Nitrophenol". In: *Catalysis Letters* 150.2 (Feb. 2020), pp. 471–481. ISSN: 1011-372X, 1572-879X. DOI: 10.1007/s10562-019-03009-w. URL: http://link.springer.com/10.1007/s10562-019-03009-w (visited on 07/25/2022).

[57] MinSheng Liu, Mark ChingCheng Lin, and ChiChuan Wang. "Enhancements of thermal conductivities with Cu, CuO, and carbon nanotube nanofluids and application of MWNT/water nanofluid on a water chiller system". In: *Nanoscale Research Letters* 6.1 (Dec. 2011), p. 297. ISSN: 1556-276X. DOI: 10.1186/1556-276X-6-297. URL: https://nanoscalereslett.springeropen.com/articles/10.1186/1556-276X-6-297 (visited on 07/24/2022).

[58] Eric W. Lemmon, Marcia L. Huber, and Mark O. McLinden. "NIST reference fluid thermodynamic and transport properties–REFPROP". In: *NIST standard reference database* 23 (2002), p. v7.

[59] Ian H. Bell et al. "Pure and pseudo-pure fluid thermophysical property evaluation and the open-source thermophysical property library CoolProp". In: *Industrial and engineering chemistry research* 53.6 (2014). Publisher: ACS Publications, pp. 2498–2508.

[60] Nicola Casari, Michele Pinelli, and Alessio Suman. "Analysis of CoolProp library for the assessment of uncertainty propagation for refrigerant fluids in state diagrams and thermodynamic properties". In: *International Journal of Refrigeration* 107 (2019). ISSN: 0140-7007. URL: https://www.sciencedirect.com/science/article/pii/S0140700719303524.

[61] Jean-François Roques. *Falling film evaporation on a single tube and on a tube bundle*. EPFL, 2004.

[62] Copper Development Association Inc. *Copper.org - C12200 Alloy*. 2022. URL: https://alloys.copper.org/alloy/C12200 (visited on 10/15/2022).

[63] B.S. Petukhov. "Heat Transfer and Friction in Turbulent Pipe Flow with Variable Physical Properties". In: *Advances in Heat Transfer*. Vol. 6. Elsevier, 1970, pp. 503–564. ISBN: 978-0-12-020006-1. DOI: 10.1016/S0065-2717(08)70153-9. URL: https://linkinghub.elsevier.com/retrieve/pii/S0065271708701539 (visited on 10/15/2022).

[64] J. R. Thome. *Engineering data book 3*. Wolverine Tube Inc, 2004.

[65] Boqi Xiao et al. "Calculation of Active Nucleation Site Density in Boiling Systems". In: *Research Journal of Applied Sciences, Engineering and Technology* 6.4 (June 20, 2013), pp. 587–592. ISSN: 20407459, 20407467. DOI: 10.19026/rjaset.6.4168. URL: http://maxwellsci.com/jp/mspabstract.php?jid=RJASETanddoi=rjaset.6.4168 (visited on 10/24/2022).

[66] Wilhelm Nusselt. "Die oberflachenkondensation des wasserdamphes". In: *VDI-Zs* 60 (1916), p. 541.

[67] M. G. Cooper. "Saturated nucleate pool boiling-a simple correlation". In: *1st UK National Heat Transfer Conference, 1984*. 1984, pp. 785–793.

[68] V. H. Atlas. "VDI-Gesellschaft Verfahrenstechnik und Chemieingenieurwesen (GVC)". In: *Ch. Part D-Thermophysical Properties, ed: Springer-Verlag, Berlin/Heidelberg Germany* (2010), pp. 121–613.

[69] Wen-Tao Ji et al. "Experimental validation of Cooper correlation at higher heat flux". In: *International Journal of Heat and Mass Transfer* 90 (2015). Publisher: Elsevier, pp. 1241–1243.

[70] Houpei Li and Pega Hrnjak. "Heat transfer coefficient, pressure drop, and flow patterns of R1234ze(E) evaporating in microchannel tube". In: *International Journal of Heat*

and Mass Transfer 138 (Aug. 2019), pp. 1368–1386. ISSN: 00179310. DOI: 10.1016/j.ijheatmasstransfer.2019.05.036. URL: https://linkinghub.elsevier.com/retrieve/pii/S001793101836321X (visited on 07/14/2022).

[71] Dieter Gorenflo et al. "Prediction methods for pool boiling heat transfer: A state-of-the-art review". In: *International Journal of Refrigeration* 43 (July 2014), pp. 203–226. ISSN: 01407007. DOI: 10.1016/j.ijrefrig.2013.12.012. URL: https://linkinghub.elsevier.com/retrieve/pii/S0140700713003915 (visited on 07/14/2022).

[72] Uzair Sajjad, Imtiyaz Hussain, and Chi-Chuan Wang. "A high-fidelity approach to correlate the nucleate pool boiling data of roughened surfaces". In: *International Journal of Multiphase Flow* 142 (Sept. 2021), p. 103719. ISSN: 03019322. DOI: 10.1016/j.ijmultiphaseflow.2021.103719. URL: https://linkinghub.elsevier.com/retrieve/pii/S0301932221001671 (visited on 07/14/2022).

[73] E. van Rooyen, M. Christians, and J. R. Thome. "Modified Wilson Plots for Enhanced Heat Transfer Experiments: Current Status and Future Perspectives". In: *Heat Transfer Engineering* 33.4 (Mar. 2012), pp. 342–355. ISSN: 0145-7632, 1521-0537. DOI: 10.1080/01457632.2012.611767. URL: http://www.tandfonline.com/doi/abs/10.1080/01457632.2012.611767 (visited on 10/22/2022).

[74] Ralph L. Webb and Christopher Pais. "Nucleate pool boiling data for five refrigerants on plain, integral-fin and enhanced tube geometries". In: *International Journal of Heat and Mass Transfer* 35.8 (Aug. 1992), pp. 1893–1904. ISSN: 00179310. DOI: 10.1016/0017-9310(92)90192-U. URL: https://linkinghub.elsevier.com/retrieve/pii/001793109290192U (visited on 07/17/2022).

[75] M. C. Chyu, J. Zheng, and Z. Ayub. "Bundle effect of ammonia/lubricant mixture boiling on a horizontal bundle with enhanced tubing and inlet quality". In: *International Journal of Refrigeration* 32.8 (2009), pp. 1876–1885.

[76] M.C. Chyu and A. Bergles. "Horizontal-tube falling-film evaporation with structured surfaces". In: *Journal of Heat Transfer* 111.2 (1989), pp. 518–524.

[77] M. Cerza and V. Sernas. "A bubble growth model for nucleate boiling in thin, falling, superheated, laminar, water films". In: *International Journal of Heat and Mass Transfer* 28.7 (July 1985), pp. 1307–1316. ISSN: 00179310. DOI: 10.1016/0017-9310(85)90161-9. URL: https://linkinghub.elsevier.com/retrieve/pii/0017931085901619 (visited on 10/31/2022).

[78] A. Salih. *Dimensionless Numbers*. 2022. URL: https://www.iist.ac.in/sites/default/files/people/numbers.html.

[79] Mirza M. Shah. "Prediction of heat transfer in evaporation of saturated falling films on bundles of horizontal tubes". In: *International Journal of Refrigeration* 131 (Nov. 2021), pp. 416–425. ISSN: 01407007. DOI: 10.1016/j.ijrefrig.2021.07.004. URL: https://linkinghub.elsevier.com/retrieve/pii/S0140700721002760 (visited on 07/06/2022).

[80] Mirza M. Shah. "Prediction of heat transfer in evaporation of saturated falling films on bundles of horizontal tubes". In: *International Journal of Refrigeration* 131 (Nov. 2021), pp. 416–425. ISSN: 01407007. DOI: 10.1016/j.ijrefrig.2021.07.004. URL: https://linkinghub.elsevier.com/retrieve/pii/S0140700721002760 (visited on 08/14/2022).

[81] E. van Rooyen and J.R. Thome. "Flow boiling data and prediction method for enhanced boiling tubes and tube bundles with R-134a and R-236fa including a comparison with falling film evaporation". In: *International Journal of Refrigeration* 41 (May 2014), pp. 60–71. ISSN: 01407007. DOI: 10.1016/j.ijrefrig.2013.03.016. URL: https://linkinghub.elsevier.com/retrieve/pii/S0140700713000716 (visited on 08/12/2022).

[82] E. van Rooyen and J.R. Thome. "Flow boiling data and prediction method for enhanced boiling tubes and tube bundles with R-134a and R-236fa including a comparison with falling film evaporation". In: *International Journal of Refrigeration* 41 (May 2014), pp. 60–71. ISSN: 01407007. DOI: 10.1016/j.ijrefrig.2013.03.016. URL: https://linkinghub.elsevier.com/retrieve/pii/S0140700713000716 (visited on 08/12/2022).

[83] Chuang-Yao Zhao et al. "Heat transfer correlation of the falling film evaporation on a single horizontal smooth tube". In: *Applied thermal engineering* 103 (2016). Publisher: Elsevier, pp. 177–186.

[84] Sumit Raj et al. "An analytical model for predicting growth rate and departure diameter of a bubble in subcooled flow boiling". In: *International Journal of Heat and Mass Transfer* 109 (2017), pp. 470–481. ISSN: 0017-9310. URL: https://www.sciencedirect.com/science/article/pii/S0017931016323377.

[85] Shoukat Alim Khan, Nurettin Sezer, and Muammer Koç. "Design, synthesis, and characterization of hybrid micro-nano surface coatings for enhanced heat transfer applications". In: *International Journal of Energy Research* 44.15 (Dec. 2020), pp. 12525–12534. ISSN: 0363-907X, 1099-114X. DOI: 10.1002/er.5685. URL: https://onlinelibrary.wiley.com/doi/10.1002/er.5685 (visited on 01/27/2023).

[86] Marelize Everts. *Course on Experimental Uncertainty Analysis*. University of Pretoria, 2022.

[87] S I Abu-Eishah. "Correlations for the Thermal Conductivity of Metals as a Function of Temperature". In: (2000), p. 14.

[88] *Normal Distribution*. 2022. URL: https://www.mathsisfun.com/data/standard-normal-distribution.html (visited on 10/16/2022).

[89] *NIST TN 1297: Appendix A. Law of Propagation of Uncertainty /textbar NIST*. URL: https://www.nist.gov/pml/nist-technical-note-1297/nist-tn-1297-appendix-law-propagation-uncertainty (visited on 10/16/2022).

[90] *Water - Ionization Constant, $pK_{/textrmw}$, of Normal and Heavy water*. URL: https://www.engineeringtoolbox.com/ionization-dissociation-autoprotolysis-constant-pKw-water-heavy-deuterium-oxide-d_2004.html (visited on 07/22/2022).

[91] E. E. Wilson. "A basis for rational design of heat transfer apparatus". In: 37.47 (1915), pp. 47–82.

[92] D. E. Briggs and E. H. Young. "Modified wilson plot techniques for obtaining heat transfer correlations for shell and tube heat exchangers". In: *Chemical Engineering Progress Symposium Series*. AIChE 65.92 (1969), pp. 35–45.

[93] J.-F. Roques and J. R. Thome. "Falling films on arrays of horizontal tubes with R-134a, part I: boiling heat transfer results for four types of tubes". In: *Heat transfer engineering* 28.5 (2007). Publisher: Taylor and Francis, pp. 398–414.

[94] *Possible reasons for decrease in HTC on CuO nanocoatings*. In collab. with J. R. Thome. 2022.

[95] Nilanjana Basu, Gopinath R. Warrier, and Vijay K. Dhir. "Onset of Nucleate Boiling and Active Nucleation Site Density During Subcooled Flow Boiling". In: *Journal of Heat Transfer* 124.4 (Aug. 1, 2002), pp. 717–728. ISSN: 0022-1481, 1528-8943. DOI: 10.1115/1.1471522. URL: https://asmedigitalcollection.asme.org/heattransfer/article/124/4/717/459991/Onset-of-Nucleate-Boiling-and-Active-Nucleation (visited on 10/24/2022).

[96] Robert Kaniowski et al. "Bubble departure diameter determination for pool boiling on surface with microchannels". In: *E3S Web of Conferences* 70 (2018). Ed. by T. Kujawa, A.A. Stachel, and Z. Zapałowicz, p. 02008. ISSN: 2267-1242. DOI: 10.1051/e3sconf/20187002008. URL: https://www.e3s-conferences.org/10.1051/e3sconf/20187002008 (visited on 10/24/2022).

[97] *surface tension /textbar Definition, Examples, and Facts /textbar Britannica*. URL: https://www.britannica.com/science/surface-tension (visited on 10/24/2022).

[98] S. P. Fisenko. "Boiling on a Substrate. Critical Size of the Bubble". In: *Journal of Engineering Physics and Thermophysics* (Oct. 28, 2022). ISSN: 1062-0125, 1573-871X. DOI: 10.1007/s10891-022-02579-8. URL: https://link.springer.com/10.1007/s10891-022-02579-8 (visited on 11/06/2022).

Appendix A:
Automatic Liquid Level Controller

As pool boiling takes place, phase change occurs and the liquid level drops from the vapour leaving the testing chamber. The drop in liquid level height was then compensated with liquid feed. The liquid feed flow rate was controlled by the calculated liquid level height, which was obtained from the hydrostatic equation approach seen in equations (A.1) and (A.2):

$$P_{bottom} = \rho_r \cdot g \cdot H_{liq} + P_{top} \tag{A.1}$$

$$H_{liq} = \frac{P_{bottom} - P_{top}}{\rho_r \cdot g} \tag{A.2}$$

It was found that the control command was very abrupt if the raw pressure data was used. The pressure data contains noise, making it very difficult for precise and responsive control.

A spectral analysis was performed on the data through a Fast Fourier Transform (FFT). A 1st order Butterworth signal filter was herewith designed with a cutoff frequency of 45 Hz for the top pressure transducer and a cutoff frequency of 60 Hz for the bottom pressure transducer so as not to cause significant lag on the signals, nor neglect the valuable information in the signals. The Butterworth filter was implemented in the LabVIEW software by prescribing the Butterworth filter as an Infinite Impulse Response (IIR) filter with forward and reverse coefficients pertaining to the behaviour of the designed filter. These filters removed the noise so that the pressure signal data could successfully be used to control the liquid level height. The performance of the Butterworth filter compared to the noisy raw signal was shown in Figure A.1:

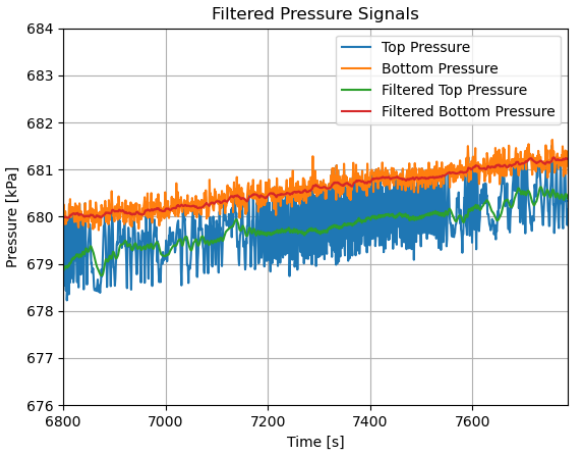

Figure A.1: Comparison of the filtered pressure signals and the noisy raw pressure signal

A PID controller was coded to use this liquid level value compared to a reference desired liquid level height to send a command to the variable speed drive pump to control the feed to the chamber with refrigerant and thus control the liquid level height. The principle was described

by equation (A.3):

$$E = H_{desired} - H_{liq} \tag{A.3}$$

The error value E was then used as an input to the PID controller to govern the variable speed drive. This filtering was only used on the live signal. Recorded data did not use this filter and instead averaged out the noise across numerous data points.

Appendix B: Calibration Procedures

B.1 General Calibration Approach

The laboratory's reference devices used to calibrate all the other sensors are the interstitial step between calibrating the FF rig's sensors to the perfect standard values. This 2-step procedure is described below:

The reference device is taken to an accredited calibration establishment to calibrate the reference sensor to the international standard by equation (B.4):

$$y_{std} = m_1 \cdot y_{ref} + c_1 \tag{B.4}$$

The calibrated reference device from equation (B.4) is then only used to calibrate the relevant sensors around the FF rig according to equation (B.5):

$$y_{ref} = m_2 \cdot y_{sensor} + c_2 \tag{B.5}$$

To define the authenticity of the reference sensor in relation to the standard (as described in (B.4)), a calibration certificate is always issued by the calibrator to specify the deviations at the calibration points and hereby provides the reference-standard bias, β.

The precision of the calibrated sensor related to the reference sensor can then be determined from its deviation to the reference using the statistical standard deviation,σ_z, of the difference between the sensor value and the reference value (attained from observing equation (B.5)), along with the student's t variable of $t = 1.96$ to incur a 95% confidence interval upon uncertainty calculations.

Using theory presented by Everts [86], the uncertainty value of the sensor used in the FF rig for uncertainty calculations can then be obtained from equation (B.6):

$$\delta z = \sqrt{\beta^2 + (\sigma_z \cdot t)^2} \tag{B.6}$$

The explained principle is used to find the uncertainty of each sensor as δz from above and then used to populate the uncertainty Table C.1 in section 4.13.

B.2 General Thermocouples

The steel sheathed K-type thermocouples in the FF rig are calibrated towards a *LAUDA Digical DCS2* digital thermometer which has 2 PT100 probes. The digital thermometer had been taken to NMISA where the thermometer had been calibrated within 0.01 K of the standard. The thermocouples from the FF rig are placed in a *LAUDA Proline* thermal bath where the water is circulated until the readings from the 2 thermometer probes are within 0.01°C before the calibration point is sampled. The same FF rig NI system is used along with a specialized VI which communicates with the thermal bath and the thermometer through serial connections to

perform the calibration.

The procedure follows to calibrate the thermocouples from 5°C to 50°C in steps of 5°C, going up and going down. After each setpoint is reached, a set 30 minute stabilization time is required before sampling may be triggered.

The thermocouple rod's thermocouples are fixated inside the thermocouple rod. They hereby require a calibration rig shown in the schematic of Figure B.2 in which the thermocouple rods are stuck to be exposed to the thermal bath water (2 thermocouple rods need to be calibrated at the same time):

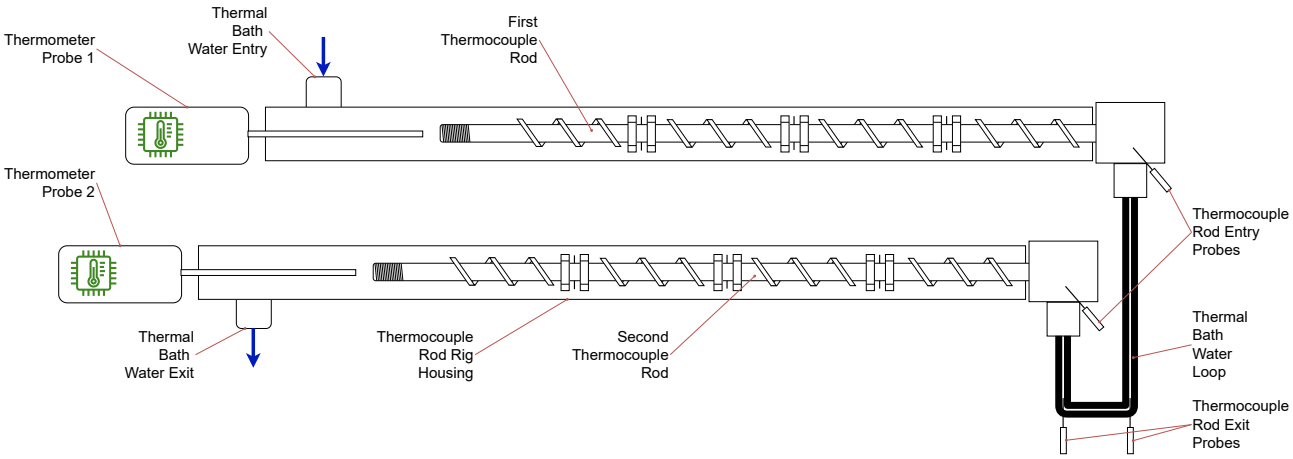

Figure B.2: Thermocouple rod calibration rig

The thermal bath water is passed through to circulate the calibration rig as shown in Figure B.2. The digital thermometer probes are stuck in each of the thermocouple rod housing pipes to measure the difference between the entry and exit thermal bath water, which are also the points furthest from each other with respect to the traveling path of the water. The entry and exit thermocouple rod probes are also an optional addition to the calibration and are inserted into the loop and at the thermocouple rod as shown. The same procedure to the calibration of the removable thermocouples then apply as described above.

The following procedure is used for the calibration of the thermocouples around the Falling Film Rig. The thermocouples surrounding the testing chamber should be calibrated most often while judgement should be used to when the other thermocouples should be tested. The thermocouples are all simultaneously recorded in the LAUDA Proline thermal bath and again using the Measure PC.

To calibrate the test chamber thermocouples:

1. Following the procedure from the above pressure transducer calibration, isolate the testing chamber and evacuate the refrigerant so that the relevant thermocouples can be removed. Make sure that when each thermocouple is removed that its insertion depth is recorded, for when they are replaced,they have to be inserted the same depth as before.
2. Each thermocouple has its own locking nut type. Some are male and some are female. Take care to keep them safe to replace them later.

3. Place all the thermocouples in the thermal bath, by suspending them in the water by sticking them in some insulation used as a lid on the bath. Make sure that they are all in one line.
4. Adjust the flow screw on the right side of the LAUDA Thermal bath by the terminal for internal flow, so that the water is mixed inside of the bath.
5. Stick both LAUDA Digical DCS2 Digital Thermometer probes on either side of the line of thermocouples through the insulation. Also make sure that they are properly suspended in the water. Let nothing touch the sides of the thermal bath.
6. Connect the LAUDA Thermal bath to the Measure PC with a data cable via USB.
7. Connect the LAUDA Digical DCS2 Thermometer to the Measure PC with a data cable via USB.
8. **Do not to enter the calibration menu of the Digical!** This erases previous calibrations.
9. Enter the menu of the Digical and enable the 'print' setting.
10. Using the same procedure as with the pressure transducer calibration, copy and create new versions of the latest 'def_array' and the 'used_probes' files, where all the thermocouples in the thermal bath to be calibrated are listed in the 'used_probes' file.
11. Open the thermometer calibration LabVIEW VI, which contains the 'Proline Bath' in its name and insert the file paths of the new 'def_array' and the 'used_probes' files.
12. Follow the on-screen settings for the automated calibration. The setting should be that the stability countdown trigger is 0.1 K and that the calibration threshold is 0.01 K. The calibration temperature range is usually done from 5°C to 50°C in steps of 5°C.
13. If there is no communication between the Measure PC and the Thermal Bath or the Digital Thermometer, go into the LabVIEW terminal and find the 'COM' line. Change it until data transmission is active.
14. After the long calibration session (may last approximately 10 hours), the same polynomial calibration fit VI appears for each thermocouple probe calibrated. Do the same MSE judgement and accept the calibration coefficients as described in the above pressure transducer calibration procedure.
15. Store all the equipment and then re-insert all the thermocouples, inserting them all back up to their previous depth. Also remember each thermocouples locking nut.
16. Do the same gas evacuation as described in the pressure transducer calibration procedure, so that all gas is removed from the isolated testing chamber and to keep the refrigerant pure. The valves may be opened again after this procedure.

B.3 Thermocouple Rods

The calibration of the thermocouples encased in the thermocouple rods (shafts) is done similarly to the calibration of the general thermocouples as described above. During the calibration of the thermocouple rods, 2 rods are calibrated simultaneously. The same LabVIEW VI is used which interfaces with the LAUDA Proline Thermal Bath and the LAUDA DCS2 Digital Thermometer as was used for the general thermocouples.

The only addition to the procedure is the use of the thermocouple rod calibration rig. The thermocouple rods are placed in this rig where water is passed from the thermal bath through the entry point of the calibration rig, then passes through one rod pipe to pass to the other pipe through a loop on the other side. The water then eventually passes through the pipe of the other thermocouple rod to reach the thermal bath again. The digital thermometer probes are inserted at the entry and exit points of the calibration rig as shown in Figure B.2.

Do the following for the setup of the thermocouple rod calibration rig:

1. Make sure the testing water is drained out of the Falling Film Rig. This is done by opening the air vent valve (red valve) at the top, the water fill side valve (with the filling line uncoupled from the tap) and opening the drain valve attached to the manifold by the rotameters (green valve).
2. Fix the two short aluminium tectra supports to the side rail of the Falling Film Rig (right next to the testing chamber). The calibration rig is to be laid down on these supports. The rig is therefore parallel to the FF Rig raised walkway space. Cable tie the calibration rig to the supports, as the rig must be securely fastened for it not to fall off when worked on. When positioning the rig, make sure that you are able to insert the thermocouple rods from the right side (the steel cabinet side). Note that 2 thermocouple rods are required to be calibrated during the session.
3. The thermocouple rods interface with the calibration rig through two stainless steel inserts. Place new O-rings on the steel inserts and then push these steel inserts into the calibration rig (they are very difficult to get in). These steel inserts acts as adapters to enable the thermocouple rods to slide over them to be inserted into the calibration rig. Insert the rods into the calibration rig using the stainless steel inserts as interfacing adapters.
4. Insert the appropriate exit water thermocouples in at the bottom of this loop pipe.
5. Removing a thermocouple rod from the testing chamber must be done carefully. Facing the testing chamber from the front, see that there is a securing nut on the left of the thermocouple rod, which ensures the two ends of the thermocouple rod do not come loose. Remove this nut (use an Allen Key or spanner dependent on the end of it if you are unable to get it off by hand). Then carefully unplug the short left side hose, remember that there is a thermocouple on that short pipe which needs to be added to the thermocouple rod calibration rig. Carefully unplug the right pipe from the testing tube and slide out the thermocouple rod. Be careful to not let the copper tube move, as refrigerant might leak out if the O-ring is disturbed.
6. Remove the plastic water pipes from the thermocouple rods by unscrewing the pipe clamps.
7. Attach the calibration rig's short water pipe to the points of the thermocouple where their water pipes normally attach to that was removed in step 6.
8. Attach the calibration rig's long water hose pipes at the other end to the thermal bath.
9. Make sure the thermal bath setting is so that the external circulation is used.

10. Carefully insert the two LAUDA Digital Thermometer probes into the ends where the water pipes come out of. The Digical interfaces with the rig using 2 sealing plates per Digical probe. Placing the 2 correct size O-rings on both sides of the seating plates, then have the flat plates on top on the outside of these seating plates with the thermometer probes going through both of them. This whole unit is then inserted into the holes where the thermocouple rods are housed. The units are then secured in place with bolts. Ensure not to bend the thermometer probes when fastening the bolts.
11. The calibration rig setup is complete. The 'General Thermocouples' procedure can now normally be used for the calibration of the Thermocouple Rods.

B.4 Pressure Transducers

The test chamber accommodates 2 *Endress+Hauser PMC 731* pressure transducers that are rated from 0 bar to 10 bar, as seen in Figure 3.5. These transducers have a factory specification of 0.1% error across all its readings [1].

These pressure transducers are individually calibrated from 100 kPa to 700 kPa (absolute) in steps of 100 kPa going up and down. The pressure transducers are removed from the rig's test chamber (but remained electronically connected to the FF rig's NI system) and attached to a mobile hand operated calibration kit where the pressure is controlled by a *WIKA CPP 30* pneumatic pump. The transducers are calibrated towards a *WIKA CPT 6400* reference pressure transducer which has a specified 0.025% uncertainty over a full measuring range. An uncertainty of 0.25 kPa is accepted since this was calculated over the full operating range of the sensor. There is no direct interface with the calibration kit and the Measure PC, so the reference measurement at each calibration point is read from a *WIKA CPH 6400* handheld display that accompanies the reference transducer [1].

Signal noise is displayed by the indicator and makes it arduous to select a value to enter into the Measure PC to calibrate at that point. The steady state minimum and maximum at the pressure point is used to obtain the average reference pressure that is then served to the Measure PC for comparison with the readings from the pressure transducers. This method proved to be very effective. At higher pressures, approximately 400 kPa and above, the readings would fluctuate erratic (and would steadily decrease over time) so as not to be able to settle on a value to enter. Herewith, the most stable value at high pressures was found to be the short-term minimum after the pressure was pumped (or released) to the calibration point. This minimum is served to the Measure PC to calibrate accordingly. The approach described above to calibrate both test chamber pressure transducers proved to be adequate upon post-calibration check.

The following procedure is for calibrating the pressure transducers. There are 2 pressure transducers used in the Falling Film Rig. Both of the display units are situated at the top of the testing chamber. The middle pressure transducer (between the two main transducers) is not in use, and is redundant in normal operation. It is a vacuum pressure transducer used when vacuuming. The two pressure transducers measure the pressures at the top and the bottom of

the testing chamber. The following guide should be used to calibrate the pressure transducers relative to the Thermoflow Laboratory reference transducer:

1. Obtain the WIKA reference pressure transducer from the Laboratory Manager. This unit is specially made for the calibration of the pressure transducers around the Thermoflow Laboratory. The WIKA reference pressure transducer is in a secure case and has a hand pump attachment.
2. Using the imperial spanners, close the relevant valves around the test chamber to isolate the test chamber from the rest of the falling film rig. Close the valve on the front and back of the test chamber on the side vapour line. Close the valve at the bottom of the test chamber on the liquid return line. There are two refrigerant liquid inlet valves at the top of the test chamber on either side. Close the red turn valve on the one end, and use a spanner to close the valve on the other end. Close the three large valves on the three large top vapour lines at the top of the test chamber. These are accessible from the back of the test chamber.
3. After all the valves are closed, the decision can be made to either salvage the little refrigerant that is contained in the isolated test chamber, or to waste the refrigerant inside (note that there is not a significant amount contained in the chamber since it is in gas form). Remove the cap of the schrader valve on the liquid drain line at the bottom of the test chamber and attach a small pressure hose with the red turn valve to it. From there the gas can slowly be leaked out with the red valve.
4. To remove the transducer, there is a frame attachment plate which needs to be screwed loose. The transducer should then be loose from the testing chamber. Loosen the large hex adapter fitting which enables the transducer and the pipe end to be connected securely.
5. Be careful because there is a copper sealing washer lying in the hex adapter fitting. It should be annealed by heating it up using a mini gas blow torch just until it turns red. Leave the washer to slowly cool down in the open air, whereafter the flat surfaces could be sanded with fine grit sandpaper before placing it back in the large hex adapter.
6. Move the pressure transducer to the aluminium supporting beam at the bottom of the test chamber and fix it there using the attachment plate, so that all the leads and cables can reach and so that the displays can be seen.
7. Screw the WIKA reference transducer's large hex adapter adapter to the bottom of the pressure transducer.
8. Attach the small hand pump pressure chamber pressure hose of the WIKA reference transducer to the large hex nut which is now fastened to the pressure transducer.
9. Screw the electronic WIKA reference transducer to the hand pump.
10. Connect the WIKA reference transducer to its readout display with its electronic data cable. The correct pressure can now be read from the WIKA handheld device's display, from where the calibration will be done.
11. The pressure is increased in the small pressure chamber of the hand held pump by compressing the handle and the pressure is relieved by turning the outlet valve on the side

(the other knob is for fine tuning of pressure - which is seldomly required to be done).

12. The calibration procedure is performed by stepping the pressure up from 1 bar to 7 bar in steps of 1 bar; and then the pressure is released in steps of 1 bar from 7 bar to 1 bar. Always be careful not to adjust the pressure to the other way in the given increasing or decreasing pressure stage.
13. On the Measure PC, there are 2 text files of relevance to this calibration procedure. Wherever applicable, ensure that the same formatting is kept as the previous for the correct functioning of the programs. The first used_probes text file describes the probe number used (should be 421 and 422 in the calibration of the bottom and top pressure transducer respectively). The other def_array text file is the rolling calibration coefficient definition matrix that is updated upon with calibration. Copy these files and create new versions of them to be updated by the calibration. The latest updated definition matrix file should always be used.
14. Use the 'Check Calibration' LabVIEW VI to do the initial diagnosis before calibration at a few pressures before the calibration. This will compare the existing calibration to the reference points. If there is a large difference, it means that previous testing data might need to be discarded.
15. Use the 'Singular Calibration' LabVIEW VI, where the used probe and the definition matrix is referenced and then the high, low, units, steps and number of calibration point settings are adjusted (for example: 700 kPa, 100 kPa, kPa, 100 kPa, 13). 'Start' the calibration on the VI after these settings have been set. The goal is to pump the handpump to the closest possible pressure points between 1 bar and 7 bar in steps of 1 bar and then release the pressure from the high point back down to 1 bar. Note that this up and down trend is done in one take. Use the setting on the reference digital display to display as many decimal digits as possible. The values change rapidly due to small leaks and good judgement should be used to decide on the average reference pressure to be used. If the pressure drops too quickly, the leaks will need to be fixed. A good guideline is to use the high and low values and average them after they have somewhat settled. Input the reference value in the relevant block on the VI and then click the calibration button to record. Move on to the next set point until complete. After the last set point is recorded and saved in the def_array file, the calibration is complete, a window will appear where the polynomial fit is chosen. Use judgement from the previous calibration polynomial degree and the MSE (Mean Square Error) to judge success. Follow the on-screen instructions to saving the updated definition matrix, as well as the session test datapoints of the probe during the calibration.
16. Use the 'Check Calibration' LabVIEW VI again after the calibration at a few pressures to deduce if the calibration was a success and whether there was an improvement upon the previous calibration prescription. The calibrated pressure should match the reference pressure to within the quoted uncertainty less the reference probe uncertainty.
17. Follow the relevant steps above if the other pressure transducer is also to be calibrated

before continuing on below.

18. Disassemble everything and return the WIKA reference pressure transducer to the Thermoflow Laboratory Manager.
19. Replace the copper annealed and sanded sealing ring in the original large hex nut (see step 5).
20. Assemble the pressure transducer back at the top of the test chamber, by also replacing the previously annealed copper washer and using the original large hex adapter nut by which the pressure sensor connects to the leading pipe and to which the smaller nut sliding over the leading pipe fastens.
21. It is now critical that the chamber is evacuated of air for the conservation of the purity of the refrigerant. Attach the vacuum pump (obtained from the Thermoflow Laboratory Manager) to the hose previously attached to the schrader valve at the bottom of the testing chamber.
22. Switch the vacuum pump on and leave it until a conventional absolute pressure of 100 Pa is reached. This may take some time.
23. Close the inline red valve on the hose attached to the vacuum pump.
24. Switch the vacuum pump off and return it to the Laboratory Manager. Leave the hose with the red valve attached to the schrader valve. It is important to realise that with a system under negative gauge pressure that an uncapped schrader valve will plunge inward and the chamber will suck in air.
25. Slowly open all the valves again that were closed at the beginning of the calibration procedure allowing refrigerant from the rest of the system to fill the test chamber.
26. When stable pressure is reached, the hose with the red inline valve may be removed. The pressure transducer is now calibrated.

B.5 Coriolis Mass Flow Meters

The mass flow rates of the glycol, testing water and the refrigerant were measured with *KROHNE CORIMASS MFM4085* coriolis mass flow meters. The testing water and glycol line have high flow rate norms and thus the 100 G model meter is used for both, whereas the refrigerant flow rate has a lower norm and thereby the 10 G model meter is used. These meters are calibrated by the manufacturer and their calibration coefficients cannot be modified. The zero point settings can be re-adjusted by closing the valves to ensure stationary fluid in the meters and instructing the zero point capture for correct orientation.

With these specific meters, the Measure PC's reading of the signal outputs from the coriolis mass flow meters is calibrated through its LabVIEW VI, incorporating the full NI systems setup, to reflect the measurement as displayed on the coriolis mass flow meters themselves. The calibration range of the 100 G model is 0 kg/s to 1.6 kg/s, whereas the 10 G model was calibrated in a range of 0 kg/s to 0.22 kg/s [1]. All coriolis flow meters operate on a 4 mA to 20 mA electric current as a communication signal to which the Measure PC is calibrated to (4 mA would represent 0 kg/s in all cases).

The 100 G model coriolis flow meter for the testing water was submitted to KROHNE for a verification check and certificate reflecting its accuracy was issued. The average deviation for a testing range from 50 L/min to 95 L/min (0.833 kg/s to 1.583 kg/s) was performed where the meter was compared to a master meter as the standard. The average deviation was reported to be -0.08%, which conforms to the manufacturer's specification. This finding is beneficial to the quoted uncertainty in Table C.1. It is assumed that the refrigerant coriolis mass flow meter being exposed to the same operating environment would display a similar satisfactory result regarding its accuracy in mass flow measurements.

B.6 Post-Calibration Check

A consistent check is performed after each calibration procedure is completed on each sensor as described in sections B.5 to B.2. This check is identical to the respective calibration procedure with the exception of any sampling being done to modify the calibration coefficients for that probe present in the NI system.

In this check, it is deduced whether the calibration was successful. The performance of the sensor to match the reference is judged through the calculation of the sensor precision parameter $\sigma_z \cdot t$ as seen in equation (B.6). If it is found that a sensor deviates too much and exceed the criteria quoted in Table C.1, the calibration for the sensor is repeated until the criteria are met.

Appendix C: Uncertainty Analysis

C.6.1 Uncertainty of Sensors

The uncertainty of each sensor in the FF rig were investigated by Bock [1] and the values summarized in Table C.1 have shown to be the most reliable in uncertainty calculations:

Table C.1: Falling film rig sensor uncertainty values

Sensor	Measurement	Uncertainty	Units
K-Type Thermocouples	Temperature	0.1	°C
Endress+Hauser PMC 731	Pressure	1	kPa
KROHNE CORIMASS MFM4085 10G (Refrigerant)	Liquid Flow Rate	0.54	%
KROHNE CORIMASS MFM4085 100G (Testing Water)	Liquid Flow Rate	0.19	%

Furthermore, the uncertainty of the tube thermal conductivity, k_t, was obtained from investigations done by Abu-Eishah [87] and was determined to be a deviation of 4%.

C.6.2 Uncertainty Theory

The uncertainty of the various measurements is calculated with a 95% confidence interval is assumed in the calculation of deviation, incorporating a student's t-variable of $t = 1.96$. The distribution of results from the mean is assumed to be of a Gaussian Normal Distribution, where 95% of the distribution is found within 1.96 standard deviations from the mean [88]. A single parameter's deviation would be calculated by:

$$\delta x = \sigma_x \cdot t \tag{C.7}$$

The deviation of each constituent parameter in the calculation of the uncertainty of a quantity is then used through the *Law of Propagation of Uncertainty* as described by NIST TN 1297 [89]:

$$\delta y = \sqrt{\sum_{i=1}^{N} \left(\frac{\partial f}{\partial x_i}\right)^2 \cdot {\delta x_i}^2} \tag{C.8}$$

The complete derivation for interstitial uncertainties can be found in Bock [1], where each of the δx components in the equations below were quantified.

Making use of the principle in equation (C.8), simply the overall equations for the heat flux and heat transfer coefficient are provided for the heat flux in equation (C.9) and outside HTC in (C.10):

$$\delta q_o = \sqrt{\begin{array}{l}\left(\frac{\partial q_o}{\partial \dot{m}_w}\cdot\delta\dot{m}_w\right)^2+\left(\frac{\partial q_o}{\partial C_{p,w}}\cdot\delta C_{p,w}\right)^2+\left(\frac{\partial q_o}{\partial T_{in}}\cdot\delta T_{in}\right)^2+\left(\frac{\partial q_o}{\partial T_{out}}\cdot\delta T_{out}\right)^2 \\ +\left(\frac{\partial q_o}{\partial D_i}\cdot\delta D_i\right)^2+\left(\frac{\partial q_o}{\partial D_o}\cdot\delta D_o\right)^2+\left(\frac{\partial q_o}{\partial L}\cdot\delta L\right)^2\end{array}} \tag{C.9}$$

$$\delta h_o = \sqrt{\begin{array}{l}\left(\frac{\partial h_o}{\partial U_o}\cdot\delta U_o\right)^2+\left(\frac{\partial h_o}{\partial R_{wall}}\cdot\delta R_{wall}\right)^2+\left(\frac{\partial h_o}{\partial h_i}\cdot\delta h_i\right)^2 \\ +\left(\frac{\partial h_o}{\partial D_i}\cdot\delta D_i\right)^2+\left(\frac{\partial h_o}{\partial D_o}\cdot\delta D_o\right)^2\end{array}} \tag{C.10}$$

C.7 Detailed Uncertainty Analysis

The uncertainty study followed to plot the heat transfer coefficient uncertainty and the heat flux uncertainty for each testing heat flux as was done in Section 4.13. It was important that both independent variable and dependent variable uncertainties theoretically exist on heat transfer performance figures, where an oval region was shaped at each plotted point in which the true heat transfer performance of the tested tube can be found with 95% confidence (as assumed in this study).

Using equations C.9 and C.10, the uncertainties for the HTCs and heat fluxes were calculated. These uncertainties could then be compared to previous studies where the same tests were conducted to observe the cogency in the performance of the FF rig.

It was seen that the current study's uncertainties exhibited the same behaviour to Christians [2] where the uncertainties for HTC were low at high testing heat fluxes and high at low testing heat fluxes. The heat flux uncertainties were high at high testing heat fluxes and low at low testing heat fluxes.

At the same heat flux of 22 kW/m^2, the current study displayed an HTC percentage uncertainty of 57%, whereas a higher HTC percentage uncertainty of 97% was achieved by Christians [2]. At the high heat flux of 60 kW/m^2, the current study displays a heat flux percentage uncertainty of 24.8%, whereas a very similar heat flux percentage uncertainty of 26.3% was achieved by Christians [2].

At a heat flux of 20 kW/m^2, the current study displayed a heat flux percentage uncertainty of 17.3%, whereas a higher HTC percentage uncertainty of 25% was achieved by Christians [2]. At the high heat flux of 60 kW/m^2, the current study displayed a heat flux percentage uncertainty of 6.4%, whereas a higher heat flux percentage uncertainty of 10.3% was achieved by Christians [2].

It was inspected that the cause of the high uncertainties are when the difference in average

temperature of the testing water ($T_{w,ave}$) and the refrigerant saturation temperature (T_{sat}) being high. This was be observed in the derivation of the first term of equation (C.10), where the difference between the testing water and the refrigerant saturation temperature was found in the denominators of the external overall heat transfer coefficient term. The decrease in HTC with heat flux was shown in Figure C.3a:

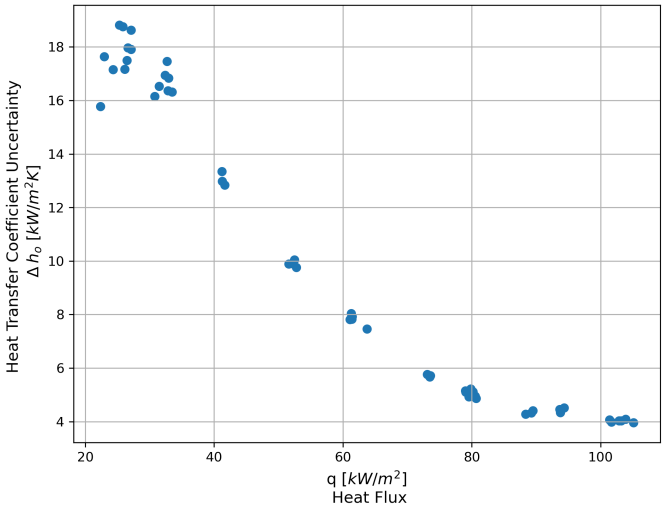

(a) Heat Transfer Coefficient uncertainty with respect to heat flux

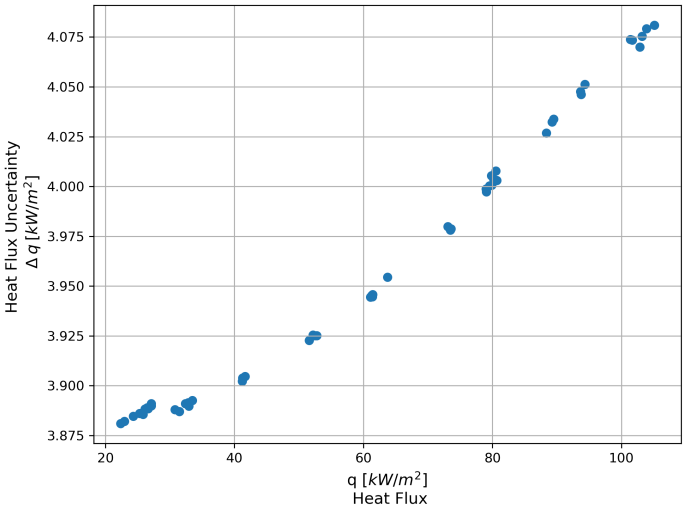

(b) Heat flux uncertainty with respect to heat flux

Figure C.3: Uncertainty deviations of HTCs and heat fluxes

The heat flux percentage uncertainty also shows to be decreasing with increasing heat flux, however, the heat flux uncertainty quantity itself was in fact increasing with increasing heat flux. The testing water temperature difference is found in the numerator of each of the terms of equation C.9, suggesting an increase in heat flux uncertainty with an increase in heat flux (which was directly proportional to the increase in temperature difference across the testing water). This was evidently shown by Figure C.3b:

However, the heat flux uncertainty percentage decreases with increasing heat flux as shown in Figure C.3b. The heat flux uncertainty increases only with approximately 200 W/m^2 over the entire 80 kW/m^2 heat flux testing range. With this, the percentage uncertainty decreases with a more rapidly increase in testing heat flux.

Ultimately, the most valuable determination from the uncertainty study was regarding the overall high uncertainty around lower heat fluxes across all studies, the HTCs surrounding the area cannot be fundamentally concentrated upon in comparison – and that the FF rig would provide highly accurate results in the higher testing heat fluxes.

Appendix D:
Tube Properties

D.8 Micro-Enhanced Tube Dimensions

The tube diameters were measured using a *Mitutoyo CD-P20p* digital vernier caliper. The measurements were documented in Table D.2 which were used in the processing of results:

Table D.2: Micro-enhanced tube diameters

Tube Name	Do	Dor	Di
Smooth	0.0191	0.0191	0.0167
Roughened	0.0191	0.0191	0.0167
GEWA-B5	0.0188	0.0174	0.0160
GEWA-KS	0.0188	0.0172	0.0149
EHPII	0.0189	0.0186	0.0160

The GEWA-B5 tube dimensions were obtained from Roques and Thome [50]. All tubes were of length $L = 0.554\,m$.

D.9 Tube Roughness

The roughnesses of the smooth and roughened tube are recorded below as measured by the profilometer:

Table D.3: Surface roughness measurements in $\mu m$for smooth and roughened tube

Tube Name	**Smooth**	**Roughened**
Grit Sandpaper	**G1200**	**G40**
	0.051	0.701
	0.046	0.698
	0.056	0.828
	0.037	0.713
	0.034	0.841
	0.045	0.732
	0.050	0.805
	0.046	0.663
	0.046	0.788
	0.018	0.616
	0.03	0.69
	0.036	0.741
	0.047	0.779
	0.045	0.791
	0.069	0.881
	0.03	0.733
	0.025	0.736
Average	**0.042**	**0.749**

Appendix E: Tube Coating Machine and the Coating Procedure

E.10 Copper Surface Conditioning

The condition of the copper surface is critical for the heat transfer performance. The process by which a copper surface ages is shown by equation (E.12). To produce copper acetate crystals (that are suspended in the solution) along with 2-Hydroxypropanoic acid as shown in equation to recondition the tube is shown by equation (E.11):

$$CuCO_3 + CH_3COOH \rightarrow Cu(COOH)_2 + (CH_3)_2CO_3 \tag{E.11}$$

$$2 \cdot Cu^{2+} + O_2 + CO_2 \rightarrow CuCO_3 + CuO \tag{E.12}$$

The reconditioning of the copper tube surfaces are included in the coating procedure used with the *Tube Coating Machine*.

E.11 Tube Coating Machine

A dedicated *Tube Coating Machine* was designed, manufactured and used in the coating process and shown in Figure E.4:

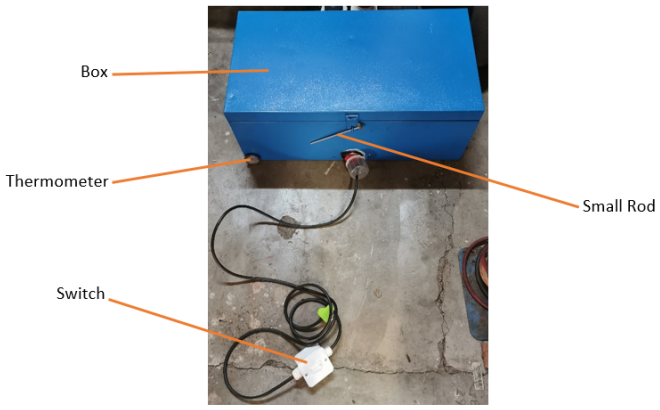

(a) Outside

(b) Inside

Figure E.4: Housing of Tube Coating Machine

Tubes are loaded into a tube (as sown in Figure E.5) to evenly expose the tubes to the coating solution where they are turned in opposite rotations to keep the solution mixed and uniform:

(a) Horizontal tube stack holder

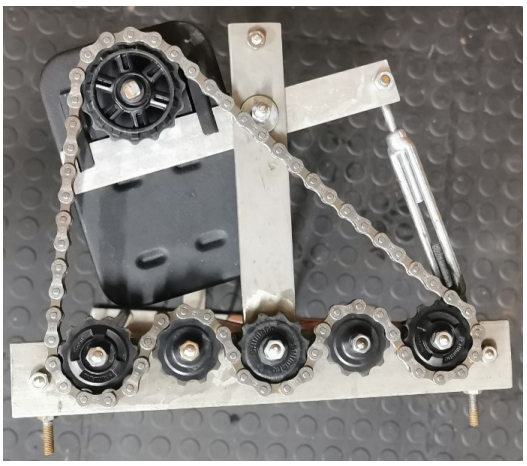

(b) Tube rack driving mechanism

Figure E.5: Housing of Tube Coating Machine

The *Tube Coating Machine* was specifically designed and constructed to fulfill the requirements of coating only the tube outside surfaces of tubes. Importantly, the *Tube Coating Machine* enables very careful control over the tubes being coated so as to have the tubes rotated at the same speed, turn the tubes in different directions to churn the solution for same exposure over all tube surfaces and to control of the alkali solution temperature to sustain the coating event. The schematic description of the *Tube Coating Machine* is given in Figure E.6:

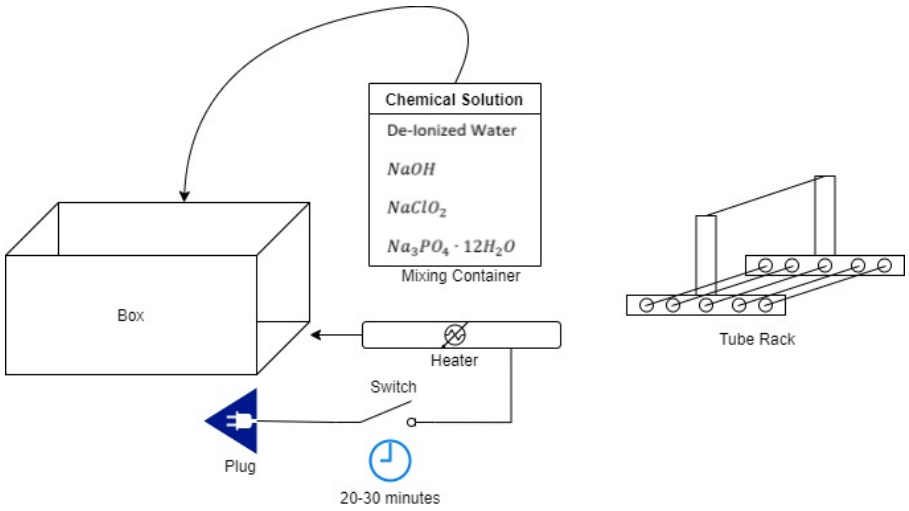

Figure E.6: Schematic of the Tube Coating Machine

The *Tube Coating Machine* has dimensions 712 mm × 379 mm × 241 mm. It is a requirement that the experimental space should have electricity for the tube coating machine. There should be facilities to rinse off if any alkaline solution should spill or if cleaning is required. The *Tube Coating Machine* contains the fumes, but a fume box is advised and should be closed as a precautionary measure and the fume extractor switched on. The equipment in the laboratory should be able to withstand the 95°C at the bottom of the box. The environment should also have a disposing point for the safe disposing of the alkali solution, which will be tapped out from the bottom of the machine and the remainder solution pumped out of the box by a siphon hand pump.

The following steps are followed to successfully coat the tubes using the Tube Coating Machine:

1. Obtain the necessary PPE: Chemically resistant approved gloves, approved white laboratory coat, long pants, closed shoes, protective eye goggles and an approved mask for fumes.
2. First rinse and then clean the inside and outside of the box, as well as the tube rack with degreaser soap.
3. Rinse off the soap on the box and the tube rack with RO water.
4. Using a brush, clean the tube rack and the inside of the box with acetone.
5. Using a brush, clean the tube rack and the inside of the box with ethanol.
6. Using a brush, clean the tube rack and the inside of the box with isopropyl alcohol.
7. Rinse the inside and outside of the box as well as the tube rack with RO water.
8. Mount the tubes on a holder (preferably not the tube rack). This can be done simply by sliding the tubes over rods and securing the rods on both sides. The tubes must be positioned over the dripping pan.
9. Using a brush and with the same intensity and number of strokes, clean the entirety of all the tubes with acetone.
10. Similarly, clean all the tubes with ethanol.
11. Similarly, clean all the tubes with isopropyl alcohol.

12. Using a separate brush, with the same intensity and the same number of strokes over the entirety of the tubes, apply the Hydrochloric Acid (HCl). Leave the tubes for 5 min before proceeding to the next step. (Ensure that a mask, goggles and gloves are equipped.)
13. Perform 3 sessions of rinsing the tubes with RO water.
14. Continue to appropriately dispose of the acid brush and the dripping pan or carefully clean them at the cleaning station.
15. Check the tension on the chain by turning the turnbuckle hook. The chain should have a play of approximately 2 cm. (This is required for the thermal expansion during coating.)
16. Place the tube rack on its side (the chain and electric motor at the bottom) and release the T-plate by undoing the 3 nuts.
17. Remove the plastic sealing caps from the tube rack rods.
18. Carefully slide the tubes into the tube rack, ensuring that they are seated properly over the sealing caps at the bottom of the tube rack.
19. Seal the tubes and lock them into position tightly wit the Nylon Insert Lock Nuts.
20. Re-attach the T-plate to secure all the tubes in position.
21. Ensure that the tubes are tightly sealed against the plastic sealing caps and also ensure that the tubes are free to rotate in the tube rack.
22. Make the solution as stipulated in section 4.3, ensuring that all safety protocols are followed along with the equipped PPE.
23. Transfer the solution to the box (with the tube rack removed) and switch on the heating element.
24. Wait approximately 20 – 30 minutes to reach the required 95°C — 100°C.
25. Switch on the electric motor and hook the tube rack handle onto the hooks underneath the lid by slotting the nuts into place on either side of one of the hooks.
26. Lower the tube rack by closing the lid and wait 20 minutes, also regulating the temperature of the solution with the thermometer (it was discovered that the saturation temperature of the solution is approximately 95°C — 100°C so the temperature regulation is not difficult).
27. Switch off the heating element and raise the lid, locking it into position by wedging the small rod vertically between the box and the lid.
28. Let the tubes drip dry and remove the tube rack from the machine.
29. Cleaning after this coating is now performed, where the tubes are rinsed with RO water.
30. The solution (having been left to become cold) can now be disposed of appropriately using a syphon pump or by other means as long as no contact with the skin occurs.
31. Wash the complete *Tube Coating Machine* as in steps 2 to 7 above for safe storage of the machine.
32. All coated copper should be rinsed with RO water and then dried with an inert N_2 stream.

E.12 Copper Oxidation Through Heating

Copper would bind to the oxygen in the atmosphere when provided with enough heat for the process's activation energy to be surpassed. Nam and Ju [55] indicated that such a 2-step reaction would occur in temperatures exceeding 260°C. This simple chemical reaction is seen in equations (E.13) and (E.14):

$$4 \cdot Cu + O_2 \rightarrow 2 \cdot Cu_2O \tag{E.13}$$

$$2Cu_2O + O_2 \rightarrow 4 \cdot CuO \tag{E.14}$$

This is a significant consideration in the manufacturing of the tubes, where the copper close to the ends reaches high enough temperatures for CuO formation such as in equation (E.14) when the stainless steel tips are attached through a brazing process. The unwanted CuO formation can then be cleaned with weak acetic acid as indicated in section 3.11.1.

Appendix F:
Calculation of pH of the Hot Alkali Solution

The following is an attempt to theoretically determine the Power of Hydrogen (pH) of the hot alkali solution as soon as the tubes are submerged for coating.

It is recognized that all of the reagent salts contain common strong base anions. The process of hydrolysis is predicted whilst the salts are suspended in solution. The details of the reagents (ingredients) of the hot alkali solution is captured in Table F.4:

Table F.4: Reagents and their quantities as from the chemicals observed

Formula	$NaClO_2$	$NaOH$	Na_3PO_4	$H_2O_{compensate}$	H_2O
Name	Sodium chlorite	Sodium hydroxide	Sodium phosphate	Compensated water	Water
Mass [kg]	0.5982	0.7976	0.6882	0.907	15.95
				16.86	

Volume Calculation: The local absolute pressure at coating location is $P_{local} = 87\ 192.8\ Pa$, hereby, using simple linear interpolation, the saturation temperature of the liquid water (in which the solution will be made) can be calculated using
TA-9, Çengel and Ghajar, 2015b [8]:

$$\frac{101325 - 87192.8}{101325 - 84550} = \frac{100 - T_{water,sat}}{100 - 95}$$

$$\therefore T_{water,sat} = 95.7877°C$$

Using the above water saturation temperature, the density of the water is calculated:

$$\frac{100 - 95.7877}{100 - 95} = \frac{12.252 - \rho_{water,95°C}}{12.252 - 12.332}$$

$$\therefore \rho_{water,95°C} = 960.933\ kg/m^3$$

The volume of the water medium can then be calculated:

$$V_{water,95°C} = \frac{m_{water}}{\rho_{water,95°C}} = \frac{16.86}{960.933}$$

$$\therefore V_{water,95°C} = 0.0175\ m^3 = 17.545\ dm^3$$

Furthermore, it is assumed that the volume of the solution is not affected by the addition of the salts and that it stays constant at the saturation temperature calculated above throughout the chemical reactions that may take place.

Hydrolysis of Sodium chlorite:

$$1 \cdot NaClO_2 \rightarrow Na^+ + 1 \cdot ClO_2^-$$

$$m_{NaClO_2} = 598.2\ g$$

$$M_{NaClO_2} = 23 + 35.5 + 16 \times 2 = 90.5\ g/mol$$

$$\therefore n_{NaClO_2} = \frac{m_{NaClO_2}}{M_{NaClO_2}} = \frac{598.2}{90.5} = 6.6099\ mol_{NaClO_2}$$

$$\therefore \frac{n_{NaClO_2}}{n_{ClO_2^-}} = \frac{1}{1} \Rightarrow n_{ClO_2^-} = 6.6099\ mol_{ClO_2^-}$$

Strong base ionization reaction:

$$ClO_2^- + H_2O \rightarrow HClO_2 + OH^-$$

$$\frac{n_{ClO_2^-}}{n_{OH^-}} = \frac{1}{1} = n_{OH^-} = 6.6099\ mol_{OH^-}$$

Hydrolysis of Sodium hydroxide:

$$1 \cdot NaOH \rightarrow Na^+ + 1 \cdot OH^-$$

$$m_{NaOH} = 797.6\ g$$

$$M_{NaOH} = 23 + 16 + 1 = 40\ g/mol$$

$$n_{NaOH} = \frac{m_NaOH}{M_{NaOH}} = \frac{797.6}{40} = 19.94\ mol_{NaOH}$$

$$\frac{n_{NaOH}}{n_{OH^-}} = \frac{1}{1} \Rightarrow n_{OH^-} = 19.94\ mol_{OH^-}$$

Hydrolysis of Sodium phosphate:

$$1 \cdot Na_3PO_4 \rightarrow 3 \cdot Na^+ + 1 \cdot PO_4^{3-}$$

$$m_{Na_3PO_4} = 688.2\ g$$

$$M_{Na_3PO_4} = 23 \times 3 + 31 + 16 \times 4 = 164\ g/mol$$

$$n_{Na_3PO_4} = \frac{m_{Na_3PO_4}}{M_{Na_3PO_4}} = \frac{688.2}{164} = 4.196\ mol_{Na_3PO_4}$$

$$\frac{n_{Na_3PO_4}}{n_{PO_4^{3-}}} = \frac{1}{1} \Rightarrow n_{PO_4^{3-}} = 4.196\ mol_{PO^3{}_4^-}$$

Strong base ionization reaction:

$$PO_4^{3-} + H_2O \rightarrow HPO^2{}_4^- + OH^-$$

$$\frac{n_{PO_4^{3-}}}{n_{OH^-}} = \frac{1}{1} = n_{OH^-} = 4.196\ mol_{OH^-}$$

Total moles of the hydroxyl anion:

$$n_{OH^-,tot} = 6.6099 + 19.94 + 4.196 = 30.7459\ mol_{OH^-}$$

Concentration of Hydroxyl anions:

$$C_{OH^-} = \frac{n_{OH^-,tot}}{V_{water,95°C}} = \frac{30.7459}{17.545} = 1.7524\, mol/dm^3$$

Water self-ionization:

The water self-ionization constant can be obtained from the following linear interpolation calculation [90], at $T_{water,sat}$:

$$\frac{100 - 95.7877}{100 - 95} = \frac{12.252 - pK_w}{12.252 - 12.332}$$

$$\therefore pK_w = 12.319$$

Hereby:

$$-\log(K_w) = pK_w = 12.319$$

$$\therefore K_w = 4.793 \times 10^{-13}$$

The ionization at $T_{w,sat} = 95.79$ is hereby:

$$K_w = [H_3O^+][OH^-]$$

$$4.793 \times 10^{-13} = [H_3O^+] \cdot 1.7524$$

$$\therefore [H_3O^+] = 2.735 \times 10^{-13}\, mol_{H_3O^+}$$

Power of Hydrogen:

$$pH = -\log([H_3O^-]) = -\log(2.735 \times 10^{-13})$$

$$\therefore pH = 12.56$$

Appendix G:
CuO Coating Thermal Resistance

The thermal tube wall resistance of a plain copper tube is calculated below per length of the tube in equations (G.15) to (G.17):

$$R_{wall,uncoated} = \frac{\ln(D_o/D_i)}{2 \cdot \pi \cdot k_t} \tag{G.15}$$

$$\Rightarrow R_{wall,uncoated} = \frac{\ln(0.01905/0.01665)}{2 \cdot \pi \cdot 340} \tag{G.16}$$

$$\therefore R_{wall,uncoated} = 6.303 \times 10^{-5}\ m \cdot K/W \tag{G.17}$$

According to Enright [54], the effective CuO coating thickness is approximately 1.5 μm according to equation (G.18), where Cu_2O inclusions are considered:

$$\delta_{coating} = \delta_{Cu_2O} + \delta_{CuO} = 1.5\ \mu m \tag{G.18}$$

The thermal wall resistance the coating imposes on the tube would therefore be:

$$R_{wall,coated} = \frac{\ln\left((D_o + 2 \cdot \delta_{coating})/D_o\right)}{2 \cdot \pi \cdot k_{CuO}} \tag{G.19}$$

$$\Rightarrow R_{wall,coated} = \frac{\ln\left((0.01905 + 2 \cdot 1.5 \times 10^{-6})/0.01905\right)}{2 \cdot \pi \cdot 33} \tag{G.20}$$

$$\therefore R_{wall,coated} = 7.594 \times 10^{-7}\ m \cdot K/W \tag{G.21}$$

Comparing the thermal wall resistance of the coating to that of the uncoated tube, the reference thermal wall resistances from (G.17) and (G.21) are used for the following equation (G.24):

$$\chi = \frac{R_{wall,coated}}{R_{wall,uncoated}} \times 100 \tag{G.22}$$

$$\chi = \frac{7.594 \times 10^{-7}}{6.303 \times 10^{-5}} \times 100 \tag{G.23}$$

$$\chi = 1.2\% \tag{G.24}$$

From (G.24) above, it is established that the thermal resistance the coating imposes on the system is insignificant with such a low comparative impact and would be excluded from all calculations and analyses.

Appendix H:
Additional SEM Micrographs

H.13 Roughened Tube

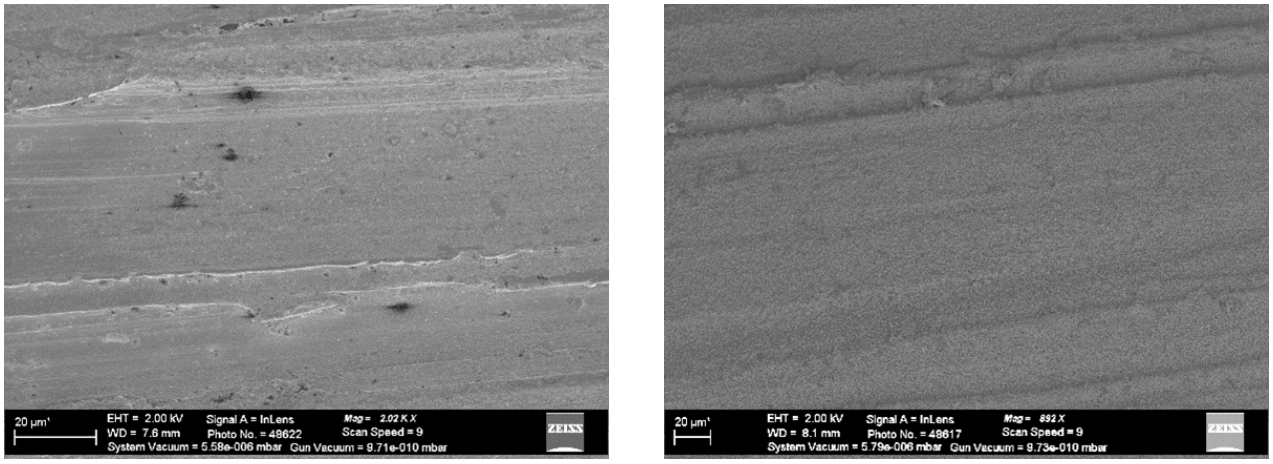

(a) Medium shot: Uncoated (b) Medium shot: Coated

Figure H.7: Medium shot uncoated and coated roughened tube SEM micrographs

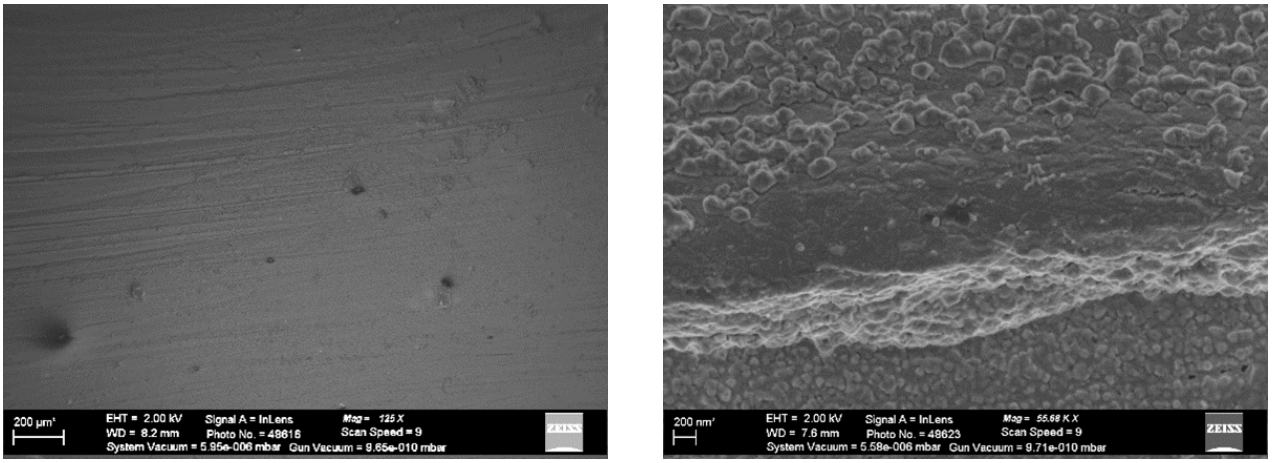

(a) Coated (b) Uncoated

Figure H.8: Additional uncoated and coated roughened tube SEM micrographs

H.14 GEWA-KS

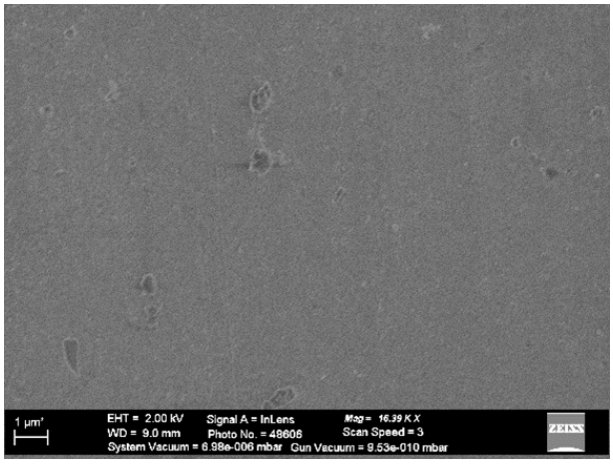

Figure H.9: Uncoated

H.15 GEWA-B5

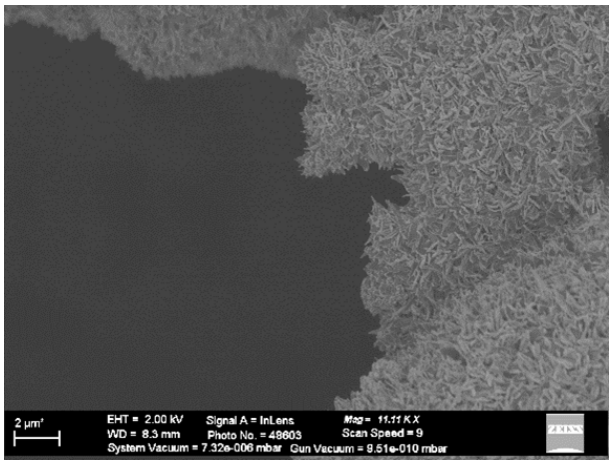

(a) Long shot of coated tube

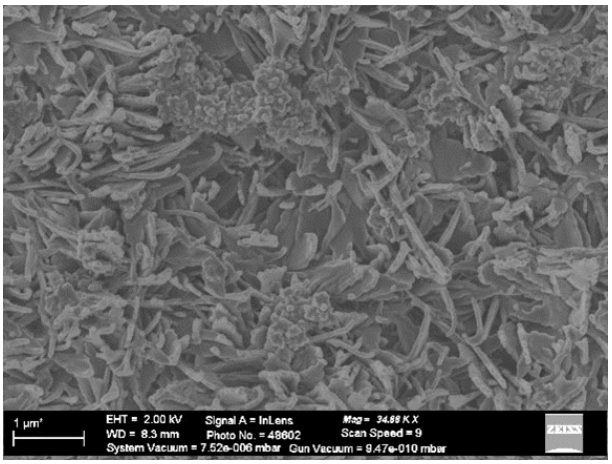

(b) Close shot of coated tube

Figure H.10: Additional coated GEWA-B5 tube SEM micrographs

H.16 EHPII

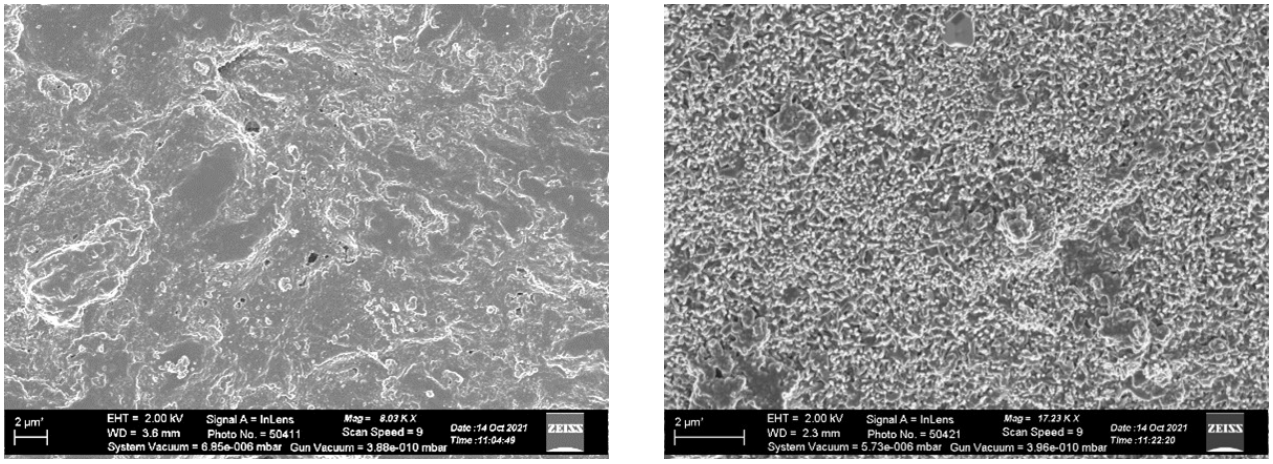

(a) Uncoated (b) Coated

Figure H.11: Additional uncoated and coated EHPII tube SEM micrographs

Appendix I:
Python Code

```
import numpy as np
import os
import pandas as pd
import CoolProp.CoolProp as cp
import pickle
from matplotlib import pyplot as plt
import matplotlib
import statistics as stats
from datetime import datetime
import platform
import sys
get_ipython().run_line_magic('matplotlib', 'notebook')
def closest_to(arr, number):
    array = np.array(arr)
    differences = abs(array - number)
    reference = min(differences)
    index = np.where(differences == reference)[0][0]
    error = number - arr[index]
    respond = {"index": index, "value": arr[index], "error": error}
    return respond
def notebook_bigger_plots(W, H):
    plt.tight_layout()
    plt.rcParams["figure.figsize"] = (W, H)
    plt.rcParams["figure.dpi"] = 150
def RMS(arr):
    var = np.array(arr)
    s = 0
    for i in var:
        s = s + i**2
    ms = s/len(var)
    rms = (ms)**(0.5)
    return rms
def correlation(function, data):
    function = np.array(function)
    data = np.array(data)
    error = []
    for i in range(len(function)):
        error.append(abs(100*((data[i] - function[i])/data[i])))
    avg_error = sum(error)/len(error)
    r = (len(function)*(sum(function*data))-sum(function)*sum(data))/((len(function)*sum(
    function**2)-(sum(function))**2)*(len(function)*sum(data**2)-(sum(data))**2))**0.5
    respond = {"avg_error":avg_error, "correlation":r}
    return respond
def interpolator(x, y, xi):
    counter = 0
    flag = True
    yi = 0
    try:
        while(flag):
            if(x[counter] < xi and xi <= x[counter+1]):
                x1 = x[counter]
                x2 = x[counter+1]
                y1 = y[counter]
                y2 = y[counter+1]
                yi = -(((x1-xi)/(x1-x2))*(y1-y2)-y1)
                flag = False
            counter = counter + 1
```

```
    except:
        yi = 0
    return yi
def MSE(observed, expected):
    import numpy as np
    observed = np.array(observed)
    expected = np.array(expected)
    n = len(observed)
    mse = (1/n) * sum((observed - expected)**2)
    return mse
def bestfit(x, y, q):
    import numpy as np
    exponents = list(np.linspace(0, q, q+1))
    exponents = exponents[::-1]
    def line(x, exponents):
        expression = []
        for i in exponents:
            expression.append(x**i)
        return expression
    A = []
    for i in x:
        A.append(line(i, exponents))
    A = np.matrix(A)
    y = np.array(y)
    v = np.matrix(y).T
    z = (A.T*A)**(-1) * A.T*v
    z = np.array(z.T)[0]
    return z
def sort(independent, dependent):
    A = independent
    B = dependent
    for j in range(len(A)):
        for i in range(len(A)-1):
            if(A[i+1] < A[i]):
                temp = A[i]
                A[i] = A[i+1]
                A[i+1] = temp
                temp = B[i]
                B[i] = B[i+1]
                B[i+1] = temp
    return A, B
def render_csv(dictionary, name):
    lengths = []
    for i in dictionary.keys():
        try:
            lengths.append(len(dictionary[i]))
        except Exception as E:
            pass
    df = pd.DataFrame()
    mode = stats.mode(lengths)
    for j in dictionary.keys():
        try:
            if(len(dictionary[j]) == mode):
                df[j] = dictionary[j]
        except:
            pass
    df.to_csv(name + ".csv", index = False)

def save_dictionary(header, body, name):
    data_dictionary = {}
    for i in range(len(header)):
```

```
118             data_dictionary[header[i]] = body[i]
119         file = open(name + ".pickle", 'wb')
120         pickle.dump(data_dictionary, file)
121         file.close()
122         file = open(name + ".data", 'w')
123         for key in data_dictionary:
124             file.write(key + "\n" + str(data_dictionary[key]) + 2*"\n")
125         file.close()
126         return data_dictionary
127 def Gorenflo10(T_sat, Ra, q, ref):
128         import CoolProp.CoolProp as cp
129         P_sat = cp.PropsSI('P', 'T', T_sat,'Q', 0, ref)/1000
130         P_crit =  cp.PropsSI('pcrit', 'T', T_sat, "Q", 0, ref)/1000
131         P_reduced = P_sat/P_crit
132         Ra_0 = 0.4
133         Pr_0 = 0.1
134         q_0 = 20e3
135         htc_0 = 4200
136         b = 35.35
137         bCu = 35.35
138         D = 10
139         n = 0.95 - 0.3*P_reduced**(0.3)
140         F_q = (q/q_0)**n
141         F_p = 0.7*P_reduced**(0.2) + 4*P_reduced + 1.4*P_reduced/(1 - P_reduced)
142         F_wR = (Ra/Ra_0)**(2/15)
143         F_wM = (b/bCu)**0.5
144         F_w = F_wM*F_wR
145         sigma_l = cp.PropsSI('I', 'T', T_sat,'Q', 0, ref)
146         P_sat_Dplus = cp.PropsSI('P', 'T', T_sat + D, 'Q', 0, ref)/1000
147         P_sat_Dminus = cp.PropsSI('P', 'T', T_sat - D, 'Q', 0, ref)/1000
148         dPdT = (P_sat_Dplus - P_sat_Dminus)/(2*D)
149         Pf = dPdT/(sigma_l*1000)
150         Pf_0 = 1
151         F_f = (Pf/Pf_0)**0.6
152         Gorenflo_alpha_o = htc_0 * F_q * F_p * F_w * F_f
153         return Gorenflo_alpha_o
154 def Nusselt(T_sat, delta_T):
155         Cp_rL = cp.PropsSI('C', 'T', T_sat, 'Q', 0, refrigerant)
156         mu_rL = cp.PropsSI('V', 'T', T_sat, 'Q', 0, refrigerant)
157         k_rL = cp.PropsSI('L', 'T', T_sat, 'Q', 0, refrigerant)
158         rho_rL = cp.PropsSI('D', 'T', T_sat, 'Q', 0, refrigerant)
159         rho_rV = cp.PropsSI('D', 'T', T_sat, 'Q', 1, refrigerant)
160         h_rV = cp.PropsSI('H', 'T', T_sat, 'Q', 1, refrigerant)
161         h_rL = cp.PropsSI('H', 'T', T_sat, 'Q', 0, refrigerant)
162         h_LV = h_rV - h_rL
163         Nusselt_alpha_o = 0.728*((rho_rL*(rho_rL - rho_rV)*g*h_LV*k_rL**3)/(mu_rL*(delta_T)*Do))
            **0.25
164         return Nusselt_alpha_o
165 def Ribatski07(T_sat, T_V, q, m_r, Ra, Do, ref, L):
166         mu_rL = cp.PropsSI('V', 'T', T_sat,'Q', 0, ref)
167         M = cp.PropsSI('M', 'T', T_sat,'Q', 0, ref)*1000
168         P_reduced = cp.PropsSI('P', 'T', T_sat,'Q', 1, ref)/cp.PropsSI('pcrit', 'T', T_sat,'Q', 1,
              ref)
169         k_rV        =    cp.PropsSI('L', 'T', T_sat, 'Q', 1, ref)
170         k_rL        =    cp.PropsSI('L', 'T', T_sat, 'Q', 0, ref)
171         rho_rV      =    cp.PropsSI('D', 'T', T_sat, 'Q', 1, ref)
172         mu_rV       =    cp.PropsSI('V', 'T', T_sat, 'Q', 1, ref)
173         nu_rV = mu_rV/rho_rV
174         Cp_rV = cp.PropsSI('C', 'T', T_sat, 'Q', 1, ref)
175         g = 9.81
176         gamma = m_r/(2*L)
```

```
    Re_f =  4*gamma/mu_rL
    F = 0.0025*Re_f**0.91

    for i in range(len(F)):
        if(F[i] > 1):
            F[i] = 1
    h_Wet = 4.2e3*P_reduced**0.22*q**0.38*M**(-0.5)*Ra**0.2
    alpha_V = k_rV/(rho_rV*Cp_rV)
    beta_V   =   1/T_V
    Ra = g*beta_V*(T_sat - T_V)*Do**3/(nu_rV*alpha_V )
    Pr = mu_rV*Cp_rV/k_rV
    Nu = (0.6 + 0.387*(Ra/(1 + (0.559/Pr)**(9/16))**(16/9))**(1/6))**2
    h_Dry = Nu * k_rL / Do
    Ribatski_alpha_o = h_Wet*F + h_Dry*(1 - F)
    return Ribatski_alpha_o
def average_deviation(theoretical, experimental):
    return (1/len(experimental))*(sum(abs((theoretical - experimental)/(experimental))*100))
def q_uncertainty(Tin, Tout, Do, m_w, Cp_w):
    T_ave = (Tin + Tout)/2
    L = 0.37
    Cp_w_dev = 0.01
    dT = 0.1
    dL_ruler = ((2*0.001)**2 + (0.5*0.001)**2)**(0.5)
    dm_w = 0.0015*(m_w + 8.3e-3/m_w)
    dCp_w = Cp_w_dev*Cp_w
    ddT = np.sqrt(2)*(dT)
    term_a = (Cp_w*(Tout - Tin)/np.pi/Do/L)*dm_w
    term_b = (m_w*(Tout - Tin)/np.pi/Do/L)*dCp_w
    term_c = (m_w*Cp_w/np.pi/Do/L)*ddT
    term_d = (-m_w*Cp_w*(Tout - Tin)/np.pi/Do/L**2)*dL_ruler
    delta_q = (term_a**2 + term_b**2 + term_c**2 + term_d**2)**0.5
    return delta_q
def Uo_uncertainty(Tsat, T_ave, q, dq, ddT):
    term_a = (1/(Tsat - T_ave))*dq
    term_b = (-q/(Tsat - T_ave)**2)*ddT
    delta_Uo = (term_a**2 + term_b**2)**0.5
    return delta_Uo
def ho_uncertainty(Uo, Rw, alpha_o, Do, Di, Tsat, Tin, Tout, q, m_w, f, Re_w, Pr_w, k_w, mu_w,
     Cp_w, k_t, Ci, dCi, all_uncertainties = False):
    T_ave = (Tin + Tout)/2
    mu_w_dev = 0.01
    Cp_w_dev = 0.01
    k_w_dev = 0.01
    Dh = 0.01597 - 8e-3
    Dw = 0.01597 + 8e-3
    Dinox = 8e-3
    dq = q_uncertainty(Tin, Tout, Do, m_w, Cp_w)
    dT = 0.1
    ddT = np.sqrt(2)*(dT)
    dm_w = 0.0015*(m_w + 8.3e-3/m_w)
    dmu_w = mu_w_dev*mu_w
    dCp_w = Cp_w_dev*Cp_w
    dk_w = k_w_dev*k_w
    dL_vernier = ((2*0.00001)**2 + (0.5*0.00001)**2 )**(0.5)
    dk_t = k_t*0.04
    def Uo_uncertainty(Tsat, T_ave, q, dq, ddT):
        term_a = (1/(Tsat - T_ave))*dq
        term_b = (-q/(Tsat - T_ave)**2)*ddT
        delta_Uo = (term_a**2 + term_b**2)**0.5
        return delta_Uo
    def Rw_uncertainty(Do, Di, Dor, dL_vernier, k_t, dk_t):
```

```
        dRwdDi = -1/2*Do/k_t/Di
        dRwdDo = 1/2/k_t*np.log(Dor/Di)
        dRwdDor = 1/2*Do/k_t/Dor
        dRwdk_t = -1/2*Do/k_t**2*np.log(Dor/Di)
        delta_Rw = ((dRwdDi*dL_vernier)**2 + (dRwdDo*dL_vernier)**2 + (dRwdDor*dL_vernier)**2
    + (dRwdk_t*dk_t)**2)**0.5
        return delta_Rw
    def Re_uncertainty(m_w, mu_w, Dw, dm_w, dmu_w, dL_vernier):
        ddL_vernier = np.sqrt(2)*dL_vernier
        term_a = (4/np.pi/mu_w/Dw)*dm_w
        term_b = (-4*m_w/np.pi/mu_w**2/Dw)*dmu_w
        term_c = (-4*m_w/np.pi/mu_w/Dw**2)*ddL_vernier
        delta_Re = (term_a**2 + term_b**2 + term_c**2)**0.5
        return delta_Re
    def f_uncertainty(Re_w, m_w, mu_w, Dw, dm_w, dmu_w, dL_vernier):
        dRe_w = Re_uncertainty(m_w, mu_w, Dw, dm_w, dmu_w, dL_vernier)
        term_a = (-79/50/(79/100*np.log(Re_w) - 41/25)**3/Re_w)*dRe_w
        delta_f = (term_a**2)**0.5
        return delta_f
    def Pr_uncertainty(mu_w, Tave, k_w, dmu_w, dCp_w, dk_w):
        term_a = (Cp_w/k_w)*dmu_w
        term_b = (mu_w/k_w)*dCp_w
        term_c = (-mu_w*Cp_w/k_w**2)*dk_w
        delta_Pr = (term_a**2 + term_b**2 + term_c**2)**0.5
        return delta_Pr
    df = f_uncertainty(Re_w, m_w, mu_w, Dw, dm_w, dmu_w, dL_vernier)
    dRe_w = Re_uncertainty(m_w, mu_w, Dw, dm_w, dmu_w, dL_vernier)
    dPr_w = Pr_uncertainty(mu_w, T_ave, k_w, dmu_w, dCp_w, dk_w)
    Nugni = ((f/8)*(Re_w-1000)*Pr_w)/(1+12.7*(f/8)**0.5*(Pr_w**(2/3)-1))
    hgni = (Nugni * k_w/(Di - Dinox))
    def hi_uncertainty(f, Re_w, Pr_w, k_w, Dh, hgni, df, dRe_w, dPr_w, dk_w, dL_vernier):
        dDh = np.sqrt(2)*dL_vernier
        term_a = (1/8*(Re_w - 1000)*Pr_w*k_w/(1 + 127/80*8**(1/2)*f**(1/2)*(Pr_w**(2/3) - 1))/
    Dh - 127/1280*f**(1/2)*(Re_w - 1000)*Pr_w*k_w/(1 + 127/80*8**(1/2)*f**(1/2)*(Pr_w**(2/3) -
     1))**2/Dh*8**(1/2)*(Pr_w**(2/3) - 1))*df
        term_b = (1/8*f*Pr_w*k_w/(1 + 127/80*8**(1/2)*f**(1/2)*(Pr_w**(2/3) - 1))/Dh)*dRe_w
        term_c = (1/8*f*(Re_w - 1000)*k_w/(1 + 127/80*8**(1/2)*f**(1/2)*(Pr_w**(2/3) - 1))/Dh
    - 127/960*f**(3/2)*(Re_w - 1000)*Pr_w**(2/3)*k_w/(1 + 127/80*8**(1/2)*f**(1/2)*(Pr_w
    **(2/3) - 1))**2/Dh*8**(1/2))*dPr_w
        term_d = (1/8*f*(Re_w - 1000)*Pr_w/(1 + 127/80*8**(1/2)*f**(1/2)*(Pr_w**(2/3) - 1))/Dh
    )*dk_w
        term_e = (-1/8*f*(Re_w - 1000)*Pr_w*k_w/(1 + 127/80*8**(1/2)*f**(1/2)*(Pr_w**(2/3) -
    1))/Dh**2)*dDh
        term_f = hgni*dCi
        delta_hi = (term_a**2 + term_b**2 + term_c**2 + term_d**2 + term_e**2 + term_f**2)
    **0.5
        return delta_hi
    dhi = hi_uncertainty(f, Re_w, Pr_w, k_w, Dh, hgni, df, dRe_w, dPr_w, dk_w, dL_vernier)
    dUo = Uo_uncertainty(Tsat, T_ave, q, dq, ddT)
    dRw = Rw_uncertainty(Do, Di, Dor, dL_vernier, k_t, dk_t)
    hi = Ci*hgni
    dhdUo = 1/(1/Uo - Rw - Do/Di/hi)**2/Uo**2
    dhdhi = -1/(1/Uo - Rw - Do/Di/hi)**2*Do/Di/hi**2
    dhdRw = 1/(1/Uo - Rw - Do/Di/hi)**2
    dhdDi = -1/(1/Uo - Rw - Do/Di/hi)**2*Do/Di**2/hi
    dhdDo = 1/(1/Uo - Rw - Do/Di/hi)**2/Di/hi
    delta_ho = ((dhdUo*dUo)**2 + (dhdhi*dhi)**2 + (dhdRw*dRw)**2 + (dhdDi*dL_vernier)**2 + (
    dhdDo*dL_vernier)**2)**0.5
    if(all_uncertainties == True):
        return {'df':df, 'dRe_w':dRe_w, 'dPr_w':dPr_w, 'dhgni':dhgni, 'dUo':dUo, 'dRw':dRw, '
    delta_h':delta_ho}
```

```
    else:
        return delta_ho
def data_collect():
    working_path = os.getcwd() + str("/")
    directories = os.listdir(working_path)
    global script_name
    for i in os.listdir():
        if(('.ipynb' in i) and ('_checkpoints' not in i)):
            script_name = i
    script_name = "Last executed with script: " + str(script_name)
    date = "Last executed date: " + str(datetime.now())
    uname = platform.uname()
    system, node, release, version, machine = "System: " + str(uname[0]), "Node: " + str(uname
    [1]), "Release: " + str(uname[2]), "Version: " + str(uname[3]), "Machine: " + str(uname
    [4])
    python_major, python_minor = sys.version_info[0], sys.version_info[1]
    python_info = "Python Version: " + str(python_major) + "." + str(python_minor)
    add_info = [script_name, date, system, node, release, version, machine, python_info]
    global T1
    global T2
    global T3
    global T_ave
    global m_w
    global m_r
    global P_up
    global P_down
    global dT_dx
    global stabilities
    global unstable_files
    data = []
    dT_dx = []
    stabilities = []
    unstable_files = []
    for i in directories:
        if (".txt" in i and ('Settings' not in i) and ('settings' not in i)):
            file_contents = []
            file = open(i, 'r+')
            file_contents.append(file.readline())
            file_contents.append(file.readline())
            probe_line = file.readline()
            file_contents.append(probe_line)
            probe_numbers = probe_line.split(" ")
            file_contents.append(file.readline())
            file_contents.append(file.readline())
            file_contents.append(file.readline())
            samples = []
            for j in range(0, 30):
                sample_line = file.readline()
                file_contents.append(sample_line)
                samples.append(sample_line.split(" "))
            df = pd.DataFrame(samples, columns = probe_numbers).drop('\n', axis = 'columns')
            stability = []
            for k in thermocouple_rod:
                maximum = max(df[str(k)].astype(np.float64))
                minimum = min(df[str(k)].astype(np.float64))
                stability.append(maximum - minimum)
            stability = max(stability)
            stabilities.append(stability)
            if(stability > tolerance):
                unstable_files.append(i)
            file.truncate(0)
```

```
            file.seek(0)
            for l in file_contents:
                file.writelines(l)
            for i in add_info:
                file.writelines(i + "\n")
            file.close()
            probe_samples = []
            for l in configured_probes:
                probe_samples.append(np.average(np.array((df[str(l)])).astype(np.float64)))
            T = probe_samples[0:6]
            Z = np.matrix(bestfit(x, T, 2))
            X = np.matrix([ np.unique(x)**2, np.unique(x)**1, np.unique(x)**0 ])
            T_poly = list(np.array(Z*X)[0])
            data.append(T_poly + probe_samples[6:])
            Z = np.array(Z)
            dT_dx.append(Z[0][0]*2*(x[0] + x[-1])/2 + Z[0][1])
        data = np.matrix(data)
        dT_dx = np.array(dT_dx)
        T1 = np.array(data[:,0].T)[0]
        T2 = np.array(data[:,1].T)[0]
        T3 = np.array(data[:,2].T)[0]
        T_ave = (T1 + T2 + T3)/3
        m_w = water_flow = np.array(data[:,3].T)[0]
        m_r = refrigerant_flow = np.array(data[:,4].T)[0]
        P_up = np.array(data[:,5].T)[0]*1e3
        P_down = np.array(data[:,6].T)[0]*1e3
x = [0.092, 0.092, 0.277, 0.277, 0.462, 0.462]
pipe_pitch = 22.3e-3
Dinox = 0.008
g = 9.81
water_flow_rate = 426
refrigerant_flow_rate = 430
top_pressure = 421
bottom_pressure = 422
L = 0.554
global autoname
global test_type
global tube_name
global surface_condition
global saturation_temperature
global test_description
global tube_identifier
try:
    autoname = True
    directories = os.listdir()
    directories_filter = []
    for i in directories:
        if((".txt" in i) and ("settings" not in i) and ("Settings" not in i) and ("SETTINGS"
    not in i)):
            directories_filter.append(i)
    directories = directories_filter
    subject = directories[0]
    elements = subject.split("_")
    test_type_element, surface_condition_element, tube_name_element, saturation_temperature =
     elements[0], elements[1][0], elements[1][1:], elements[3].replace("C", "")
    if(test_type_element == "FF"):
        test_type = "Falling Film Boiling"
    elif(test_type_element == "PB"):
        test_type = "Pool Boiling"
    elif(test_type_element == "C"):
        test_type = "Condensation"
```

```
406     elif(test_type_element == "RS"):
407         test_type = "Film Reynolds Sweep"
408     elif(test_type_element == "WP"):
409         test_type = "Wilson Plot Analysis"
410     if(surface_condition_element == "U"):
411         surface_condition = "Uncoated"
412     elif(surface_condition_element == "C"):
413         surface_condition = "Coated"
414     if(tube_name_element == "G1200"):
415         tube_name = "Smooth Tube"
416         tube_identifier = 0
417 
418     elif(tube_name_element == "G40"):
419         tube_name = "Roughened Tube"
420         if(surface_condition == "Uncoated"):
421             tube_identifier = 2
422         else:
423             tube_identifier = 3
424 
425     elif(tube_name_element == "GEWAB" or tube_name_element == "GEWA-B" or tube_name_element ==
     "GEWAB5" or tube_name_element == "GEWA-B5"):
426         tube_name = "GEWA-B5 Tube"
427         if(surface_condition == "Uncoated"):
428             tube_identifier = 4
429         else:
430             tube_identifier = 5
431 
432     elif(tube_name_element == "GEWAK" or tube_name_element == "GEWAKS" or tube_name_element ==
     "GEWA-K" or tube_name_element == "GEWA-KS"):
433         tube_name = "GEWA-KS Tube"
434         if(surface_condition == "Uncoated"):
435             tube_identifier = 6
436         else:
437             tube_identifier = 7
438 
439     elif(tube_name_element == "EHPII"):
440         tube_name = "EHPII Tube"
441         if(surface_condition == "Uncoated"):
442             tube_identifier = 8
443         else:
444             tube_identifier = 9
445 
446     elif(tube_name_element == "Christians"):
447         tube_name = "Christians Tube"
448         tube_identifier = 10
449 
450     test_description = test_type + " Test of " + surface_condition + " " + tube_name + " at "
    + saturation_temperature + "C Saturation Temperature"
451     print("NAME OF THIS TEST: \n " + str(test_description))
452 except Exception as e:
453     autoname = False
454     print("Automatic Naming Failed. Please name the test manually.")
455     print()
456     print("Error: " + e)
457     print()
458     print("Beware to manually change the name, tube name, tube parameters and other tube \n
    settings in the rest of the processing code everywhere in the else statements for the '
    autoname' variable!")
459     test_description = input("Enter the name of this test: ")
460 
461     satisfied = True
```

```
462     while(satisfied):
463         test_type_element = input("Enter test type: 'FF' - Falling Film Boiling, 'PB' - Pool
    Boiling, 'C' - Condensation, 'RS' - Film Reynolds Sweep, 'WP' - Wilson Plot Analysis")
464         if(test_type_element == "FF"):
465             test_type = "Falling Film Boiling"
466             satisfied = False
467         elif(test_type_element == "PB"):
468             test_type = "Pool Boiling"
469             satisfied = False
470         elif(test_type_element == "C"):
471             test_type = "Condensation"
472             satisfied = False
473         elif(test_type_element == "RS"):
474             test_type = "Film Reynolds Sweep"
475             satisfied = False
476         elif(test_type_element == "WP"):
477             test_type = "Wilson Plot Analysis"
478             satisfied = False
479 
480     satisfied = True
481     while(satisfied):
482         surface_condition_element = input("Enter surface condition: U - Uncoated, C - Coated")
483         if(surface_condition_element == "U"):
484             surface_condition = "Uncoated"
485         elif(surface_condition_element == "C"):
486             surface_condition = "Coated"
487 
488     satisfied = True
489     while(satisfied):
490         tube_name_element = input("Enter name of tube (U - Uncoated, C - Coated): G1200, UG40,
     CG40, UGEWAB, CGEWAB, UGEWAKS, CGEWAKS, UEHPII, CEHPII")
491         if(tube_name_element == "G1200"):
492             tube_name = "Smooth Tube"
493             tube_identifier = 0
494             satisfied = False
495         elif(tube_name_element == "UG40"):
496             tube_name = "Roughened Tube"
497             tube_identifier = 2
498             satisfied = False
499         elif(tube_name_element == "CG40"):
500             tube_name = "Roughened Tube"
501             tube_identifier = 3
502             satisfied = False
503         elif(tube_name_element == "UGEWAB" or tube_name_element == "UGEWA-B" or
    tube_name_element == "UGEWAB5" or tube_name_element == "UGEWA-B5"):
504             tube_name = "GEWA-B5 Tube"
505             tube_identifier = 4
506             satisfied = False
507         elif(tube_name_element == "CGEWAB" or tube_name_element == "CGEWA-B" or
    tube_name_element == "CGEWAB5" or tube_name_element == "CGEWA-B5"):
508             tube_name = "GEWA-B5 Tube"
509             tube_identifier = 5
510             satisfied = False
511         elif(tube_name_element == "UGEWAK" or tube_name_element == "UGEWAKS" or
    tube_name_element == "UGEWA-K" or tube_name_element == "UGEWA-KS"):
512             tube_name = "GEWA-KS Tube"
513             tube_identifier = 6
514             satisfied = False
515         elif(tube_name_element == "CGEWAK" or tube_name_element == "CGEWAKS" or
    tube_name_element == "CGEWA-K" or tube_name_element == "CGEWA-KS"):
516             tube_name = "GEWA-KS Tube"
```

```
            tube_identifier = 7
            satisfied = False
        elif(tube_name_element == "UEHPII"):
            tube_name = "EHPII Tube"
            tube_identifier = 8
            satisfied = False
        elif(tube_name_element == "CEHPII"):
            tube_name = "EHPII Tube"
            tube_identifier = 9
            satisfied = False
        elif(tube_name_element == "Christians"):
            tube_name = "Christians Tube"
            tube_identifier = 10
            satisfied = False
name = test_description
output = True
save_figures = True
save_data = True
uncertainty = False
indicate_stability = True
tolerance = 0.1
thermocouple_rod_1 = [118, 119, 120, 121, 122, 123]
thermocouple_rod_2 = [206, 205, 204, 203, 202, 201]
thermocouple_rod_3 = [222, 222, 221, 220, 219, 218]
thermocouple_rod_4 = [415, 414, 413, 412, 411, 411]
thermocouple_rods = [thermocouple_rod_1, thermocouple_rod_2, thermocouple_rod_3,
    thermocouple_rod_4]
thermocouple_rod_choice = 3
bock_thin_plain_tube =  [0, "Cu", 340, 0.01905, 0.01905, 0.01665, 0.046, 1.25, 0.1]
dian_thick_plain_tube = [1, "Cu", 340, 0.01905, 0.01905, 0.01605, 0.056, None, 0.1]
UG40 = [2, "Cu", 340, 0.01905, 0.01905, 0.01665, 0.74, 1.25, 0.1]
CG40 = [3, "Cu", 340, 0.01905, 0.01905, 0.01665, 0.74, 1.25, 0.1]
UGEWAB5 = [4, "Cu", 340, 0.01884, 0.01738, 0.01597, None, 4.09, 0.15]
CGEWAB5 = [5, "Cu", 340, 0.01884, 0.01738, 0.01597, None, 4.09, 0.15]
UGEWAKS = [6, "Cu", 340, 0.018842, 0.017242, 0.014922, None, 3.67, 0.09]
CGEWAKS = [7, "Cu", 340, 0.018842, 0.017242, 0.014922, None, 3.67, 0.09]
UEHPII = [8, "Cu", 340, 0.01890142857, 0.01861, 0.016, None, 4.07, 0.22]
CEHPII = [9, "Cu", 340, 0.01890142857, 0.01861, 0.016, None, 4.07, 0.22]
Christians = [10, "Cu", 340, 0.01894, 0.0187, 0.01512, None, 1, 0.1]
tubes = [bock_thin_plain_tube, dian_thick_plain_tube, UG40, CG40, UGEWAB5, CGEWAB5, UGEWAKS,
    CGEWAKS, UEHPII, CEHPII, Christians]
if(autoname):
    tube_choice = tube_identifier
else:
    tube_choice = tube_identifier
    print("ENSURE THE CORRECT TUBE IS CHOSEN!")
refrigerants = ['R134A', 'R245FA']
refrigerant_choice = 0
thermocouple_rod = thermocouple_rods[thermocouple_rod_choice]
refrigerant = refrigerants[refrigerant_choice]
configured_probes = thermocouple_rod + [water_flow_rate, refrigerant_flow_rate, top_pressure,
    bottom_pressure]
tube_nb = tubes[tube_choice][0]
material = tubes[tube_choice][1]
k_t = tubes[tube_choice][2]
Do = tubes[tube_choice][3]
Dor = tubes[tube_choice][4]
Di = tubes[tube_choice][5]
Ra = tubes[tube_choice][6]
Ci = tubes[tube_choice][7]
dCi = tubes[tube_choice][8]
```

```
575 Ao = np.pi*Do*(x[-1] - x[0])
576 Ai = np.pi*Di*(x[-1] - x[0])
577 if(test_type_element == "C"):
578     print("Option 1 engaged: CONDENSATION")
579     data_collect()
580     Cp_w = cp.PropsSI("C", "T", T2, "Q", 0, "water")
581     mu_w = cp.PropsSI("V", "T", T2, "Q", 0, "water")
582     rho_w = cp.PropsSI("D", "T", T2, "Q", 0, "water")
583     k_w = cp.PropsSI("L", "T", T2, "Q", 0, "water")
584     Pr_w = mu_w*Cp_w/k_w
585     Re_w = (4/(np.pi*(Di + Dinox)))*(m_w/mu_w)
586     Dh = Di - Dinox
587     Dw = Di + Dinox
588     T_sat = cp.PropsSI("T", "P", P_up, "Q", 1, refrigerant)
589     q = abs(((m_w*Cp_w)/(np.pi*Do))*dT_dx)
590     first_delta_T = T_sat - T1
591     second_delta_T = T_sat - T3
592     TLMTD = (first_delta_T - second_delta_T)/np.log(first_delta_T/second_delta_T)
593     Uo = abs(q/(T_sat - T2))
594     Rw = np.log(Dor/Di)/(2*np.pi*k_t)
595     f = (0.79*np.log(Re_w) - 1.64)**(-2)
596     Nu_Gnielisnki = Ci*((f/8)*(Re_w - 1000)*Pr_w)/(1 + 12.7*(f/8)**0.5*(Pr_w**(2/3) - 1))
597     alpha_i = Nu_Gnielisnki*k_w/(Di - Dinox)
598     alpha_o = 1/(1/Uo - Rw*Do - (1/(alpha_i*Di))*Do)
599     T_s = T_sat - q/alpha_o
600     delta_T = T_sat - T_s
601     Nusselt_alpha_o = Nusselt(T_sat, delta_T)
602     error = abs(((Nusselt_alpha_o - alpha_o)/Nusselt_alpha_o)*100)
603     testing_delta_T = np.linspace(0.5, 20, 100)
604     Nusselt_alpha_o = Nusselt(sum(T_sat)/len(T_sat), testing_delta_T)
605     heat_flux_diagnosis = False
606     if(output):
607         title = name
608         plt.figure(num = title, figsize = (8, 6), dpi = 300)
609         plt.title(title + "\n")
610         plt.xlabel("$\Delta$$T_{sh}$ [K] \n Saturation Temperature to Tube Surface Temperature
     Difference")
611         plt.ylabel("Outside Surface Heat Transfer Coefficient \n $h_O$ [kW/$m^2$K]")
612         if(tube_choice == 0 or tube_choice == 2):
613             plt.plot(testing_delta_T, 1.05*Nusselt_alpha_o/1000, 'y—', label = "5%")
614             plt.plot(testing_delta_T, 0.95*Nusselt_alpha_o/1000, 'y—')
615             plt.plot(testing_delta_T, 1.10*Nusselt_alpha_o/1000, 'g—', label = "10%")
616             plt.plot(testing_delta_T, 0.90*Nusselt_alpha_o/1000, 'g—')
617             plt.plot(testing_delta_T, Nusselt_alpha_o/1000, label = 'Nusselt Solution', color
    = 'red')
618             plt.scatter(delta_T, alpha_o/1000, label = 'Current Study: G1200 Tube, $R_a$ =
    0.05 $\mu$m', color = "blue")
619         else:
620             plt.scatter(delta_T, alpha_o/1000, color = "blue")
621         if(heat_flux_diagnosis):
622             for i in range(len(q)):
623                 plt.gca().annotate(str(round(q[i]/1000)), (delta_T[i], (alpha_o/1000)[i]),
    size = '10')
624         plt.gca().yaxis.set_major_locator(matplotlib.ticker.MultipleLocator(0.1*10))
625         plt.gca().yaxis.set_minor_locator(matplotlib.ticker.MultipleLocator(0.1))
626         plt.gca().xaxis.set_ticks_position('both')
627         plt.gca().yaxis.set_ticks_position('both')
628         if(indicate_stability):
629             for i in range(len(stabilities)):
630                 if(stabilities[i] > tolerance):
631                     plt.scatter(delta_T[i], alpha_o[i]/1000, color = "red")
```

```
        plt.grid()
        plt.show()
        if(save_figures):
            if(os.path.exists(os.getcwd() + "\\Results") == False):
                os.mkdir(os.getcwd() + "\\Results")
            plt.savefig(os.getcwd() + "\\Results\\" + title + ".pdf")
        title = name + " (Heat Flux)"
        plt.figure(title, figsize = (8, 6), dpi = 300)
        plt.title(title + "\n")
        plt.xlabel("q [kW/$m^2$] \n Heat Flux")
        plt.ylabel("Outside Surface Heat Transfer Coefficient \n $h_O$ [kW/$m^2$K]")
        plt.scatter(q/1000, alpha_o/1000)
        if(indicate_stability):
            for i in range(len(stabilities)):
                if(stabilities[i] > tolerance):
                    plt.scatter(q[i]/1000, alpha_o[i]/1000, color = "red")
        plt.gca().yaxis.set_major_locator(matplotlib.ticker.MultipleLocator(0.1*10))
        plt.gca().yaxis.set_minor_locator(matplotlib.ticker.MultipleLocator(0.1))
        plt.gca().xaxis.set_ticks_position('both')
        plt.gca().yaxis.set_ticks_position('both')
        plt.legend()
        plt.grid()
        plt.plot()
        if(save_figures):
            if(os.path.exists(os.getcwd() + "\\Results") == False):
                os.mkdir(os.getcwd() + "\\Results")
            plt.savefig(os.getcwd() + "\\Results\\" + title + ".pdf")
    print("Maximum error deviation between experiment data and Nusselt theoretical prediction: ", round(max(error), 2), " %")
    if(save_data):
        if(os.path.exists(os.getcwd() + "\\Results") == False):
            os.mkdir(os.getcwd() + "\\Results")
        header = ['Nu_Gnielisnki', 'P_down', 'P_up', 'Pr_w', 'Re_w', 'T1', 'T2', 'T3', 'TLMTD', 'T_ave', 'T_s', 'T_sat', 'Uo', 'alpha_i', 'alpha_o', 'bottom_pressure', 'configured_probes',
                  'delta_T', 'f', 'k_w', 'm_r', 'm_w', 'mu_w', 'q', 'refrigerant', 'rho_w', 'thermocouple_rod', 'thermocouple_rod_1', 'thermocouple_rod_2', 'thermocouple_rod_3', 'thermocouple_rod_4',
                  'thermocouple_rod_choice', 'top_pressure', 'tube_choice', 'water_flow_te', 'x', 'Rw', 'Do', 'Di', 'Dh', 'Dw', 'Dor', 'Cp_w']
        body = [Nu_Gnielisnki, P_down, P_up, Pr_w, Re_w, T1, T2, T3, TLMTD, T_ave, T_s, T_sat, Uo, alpha_i, alpha_o, bottom_pressure, configured_probes,
                  delta_T, f, k_w, m_r, m_w, mu_w, q, refrigerant, rho_w, thermocouple_rod, thermocouple_rod_1, thermocouple_rod_2, thermocouple_rod_3, thermocouple_rod_4,
                  thermocouple_rod_choice, top_pressure, tube_choice, water_flow_rate, x, Rw, Do, Di, Dh, Dw, Dor, Cp_w]
        data_dictionary = save_dictionary(header, body, os.getcwd() + "\\Results\\" + name)

        render_csv(data_dictionary, os.getcwd() + "\\Results\\" + name)
if(test_type_element == "PB" or test_type_element == "WP"):
    print("Option 2 engaged: POOL BOILING")
    data_collect()
    Cp_w = cp.PropsSI("C", "T", T2, "Q", 0, "water")
    mu_w = cp.PropsSI("V", "T", T2, "Q", 0, "water")
    rho_w = cp.PropsSI("D", "T", T2, "Q", 0, "water")
    k_w = cp.PropsSI("L", "T", T2, "Q", 0, "water")
    Pr_w = mu_w*Cp_w/k_w
    Re_w = (4/(np.pi*(Di + Dinox)))*(m_w/mu_w)
    Dh = Di - Dinox
    Dw = Di + Dinox
    q = abs(((m_w*Cp_w)/(np.pi*Do))*dT_dx)
```

```
    T_sat = cp.PropsSI("T", "P", P_up, "Q", 0, refrigerant)
    first_delta_T = T_sat - T1
    second_delta_T = T_sat - T3
    TLMTD = (first_delta_T - second_delta_T)/np.log(first_delta_T/second_delta_T)
    Uo = abs(q/(T_sat - T2))
    R_total = 1/(Uo*Ao)
    Rw = Do/(2*k_t)*np.log(Dor/Di)
    R_wall = np.log(Dor/Di)/(2*np.pi*k_t*(x[-1] - x[0]))
    f = (0.79*np.log(Re_w) - 1.64)**(-2)
    Nu_Gnielisnki = Ci*((f/8)*(Re_w - 1000)*Pr_w)/(1 + 12.7*(f/8)**0.5*(Pr_w**(2/3) - 1))
    alpha_i = Nu_Gnielisnki*k_w/(Di - Dinox)
    R_inside = 1/(alpha_i*Ai)
    alpha_o = 1/(1/Uo - Rw - (1/(alpha_i*Di))*Do)
    R_outside = 1/(alpha_o*Ao)
    T_s = T_sat + q/alpha_o
    delta_T = T_s - T_sat
    dq = q_uncertainty(T1, T3, Do, m_w, Cp_w)
    dho = ho_uncertainty(Uo, Rw, alpha_o, Do, Di, T_sat, T1, T3, q, m_w, f, Re_w, Pr_w, k_w,
    mu_w, Cp_w, k_t, Ci, dCi, all_uncertainties = False)
    if(test_type_element == "PB" or test_type_element == "WP"):
        if(Ra != None):
            Pr = P_up/cp.PropsSI("pcrit", "T", T_ave, "Q", 1, refrigerant)
            Rp = Ra/0.4
            M = cp.PropsSI("M", "T", T_ave, "Q", 1, refrigerant)*1000
            Cooper_alpha_o = 90*Pr**(0.12 - 0.2*np.log10(Rp))*(-np.log10(Pr))**(-0.55)*M
    **(-0.5)*q**(0.67)
            error = ((Cooper_alpha_o - alpha_o)/Cooper_alpha_o)*100
        title = name
        if(output):
            plt.figure(num = title, figsize = (8, 6), dpi = 300)
            plt.title(title + "\n")
            plt.xlabel("$q$ [kW/$m^2$] \n Heat Flux")
            plt.ylabel("Tube Outside Surface Heat Transfer Coefficient \n $h_O$ [kW/$m^2$K]")

            plt.scatter(q/1000, alpha_o/1000, label = tube_name)
            if(uncertainty): plt.errorbar(q/1000, alpha_o/1000, yerr = dho/1000, xerr = dq
    /1000, fmt = 'none', ecolor = 'red')
            plt.yscale('log')
            plt.xscale('log')
            plt.gca().xaxis.set_major_formatter(matplotlib.ticker.FormatStrFormatter('%d'))
            plt.gca().xaxis.set_major_locator(matplotlib.ticker.MultipleLocator(10*1))
            plt.gca().xaxis.set_minor_locator(matplotlib.ticker.MultipleLocator(1*1))
            plt.setp(plt.gca().get_xminorticklabels(), visible = False)
            plt.gca().yaxis.set_major_formatter(matplotlib.ticker.FormatStrFormatter('%d'))
            plt.gca().yaxis.set_major_locator(matplotlib.ticker.MultipleLocator(1*10))
            plt.gca().yaxis.set_minor_locator(matplotlib.ticker.MultipleLocator(0.1*10))
            plt.setp(plt.gca().get_yminorticklabels(), visible = False)
            plt.gca().yaxis.set_ticks_position('both')
            plt.gca().xaxis.set_ticks_position('both')
            plt.grid()
            plt.legend()
            if(tube_identifier == 0 or tube_identifier == 1):
                plt.ylim([1, 15])
                plt.xlim([15, 109])
            else:
                plt.ylim([5, 50])
                plt.xlim([15, 109])
            plt.show()

        if(save_figures):
            if(os.path.exists(os.getcwd() + "\\Results") == False):
```

```
                os.mkdir(os.getcwd() + "\\Results")
            plt.savefig(os.getcwd() + "\\Results\\" + title + " (Boiling Curve)" + ".pdf")

        if(Ra != None): print("Maximum error of data with respect to the Cooper Relation: ", round(max(error), 2), " %")

        if(test_type_element == "WP"):
            print("Option 3 amended: WILSON PLOT THERMAL RESISTANCES")
            title = "Thermal Resistances \n" + name
            plt.figure(num = title, figsize = (8, 6), dpi = 300)
            plt.title(title + "\n")
            plt.xlabel("$Re_{w}$ \n Water Reynolds Number", size = 12)
            plt.ylabel("Normalized Thermal Resistances \n $R/Ro$ [K/W]", size = 12)
            plt.scatter(Re_w, R_wall/R_total, label = "$R_w$: Wall")
            plt.scatter(Re_w, R_outside/R_total, label = "$R_o$: Outside")
            plt.scatter(Re_w, R_inside/R_total, label = "$R_i$: Inside")
            plt.grid()
            plt.legend()
            plt.show()

            if(save_figures):
                if(os.path.exists(os.getcwd() + "\\Results") == False):
                    os.mkdir(os.getcwd() + "\\Results")
                plt.savefig(os.getcwd() + "\\Results\\" + title.replace("\n", "") + ".pdf")

        if(save_data):
            if(os.path.exists(os.getcwd() + "\\Results") == False):
                os.mkdir(os.getcwd() + "\\Results")

            header = ['Nu_Gnielisnki', 'P_down', 'P_up', 'Pr_w', 'Re_w', 'T1', 'T2', 'T3', 'TLMTD', 'T_ave', 'T_s', 'T_sat', 'Uo', 'alpha_i', 'alpha_o', 'bottom_pressure', 'configured_probes',
                      'delta_T', 'f', 'k_w', 'm_r', 'm_w', 'mu_w', 'q', 'refrigerant', 'rho_w', 'thermocouple_rod', 'thermocouple_rod_1', 'thermocouple_rod_2', 'thermocouple_rod_3', 'thermocouple_rod_4',
                      'thermocouple_rod_choice', 'top_pressure', 'tube_choice', 'water_flow_te', 'x', 'Rw', 'Do', 'Di', 'Dh', 'Dw', 'Dor', 'Cp_w', 'dho', 'dq']
            body = [Nu_Gnielisnki, P_down, P_up, Pr_w, Re_w, T1, T2, T3, TLMTD, T_ave, T_s, T_sat, Uo, alpha_i, alpha_o, bottom_pressure, configured_probes,
                    delta_T, f, k_w, m_r, m_w, mu_w, q, refrigerant, rho_w, thermocouple_rod, thermocouple_rod_1, thermocouple_rod_2, thermocouple_rod_3, thermocouple_rod_4,
                    thermocouple_rod_choice, top_pressure, tube_choice, water_flow_rate, x, Rw, Do, Di, Dh, Dw, Dor, Cp_w, dho, dq]
            if(Ra != None):
                header.append('error')
                body.append(error)
                header.append('Cooper_alpha_o' + str(Ra))
                body.append(Cooper_alpha_o)
            data_dictionary = save_dictionary(header, body, os.getcwd() + "\\Results\\" + name)

            render_csv(data_dictionary, os.getcwd() + "\\Results\\" + name)


def falling_film(Ra, falling = False):
    data_collect()
    global q
    global first_delta_T
    global second_delta_T
    global TLMTD
    global Cp_w
```

```
    global mu_w
    global rho_w
    global k_w
    global Pr_w
    global Re_w
    global T_sat
    global Cp_rL
    global mu_rL
    global k_rL
    global rho_rL
    global rho_rV
    global h_rV
    global h_rL
    global sigma_ref
    global nu_rL
    global Uo
    global Rw
    global f
    global Nu_Gnielisnki
    global alpha_i
    global alpha_o
    global T_s
    global delta_T
    global sigma
    global ReStar
    global gamma
    global Re_r
    global Dh
    global Dw
    global dho
    global dq
    Cp_w = cp.PropsSI("C", "T", T2, "Q", 0, "water")
    mu_w = cp.PropsSI("V", "T", T2, "Q", 0, "water")
    rho_w = cp.PropsSI("D", "T", T2, "Q", 0, "water")
    k_w = cp.PropsSI("L", "T", T2, "Q", 0, "water")
    Pr_w = mu_w*Cp_w/k_w
    Re_w = (4/(np.pi*(Di + Dinox)))*(m_w/mu_w)
    Dh = Di - Dinox
    Dw = Di + Dinox
    T_sat = cp.PropsSI("T", "P", P_up, "Q", 0, refrigerant)
    Cp_rL = cp.PropsSI("C", "P", P_up, "Q", 0, refrigerant)
    mu_rL = cp.PropsSI('V', 'P', P_up, 'Q', 0, refrigerant)
    k_rL = cp.PropsSI('L', 'P', P_up, 'Q', 0, refrigerant)
    rho_rL = cp.PropsSI('D', 'P', P_up, 'Q', 0, refrigerant)
    rho_rV = cp.PropsSI('D', 'P', P_up, 'Q', 1, refrigerant)
    h_rV = cp.PropsSI('H', 'P', P_up, 'Q', 1, refrigerant)
    h_rL = cp.PropsSI('H', 'P', P_up, 'Q', 0, refrigerant)
    sigma_ref = cp.PropsSI('I', 'P', P_up, 'Q', 0, refrigerant)
    nu_rL = mu_rL/rho_rL
    first_delta_T = T_sat - T1
    second_delta_T = T_sat - T3
    TLMTD = (first_delta_T - second_delta_T)/np.log(first_delta_T/second_delta_T)
    q = abs(((m_w*Cp_w)/(np.pi*Do))*dT_dx)
    Uo = abs(q/(T_sat - T2))
    Rw = Do/(2*k_t)*np.log(Dor/Di)
    f = (0.79*np.log(Re_w) - 1.64)**(-2)
    Nu_Gnielisnki = Ci*((f/8)*(Re_w - 1000)*Pr_w)/(1 + 12.7*(f/8)**0.5*(Pr_w**(2/3) - 1))
    alpha_i = Nu_Gnielisnki*k_w/(Di - Dinox)
    alpha_o = 1/(1/Uo-Rw-1/alpha_i*Do/Di)
    T_s = T_sat + q/alpha_o
    delta_T = T_s - T_sat
```

```
    sigma = (sigma_ref/(g*(rho_rL - rho_rV)))
    ReStar = q*sigma/((h_rV - h_rL)*rho_rV*nu_rL)
    gamma = m_r/(2*L)
    Re_r = 4*gamma/mu_rL
    dq = q_uncertainty(T1, T3, Do, m_w, Cp_w)
    dho = ho_uncertainty(Uo, Rw, alpha_o, Do, Di, T_sat, T1, T3, q, m_w, f, Re_w, Pr_w, k_w,
    mu_w, Cp_w, k_t, Ci, dCi, all_uncertainties = False)
    if(falling):

        title = name
        if(output):
            plt.figure(num = title, figsize = (8, 6), dpi = 300)
            plt.title(title + "\n")
            plt.xlabel("$q$ [kW/$m^2$] \n Heat Flux")
            plt.ylabel("Tube Outside Surface Heat Transfer Coefficient \n $h_O$ [kW/$m^2$K]")

            if(Ra != None):
                if(input("Do you want to add Cooper's Relation to the plot? [y/n]") == 'y'):

                    Pr = P_up/cp.PropsSI("pcrit", "T", T_ave, "Q", 1, refrigerant)
                    Ra = 0.04
                    Rp = Ra/0.4
                    M = cp.PropsSI("M", "T", T_ave, "Q", 1, refrigerant)*1000

                    Cooper_alpha_o = 90*Pr**(0.12 - 0.2*np.log10(Rp))*(-np.log10(Pr))**(-0.55)
    *M**(-0.5)*q**(0.67)
                    q_Cooper, Cooper_alpha_o = sort(q.copy(), Cooper_alpha_o)
                    plt.plot(q_Cooper/1000, (Cooper_alpha_o)/1000, label = 'Cooper Relation:
    $Ra = $'+str(Ra)+" $\mu$m", color = 'red')
                if(input("Do you want to add the Ribatski Relation to the plot?") == 'y'):
                    T_V = T_sat
                    plt.plot(q/1000, Ribatski07(T_sat, T_V, q, m_r, Ra, Do, refrigerant, L)
    /1000, label = 'Ribatski and Thome Model: $R_a$ = ' + str(Ra) + ' $\mu$m')
                if(input("Do you want to add the Gorenflo Relation to the plot?") == 'y'):
                    plt.plot(q/1000, Gorenflo10(T_sat, Ra, q, refrigerant)/1000, label = '
    Gorenflo Model: $R_a$ = ' + str(Ra) + ' $\mu$m')
            plt.scatter(q/1000, alpha_o/1000, label = 'GEWA-B')
            plt.yscale('log')
            plt.xscale('log')
            plt.gca().xaxis.set_major_formatter(matplotlib.ticker.FormatStrFormatter('%d'))
            plt.gca().xaxis.set_major_locator(matplotlib.ticker.MultipleLocator(10))
            plt.gca().xaxis.set_minor_locator(matplotlib.ticker.MultipleLocator(1))
            plt.setp(plt.gca().get_xminorticklabels(), visible = False)
            plt.gca().yaxis.set_major_formatter(matplotlib.ticker.FormatStrFormatter('%d'))
            plt.gca().yaxis.set_major_locator(matplotlib.ticker.MultipleLocator(1))
            plt.gca().yaxis.set_minor_locator(matplotlib.ticker.MultipleLocator(0.1))
            plt.setp(plt.gca().get_yminorticklabels(), visible = False)
            plt.gca().yaxis.set_ticks_position('both')
            plt.gca().xaxis.set_ticks_position('both')
            if(tube_identifier == 0 or tube_identifier == 1):
                plt.ylim([1, 15])
                plt.xlim([15, 109])
            else:
                plt.ylim([5, 50])
                plt.xlim([15, 109])
            plt.grid()
            plt.legend()
            plt.show()

        if(save_figures):
            if(os.path.exists(os.getcwd() + "\\Results") == False):
```

```
                os.mkdir(os.getcwd() + "\\Results")
            plt.savefig(os.getcwd() + "\\Results\\" + title + ".pdf")

        if(save_data):
            if(os.path.exists(os.getcwd() + "\\Results") == False):
                os.mkdir(os.getcwd() + "\\Results")


            header = ['Nu_Gnielisnki', 'P_down', 'P_up', 'Pr_w', 'Re_w', 'T1', 'T2', 'T3', '
    TLMTD', 'T_ave', 'T_s', 'T_sat', 'Uo', 'alpha_i', 'alpha_o', 'bottom_pressure', '
    configured_probes', 'delta_T', 'f', 'k_w', 'm_r', 'm_w', 'mu_w', 'q', 'refrigerant', '
    rho_w', 'thermocouple_rod', 'thermocouple_rod_1', 'thermocouple_rod_2', '
    thermocouple_rod_3', 'thermocouple_rod_4', 'thermocouple_rod_choice', 'top_pressure', '
    tube_choice', 'water_flow_rate', 'x', 'gamma', 'Re_r', 'Rw', 'Do', 'Di', 'Dh', 'Dw', 'Dor
    ', 'Cp_w', 'dho', 'dq']
            body = [Nu_Gnielisnki, P_down, P_up, Pr_w, Re_w, T1, T2, T3, TLMTD, T_ave, T_s,
    T_sat, Uo, alpha_i, alpha_o, bottom_pressure, configured_probes, delta_T, f, k_w, m_r, m_w
    , mu_w, q, refrigerant, rho_w, thermocouple_rod, thermocouple_rod_1, thermocouple_rod_2,
    thermocouple_rod_3, thermocouple_rod_4, thermocouple_rod_choice, top_pressure, tube_choice
    , water_flow_rate, x, gamma, Re_r, Rw, Do, Di, Dh, Dw, Dor, Cp_w, dho, dq]
            data_dictionary = save_dictionary(header, body, os.getcwd() + "\\Results\\" + name
    )

            render_csv(data_dictionary, os.getcwd() + "\\Results\\" + name)

if(test_type_element == "FF"):
    print("Option 4 engaged: FALLING FILM BOILING")
    falling_film(Ra, falling = True)
if(test_type_element == "RS"):
    print("Option 5 engaged: FALLING FILM REYNOLDS SWEEP")
    falling_film(Ra, falling = False)
    q_RS = round(stats.mean(q)/1000/10)*10
    max_gamma = 0
    max_gamma_position = 0
    for i in range(len(gamma)):
        if(gamma[i] > max_gamma):
            max_gamma = gamma[i]
            max_gamma_position = i
    alpha_o_base = alpha_o[max_gamma_position]
    alpha_o_normalized = alpha_o/alpha_o_base
    title = "$\Gamma_r$: " + name
    plt.figure(num = title, figsize = (8, 6), dpi = 300)
    plt.title(title + "\n" + " at " + str(q_RS) + " $kW/m^2$ + \n")
    plt.xlabel("$\Gamma_r$ \n $[kg/(s \cdot m)]$")
    plt.ylabel("Outside Surface Heat Transfer Coefficient \n $h_O$ [kW/$m^2$K]")
    plt.scatter(gamma, alpha_o/1000, label = tube_name, color = "black")
    plt.gca().yaxis.set_ticks_position('both')
    plt.gca().xaxis.set_ticks_position('both')
    plt.ylim([0, max(alpha_o/1000)+1])
    plt.grid()
    plt.show()
    if(save_figures):
        if(os.path.exists(os.getcwd() + "\\Results") == False):
            os.mkdir(os.getcwd() + "\\Results")
        plt.savefig(os.getcwd() + "\\Results\\Gamma " + name + ".pdf")
    title = "$Re_r$: " + name
    plt.figure(num = title, figsize = (8, 6), dpi = 300)
    plt.title(title +"\n" + " at " + str(q_RS) + " $kW/m^2$ + \n")
    plt.xlabel("$Re_r$")
    plt.ylabel("Outside Surface Heat Transfer Coefficient \n $h_O$ [kW/$m^2$K]")
    plt.scatter(Re_r, alpha_o/1000, label = tube_name, color = "black")
```

```
    plt.gca().yaxis.set_ticks_position('both')
    plt.gca().xaxis.set_ticks_position('both')
    plt.ylim([0, max(alpha_o/1000)+1])
    plt.grid()
    plt.show()
    if(save_figures):
        if(os.path.exists(os.getcwd() + "\\Results") == False):
            os.mkdir(os.getcwd() + "\\Results")
        plt.savefig(os.getcwd() + "\\Results\\Re " + name + ".pdf")
    if(save_data):
        if(os.path.exists(os.getcwd() + "\\Results") == False):
            os.mkdir(os.getcwd() + "\\Results")

        header = ['Nu_Gnielisnki', 'P_down', 'P_up', 'Pr_w', 'Re_w', 'T1', 'T2', 'T3', 'TLMTD', 'T_ave', 'T_s', 'T_sat', 'Uo', 'alpha_i', 'alpha_o', 'bottom_pressure', 'configured_probes', 'delta_T', 'f', 'k_w', 'm_r', 'm_w', 'mu_w', 'q', 'refrigerant', 'rho_w', 'thermocouple_rod', 'thermocouple_rod_1', 'thermocouple_rod_2', 'thermocouple_rod_3', 'thermocouple_rod_4', 'thermocouple_rod_choice', 'top_pressure', 'tube_choice', 'water_flow_rate', 'x', 'gamma', 'Re_r', 'Rw', 'Do', 'Di', 'Dh', 'Dw', 'Dor', 'Cp_w', 'dho', 'dq', 'alpha_o_normalized']
        body = [Nu_Gnielisnki, P_down, P_up, Pr_w, Re_w, T1, T2, T3, TLMTD, T_ave, T_s, T_sat, Uo, alpha_i, alpha_o, bottom_pressure, configured_probes, delta_T, f, k_w, m_r, m_w, mu_w, q, refrigerant, rho_w, thermocouple_rod, thermocouple_rod_1, thermocouple_rod_2, thermocouple_rod_3, thermocouple_rod_4, thermocouple_rod_choice, top_pressure, tube_choice, water_flow_rate, x, gamma, Re_r, Rw, Do, Di, Dh, Dw, Dor, Cp_w, dho, dq, alpha_o_normalized]
        data_dictionary = save_dictionary(header, body, os.getcwd() + "\\Results\\" + name + " at {} kWm2".format(str(q_RS)))

        render_csv(data_dictionary, os.getcwd() + "\\Results\\" + name + " at {} kWm2".format(str(q_RS)))
print()
print("Stabilities:")
print(np.round(np.array(stabilities), 3))
print()
print("Unstable File Names:")
for m in unstable_files:
    print(m)
if(test_type_element == "WP"):
    T_sat = cp.PropsSI("T", "P", P_up, "Q", 1, refrigerant)
    Cp_w = cp.PropsSI("C", "T", T2, "Q", 0, "water")
    mu_w = cp.PropsSI("V", "T", T2, "Q", 0, "water")
    rho_w = cp.PropsSI("D", "T", T2, "Q", 0, "water")
    k_w = cp.PropsSI("L", "T", T2, "Q", 0, "water")
    Pr_w = mu_w*Cp_w/k_w
    Re_w = (4/(np.pi*(Di + Dinox)))*(m_w/mu_w)
    qo = q
    dqo = dq
    Uo_measured = qo/(T2 - T_sat)
    f = (0.79*np.log(Re_w) - 1.64)**(-2)
    hgni = (((f/8)*(Re_w - 1000)*Pr_w)/(1 + 12.7*(f/8)**0.5*(Pr_w**(2/3) - 1)))*(k_w/(Di - Dinox))

    stdev_q = stats.stdev(qo)
    ave_q = stats.mean(qo)
    stringency = 1.5

    qo_new = []
    dqo_new = []
    Uo_measured_new = []
    f_new = []
```

```
    hgni_new = []
    T_sat_new = []
    T2_new = []
    Cp_w_new = []
    Nu_Gnielisnki_new = []
    P_down_new = []
    P_up_new = []
    Pr_w_new = []
    R_inside_new = []
    R_outside_new = []
    R_total_new = []
    Re_w_new = []
    T1_new = []
    T3_new = []
    TLMTD_new = []
    T_ave_new = []
    T_s_new = []
    Uo_new = []
    alpha_i_new = []
    alpha_o_new = []
    dT_dx_new = []
    delta_T_new = []
    dho_new = []
    dq_new = []
    k_w_new = []
    m_r_new = []
    m_w_new = []
    mu_w_new = []
    rho_w_new = []

    for i in range(len(qo)):
        if((qo[i] >= ave_q - stringency*stdev_q) and (qo[i] <= ave_q + stringency*stdev_q)):
            qo_new.append(qo[i])
            dqo_new.append(dqo[i])
            Uo_measured_new.append(Uo_measured[i])
            f_new.append(f[i])
            hgni_new.append(hgni[i])
            T_sat_new.append(T_sat[i])
            T2_new.append(T2[i])
            Cp_w_new.append(Cp_w[i])
            Nu_Gnielisnki_new.append(Nu_Gnielisnki[i])
            P_down_new.append(P_down[i])
            P_up_new.append(P_up[i])
            Pr_w_new.append(Pr_w[i])
            R_inside_new.append(R_inside[i])
            R_outside_new.append(R_outside[i])
            R_total_new.append(R_total[i])
            Re_w_new.append(Re_w[i])
            T1_new.append(T1[i])
            T3_new.append(T3[i])
            TLMTD_new.append(TLMTD[i])
            T_ave_new.append(T_ave[i])
            T_s_new.append(T_s[i])
            Uo_new.append(Uo[i])
            alpha_i_new.append(alpha_i[i])
            alpha_o_new.append(alpha_o[i])
            dT_dx_new.append(dT_dx[i])
            delta_T_new.append(delta_T[i])
            dho_new.append(dho[i])
            dq_new.append(dq[i])
            k_w_new.append(k_w[i])
```

```
            m_r_new.append(m_r[i])
            m_w_new.append(m_w[i])
            mu_w_new.append(mu_w[i])
            rho_w_new.append(rho_w[i])

    qo = np.array(qo_new)
    dqo = np.array(dqo_new)
    Uo_measured = np.array(Uo_measured_new)
    f = np.array(f_new)
    hgni = np.array(hgni_new)
    T_sat = np.array(T_sat_new)
    T2 = np.array(T2_new)
    Cp_w = np.array(Cp_w_new)
    Nu_Gnielisnki = np.array(Nu_Gnielisnki_new)
    P_down = np.array(P_down_new)
    P_up = np.array(P_up_new)
    Pr_w = np.array(Pr_w_new)
    R_inside = np.array(R_inside_new)
    R_outside = np.array(R_outside_new)
    R_total = np.array(R_total_new)
    Re_w = np.array(Re_w_new)
    T1 = np.array(T1_new)
    T3 = np.array(T3_new)
    TLMTD = np.array(TLMTD_new)
    T_ave = np.array(T_ave_new)
    T_s = np.array(T_s_new)
    Uo = np.array(Uo_new)
    alpha_i = np.array(alpha_i_new)
    alpha_o = np.array(alpha_o_new)
    dT_dx = np.array(dT_dx_new)
    delta_T = np.array(delta_T_new)
    dho = np.array(dho_new)
    dq = np.array(dq_new)
    k_w = np.array(k_w_new)
    m_r = np.array(m_r_new)
    m_w = np.array(m_w_new)
    mu_w = np.array(mu_w_new)
    rho_w = np.array(rho_w_new)

    k = k_t
    Ao = np.pi*Do*(x[-1] - x[0])
    Ai = np.pi*Di*(x[-1] - x[0])
    L = x[-1] - x[0]


    dhgni = 0
    dL = ((2*0.001)**2 + (0.5*0.001)**2)**(0.5)
    dDi = ((2*0.00001)**2 + (0.5*0.00001)**2 )**(0.5)
    dDo = ((2*0.00001)**2 + (0.5*0.00001)**2 )**(0.5)
    dk = 0.04
    dT_sat = 0.01*T_sat
    dT2 = 0.1

    dAidDi = np.pi*L
    dAidL = np.pi*Di
    dAi = np.sqrt((dAidDi*dDi)**2 + (dAidL*dL)**2)
    dx = np.sqrt(dhgni**2/(Ai**2 * hgni**4) + dAi**2/(Ai**4 * hgni**2))


    dAo = np.sqrt(np.pi**2*Do**2*dL**2 + np.pi**2*L**2*dDo**2)
    dUo = np.sqrt(dT2**2*qo**2/(T2 - T_sat)**4 + dT_sat**2*qo/(T2 - T_sat)**2 + dqo**2/(T2 -
```

```
    T_sat)**2)
1129    dy = np.sqrt(dk**2*np.log(Do/Di)**2/(4*np.pi**2*L**2*k**4) + dL**2*np.log(Do/Di)**2/(4*np.
        pi**2*L**4*k**2) + dDo**2/(4*np.pi**2*Do**2*L**2*k**2) + dDi**2/(4*np.pi**2*Di**2*L**2*k
        **2) + dUo**2/(Ao**2*Uo**4) + dAo**2/(Ao**4*Uo**2))
1130
1131
1132    hypotenuse_uncertainty = (dx**2 + dy**2)**0.5
1133    influence = max(hypotenuse_uncertainty) - hypotenuse_uncertainty
1134    weights = influence/sum(influence)
1135    a, b = bestfit(1/(hgni*Ai), (1/(Uo_measured*Ao) - np.log(Do/Di)/(2*np.pi*k*L)), 1)
1136    Ci = 1/a
1137    Uo_predicted = (( 1/(Ci*hgni*Ai) + np.log(Do/Di)/(2*np.pi*k*L) + b)**(-1))/Ao
1138    Uo_m, Uo_c = bestfit(Uo_predicted, Uo_measured, 1)
1139    plt.figure("Wilson Plot Regression", figsize = (8, 6), dpi = 300)
1140    plt.title(name + "\n and constant heat flux of {} $kW/m^2$".format(str(int(np.round(stats.
        mean(qo/1000)/10)*10))) + "\n")
1141    plt.xlabel("$\dfrac{1}{h_{gni} \cdot A_i}$", size = 12)
1142    plt.ylabel("$\dfrac{1}{U_o \cdot A_o} \; - \; \dfrac{ln(D_o/D_i)}{2 \cdot \pi \cdot k \
        cdot L}$", size = 12)
1143    plt.scatter(1/(hgni*Ai), 1/(Uo_measured*Ao) - np.log(Do/Di)/(2*np.pi*k*L))
1144    x = np.linspace(plt.gca().get_xlim()[0], plt.gca().get_xlim()[1], 1000)
1145    plt.plot(x, a*x + b)
1146    plt.grid()
1147    plt.show()
1148    print("Ci = ", Ci)
1149
1150    if(save_figures):
1151        if(os.path.exists(os.getcwd() + "\\Results") == False):
1152            os.mkdir(os.getcwd() + "\\Results")
1153        if(os.path.exists(os.getcwd() + "\\Results") == False):
1154            os.mkdir(os.getcwd() + "\\Results")
1155        plt.savefig(os.getcwd() + "\\Results\\" + name + " (Wilson Plot Regression)" + ".pdf")
1156    plt.figure("Overall Comparisons", figsize = (8, 6), dpi = 300)
1157    plt.title("Overall Heat Transfer Coefficients Comparison \n")
1158    plt.xlabel("Predicted $U_o$", size = 12)
1159    plt.ylabel("Measured $U_o$", size = 12)
1160    plt.scatter(Uo_predicted, Uo_measured)
1161    x = np.linspace(plt.gca().get_xlim()[0], plt.gca().get_xlim()[1], len(Uo_measured))
1162    plt.plot(x, Uo_m*x + Uo_c)
1163    plt.grid()
1164    plt.show()
1165    print("Gradient of bestfit (Ideally 1): Uo_m = ", Uo_m)
1166    print("Offset (Ideally 0): Uo_c = ", Uo_c)
1167    print("Correlation Constant: r = ", correlation(Uo_m*x + Uo_c, Uo_measured)["correlation"
        ])
1168
1169    if(save_figures):
1170        if(os.path.exists(os.getcwd() + "\\Results") == False):
1171            os.mkdir(os.getcwd() + "\\Results")
1172        if(os.path.exists(os.getcwd() + "\\Results") == False):
1173            os.mkdir(os.getcwd() + "\\Results")
1174        plt.savefig(os.getcwd() + "\\Results\\" + name + " (Measured and Predicted Comparison)
    " + ".pdf")
1175    if(save_data):
1176        if(os.path.exists(os.getcwd() + "\\Results") == False):
1177            os.mkdir(os.getcwd() + "\\Results")
1178
1179        header = ['Nu_Gnielisnki', 'P_down', 'P_up', 'Pr_w', 'Re_w', 'T1', 'T2', 'T3', 'TLMTD'
    , 'T_ave', 'T_s', 'T_sat', 'Uo', 'alpha_i', 'alpha_o', 'bottom_pressure', '
    configured_probes', 'delta_T', 'f', 'k_w', 'm_r', 'm_w', 'mu_w', 'q', 'refrigerant', '
    rho_w', 'thermocouple_rod', 'thermocouple_rod_1', 'thermocouple_rod_2', '
```

```
    thermocouple_rod_3', 'thermocouple_rod_4', 'thermocouple_rod_choice', 'top_pressure', '
    tube_choice',  'water_flow_rate', 'x', 'Rw', 'Do', 'Di', 'Dh', 'Dw', 'Dor', 'Cp_w', 'dho',
     'dq', 'Ci']
1180        body = [Nu_Gnielisnki, P_down, P_up, Pr_w, Re_w, T1, T2, T3, TLMTD, T_ave, T_s, T_sat,
     Uo, alpha_i, alpha_o, bottom_pressure, configured_probes, delta_T, f, k_w, m_r, m_w, mu_w
    , q, refrigerant, rho_w, thermocouple_rod, thermocouple_rod_1, thermocouple_rod_2,
    thermocouple_rod_3, thermocouple_rod_4, thermocouple_rod_choice, top_pressure, tube_choice
    , water_flow_rate, x, Rw, Do, Di, Dh, Dw, Dor, Cp_w, dho, dq, Ci]
1181        data_dictionary = save_dictionary(header, body, os.getcwd() + "\\Results\\" + name)
1182
1183        render_csv(data_dictionary, os.getcwd() + "\\Results\\" + name)
1184
1185 else:
1186     print("This dataset is not suited for the Wilson Plot Analysis!")
1187
1188
```

Appendix J:
Heat Flux Calculation End-Point Temperatures

By previous studies, the gradient $\frac{dT_w}{dx}$ is estimated at the midpoint of the first and the last thermocouple positions (the tube section length considered) to be used in equation (4.1). Using estimate derivatives of polynomial equations become a tedious application in calculations. Calculus theory was therefore applied to develop equation (4.1) to a practical form to provide the exact tube midpoint gradient:

By the Mean Value Theorem, there exists at least one point, σ, along a function curve between two points, θ and λ, where the gradient at that point is equal to the average gradient between those two points:

$$f'(\sigma) = \frac{f(\theta) - f(\lambda)}{\theta - \lambda} \tag{J.25}$$

Knowing that the polynomial fit is a 2^{nd} degree polynomial equation, the generalized form is as shown in equation (J.26):

$$f(x) = ax^2 + bx + c \tag{J.26}$$

Combining equations (J.26) and (J.25) with inputs of θ, λ and σ; the following is achieved in equation (J.27):

$$\sigma = \frac{\theta + \lambda}{2} \tag{J.27}$$

Observing equation (J.27), it is seen that the point which the Mean Value Theorem refers to is between the first and the last point. Hereby, with equations (J.27) and (J.25), the exact gradient at the midpoint is calculated using the inlet and outlet and the local heat flux at the middle of the tube is determined using equations (J.28) and (J.29). $C_{w,p}$ is obtained from *CoolProp* at the average water temperature from equation (4.2) below:

$$L = x_{out} - x_{in} \tag{J.28}$$

$$\dot{q}_o = \frac{m_w C_{w,p}(T_{w,out} - T_{w,in})}{\pi D_o (x_{out} - x_{in})} = \frac{m_w C_{w,p}(T_{w,out} - T_{w,in})}{\pi D_o L} \tag{J.29}$$

Appendix K: Additional Results

K.17 Pool Boiling

Additional observations for the EHPII tube is described below for the 60 kW/m^2 case, since it portrays similar information to those given by the 20 kW/m^2 and 100 kW/m^2 cases:

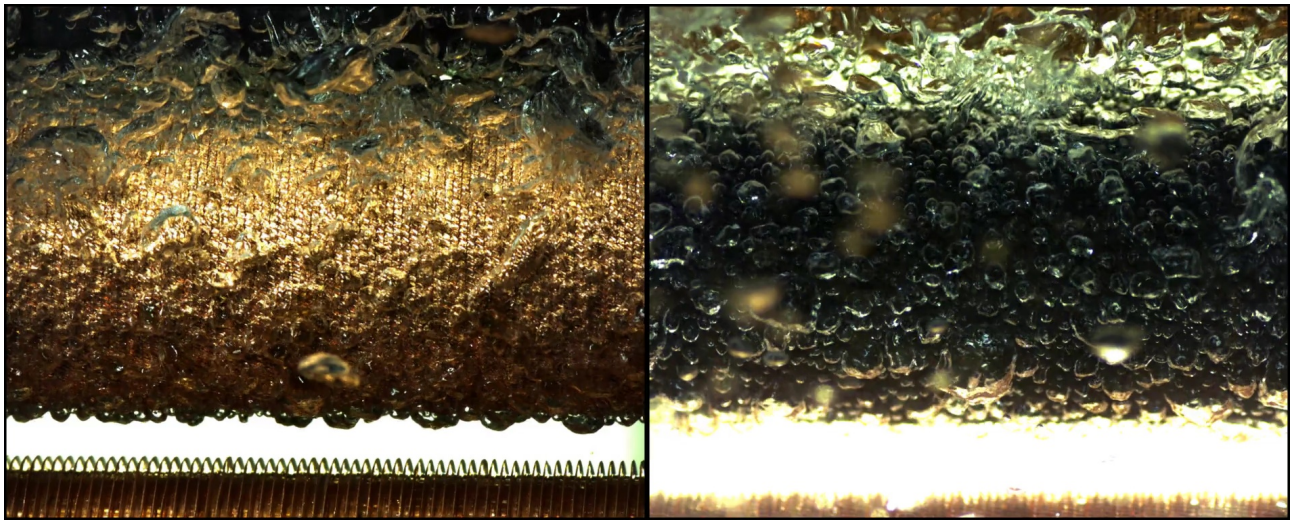

(i) Uncoated (ii) Coated

(a) 5°C

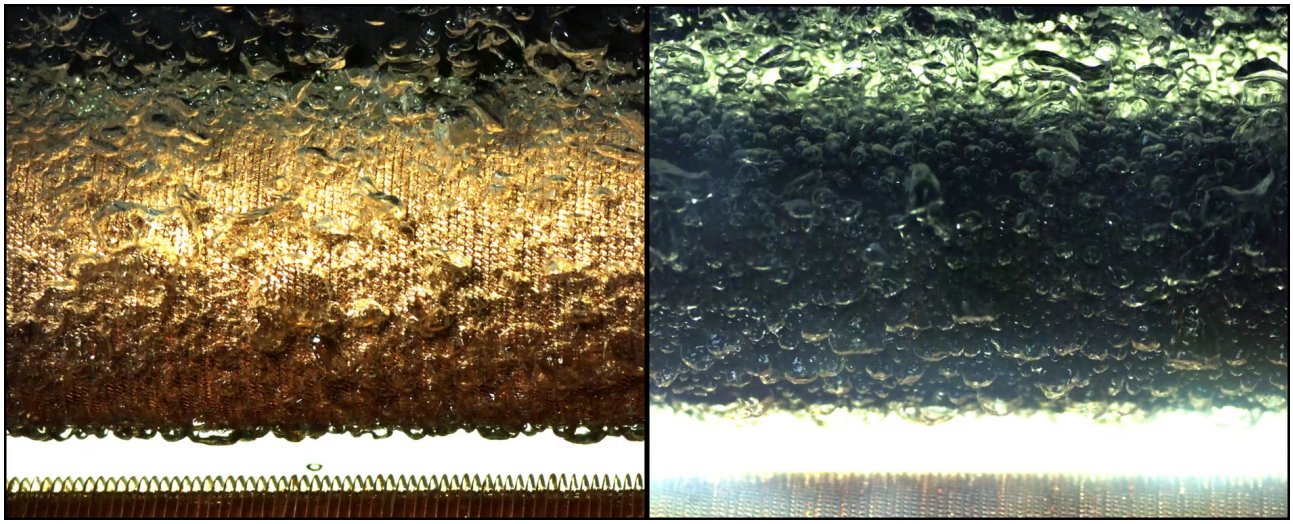

(i) Uncoated (ii) Coated

(b) 25°C

Figure K.12: Pool boiling comparison of EHPII at 60 kW/m^2

When the high speed footage at 60 kW/m^2 is analyzed, it is seen again that the bubble sizes were larger for the coated EHPII tube than the uncoated EHPII tube. The bubble density is visually inspected to be relatively the same between the uncoated and coated EHPII tubes in both saturation temperature cases.

Furthermore, no other difference across the saturation temperatures could be identified other

than the bubble sizes being bigger for the lower saturation temperature because of the lower saturation pressure acting on the bubbles. This correlates with the pool boiling HTCs in Figure 7.11 being similar at this point.

K.18 Condensation

The condensation data from the current study was also validated against Zhao and Gstöhl for a smooth copper tube in the heat flux domain. The dataset of Zhao was, however, at a saturation temperature of $T_{sat} = 40°C$ and was only used as reference. The relative comparison was made in Figure K.13:

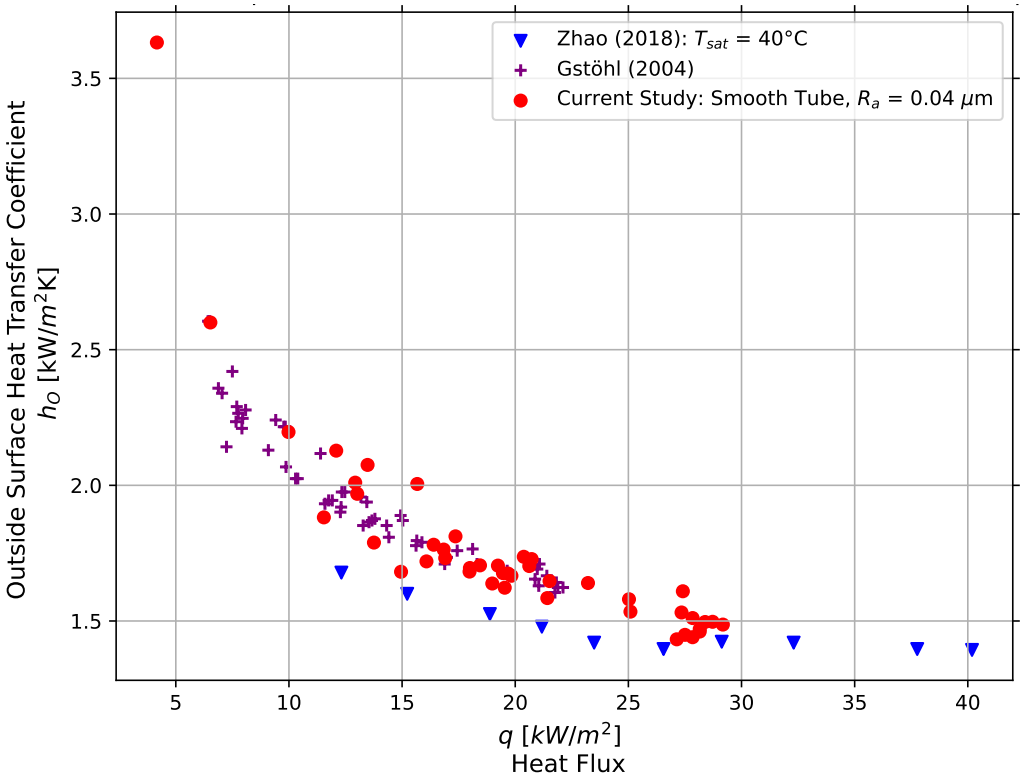

Figure K.13: Smooth tube condensation test validation with respect to heat flux

Studying Figure K.13, it was found that the condensation data of the current study compliments data from Zhao well despite the saturation temperature difference. The results were in good accordance with condensation data from Gstöhl ($T_{sat} = 30°C$).

Appendix L:
Wilson Plot Investigation

L.19 Motivation for LTCM Wilson Plot Analyses

The Wilson Plot methodology has been developed over time and was modified as required based on the types of tubes being studied regarding the proportionality of the thermal resistances of the tube. The reliability of the results from the Wilson Plot analysis was dependent on the thermal resistance ratios of the tube regarding the wall thermal resistance, R_t, the tube outside resistance, R_o, and the tube inside resistance, R_i. These were taken into account in deciding which Wilson Plot analysis method was best for calculating the inside characterisation coefficient.

Known as the LTCM method, it was originally brought up by Wilson [91], was implemented by Briggs and Young [92] and modified by Christians, Van Rooyen and Thome [73] to accommodate enhanced tube Wilson Plot analyses.

It was particularly difficult to characterise micro-enhanced tubes since both sides of the tube wall were often enhanced, posing an equal thermal resistance weight on both the outside and inside thermal resistances. The Wilson Plot method used in the current study was found to be most reliable for analyzing the enhanced tubes for which it was specially developed despite having the outside and inside thermal resistances closely matching. This was seen through validation of Wilson Plot coefficients between the Smooth Tube and the Roughened Tube where the inside thermal resistance was significantly less than the outside thermal resistance in the case of using constant heat flux of 20 $kW/m^2$for the Smooth Tube, whereas the inside thermal resistance was more than the outside thermal resistance using a constant heat flux of 50 $kW/m^2$for the Roughened Tube. Nevertheless, both analyses achieved the same results. It was found by conducting the LTCM Wilson Plot test at 100 kW/m^2in pool boiling configuration that the inside thermal resistance was mostly matched to the outside thermal resistance to guarantee accurate results. The uncertainty at a higher heat flux was also much less, ensuring a more reliable calculation of the inside Wilson Plot coefficient using the LTCM approach. It could also be seen by the assumption in equation (L.33) below that the outside thermal resistance in equation (L.30) would tend to be lower with a higher heat constant flux.

The Wilson Plot coefficients were obtained in section L.20 below, where after the thermal resistances and visual rendering of the Wilson Plot regression analyses were portrayed in section L.21.

L.20 Wilson Plot Coefficients

The LTCM Wilson Plot method employed a secondary regression step where a regression line was fit through a dense cluster of points that was *conceptually* only to be a single point since the heat flux was ideally kept constant. In order to alleviate any mathematical discrepancy, the following simple non-iterative Wilson Plot approach was derived.

Starting with the overall heat transfer thermal resistances equation:

$$\frac{1}{U_o \cdot A_o} = \frac{1}{h_i \cdot A_i} + \frac{\ln D_o/D_i}{2 \cdot k_t \cdot L \cdot \pi} + \frac{1}{h_o \cdot A_o} \tag{L.30}$$

The equation (L.30) was re-ordered to be in the following form:

$$\frac{1}{U_o \cdot A_o} - \frac{\ln D_o/D_i}{2 \cdot k_t \cdot L \cdot \pi} = \frac{1}{h_i \cdot A_i} + \frac{1}{h_o \cdot A_o} \tag{L.31}$$

Where the inside HTC was retrieved from the Gnielinski correlation:

$$h_i = C_i \cdot h_{Gnie} \tag{L.32}$$

The changing variables in the Wilson Plot was recognised to be T_{mid} in the calculation of the overall heat transfer coefficient equation for U_o; and the Reynolds number Re_w contained within the Gnielinski correlation for h_{Gnie}.

The outside HTC in equation (L.31) was initially assumed to be the boiling curve form:

$$h_o = C_o \cdot q_o^m \tag{L.33}$$

In compliance to the LTCM method's assumed outside HTC form, it was recognized that all the parameters contained within equation (L.33) are constants being solved for through iteration, or are *conceptually* constant in the case of heat flux q_o (a boiling curve is a function of heat flux where a singular HTC was expected for each heat flux point). The outside area, A_o, was also constant.

Hereby, without neglecting any possible influence on the inside Wilson Plot coefficient C_i, the following Wilson Plot regression form was developed from equation (L.34) to equation (L.35):

$$\frac{1}{U_o \cdot A_o} - \frac{\ln D_o/D_i}{2 \cdot k_t \cdot L \cdot \pi} = \frac{1}{C_i} \cdot \frac{1}{h_{Gnie} \cdot A_i} + \frac{1}{C_o \cdot q_o^m \cdot A_o} \tag{L.34}$$

$$\frac{1}{U_o \cdot A_o} - \frac{\ln D_o/D_i}{2 \cdot k_t \cdot L \cdot \pi} = \frac{1}{C_i} \cdot \frac{1}{h_{Gnie} \cdot A_i} + C \tag{L.35}$$

The straight line regression was applied to equation (L.35) in the form:

$$y = m \cdot x + C \tag{L.36}$$

Where the following associations were made between equations (L.36) and (L.35):

$$y = \frac{1}{U_o \cdot A_o} - \frac{\ln D_o/D_i}{2 \cdot k_t \cdot L \cdot \pi} \tag{L.37}$$

$$m = \frac{1}{C_i} \tag{L.38}$$

$$x = \frac{1}{h_{Gnie} \cdot A_i} \tag{L.39}$$

$$C = \frac{1}{C_o \cdot q_o^m \cdot A_o} \tag{L.40}$$

The linear regression hereby also solved for C, but had no relevance in the data reduction afterwards. The uncertainty in C would also have no effect on C_i, since this was only acting in a vertical shift of the regression line.

The LTCM method included the uncertainty of each point as weightings to adjust the regression line. The incorporation of weightings was left out in the above approach since the filtering of the heat flux domain caused disproportionate weightings to the regression applied to the Wilson Plot leading to poor results.

To accommodate the skill of the researcher to keep the heat flux constant, the following filter was applied to the heat flux domain before Wilson Plot analysis:

$$x \in \{x |\, x - S \cdot \sigma_x \leqslant x \leqslant x + S \cdot \sigma_x\} \tag{L.41}$$

Where the stringency parameter, S, was investigated to be best set at 1.5 to correspond to an approximate 86.64% of data retention and ensuring a quality domain for the Wilson Plot analysis.

The above approach also applied to the same Wilson Plot data-sets to support the LTCM Wilson Plot results, where the Wilson Plot coefficients for the uncoated and coated tubes in the current study were separately analysed in Table L.5 to deduce similarity:

Table L.5: Separate Wilson Plot coefficients for uncoated and coated tubes

Surface Condition	Tube Name	1st	2nd	3rd	Average	Standard Deviation	Uncertainty	Analysis Method
Uncoated	Smooth	1.26					0.10	LTCM
	Roughened	1.22					0.10	
	GEWA-B5	4.08					0.15	
	GEWA-KS	3.74	3.65	3.68	3.69	0.04	0.07	
	EHPII	4.17	4.15	4.17	4.17	0.01	0.02	
Coated	GEWA-KS	3.60	3.70		3.65	0.05	0.10	
	EHPII	3.92	3.96		3.94	0.02	0.04	
Uncoated	Smooth	1.28						CERG
	Roughened	1.20						
	GEWA-B5	4.20						
	GEWA-KS	3.91	3.86	3.83	3.86	0.03	0.06	
	EHPII	4.48	4.50	4.52	4.50	0.02	0.03	
Coated	GEWA-KS	3.83	3.85		3.84	0.01	0.02	
	EHPII	4.24	4.29		4.27	0.02	0.04	

Where the uncertainties of the Smooth Tube, Roughened Tube and GEWA-B5 tube using the LTCM method were obtained from previous studies and only single Wilson Plot analyses were performed for validation [1, 93].

Comparing the difference in Wilson Plot coefficients between the uncoated and coated tube types, it was seen from Table L.5 in section 6 that there was not much difference between them. These findings motivated the same Wilson Plot coefficient to be used for a tube type regardless if they were uncoated or coated.

The difference in results between the iterative and non-iterative methods were expected since they are obtained from different approaches. However, as the deviation between the results are reasonable yet close, the Wilson Plot coefficients are verified. The LTCM Wilson Plot coefficients indicated by the blue coloured cells in Table 6.1 were the were to be used for the respective tube type.

L.21 Thermal Resistances for Wilson Plot Analyses

Samples of the Wilson Plot analyses using the CERG method were depicted below, where the Wilson Plot regression for each tube type was done. After the Wilson Plot coefficients were obtained, it was possible to view the thermal resistance ratios at each testing water Reynolds number.

L.21.1 Smooth Tube

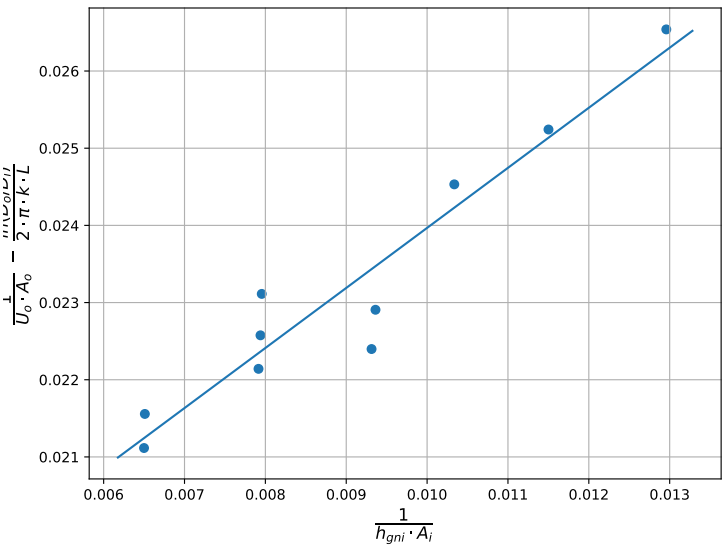

Wilson Plot regression

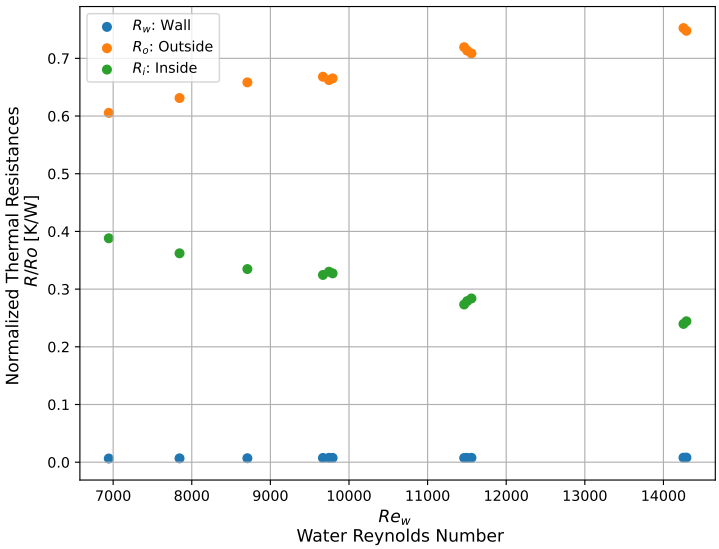

Thermal resistances

Figure L.14: Wilson Plot analysis of Smooth Tube

The Wilson plot regression for the Smooth Tube was depicted in Figure L.14. The thermal resistance ratios show that the internal thermal resistance was very low compared to the outside thermal resistance, yet the expected Wilson Plot coefficient was obtained.

L.21.2 Roughened Tube

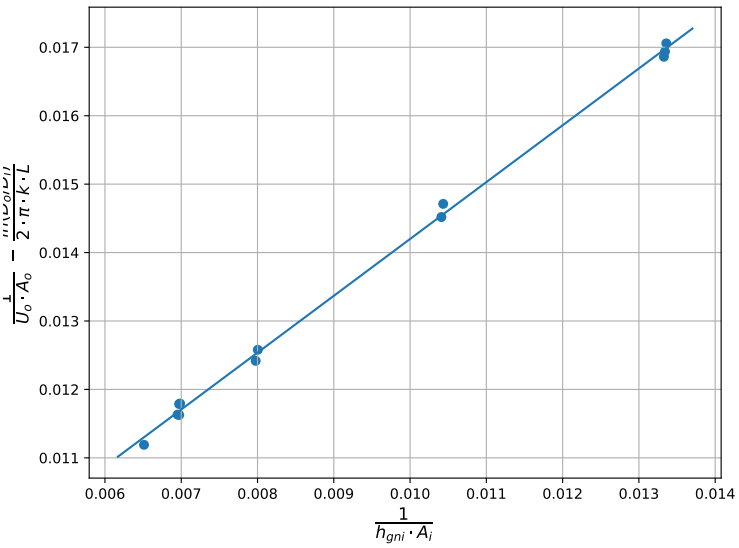

Wilson Plot regression

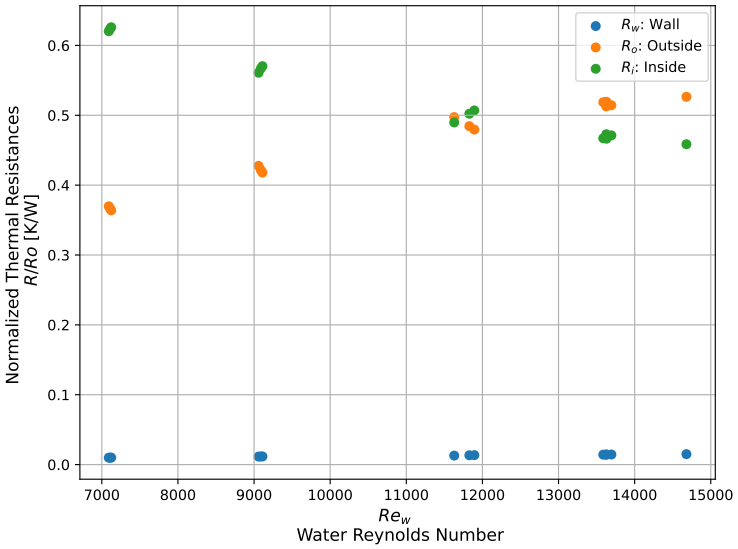

Thermal resistances

Figure L.15: Wilson Plot analysis of Roughened Tube

The Wilson plot regression for the Smooth Tube was depicted in Figure L.14. The thermal resistance ratios show an inside and outside thermal resistance that are closely matched and the expected Wilson Plot coefficient was obtained.

L.21.3 GEWA-B5

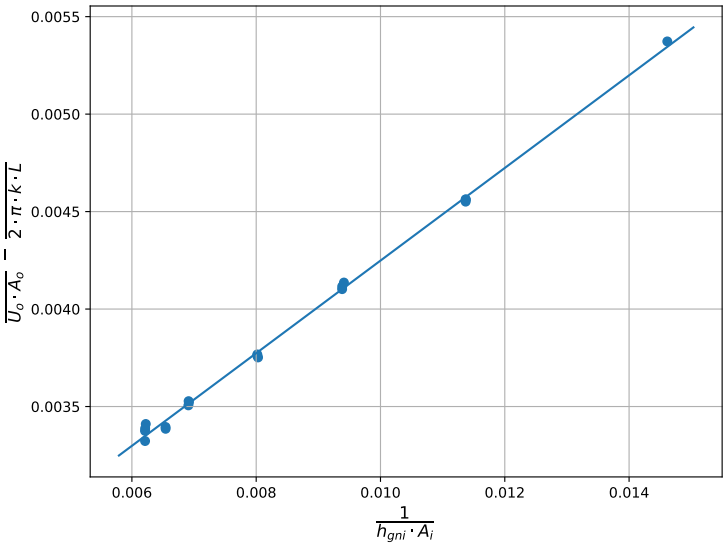

Wilson Plot regression

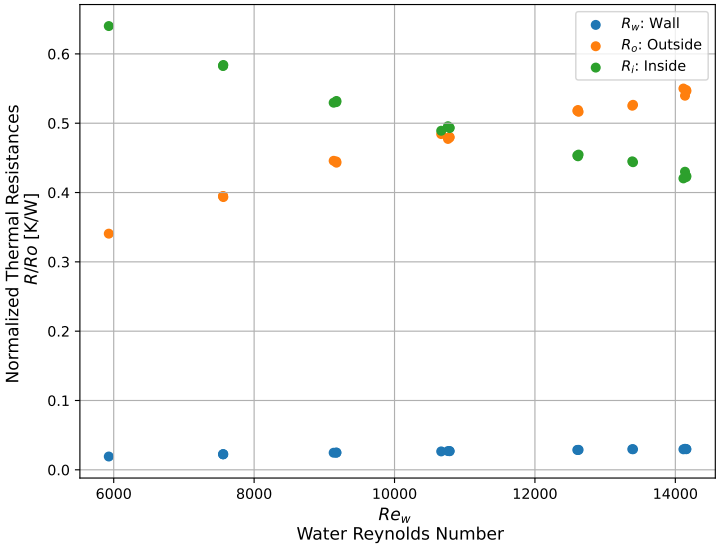

Thermal resistances

Figure L.16: Wilson Plot analysis of GEWA-B5 Tube

The thermal resistance graph in L.16b show that the thermal resistances of the inside and outside generally match. Analogous to the Rough Tube, the expected Wilson Plot coefficient was obtained.

L.21.4 GEWA-KS

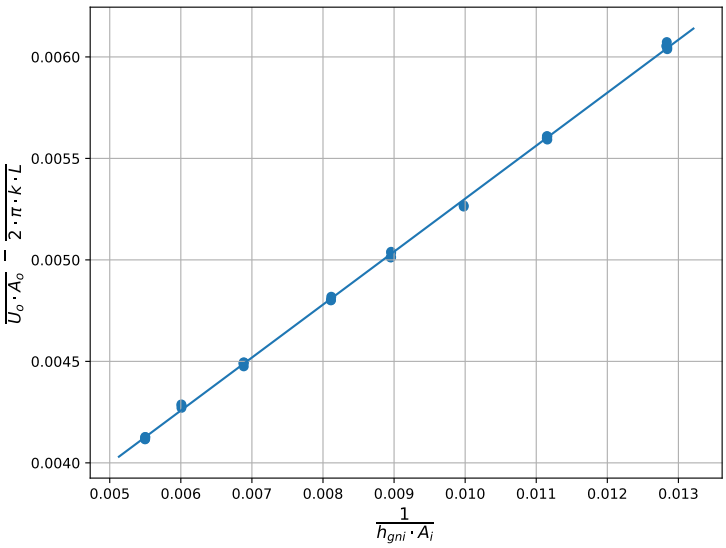

Wilson Plot regression

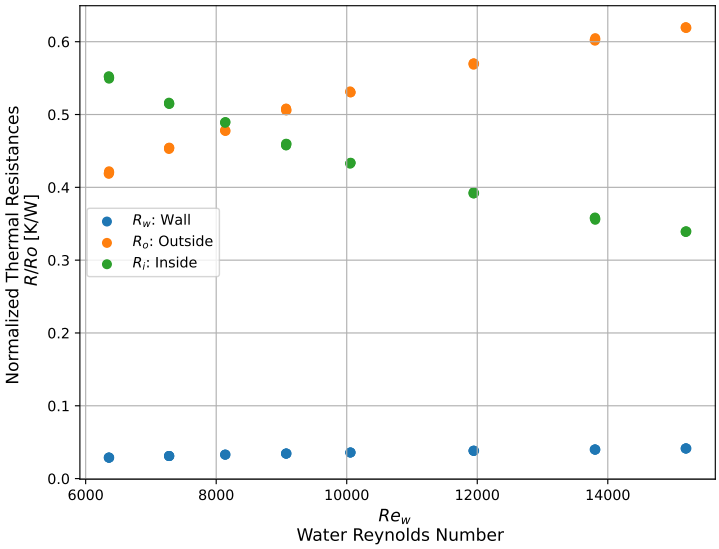

Thermal resistances

Figure L.17: Wilson Plot analysis of GEWA-KS Tube

The thermal resistance graph in L.17b show that the thermal resistances of the inside and outside also generally match. According to the observations of the Rough Tube, the obtained Wilson Plot coefficient was regarded as accurate.

L.21.5 EHPII

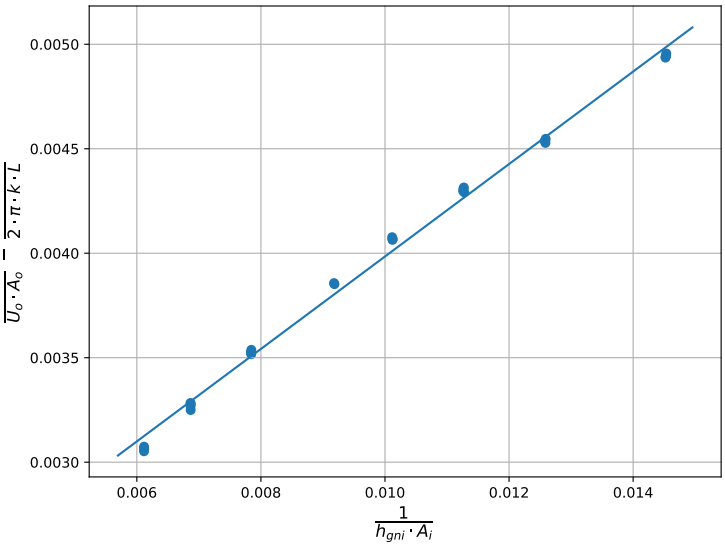

Wilson Plot regression

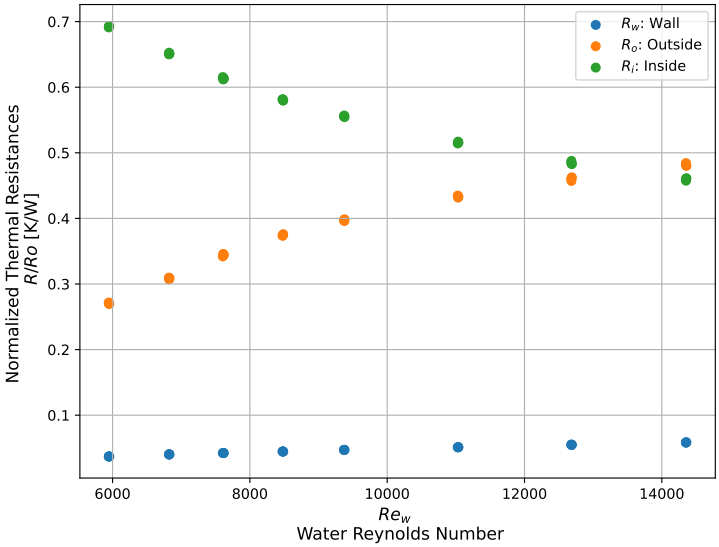

Thermal resistances

Figure L.18: Wilson Plot analysis of EHPII Tube

The thermal resistance graph in L.17b show that the inside thermal resistance is more than the outside thermal resistance. According to the findings by van Rooyen and Thome [73] the obtained Wilson Plot coefficient was reliable.

Appendix M:
Nucleation and Bubble Density

The nucleation site density (as the camera position was always the same, the count is referred too as the density) and the bubble density could be determined for the GEWA-B5 tube in pool boiling at $20kW/m^2$where the inundation of bubbles did not obscure the high speed footage.

The process of counting the still frames for this case is shown below:

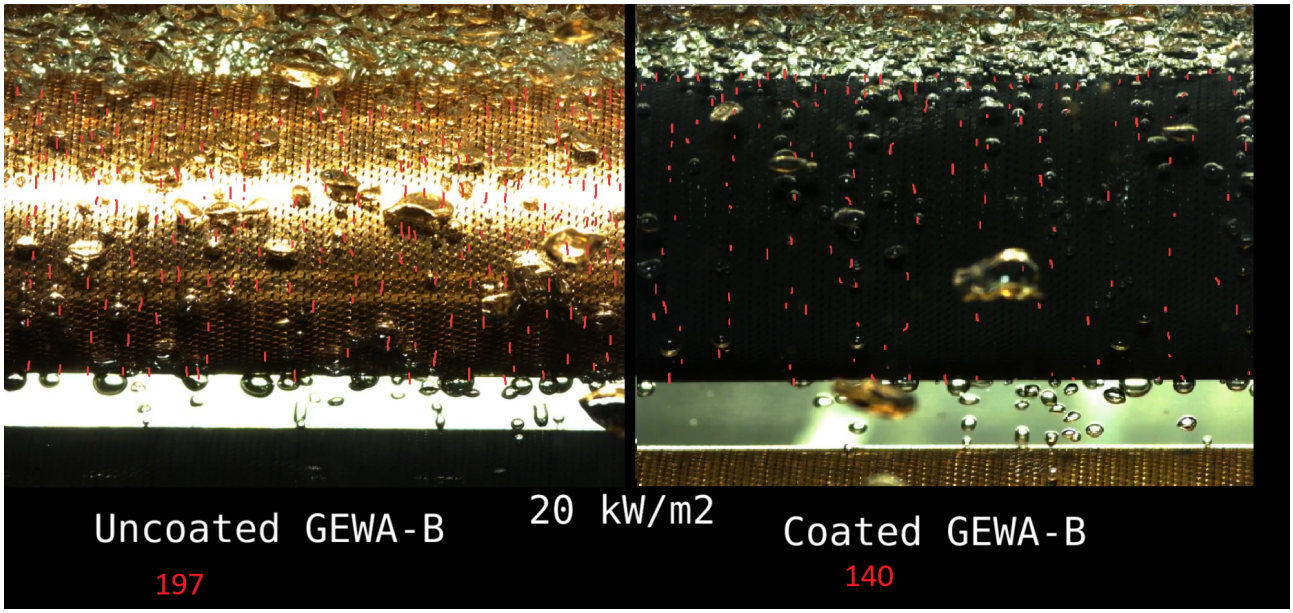

Figure M.19: Nucleation site counting for GEWA-B5 at $20kW/m^2$in pool boiling at 5°Cin R134a

The above counting in Figure M.19 yielded a nucleation site count of 197 for the uncoated tube and 140 for the coated tube. This results in a lower nucleation site density of $\frac{140}{197} = 0.71$ of the uncoated tube by the coating.

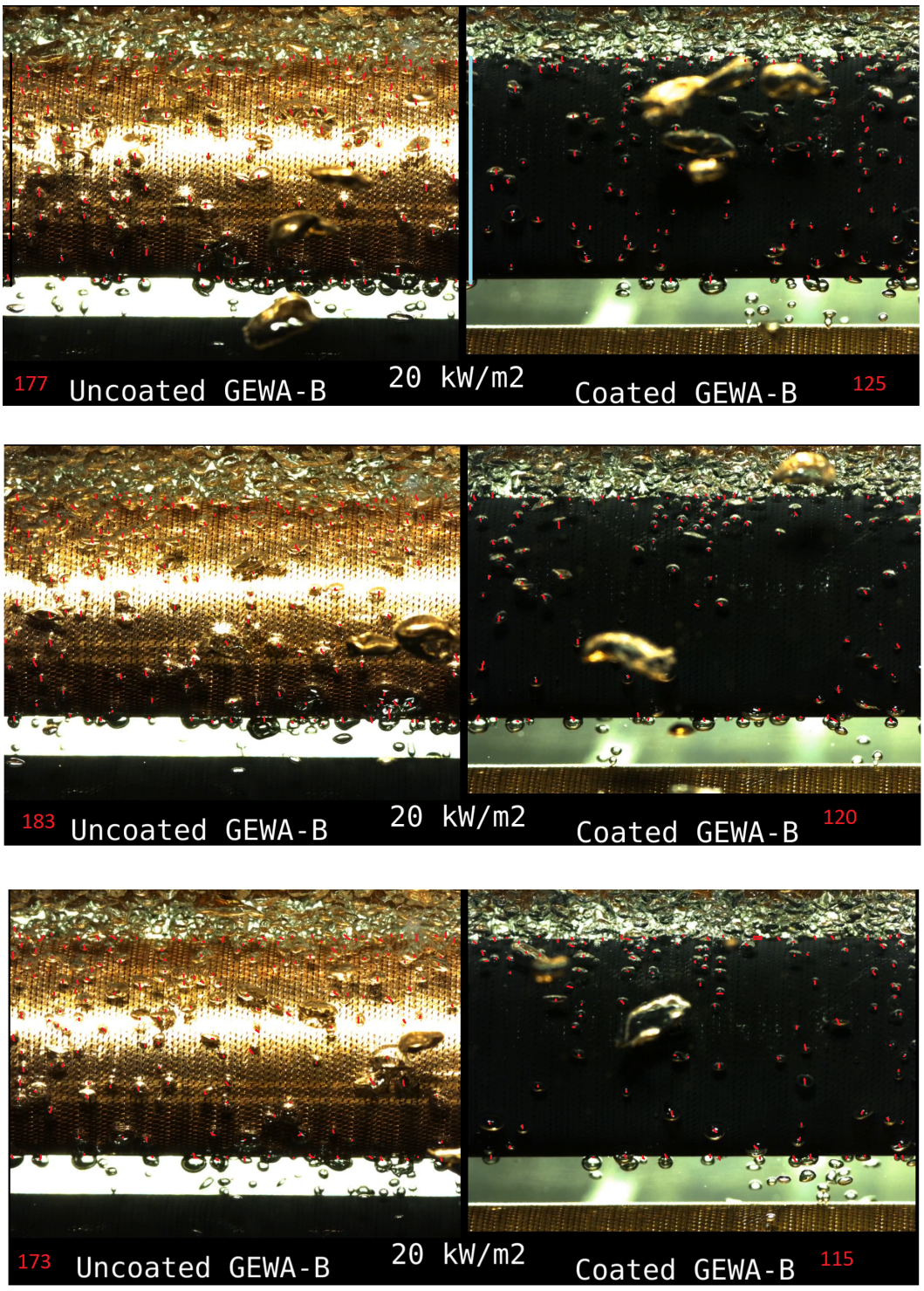

Figure M.20: Bubble counting for GEWA-B5 at $20kW/m^2$in pool boiling at 5°Cin R134a

The bubble counting in Figure M.20 above yielded in a decrease in bubble count be the coating where the number of bubbles for the coated tube was $\frac{125+120+115}{177+183+173} = 0.68$ of that of the uncoated tube.

Appendix N:
Heat Transfer Analyses Models for the Nanocoating

N.22 Simple Nucleation Model

The following mathematical models have been applied, as derived and adapted from previous studies, to typically describe the heat transfer degradation by a nanocoating with low interconnectivity and constructed from random sharp nanostructures:

Since the CuO nanostructure cavities could not reliably be measured from the planar SEM photographs and the R134a liquid contact angle measured at the same testing conditions, it is assumed that the Bankoff [9] criteria is fulfilled in equation (N.42) below, where the contact angle θ between the liquid R134a and the CuO coated surface is larger than the opportune nanocoating cavity angle β since the nanocoating is on micro-scale, such that vapour entrapment is possible and nucleation can occur in the nanocoating cavities.

$$\theta > \beta \tag{N.42}$$

The following simple nucleation equation in the Claperyon-Clausius form as expressed by Xiangdong et al. [28] with respect to the cavity radius in equation (N.43) form thereby applied to those nano-cavities undergoing nucleation:

$$T_o - T_{sat} = \frac{4 \cdot \sigma \cdot T_{sat}}{r_c \cdot \rho_v \cdot h_{fg}} \cdot K \tag{N.43}$$

$$K = \begin{cases} 1 \; ; \; \theta \leqslant 90^\circ \\ \sin(\theta) \; ; \; \theta > 90^\circ \end{cases} \tag{N.44}$$

Where K would be taken as 1 in (N.43) from the assumption in equation (N.44).

Observing equation (N.43), it was noted by Xiangdong et al. [28], Thome [94] and Attinger et al. [34] that a very small cavity with radius r_c would relate to a very high temperature superheat $(T_o - T_{sat})$ for nucleation. Hereby, the nucleation site density on a CuO nanocoated surface would most likely not be increased due to the coating nanostructures.

N.23 Critical Bubble Radius

To aid the explanation of rapid bubble development where the bubbles seemed to have become trapped on the GEWA-B5 surface under pool boiling, the following model is provided:

The slow hydraulic movement resulted in the bubble not to sufficiently grow past the critical bubble radius r_b, as in equation N.45 below, The critical bubble radius in relation to the superheat is observed through the Claperyon-Clausius equation accommodating the Young-

Laplace equation for a bubble as expressed by Nilanjana et al. [95] and is given by:

$$T_o - T_{sat} = \frac{2 \cdot \sigma \cdot T_{sat}}{r_b \cdot \rho_v \cdot h_{fg}} \tag{N.45}$$

N.24 Evaporative Heat Flux

Another possible contributor to the degradation of HTCs could be the evaporative heat flux component being degraded by the CuO nanocoating.

The effect of the CuO coating within the total heat transfer is alluded to with the total heat flux description as stipulated by Rohsenow et al. [9] and interpreted by Xiangdong et al. [28] through:

$$q = q_e + q_c + q_q + q_{ch} \tag{N.46}$$

The evaporative heat flux, q_e, is necessary to be increased to enhance HTCs and is thereby the focus. The flooding of cavities decreased the evaporative heat flux component in equation N.46 by the thickening of the superheating micro-layer and consequently reduced the HTCs [28]. The heat transfer would then likely redistribute back to the other heat transfer mechanisms as described in equation (N.46). It would be more beneficial for such coatings which enhances surface wettability and which have such high surface energy (strong interactivity between the surface and the boiling medium) to delay the CHFs due to nucleation site flooding and the strong liquid supply to working nucleation sites than to enhance HTCs.

N.25 Bubble Departure Size on Nanocoated Surfaces

Pursuing the cause of the larger bubbles, the liquid surface tension difference and liquid contact angles must be quantified. It would be beneficial for future studies to investigate the more accurate bubble departure diameters using the exact measured CuO nano-cavity widths and the contact angles of the specific working medium (not with water, but refrigerant). These could be used along with the bubble departure diameter equation as presented by Robert et al. [96] in equation (N.47) below to better quantify the difference in bubble diameter departure sizes from the uncoated to coated surfaces during boiling:

$$d_b = \left(\frac{12 \cdot \sigma \cdot w \cdot \sin \Theta}{\pi \cdot g \cdot (\rho_l - \rho_v)} \right)^{1/3} \tag{N.47}$$

N.26 Falling Film Boiling Configuration Enhancement

It is expected to see the greater falling film boiling heat transfer enhancement for all tubes at lower heat fluxes for both uncoated and coated cases. This is explained by Cerza [36] through equation (N.48) below, where the effective heat transfer coefficient comprised of both boiling

heat transfer, h_{boi}, and the full effects of the falling film encapsulated by the forced convection heat transfer coefficient, h_{fc}:

$$h_{tot} = h_{fc} + \frac{A_{boi}}{A_{tot}} \cdot (h_{boi} - h_{fc}) \tag{N.48}$$

N.27 Surface Tension of the Surface-Liquid-Vapour Interface

The surface tension of the bubbles during boiling would be different between the uncoated and CuO coated tube surfaces, especially at bubble departure. The addition of the CuO coating changes the liquid-solid interface behaviour through the greater wettability characteristic to incur different liquid-solid contact angles. The surface tension is dependent on the directions of attraction forces between the bubble surface molecules and the liquid-solid-gas interface [97] and it is highly likely that it would increase with the strengthening of adhesive forces. This is observed through equation N.49 for a bubble in a conical deepening as presented by Fisenko [98], where it is seen that the liquid-vapour surface tension would increase with a decrease in liquid contact angle θ:

$$\sigma_{s,v} = \sigma_{liq,s} + \sigma_{liq,v} \cdot \cos(\theta) \tag{N.49}$$

Appendix O:
Falling Film Dryout Tests

O.28 GEWA-KS

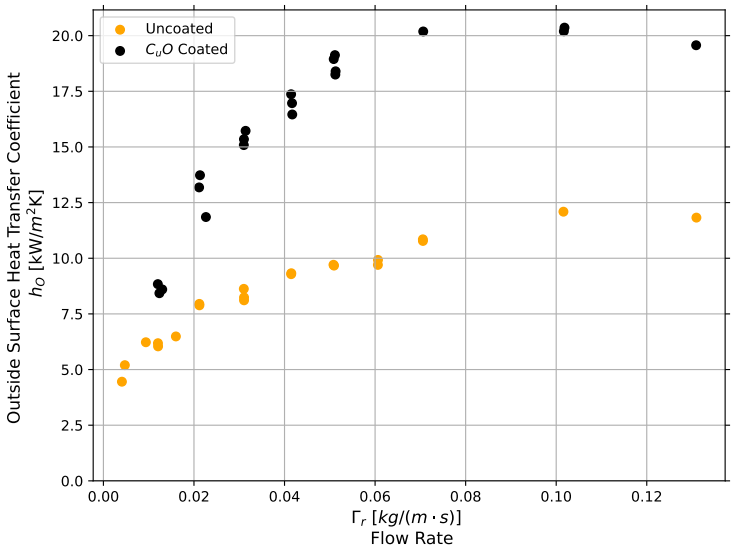

(a) Dryout inspection

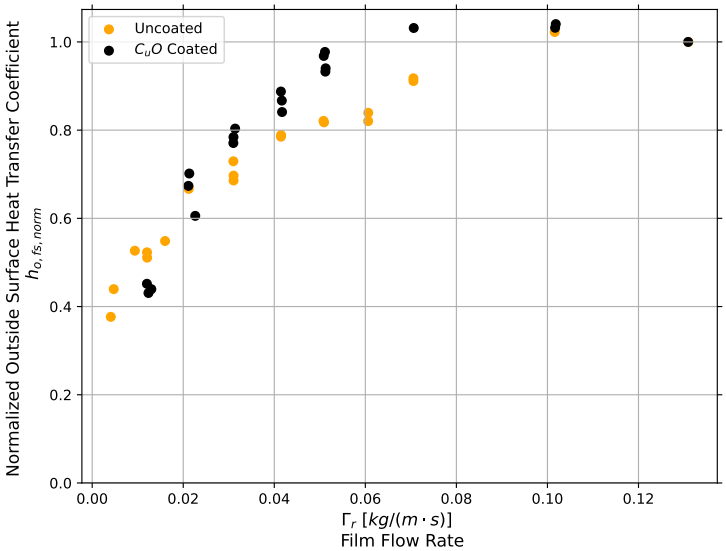

(b) Normalized HTCs

Figure O.21: 20 kW/m^2 Film dryout tests of GEWA-KS at 5°C saturation temperature

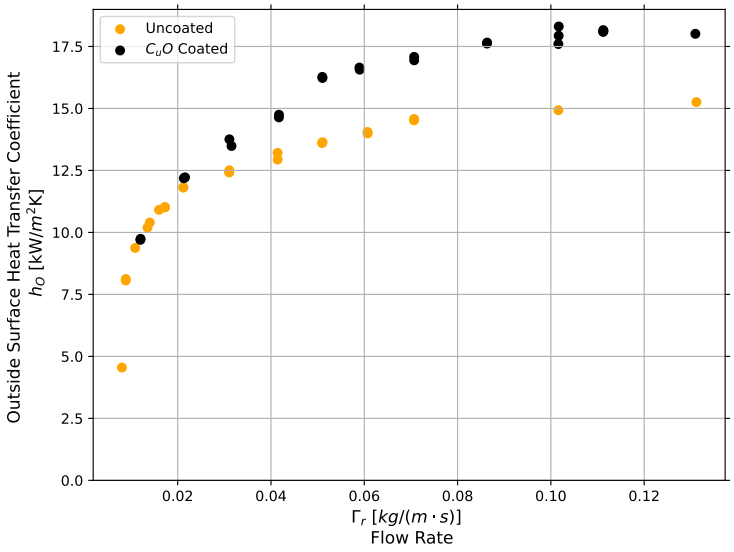

(a) Dryout inspection

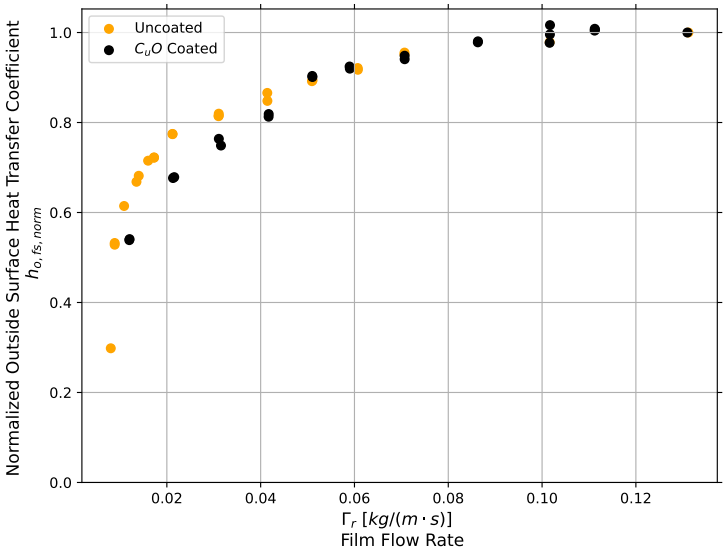

(b) Normalized HTCs

Figure O.22: 50 kW/m^2 Film dryout tests of GEWA-KS at 5°C saturation temperature

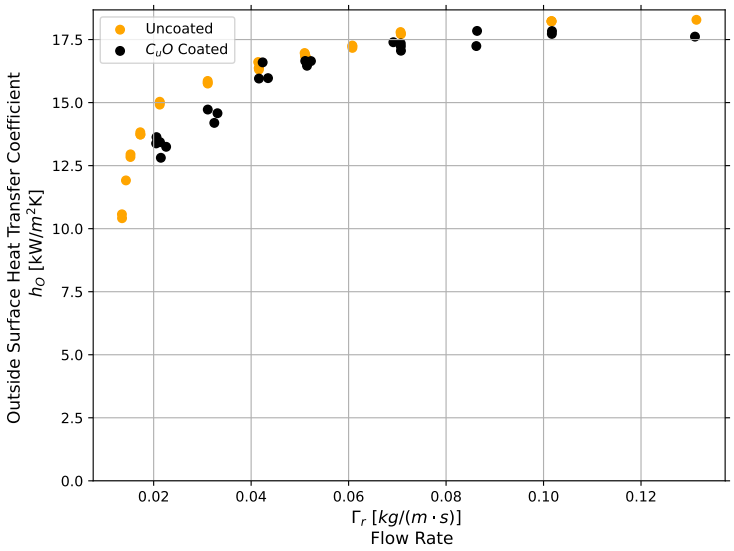

(a) Dryout inspection

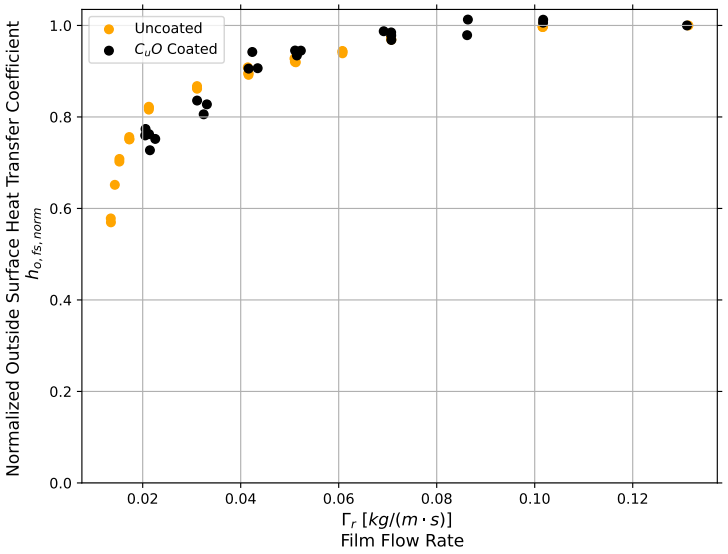

(b) Normalized HTCs

Figure O.23: 80 kW/m^2 Film dryout tests of GEWA-KS at 5°C saturation temperature

O.29 GEWA-B5

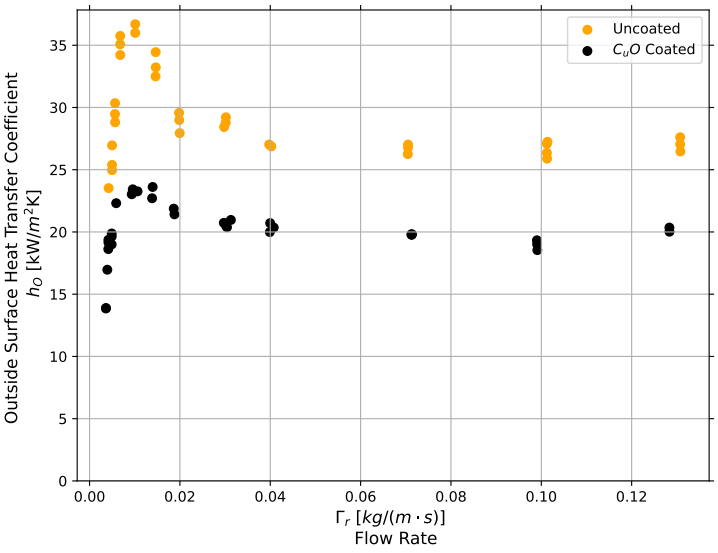

Dryout inspection

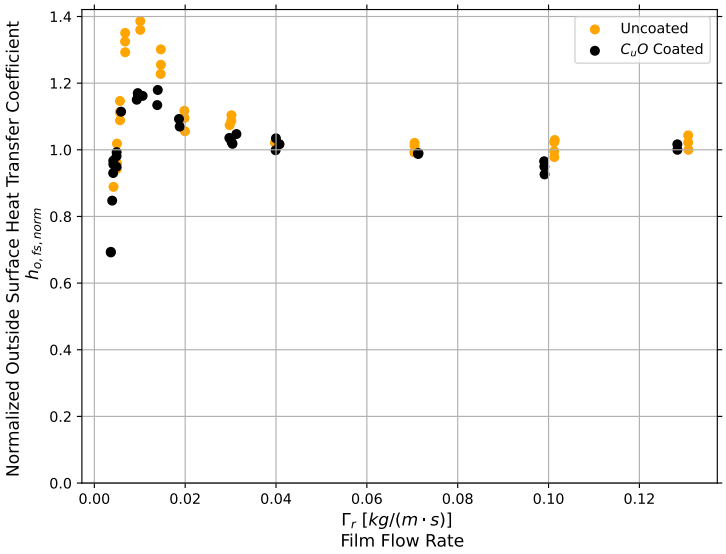

Normalized HTCs

Figure O.24: 20 kW/m^2 Film dryout tests of GEWA-B5 at 5°C saturation temperature

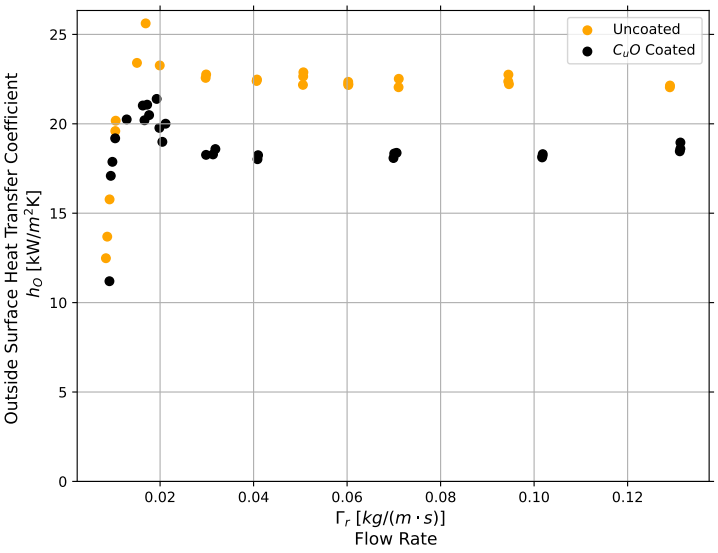

Dryout inspection

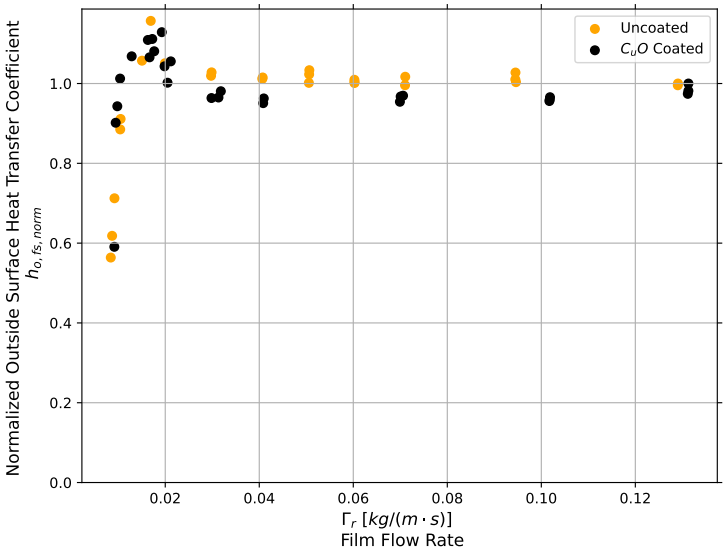

Normalized HTCs

Figure O.25: 50 kW/m^2 Film dryout tests of GEWA-B5 at 5°C saturation temperature

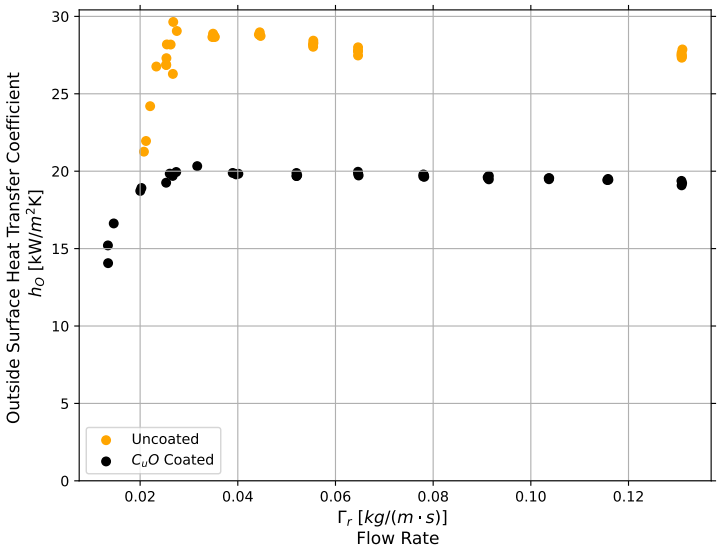

Dryout inspection

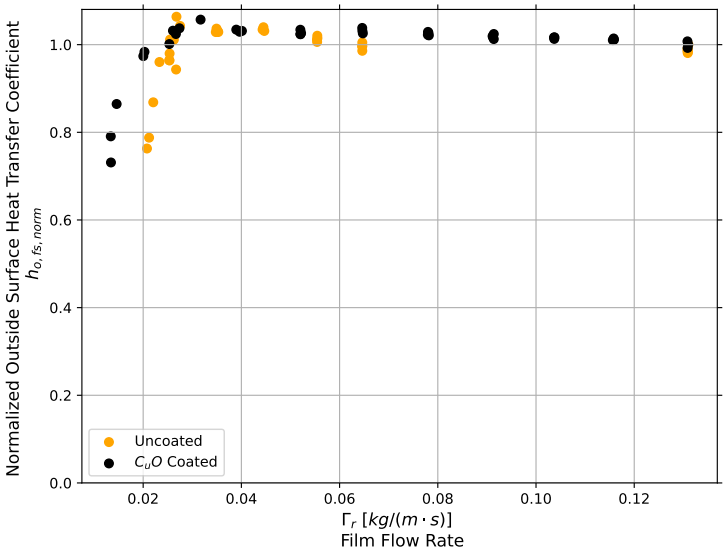

Normalized HTCs

Figure O.26: 80 kW/m^2 Film dryout tests of GEWA-B5 at 5°C saturation temperature

O.30 EHPII

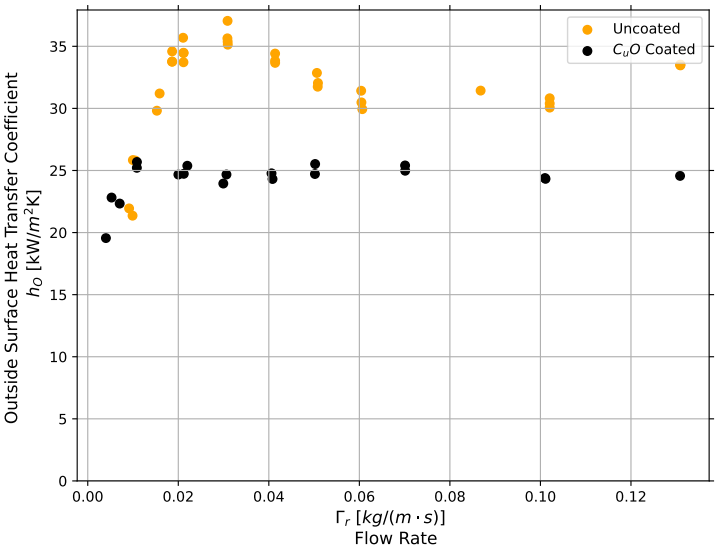

Dryout inspection

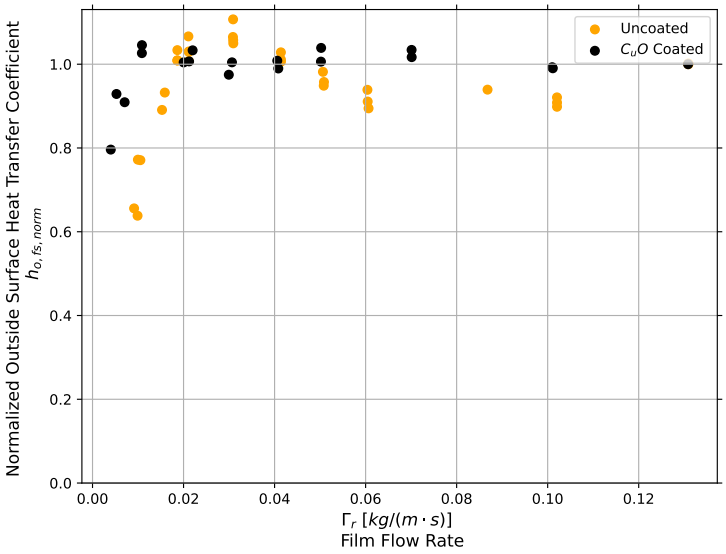

Normalized HTCs

Figure O.27: 20 kW/m^2 Film dryout tests of EHPII at 5°C saturation temperature

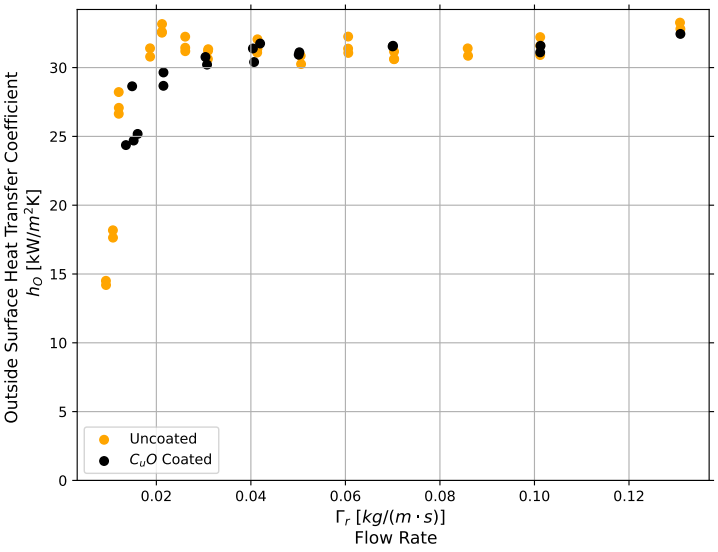

Dryout inspection

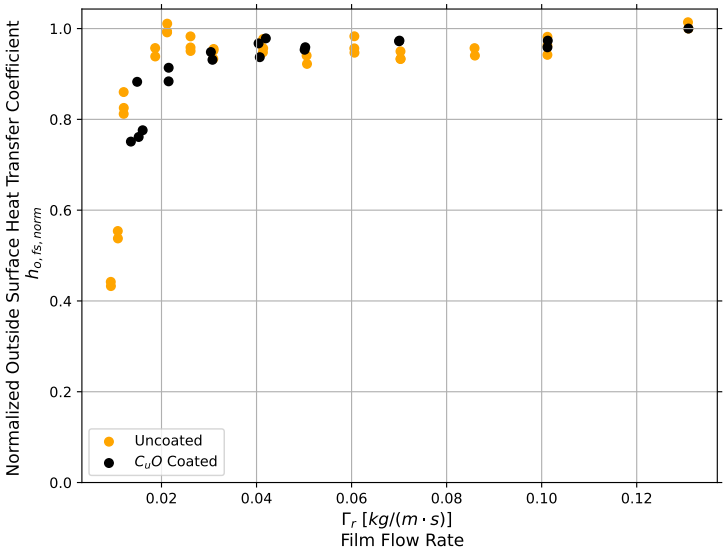

Normalized HTCs

Figure O.28: 50 kW/m^2 Film dryout tests of EHPII at 5°C saturation temperature

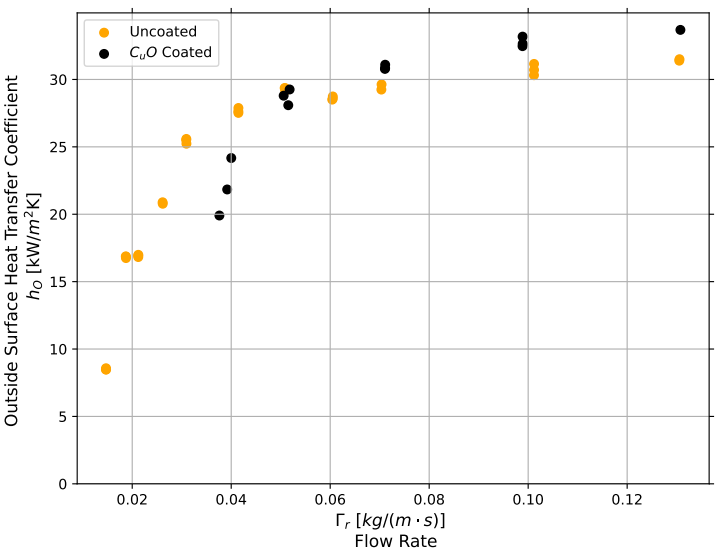

Dryout inspection

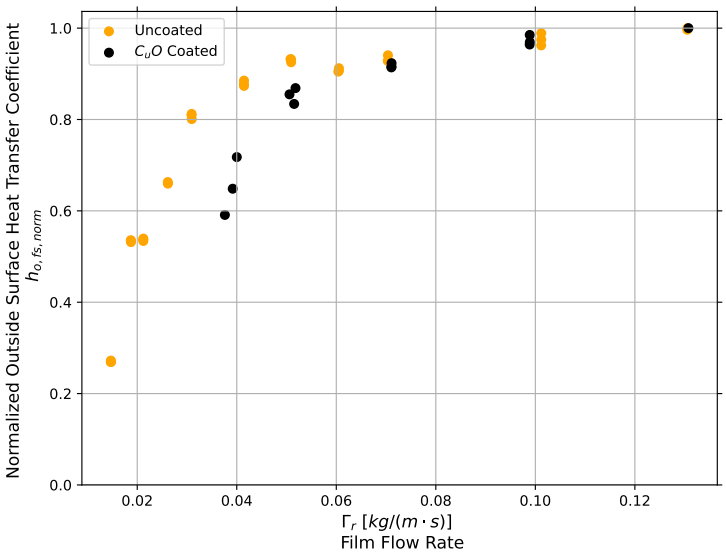

Normalized HTCs

Figure O.29: 80 kW/m^2 Film dryout tests of EHPII at 5°C saturation temperature

Appendix P:
Normalized Cooper Correlation

If the Cooper correlation was assumed perfect, the data between the current study and Bock for the smooth tube pool boiling case can be normalized to the respective roughness terms according to equations (P.50) and (P.51):

$$C_{smooth} = h_o/(90 \cdot Pr^{0.12-0.2\cdot\log(0.04/0.4)}) \tag{P.50}$$

$$C_{Bock} = h_{o,Bock}/(90 \cdot Pr^{0.12-0.2\cdot\log(0.18/0.4)}) \tag{P.51}$$

Force-fitting the Cooper correlation to the data-sets produced Figure P.30, which showed very little perceptive deviation:

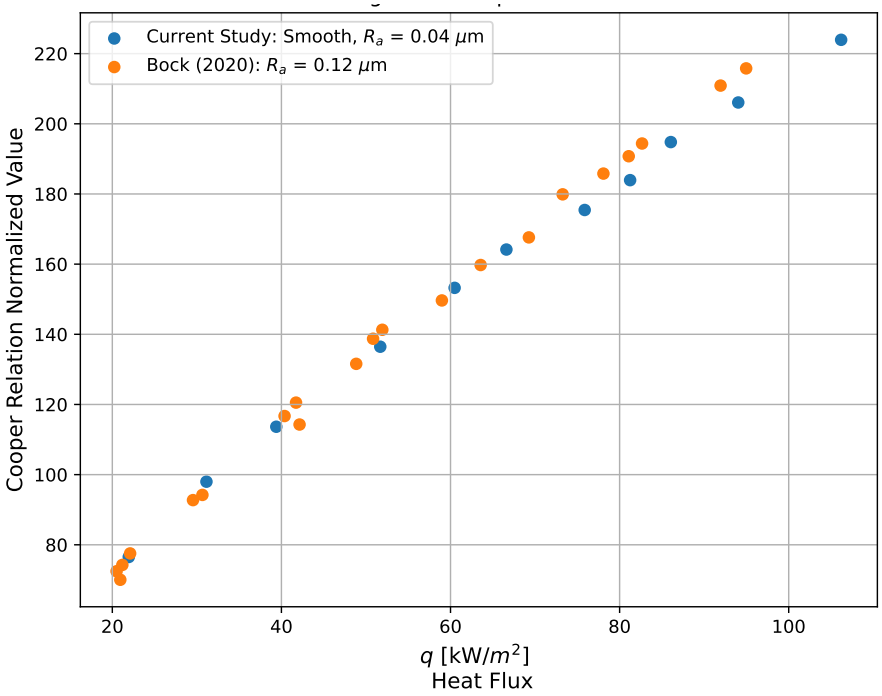

Figure P.30: Cooper correlation normalized pool boiling data comparison of smooth tube